



Università degli Studi di Cagliari

**PHD DEGREE**

Physics

Cycle XXXII

**Design and test of a timing optimized 3D silicon sensor for  
HL-LHC experiments**

Scientific Disciplinary Sectors

FIS/01 FIS/04

PhD Student:

ANGELO LOI

Coordinator of the PhD Programme:

Prof. PAOLO RUGGERONE

Supervisor:

Dott. ADRIANO LAI

Final exam. Academic Year 2018 – 2019

Thesis defence: February 2020 Session





Angelo Loi gratefully acknowledges Sardinian Regional Government for the financial support of his PhD scholarship (P.O.R. Sardegna F.S.E. - Operational Programme of the Autonomous Region of Sardinia, European Social Fund 2014-2020 - Axis III Education and training, Thematic goal 10, Investment Priority 10ii), Specific goal 10.5.



Furthermore, Angelo Loi gratefully acknowledges the INFN-TIMESPOT project and the LHCb Cagliari division for their very important logistical and scientific support during the entire PhD.



## Ringraziamenti:

I intend to write the following acknowledgements in Italian, in order to be more comprehensive for most of the people I want to dedicate this work!

Sono stati 3 anni faticosi in cui mi sono addentrato in una disciplina molto di nicchia la cui fama iniziai a sentire all'inizio della laurea magistrale. In 3 anni di dottorato posso garantire che la mia crescita sia stata non solo di tipo professionale ma anche caratteriale, capendo (a grandi caratteri) che il mondo della ricerca non è soltanto scienza pura e lavoro sodo ma è soprattutto interazione tra individui. Individui che insieme formano un collettivo, una collaborazione che aspira ad un unico obiettivo. È stato difficile per me (e lo è tutt'ora in certe situazioni) interagire con un gran numero di persone ma è grazie al supporto della gente che mi sta intorno, in particolare quella che mi sta vicina da decenni soprattutto fuori dal dipartimento, che con la loro motivazione e incitamento hanno fatto sì che sia ancora qua in questo ufficio del dipartimento di fisica, ad aspettare all'esaminazione finale del dottorato.

In parte questo dottorato è anche il loro.

Ringrazio in assoluto i miei genitori, **Gina Cabras** e **Italo Loi** per tutta la loro educazione, supporto e incoraggiamento dati negli ultimi anni e mio fratello **Marco Loi**, persona di grande carattere e rigore, che mi ha sempre incitato di non arrendermi nei momenti più difficili.

Non posso che non dimenticarmi degli amici più vicini, quelli di vecchissima data conosciuti in Germania, come **Marvin Perez Camacho** e **Giusy Giardina** e coloro che ho conosciuto nei primissimi anni di vita in Sardegna: **Carlo Piras**, **Lorenzo Serra** e **Gabriele Melis**. Amici che sono riusciti a togliermi un po' di quel rigore tedesco che avevo, mostrando che si può essere bravi senza rinunciare agli aspetti più "umani" della vita.

Ovviamente non posso dimenticarmi degli amici conosciuti all'università sia dentro che fuori il dipartimento di fisica: **Gabriele Traversari**, **Pasquale Mattu**, **Patrizio Beccu**, **Claudia Macciò**, **Jessica Satta**, **Gabriele Sarigu**, **Davide Brundu** e **Mattia Taccori**.

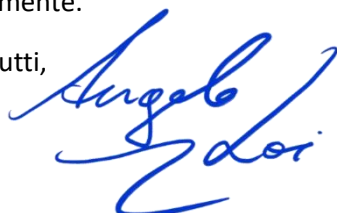
Un grande Dankeschön anche a **Matteo Pais** per la compagnia intellettuale e culturale durante il tempo libero in ufficio e per i suoi suggerimenti.

Vanno citate in particolare due persone conosciute nello stesso mese di quel lontano 2015, quando ero ancora un ansioso e diffidente studente del corso di laurea magistrale. Uno come collega e grande amico, fonte di grandi suggerimenti e motivazione: **Luigi Casu**. L'altra, conosciuta alla casa dello studente di via Biasi. Persona dal carattere raro che nei giorni d'oggi la rende una persona di valore inestimabile: **Federica Sanna**.

Gli ultimi ringraziamenti vanno senza ombra di dubbio al mio Supervisore, Dottor **Adriano Lai**, per avermi concesso questa grande opportunità di lavorare all'interno di questo prestigioso progetto.

Ringrazio anche gli altri colleghi e ricercatori con cui ho interagito negli ultimi 4 anni, acquisendo importanti competenze ed esperienze: Dottor **Alessandro Cardini**, Dottor **Andrea Contu** e Dottor **Sandro Cadeddu** di Cagliari, Professore **Gian Franco Dalla Betta**, dottor **Roberto Mendicino**, così come Dottor **Paola Collins** e Dottor **Victor Coco** durante il mio periodo di formazione a Trento e al CERN rispettivamente.

Grazie a tutti,





# Abstract

The future High Luminosity Large Hadron Collider (HL-LHC) is a large upgrade program of the LHC at CERN which will allow to run all experiments at higher luminosity after 2025. The advantage of running experiments at higher luminosity is an increment of the collected data at the cost of a stronger impact on the detector systems lifespan, track reconstruction efficiency and data acquisition due to an increased radiation damage and the high event pile-up. Especially for tracking detectors close to the interaction point, like the LHCb VELO detector, those problems will be a greater issue, with a potential radiation damage above  $1 * 10^{16}$  MeV  $n_{eq}cm^{-2}$  and a pile-up above 100 events per bunch crossing for ATLAS and 40 for LHCb.

The need for a new generation of tracking detectors capable of operating at those conditions, with same or better track reconstruction performances, leads to the development of new methods and technologies. For example, according to preliminary simulations performed by the LHCb collaboration, using as reference the upgrade-I model of the VELO and running the detector in high luminosity environment, the best way to ensure high track reconstruction efficiency is using particle tracking with high space resolution coupled with high resolution time measurement below 200 ps. Radiation damage on the other hand forces the development of new sensor technologies, like 3D sensors or diamond sensors which present an intrinsic high radiation hardness compared to classic planar devices. The INFN-CSN5 TIMESPOT project aims to develop a first prototype of a next generation 4D tracking detector, featuring small pitch and timing optimised 3D silicon and diamond sensors, a 28 nm CMOS technology based read-out chip and real-time tracking algorithms.

This work presents the development and test of the timing optimised 3D silicon, starting from the first computer aided design (CAD) sketch to the first test beam results obtained using the first prototype.

Chapter 1 describes the scientific motivations of this work, introducing to the main aspects of the HL-LHC and the challenge it sets to future tracking detectors. The chapter also briefly describes the phase-I upgrade of the LHCb Vertex Locator (VELO) detector and first proposals and ideas for the high luminosity LHCb (phase-II) upgrade. Chapter finishes with the presentation and general

description of the INFN-TIMESPOT project.

Chapter 2 and 3 shows the physical principles of silicon sensors and introduces 3D silicon sensor for timing purposes respectively.

Chapter 4 describes the design activity carried out to define a timing optimised 3D silicon sensor. The chapter starts presenting the motivations that force to develop a customised electrode geometry for a 3D silicon sensor in order to optimise it for high resolution time measurement. It continues describing the design activity, based on Technology CAD design, and the selection of the final geometry. The selection was based on a first analysis of the electric field, considering especially coverage, uniformity and the presence of low electric field areas. The development of Ramo-maps allowed a more detailed selection, based on the current induction over the entire sensor volume. The chapter ends with the presentation of the final electrode design, a square pixel shaped pixel with 3 parallel trench-electrodes and its fabrication, performed by Fondazione Bruno Kessler (FBK) in Trento.

Chapter 5 describes sensor operation in time domain, starting with TCAD simulations and introducing a different approach using GEANT4 simulations to enhance the detail of the energy deposits in TCAD. The chapter ends presenting the results based on those simulations and introduces to chapter 6 with the results obtained using TCoDe. Chapter 6 describes purpose and structure of the TIMESPOT CODE for DETECTOR simulation and its validation using TCAD as reference tool. Chapter 7 concludes this work presenting the first experimental measurements performed on the sensor, bonded on different electronic readouts, using a 200 fs pulsed infra red laser source and a successive test beam performed at the Paul Scherrer Institute (PSI) in Zurich.

# Contents

<b>1</b>	<b>Introduction</b>	<b>17</b>
1.1	The Large Hadron Collider . . . . .	17
1.1.1	General structure . . . . .	17
1.1.2	Luminosity . . . . .	19
1.2	The High Luminosity upgrade . . . . .	20
1.2.1	Critical aspects of the HL-LHC . . . . .	21
1.3	High Luminosity at LHCb . . . . .	23
1.3.1	The VELO phase-I upgrade as a step forward towards high luminosity . . . . .	24
1.3.2	Limits of the phase-I VELO in high luminosity . . . . .	30
1.4	The TIMESPOT project . . . . .	32
1.4.1	Contribution of this work in TIMESPOT . . . . .	34
<b>2</b>	<b>Introduction to silicon sensors</b>	<b>35</b>
2.1	Conduction in solids . . . . .	35
2.1.1	Physical properties of silicon . . . . .	36
2.1.2	Charge motion in silicon . . . . .	36
2.1.3	Doping . . . . .	39
2.2	The pn-junction . . . . .	41
2.3	Silicon diode as particle sensor . . . . .	42
2.3.1	General characteristics . . . . .	42
2.3.2	Particle-matter interaction . . . . .	45
2.3.3	Energy transfer of charged particles . . . . .	46
2.3.4	Signal formation in silicon sensors . . . . .	47
2.4	Radiation damage . . . . .	52
2.4.1	Radiation damage effects on sensor performance . . . . .	54
2.4.2	Radiation damage effects on signal formation . . . . .	55
2.4.3	Radiation damage mitigation techniques . . . . .	55
2.5	Overview of particle sensors . . . . .	56
2.5.1	Planar sensors . . . . .	56
2.5.2	Avalanche sensors . . . . .	57
2.5.3	3D sensors . . . . .	58

<b>3</b>	<b>3D sensors for fast timing applications</b>	<b>59</b>
3.1	3D sensors . . . . .	60
3.1.1	Structure and fabrication . . . . .	60
3.1.2	Applications . . . . .	63
3.2	3D and timing . . . . .	65
3.2.1	Total time resolution of a particle detector system . . . . .	65
3.2.2	Timing error sources in 3D silicon sensors . . . . .	70
3.2.3	First experimental results . . . . .	72
3.3	Approach to develop a timing optimised 3D sensor . . . . .	73
<b>4</b>	<b>Sensor development and production</b>	<b>75</b>
4.1	Description of the problem . . . . .	75
4.2	Specifications and design approach . . . . .	77
4.3	Explored Geometries . . . . .	79
4.3.1	Hexagonal pixel geometries . . . . .	80
4.3.2	Square shaped geometries . . . . .	82
4.3.3	Evaluation of closed and semi-closed pixel geometries . . . . .	85
4.4	Ramo Maps . . . . .	86
4.5	3D sensor modeling . . . . .	91
4.5.1	Capacitance simulation . . . . .	93
4.6	Prototype sensor production . . . . .	94
<b>5</b>	<b>Sensor operation simulation</b>	<b>99</b>
5.1	Motivation . . . . .	99
5.2	Sentaurus TCAD transient simulations . . . . .	100
5.2.1	Sentaurus Device Heavy Ion Model . . . . .	101
5.3	Critical aspects of pure TCAD sensor operation simulation . . . . .	103
5.4	TCAD simulations with GEANT4 deposit . . . . .	105
5.5	Mesh strategy for 3D model transient simulation . . . . .	109
5.6	Results . . . . .	116
5.6.1	TCAD 2D model simulation . . . . .	116
5.6.2	3D model simulation . . . . .	124
5.6.3	Results obtained with TCoDe . . . . .	128
<b>6</b>	<b>TCoDe</b>	<b>133</b>
6.1	Motivations and general description . . . . .	133
6.2	Program structure . . . . .	134
6.2.1	Configuration . . . . .	134
6.3	Validation, Performance . . . . .	140
6.3.1	Performance . . . . .	140
6.3.2	Tool validation using TCAD . . . . .	142
6.4	Next developments . . . . .	150

0.0. CONTENTS	11
<b>7 TIMESPOT sensor tests</b>	<b>153</b>
7.1 The test structures and board . . . . .	153
7.2 IV characteristic measurement . . . . .	155
7.3 Laser stimulation . . . . .	158
7.3.1 Set-up . . . . .	158
7.3.2 Results . . . . .	159
7.4 Test-beam . . . . .	161
7.4.1 Set-up . . . . .	161
7.4.2 Analysis . . . . .	164
7.4.3 Results . . . . .	169
<b>Conclusions</b>	<b>173</b>
<b>Bibliography</b>	<b>175</b>



## Personal Records during PhD

- **Co-author in LHCb publications since July 2018**
- **A. Loi**, G. F. Dalla Betta, A. Lai, R. Mendicino, S. Vecchi, Design and simulation of 3D-silicon sensors for future vertex detectors, 2018 IEEE Nuclear Science Symposium and Medical Imaging Conference Proceedings (NSS/MIC), 2019
- **A. Loi**, A. Contu, R. Mendicino, G. T. Forcolin, A. Lai, G. F. Dalla Betta, M. Boscardin, S. Vecchi, Timing optimization for 3D silicon sensors, Nucl. Instrum. and Methods, section A, Available online 7 August 2019, 162491
- G.T. Forcolin, R. Mendicino, M. Boscardin, A. Lai, **A. Loi**, S. Ronchin, S. Vecchi, G.-F. Dalla Betta, Development of 3D trenched-electrode pixel sensors with improved timing performance, 2019 JINST 14 C07011
- R. Mendicino, G.T. Forcolin, M. Boscardin, F. Ficorella, A. Lai, **A. Loi**, S. Ronchin, S. Vecchi, G. F. Dalla Betta, 3D trenched-electrode sensors for charged particle tracking and timing, Nucl. Instrum. and Methods, section A, Volume 927, 21 May 2019, Pages 24-30
- **A. Loi**, A. Lai, G.F. Dalla Betta, R.Mendicinod, S.Vecchi, Simulation of 3D-Silicon sensors for the TIMESPOT project, Nucl. Instrum. and Methods, section A, Volume 936, 21 August 2019, Pages 701-702
- S. Cadeddu, L. Casu, D. Brundu, A. Cardini, A. Lai, **A. Loi**, The nSYNC ASIC for the new readout electronics of the LHCb Muon Detector Upgrade, Nucl.Instrum.Meth. 936 (2018) 378-379
- **A. Loi**, 3D DETECTORS WITH HIGH SPACE AND TIME RESOLUTION, Journal of Physics: Conference Series, vol. 956, 012012, 2018.
- S. Cadeddu, A. Aloisio, F. Ameli, P. Bifulco, V. Bocci, L. Casu, R. Giordano, V. Izzo, A. Lai, **A. Loi**, S. Mastroianni, A TIME-TO-DIGITAL CONVERTER BASED ON A DIGITALLY CONTROLLED OSCILLATOR; Conference Proceedings IEEE, Padova, June 2016.
- S. Cadeddu, A. Aloisio, F. Ameli, P. Bifulco, V. Bocci, L. Casu, R. Giordano, V. Izzo, **A. Loi**, A. Lai, S. Mastroianni, A FULLY-DIGITAL AND FULLY SYNTHETIZABLE TDC FOR HIGH ENERGY PHYSICS EXPERIMENTS; Conference Proceedings IEEE, CRACOVIA, June 2016.



*"I give you a toast: The undiscovered country . . . the future"*

---

Chancellor Gorkon, Star Trek VI, the undiscovered country, Film, 1991



# Chapter 1

## Introduction

This chapter introduces the main context of application of this work: the Large Hadron Collider (LHC) at CERN and its high luminosity upgrade scheduled for 2026. Current advanced state of the art tracking detectors at CERN, like the new LHCb-VELO for upgrade-I, cannot cope with the harsh environmental conditions at higher luminosities. Due to the restricted performances, a novel, more performing tracking detector generation must be developed, with a special focus on radiation hardness and better time and space resolution.

This chapter will briefly describe the LHC, the concepts of luminosity and pile-up and introduces the general features of the HL-LHC and the challenges it sets to future detectors. A special focus is dedicated to the LHCb-VELO, the most precise and closest to the interaction point tracking detector at the LHC. This chapter will also show the performances and structure of the new VELO for the upgrade-I, currently under construction, show the final tests before installation, and its limitations for the high luminosity upgrade, demonstrating the need for a future high performance tracking detector.

The chapter closes with the introduction of the INFN-TIMESPOT project, describing its main purpose, structure and how this PhD work fits into it.

### 1.1 The Large Hadron Collider

#### 1.1.1 General structure

The LHC is the largest and most powerful circular particle accelerator currently in operation. It is located underground in a circular, 27km long and 4m wide tunnel at the European Organization for Nuclear Research (CERN) in Geneva, which previously hosted the Large Electron-Positron collider (LEP).

The LHC is capable of accelerating bunches of protons or lead nuclei at velocities close to the speed of light arranged into two different beams, one moving clockwise and the other moving counter-clockwise. Every beam stores 2808 (600)

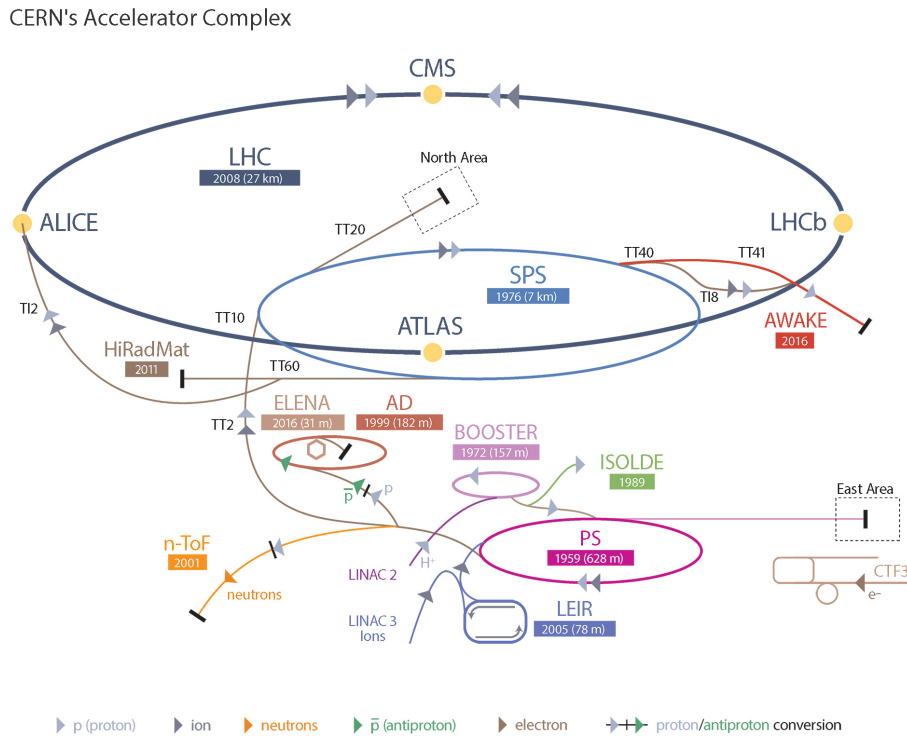


Figure 1.1: CERN accelerator complex.

bunches, each of them filled with approximately 120 billion protons (70 million lead ions). Collisions between opposing particle beams happen at the 4 main interaction points, which host four main experiments. In order to achieve acceleration and hold the bunches inside the beam line, the LHC is built up by almost 10000 super conductive magnets, 1232 of which are dipole magnets of the beam line. The LHC is operational since 2008 and, since then, its experiments have collected approximately  $300 \text{ fb}^{-1}$  of data, making important experimental discoveries like the Higgs boson [1], the CP violation in charm [2] or the penta-quark [3].

**Particle acceleration process:** The LHC is the final acceleration ring of a more complex structure built up by different linear and circular accelerators used to accelerate the protons or lead atoms at the final energy of few TeV. Depending on the accelerated particles, the procedure involves a different number of accelerators and ionisation stations before the beam is injected as a sequence of bunches into the LHC. A general layout of the accelerator complex at CERN is shown in figure 1.1. Basically the particle acceleration starts from a gas bottle filled with pure  $^1\text{H}$  isotope or from a melted lead pellet, depending on the chosen particles. Focusing the attention on protons, the original hydrogen molecules are split into their atoms and ionised. The remaining protons are accelerated through the linac-2, linear

accelerator which gives the protons a final energy of 50 MeV before injecting the bunch into the proton synchrotron booster (PSB), which accelerates the particles at 1.4 GeV. Before entering in the LHC, the proton bunches pass through the proton synchrotron (PS) and the super proton synchrotron, reaching a final energy of 450 GeV before the bunches are filled in the LHC. The entire filling process takes less than 5 min and their final acceleration at 6.5 TeV takes other 20 min. Lead atoms follow a similar acceleration process which is a bit more complicated due to the larger amount of electrons which must be removed before filling the lead nuclei in the LHC with an energy of 1.38 TeV.

**Experiments:** LHC hosts 8 experiments, 4 large experiments and 4 smaller experiments, each of them designed and built to observe specific interactions generated by the beam collisions.

- **A Toroidal LHC ApparatuS** (ATLAS) is one of two general purpose experiments designed to look on new particles and physics.
- **Compact Muon Solenoid** (CMS) is the second general purpose experiment.
- **Large Hadron Collider Beauty** (LHCb) designed to observe rare  $B$  decay processes and observation of CP-violation.
- **A Large Ion Collider Experiment** (ALICE) which is designed to observe quark gluon plasma produced by lead-lead beam collisions.

### 1.1.2 Luminosity

Aside the collision energy, the second parameter which describes the performances of a particle accelerator is its luminosity. The instantaneous (or peak) luminosity produced by the accelerator is defined as the number of interactions in a specific time interval  $\frac{dN}{dt}$ :

$$\mathcal{L} = \frac{1}{\sigma} \frac{dN}{dt} \quad (1.1)$$

Where  $\sigma$  is the cross section of the observed interaction and  $\mathcal{L}$  is measured in  $cm^{-2}s^{-1}$ . In the case of the LHC, the collisions are between crossing beam bunches colliding at a frequency of 40 MHz.

The luminosity of an accelerator depends on different factors, starting from geometrical dependencies like the collision angle and superposition of the colliding bunches, the number of particles per bunch, their collision frequency and the bunch shape [4].

The integrated luminosity  $\mathcal{L}_{int}$  ( $\mathcal{L}$  integrated in time) allows to quantify the amount of observed events in a specific time interval, known also as sensitive time (the time

in which the accelerator is operating, excluding all dead times like the time need to refill the bunches).

$$\mathcal{L}_{int} = \int \mathcal{L} dt \quad (1.2)$$

Integrating the luminosity only over the time interval of a single bunch crossing, the number of observed events is defined as pileup  $\mu$ . The pileup per bunch crossing depends from the number of bunches  $n_b$  stored in the accelerator, the interaction cross section  $\sigma$ , the luminosity  $\mathcal{L}$  and the collision frequency  $f_{bx}$ .

$$\mu = \frac{\sigma \mathcal{L}}{n_b f_{bx}} \quad (1.3)$$

During the first 10 years of operation, from 2009 to the end of 2018, the LHC collected almost  $400 \text{ fb}^{-1}$  of integrated luminosity,  $180 \text{ fb}^{-1}$  for ATLAS and CMS each and  $9 \text{ fb}^{-1}$  for LHCb. The instantaneous luminosity reached on those 3 experiments was  $2 * 10^{34} \text{ cm}^{-2} \text{ s}^{-1}$  for ATLAS and CMS only at the end of 2018 and  $4 * 10^{32} \text{ cm}^{-2} \text{ s}^{-1}$  for LHCb, achieving a pileup of  $\sim 40$  (with peaks of 80) and  $\sim 2$  for LHCb [5].

## 1.2 The High Luminosity upgrade

The High Luminosity Large Hadron Collider (HL-LHC) is a large upgrade program at the LHC which consists in important modifications on the entire accelerator facility at CERN in order to increase the maximum instantaneous luminosity at the LHC to  $2 * 10^{35} \text{ cm}^{-2} \text{ s}^{-1}$  starting from 2026 (Fig. 1.2). This will allow to collect more than  $250 \text{ fb}^{-1}$  of integrated luminosity per year for experiments like ATLAS or CMS, more than the integrated luminosity of run-I and II put together. Most of the incoming upgrades will be installed during the long shut-down-3 from 2024 to 2026. The importance of running the LHC at higher luminosities compared to the first 10 years of operation depends on the limitations of statistical gain reached by the accelerator after the first 10 years. Holding this luminosity configuration for more years does not increase considerably the statistics, therefore, an increment of the collision event rate is the only viable solution [6].

The HL-LHC will undergo major hardware modifications. One of them is a complete redesign of the bunch formation procedure at the PS, in order to generate brighter bunches without increasing the number of protons in the bunch. This upgrade is already ongoing during LS-2 and will provide a maximum instantaneous luminosity of  $2 * 10^{34} \text{ cm}^{-2} \text{ s}^{-1}$  from 2021 onwards. Also the magnet and accelerator systems will receive some modifications, with the replacement of some of the superconducting magnets close to the interaction regions and the installation of "crab cavities", which will allow a real time control of the beam focus in order to keep constant luminosity with decreasing number of protons in the bunch. This will lead to a reduction of

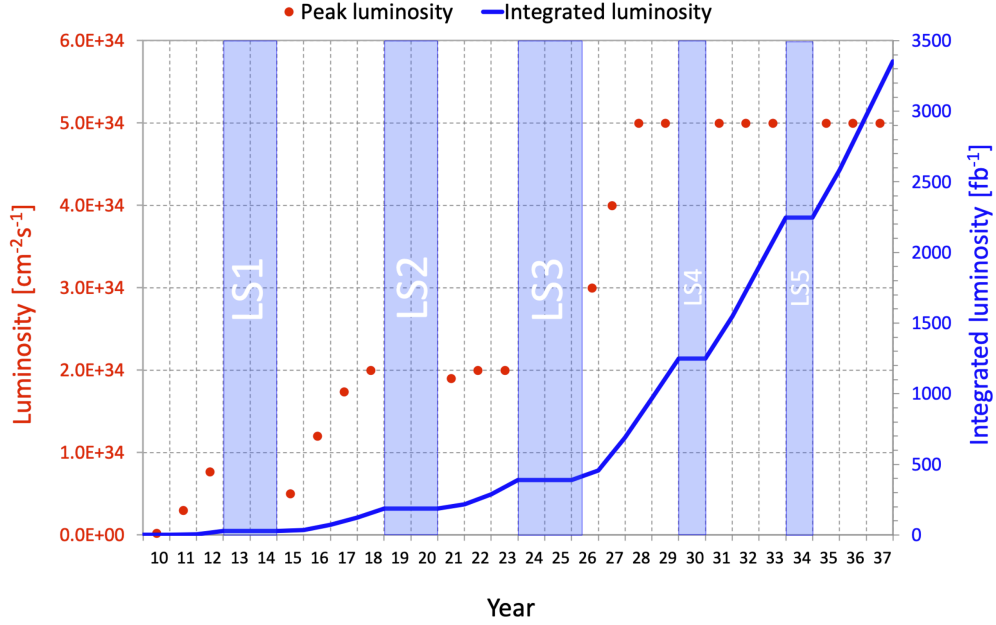


Figure 1.2: Long term luminosity program of the LHC. The values of peak and integrated luminosity are referred to operational values of ATLAS and CMS [6].

the peak luminosity from its maximum value of  $2 \cdot 10^{35} \text{ cm}^{-2} \text{ s}^{-1}$  to  $5 \cdot 10^{34} \text{ cm}^{-2} \text{ s}^{-1}$  for ATLAS and CMS, but with the advantage to hold it constant for most of the collision time (Fig. 1.3).

This luminosity levelling procedure is already used in LHCb in order to hold a constant pileup in time without the need to apply any correction on the analysis due to a decreasing number of the observed events [8].

### 1.2.1 Critical aspects of the HL-LHC

Having higher luminosity raises the required performances of all detectors. Especially two critical issues influences hardware operation and data acquisition. Operating at  $5 \cdot 10^{34} \text{ cm}^{-2} \text{ s}^{-1}$  or higher in ATLAS and CMS and  $2 \cdot 10^{34} \text{ cm}^{-2} \text{ s}^{-1}$  at LHCb will produce a pileup of 180 [9] and 50 [5] respectively. The high pileup, if not properly handled, will cause inefficiencies in the track reconstruction which may cancel the benefits of a higher luminosity. A first demonstration of this problem was observed by the CMS collaboration in 2012 during a special data run, where collisions at a relative high pileup of 78 were produced [6] (Fig. 1.4), showing a strong reduction of the reconstructed vertexes. Therefore, the luminosity increment in HL-LHC forces all experiments to develop new technologies in order to avoid a lower tracking efficiency. Solutions to avoid these problems are an increased segmentation of the tracking detectors, achieved using a lower material budget, pixel sensors with smaller size and the usage of time measurement with resolutions lower than 500 ps,

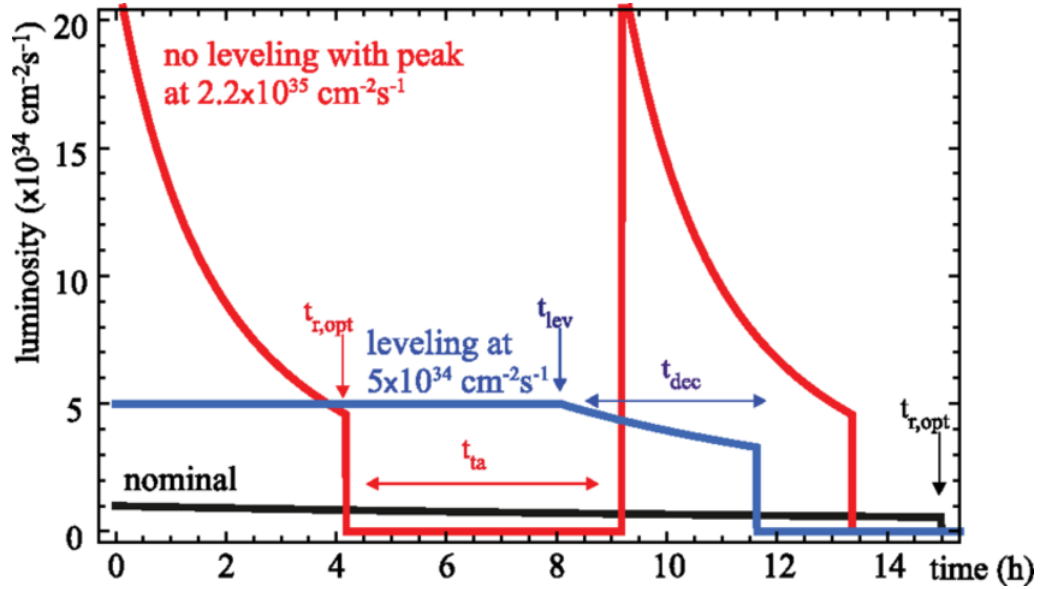


Figure 1.3: Luminosity levelling (blue plot) foreseen for the HL-LHC compared to un-levelled luminosity using the maximum peak luminosity of the HL-LHC (red plot). Black plot shows the current LHC nominal luminosity. [7].

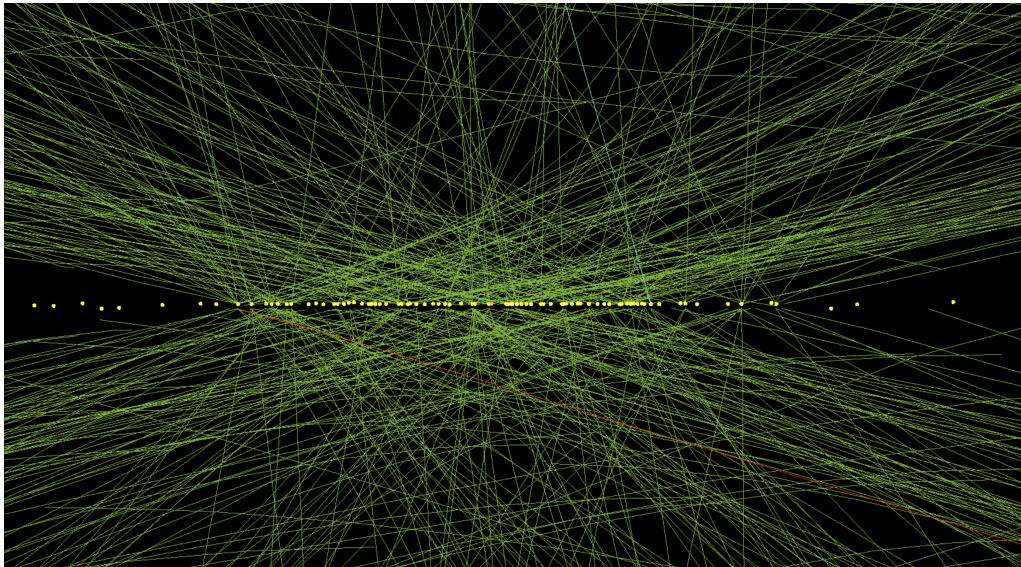


Figure 1.4: Special data run of CMS in 2012, producing beam collisions with a pileup of 78 [6].

as already implemented within the NA62 experiment in the GigaTracker detector [10]. ATLAS and CMS will also follow a similar approach and are already working on the development of a 4D tracking system with a dedicated high resolution space tracking detector close to the interaction point and a timing layer [13] [12].

A second factor is the radiation damage caused by the larger number of collisions and their products. In the case of ATLAS and CMS the high luminosity will produce a collision rate of approximately  $5 * 10^9$  collisions per second with an expected maximum fluency of  $2 * 10^{16}$  MeV  $n_{eq}cm^{-2}$ . In LHCb the situation is even worse, due to the closer distance, its vertex detector will be exposed to a fluency of  $1 * 10^{17}$  MeV  $n_{eq}cm^{-2}$  on the points closest to the beamline [5]. The products of those collisions, especially charged particles, will increase radiation damage on the sensors, read-out electronics and other secondary systems present in the detector system. Since most detectors will receive during a year the equivalent dose of the first ten years of operation of LHC, new solutions in terms of radiation hardness or simpler replacement must be developed.

## 1.3 High Luminosity at LHCb

The Large Hadron Collider Beauty detector is a flavour physics oriented experiment, designed to detect decays of  $b$ - and  $c$ -hadrons for the study of CP violation and rare decays. The detector is a single arm spectrometer and is able to observe  $b\bar{b}$  production primarily in the forward direction [14].

The luminosity at LHCb is lower than the one of the ATLAS and CMS experiments at the LHC, but this is necessary to perform the high precision measurements. In fact, during run-I and run-II, LHCb operated at a luminosity of  $4 * 10^{32}$   $cm^{-2}s^{-1}$ . Before starting with the HL phase, the experiment will receive an intermediate upgrade program, called phase-I, operating at a 5 times higher luminosity ( $2 * 10^{33}$   $cm^{-2}s^{-1}$ ) for the runs III and IV. The pileup at this luminosity is expected to be  $\sim 8$  and some major hardware modifications are needed in order to keep or even improve the performances. LHCb Upgrade-II will arrive 5 years later than ATLAS and CMS, during run-V in 2031 and will operate at a luminosity ten times higher than during run-IV ( $2 * 10^{34}$   $cm^{-2}s^{-1}$ ) (Tab. 1.1). This implies an average pileup of  $\sim 50$  [5] and the collection in a single year of the same amount of data as in all previous years put together. With the increased luminosity, the LHCb collaboration expects to obtain important information in CP violation, lepton universalities, and possibly first evidence for New Physics (NP) beyond the Standard Model (SM), as outlined in the letter of interest for the upgrade phase II [5] and the LHCb-phase-II physics case [15].

Experiment	LHC run	Period	$\mathcal{L}$ [ $cm^{-2}s^{-1}$ ]	$\mathcal{L}_{int}$ [ $fb^{-1}$ ]
Phase-0 LHCb	1 ; 2	2010/12 ; 2015/18	$4 * 10^{32}$	8
Phase-I LHCb	3 ; 4	2021/23 ; 2026/29	$2 * 10^{33}$	50
Phase-II LHCb	5 ..	2031/33 ; 2035 ..	$2 * 10^{34}$	300

Table 1.1: Luminosity program for the LHCb experiment [5].

### 1.3.1 The VELO phase-I upgrade as a step forward towards high luminosity

A critical issue is the tracking efficiency of the LHCb main vertex tracking detector, the VELO. In its first version, now decommissioned, the detector was based on a silicon strip sensor with semicircular configuration positioned 7 mm from the beam line and distributed over 40 tracking modules along all the beam collision area. The tracking detector had a readout of 1 MHz and was designed for a maximum radiation fluency of  $1^{14}$  MeV  $n_{eq}$   $cm^{-2}$ . This performances allowed track and vertex reconstruction with more than 99 % efficiency, operating at the relatively low luminosities of Run-I and Run-II.

For Run-III and IV the old VELO is being replaced by an upgraded version. The new detector features a new high granularity planar pixel sensor produced by Hamamatsu and bump bonded on a dedicated VELOPIX ASIC, a 40 MHz readout and a CO<sub>2</sub> based cooling system [16]. Another important feature is a shorter distance of 5 mm of the tracking modules from the beam line. The VELOPIX ASIC is basically the operational core of the hybrid sensor modules and it is based on the TIMEPIX-3 ASIC and built with the same 130 nm technology. It can drive a 256 x 256 pixel array with a pitch of 55  $\mu$ m, arranged in 2 x 4 pixel groups called super pixels. Compared to the TIMEPIX3, the time to digital converter is removed, which means that it does not provide time measurement, and its input is designed for a maximum leakage current of 12 nA per pixel expected on the most exposed pixels close to the beam line at the end of run-IV [17].

The structure of a hybrid sensor module is shown in picture 1.6. 3 VELOPIX ASICs are bump bonded together on a single Hamamatsu planar sensor with a 256 x 768 pixels matrix. 4 of those hybrid sensors are mounted together on a single tracking arm, 2 of them for each side.

During this PhD an activity was carried out by testing the Hybrid VELOPIX-Sensor tiles before being installed in the tracking arms. The next paragraphs describes briefly the tests and results.

**VELO Tiles test:** The sensor hybrids, before being installed in the tracking arms, must pass a last quality check which verifies their correct functioning and measures their performances. This operation is needed in order to select the tiles with the best performances in terms of low leakage current and noise for the regions

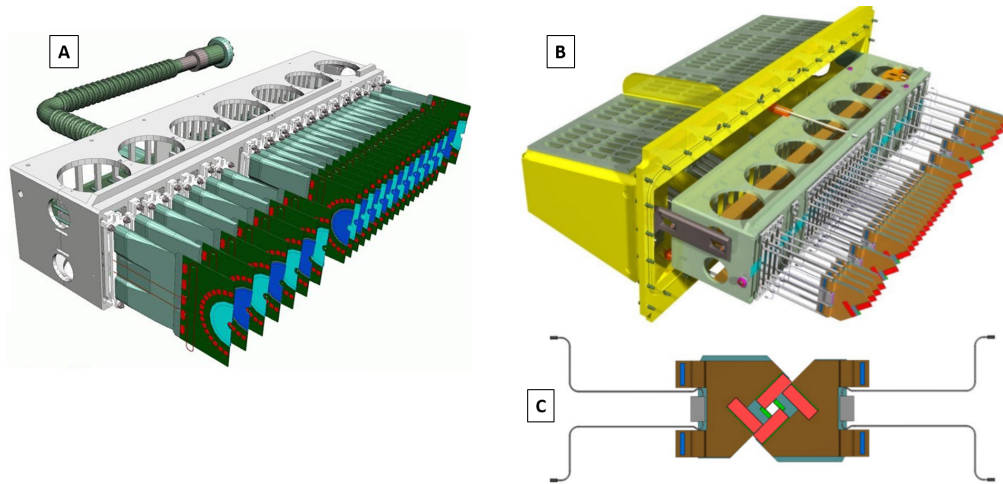


Figure 1.5: Comparison between old (A) [18] and phase-I VELO design (B) [19]. Both 3D models show half of the detector, highlighting their sensor structure, strip for the first generation VELO and high granularity pixel sensors for the second generation VELO. Also their orientation is changed, passing from a semi circular sensor module to an rectangular module (highlighted in red in (C)).

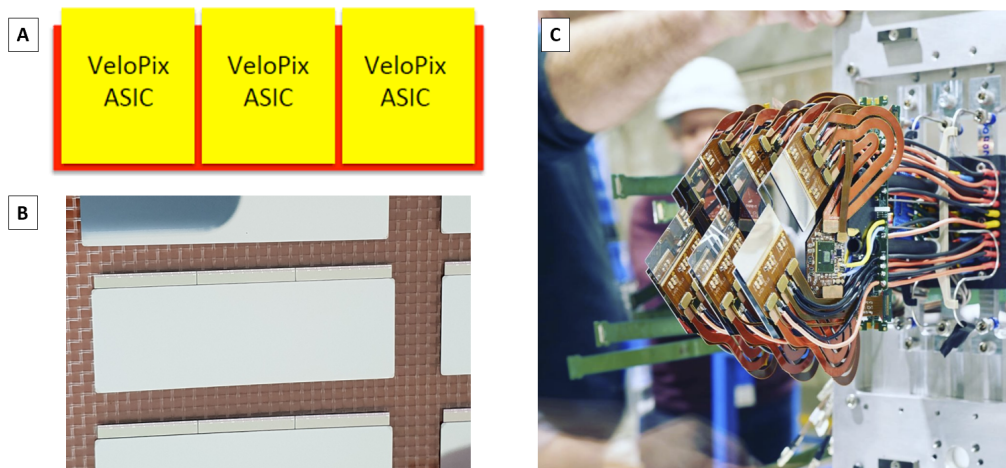


Figure 1.6: Sensor hybrid for the VELO upgrade. (A) Structure of the VELOPIX triplet, showing how the 3 VELOPIX ASICs are bonded to the sensor. (B) shows a real sensor module of the preproduction run. (C) shows first triplets mounted on ready VELO tracking arms (Source: @lhcbexperiment, Instagram.com)

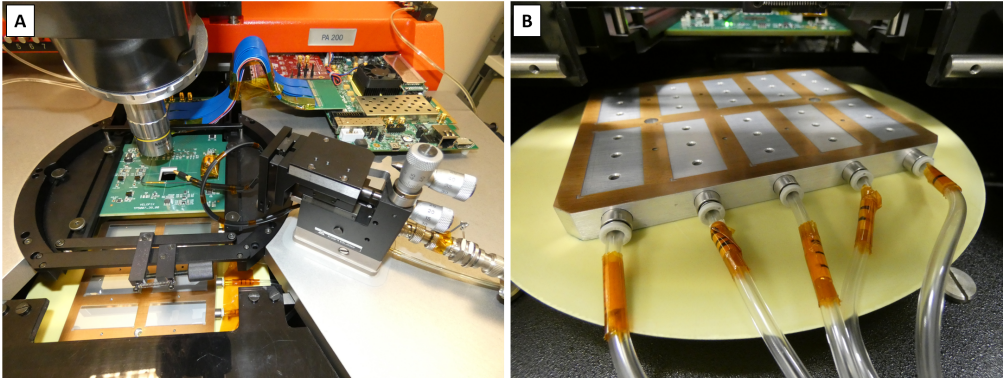


Figure 1.7: VELOPIX setup for current and register test (A) showing the SPIDR board, high voltage bias supply and a complete filled Jig. (B) Jig with connected vacuum tubes.

of the tracker with the highest fluency values.

The quality test was divided in 3 main parts, each of them with a dedicated test-bench. The first part was focused on a current, noise and register test of the VELOPIX ASIC, performed in parallel with a coarse leakage current measurement of the pixel matrix. The second part was controlling the quality of the bump-bonding procedure and the response of the VELOPIX analog front-end. The last part repeated the IV curve of the Hamamatsu sensor over the entire expected voltage range in order to see if there are consistent changes in the IV-response compared to the IV curves performed directly on the sensor wafer. The whole procedure was performed in the clean room of the CERN silicon facility.

**Current and register test:** For the current and register test a semi-automatic probe-station Karl-Suss PA-200 was used. The probe-station featured a customised support, the jig, to host a total of 10 tiles, a probe card with 128 needles in order to have a direct connection with all pads of the VELOPIX ASIC (Fig. 1.7.A). The probecard was connected directly to a general purpose readout board SPIDR [20], which sends the commands to the VELOPIX. The entire set-up was runned by a software, written in Python, which controls the movements of the probe-station and the communication of the SPIDR board with the VELOPIX ASIC. The jig itself is positioned over the chuck of the probe-station and fixed with the vacuum provided by the chuck in order to stand still during the entire procedure. The jig itself is connected directly to a separate vacuum pump which applies a small vacuum to the single positions in order to keep the single VELOPIX-sensor modules still during the test.

After the loading and orientation, a first fast current test started. This test allowed immediately to see if the needles of the probe-card correctly touched the VELOPIX pads. The total test consisted in:

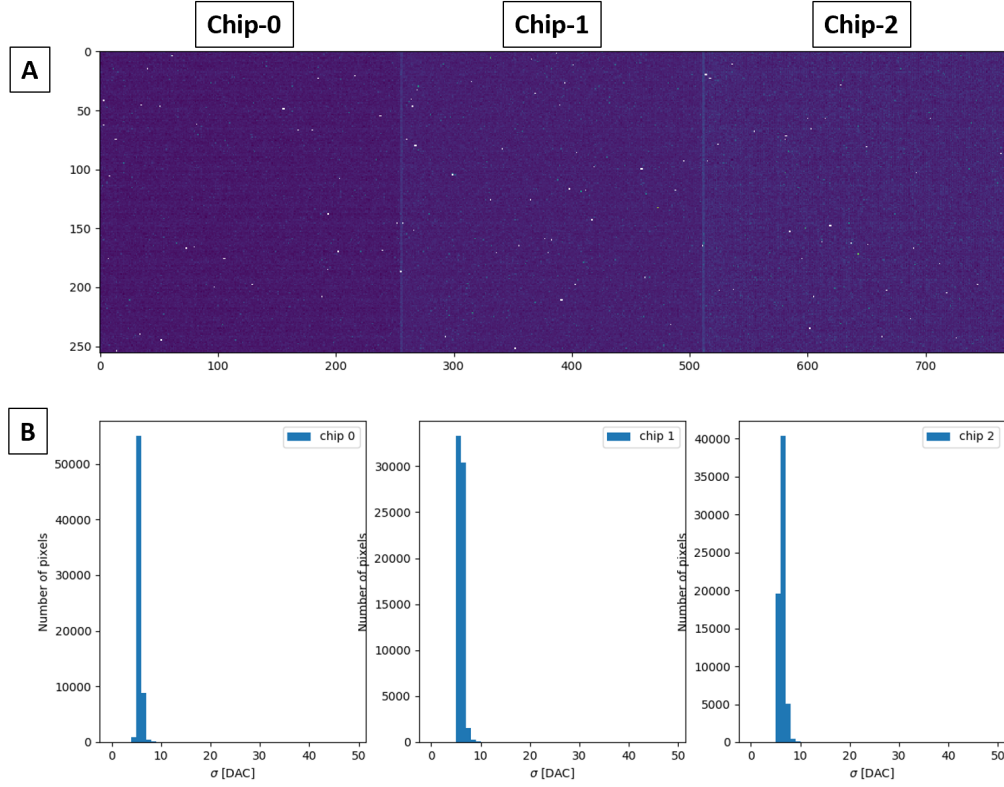


Figure 1.8: Noise map of one of the first VELO hybrid sensors. (A) represents the noise map over the entire pixel matrix and (B) their distribution

- A **Current test** to understand if the ASIC is operating at the desired voltage and current of 1.2V and if the Hamamatsu sensor is correctly working. For this purpose the voltage generator which provides the bias voltage was set with a maximum supply current of 1  $\mu$ A. The leakage current expected for the entire pixel matrix was less than 80 nA. With the set threshold it would result easy to identify short circuited or damaged sensors and isolate them for refurbishment.
- A successive **register test** of all the VELOPIX register. The system tested all single pixel and super pixel register were tested.
- Measurement of the **noise level**.

All the data collected was used to define a noise map and distribution for every single VELOPIX ASIC. The distribution was used for a quantitative and the map for a more qualitative analysis of the sensor performances (Fig. 1.8).

**Bonding** The bonding test was performed on the same set-up but with small modifications. The necessary response of the pixel is provided using a  $^{90}\text{Sr}$  source

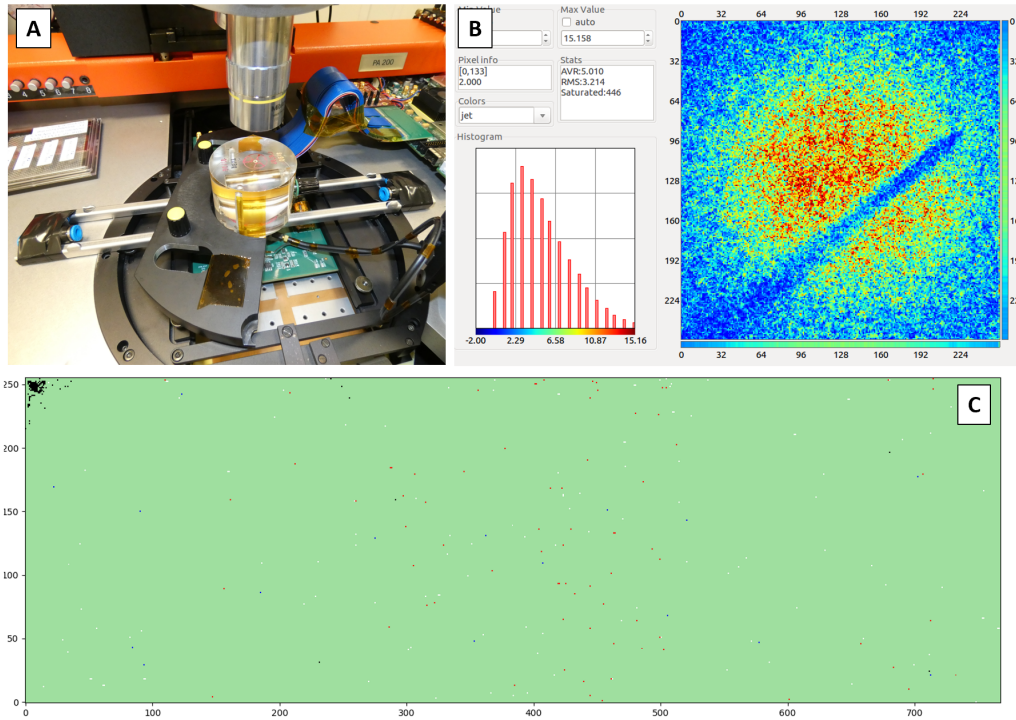


Figure 1.9: Set-up for bump bonding quality test (A). VELOPIX response after 15 minutes of  $\beta$ -ray exposure (B). The line in the middle of the spot is the high voltage needle used to provide the bias voltage on the silicon sensor. (C) shows a bump-bonding map of a single tile with a region of un-bonded pixels (black dots at the higher left corner).

which emits high ionising  $\beta$ -rays. The source is directly positioned over one single ASIC for approximately 15 minutes. During this time interval, the system, like a photo camera with opened shutter, saves all the counts of every pixel. The exposition time is considered enough to generate at least 100 counts/pixel and to stimulate all the pixel matrix, reducing the probability practically to 0 that the  $\beta$ -ray beam lost one pixel. This information is used to define a bonding map of the pixel which shows the bonded (green dots) and un-bonded (black dots) pixel (Fig. 1.9).

**IV-test** The IV test is needed to control that the IV response of the planar sensor is not strongly changed after being cut from the wafer. In order to perform this test, a dedicated set-up was arranged that holds all tiles inside a vacuum. Bias is provided by two needles, one touches the 0V contact on the VELOPIX and the second one touches the lower surface of the sensor. The voltage ramp goes from 0 V to 1000 V in reverse bias. The final IV response is compared with the curve done on the wafer before the sensor was cut and after the bump bonding procedure before being shipped at CERN (Fig. 1.10).

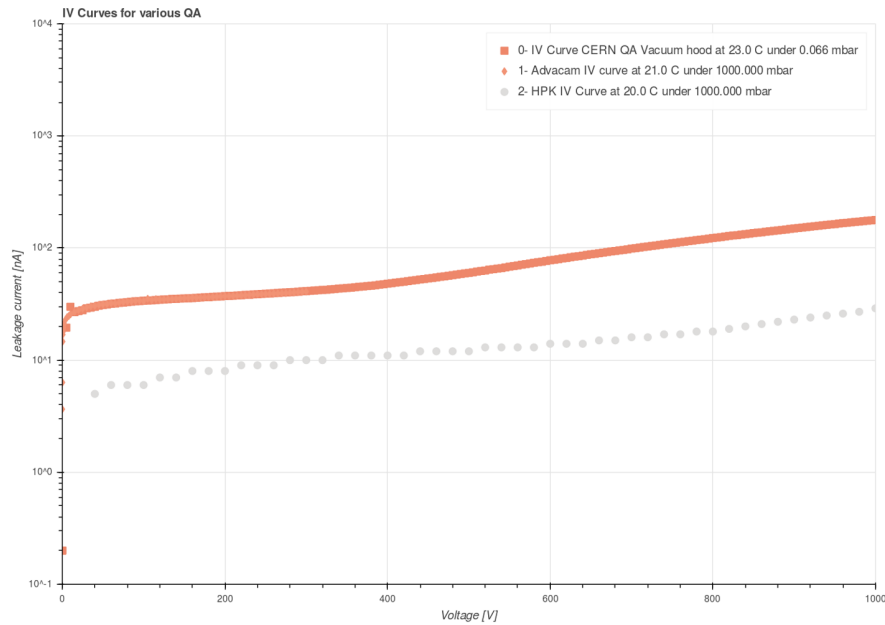


Figure 1.10: Comparison between IV response of the VELO sensors in reverse bias. Grey plot is the wafer test performed by Hamamatsu, the orange dot plot and orange line are the IV tests performed at CERN and Advacam respectively.

**Results** During this first control run, 173 out of the 650 VELOPIX triplets were tested, all of them from the first production run. The quality test showed 15 malfunctioning triplets, meaning that the final production reached a yield of 90 %. In particular, five were already damaged when they arrived at CERN, one of them presented a non correctly-bonded VELOPIX. Four had an anomalous high leakage current and broke later during IV-test. Other four passed the first two tests but their IV response changed completely from the wafer test. The remaining two were damaged unfortunately during the tests using a too high contact pressure of the needles. From those 15 triplets, 10 were resent back for refurbishment.

Most of the remaining tiles showed very low noise and are ideal for regions with the highest fluencies. Moreover noise-level measured over the remaining functioning modules was only 10 % higher compared to the wafer test (Fig. 1.11) Before leaving the activity directly to the LHCb-VELO group, consolidation work was performed in order to guarantee a safe and fast testing of the tiles, minimising human error. This work included a video tutorial of the test procedures and a check-list, which must be followed step by step, confirming every passage before passing to the next. Currently, the last triplets are under quality test and most of the first production triplets are already mounted on the tracking arms of the VELO, which will be installed in LHCb in 2020.

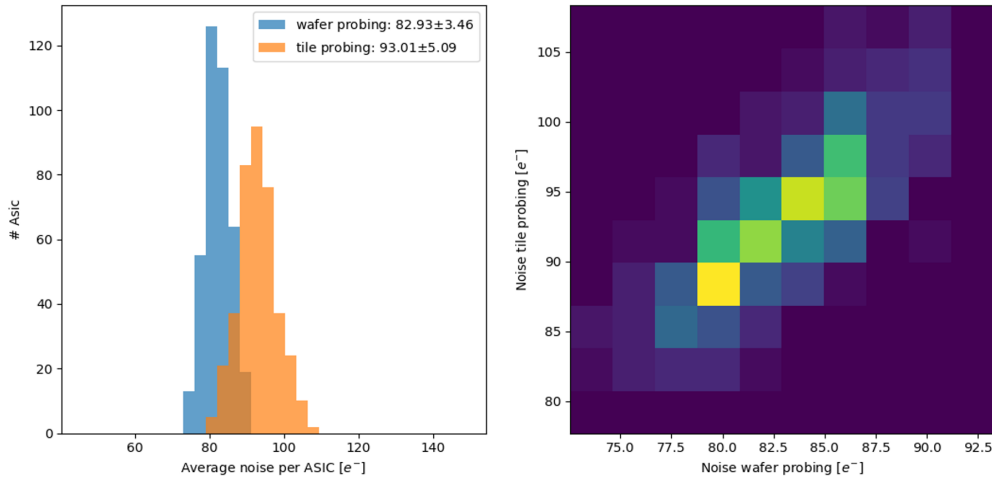


Figure 1.11: Comparison between noise level measured directly on the wafer and later on the finished modules.

### 1.3.2 Limits of the phase-I VELO in high luminosity

The VELO-I will operate from 2021 and it is foreseen that its operation will continue until the end of run-IV in 2029, at the beginning of the LS-4. This means that the LHCb-VELO will operate in both pre-HL era and HL-era. During both periods the luminosity at the interaction point will be hold constant at  $2 \cdot 10^{33} \text{ cm}^{-2} \text{ s}^{-1}$  with a pileup of about  $\sim 8$  events per bunch crossing.

After LS-4 it is foreseen that LHCb will operate at a 10 times higher peak luminosity, with an average pileup per bunch crossing of 50. The LHCb collaboration already performed exploratory studies, using as reference the phase-I VELO in order to understand the effects on vertex and track reconstruction. The simulations were carried out at the expected luminosity of  $2 \cdot 10^{34} \text{ cm}^{-2} \text{ s}^{-1}$  and measuring the track reconstruction efficiency and percentage of ghost tracks by changing some parameters like the pixel size, removing completely the RF-foil or adding new features like ps-fast timing.

The results of this study, presented in [5] show that the reconstruction of ghost tracks will increase from 1.6 % to 40 %, and track reconstruction efficiency will drop from the current 99 % to 96 % with an associate reduction of the resolution of the impact parameter (Fig. 1.12).

Possible solutions to this issue are a reduction to 25 % of the surface of the single pixel, passing from current  $55 \mu\text{m}$  to a  $27.5 \mu\text{m}$  pitch, or a complete removal of the RF-foil. The RF-foil is the external shield of the VELO which holds separate the LHC vacuum from the VELO vacuum. The RF-foil has the largest contribution in material budget and only its removal would be enough to allow the current VELO to operate at HL with a ghost rate equal to the one predicted in phase-I (Fig. 1.13). A second alternative is adding timing measurements in the track reconstruction,

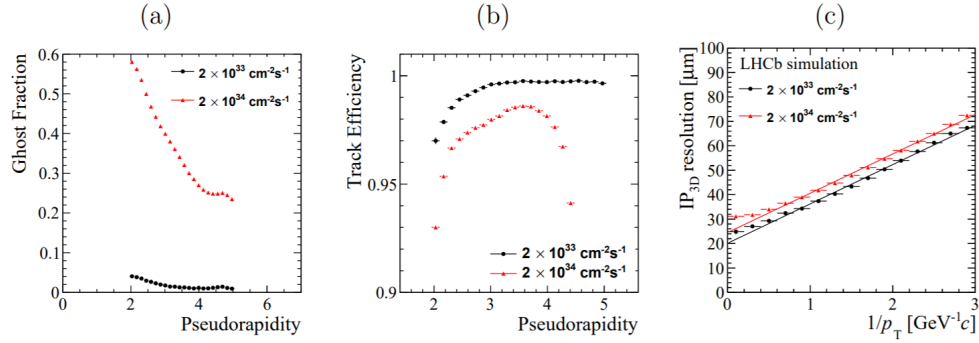


Figure 1.12: Behaviour of the VELO-phase-I detector in high luminosity environment (red plot) compared to the current design luminosity (black plots) [5]: (a) ghost rate vs. pseudorapidity. (b) tracking efficiency vs. pseudorapidity. (c) IP resolution vs.  $1/p_T$

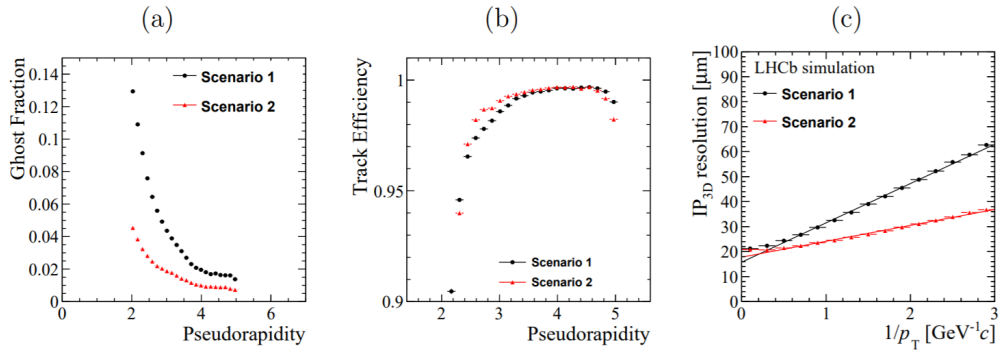


Figure 1.13: Behaviour of the VELO-phase-I detector in high luminosity environment without RF-foil and  $55 \mu\text{m}$  pixel pitch (red plot) compared with a similar design having the RF-foil and a 25 % smaller pixel size (black plot). [5]

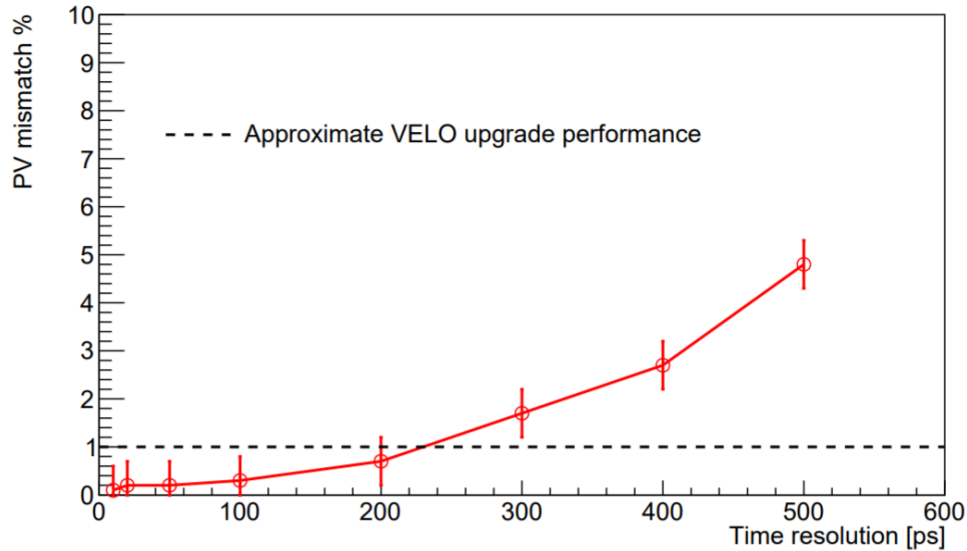


Figure 1.14: PV mismatch at high luminosity in a VELO-phase-I detector with added time measurement. The mismatch is computed as a function of the used time resolution, showing how below 200 ps mismatch goes below 1 % [5].

as already ATLAS and CMS are doing. In LHCb the use of 4D tracking close to the interaction point could provide high performance in track reconstruction, reducing the mismatch at 1 % if the time resolution on the single hit is at least 200 ps (already achieved by the NA62 experiment [10]) (Fig. 1.14). A second aspect is the high radiation environment the 52 VELO modules will be exposed to. It is estimated that the dose will be close to the  $10^{17}$  MeV  $n_{\text{eq}} \text{ cm}^{-2}$ , higher than ATLAS and CMS, due to the vicinity of the tracking modules to the beam.

## 1.4 The TIMESPOT project

The previous sections highlighted the fact that high pileup and high radiation degradation will play an important role in the high luminosity LHC. For tracking detectors positioned close to the interaction point the conditions are so extreme that new R&D activity must be pursued in order to define solutions and technologies capable of resist and operate with high efficiency. Three factors will play an important role:

- Vertex- and track-reconstruction with extreme high granularity sensors and introduction of time measurements of the observed events. Time resolution should be lower than 200 ps and space resolution lower than 50  $\mu\text{m}$ ;
- Strong reduction of the material budget along all detector. In particular a complete removal of the beam containment structures would have a significant

enhancement of the space resolution. Reduction of the sensor thickness is also a possibility but must be optimised in order to still have enough thickness to collect enough energy from the passing particle;

- High radiation resistance for sensors and electronics in order to operate at fluencies of  $10^{17}$  MeV  $n_{eq}$   $cm^{-2}$  for few years. Also the possibility of fast replaceable elements should be considered.

Moreover, the data output must be increased in order to preserve all information related to the hit map and associated timing information, which is estimated to be few Tbit/s. All these requirements push the need for a new generation of 4D tracking detectors which integrates the newest advances in particle tracking and data transfer.

One of the first experiments which aims to develop a first prototype of advanced 4D high luminosity high performance tracking detector is the Time and Space real time Operating Tracker or briefly TIMESPOT. TIMESPOT is a 3 year long, INFN-CSN-5 funded experiment, which involves 10 INFN sections localised over all Italy. It merges the experience of scientists working on larger high energy physics experiments such as LHCb, ATLAS, CMS, CT-PPS, 3Dose, NA62 and UFSD. TIMESPOT will include in the final prototype state of the art technology, starting from extreme radiation and timing optimised 3D silicon and diamond sensors. The sensor will be bonded on a dedicated CMOS ASIC which will be produced with 28 nm scale. Fast readout boards will guarantee data transfer and real-time track-reconstruction. For this purpose, TIMESPOT is divided in 6 work packages (WP) each of them focused with one aspect of the final tracking technology.

**WP-1:** Work package 1 is focused on the design, simulation, fabrication of a timing optimised 3D silicon sensor. 3D silicon sensors are a relatively new and promising sensor technology, capable of fast timing and with high radiation resistance, thanks to decoupled inter-electrode spacing from the sensor thickness [21]. WP-1 explores an optimised electrode geometry by following the suggestions of Sherwood Parker of an parallel electrode configuration [22]. Also other geometries will be included in the study, like hexagonal shaped pixel design. The Fondazione Bruno Kessler (FBK) [11] is responsible for the production of the sensor device which will be produced with a single side fabrication process [23].

**WP-2:** Work package 2 is focused on the design, simulation, fabrication of a timing optimised 3D diamond sensor. Diamond as sensor medium presents some important advantages like an almost 3 times higher charge mobility, almost zero leakage current and the highest intrinsic radiation hardness of all materials. Therefore, diamond sensors can collect charges even in less than 50 ps. On the other hand, the larger band-gap of diamond implies a lower number of electron hole pairs than in silicon, which means that the electronics must provide additional amplification in

order to have a sufficiently high signal.

The fabrication of diamond sensor is affected by critical issues. At first, a diamond wafer must be grown using deposition techniques like chemical vapour deposition (CVD) [25]. This technology is not yet optimised for production of large volumes. Moreover mono-crystal growth is hard to achieve for larger surfaces. A second problem is the formation of the electrodes, which must be graphitised in the diamond lattice with a laser. This burning process, which transform the carbon from diamond to graphite, produces electrodes with a high resistance. TIMESPOT will also attempt to improve the electrode fabrication process.

**WP-3:** Both diamond and silicon 3D sensors will be mounted on a customised ASICs like the VELOPIX sensor modules. Those ASICs will be produced in a 28 nm scale CMOS already used in the ATLAS FTK [26] and the ScalTech28 CSN-5 project [27]. The technology takes less space and is better suited for high granularity pixel matrices with small pixel pitch. Radiation hardness is expected to be higher due to the smaller energy deposits the ionising radiation can leave in the medium. The ASIC will implement an analog front-end with a optimised low noise and fast amplifier and shaper. For time measurement a Constant Fraction Discriminator (CFD) is suggested as the optimum solution. Time measurement is left to a time to digital converter which will be implemented on each pixel or, in will cover groups of 4 or 8 pixel, similar to the super pixel architecture of the TIMEPIX-3 or VELOPIX ASIC.

**WP-4 to WP-6:** WP-4 and WP-5 are focused on the development of high speed and high data transfer boards and real time reconstruction of the particle tracks, using high speed FPGAs. WP6 is focused on the final system integration of all technologies developed in the previous work packages in a first prototype of an tracking detector.

### 1.4.1 Contribution of this work in TIMESPOT

This work is part of the work package 1 activity and will describe in the next chapters the design, simulation, fabrication and test of an timing optimised 3D silicon sensor. For this purpose new exploration methods were defined and new simulation tools designed in order to achieve the required result.

# Chapter 2

## Introduction to silicon sensors

This chapter introduces the physics of silicon based solid state sensors and simplest application, the *pn*-junction.

A special focus is dedicated on charge drift and diffusion, electric field formation and signal formation in silicon sensors, which are the fundamental physical phenomena used in this work to analyse the timing performances of the silicon sensor. Also the Ramo theorem is introduced and one of its analytical solutions displayed.

The chapter concludes with a brief overview about radiation damage and some of the current solid state sensors.

### 2.1 Conduction in solids

The electrical properties of solid materials depend strongly on their energy level structure. Compared to single atoms, where the electrons occupy a discrete number of energy levels, in solids the most external electrons of the atoms, which are weakly bound, are de-localised and fill continuous energy bands, separated each other by forbidden gaps.

The band structure of a solid is made by the valence, the conduction and some prohibited bands. At 0 K temperature, a solid material has all its electrons located in the valence band, while the first conduction band results empty. Depending on the energetic distance between valence and conduction band, called band gap, a solid presents specific physical properties and can be distinguished in insulators, semiconductors and conductors. In conductors, valence and conduction band are overlapped and electrons can move freely over all the solid. In insulators instead the band gap is far larger than the average thermal energy of the electrons ( $\frac{N}{2}k_B T \ll E_{bg}$ , with  $N$  the number of degrees of freedom of the electron in the lattice,  $k_B$  the Boltzmann constant and  $T$  the temperature). Therefore, it is practically impossible that insulators can conduct current in normal environmental conditions. In semiconductors the band gap has an similar energy to the thermal energy of the electrons. At temperatures higher than 0 K electrons have enough energy and pass from the valence

to the conduction band, leaving a vacancy in the silicon lattice. The semiconductor at this point is capable of conducting a small current. The left vacancy attracts other electrons from close bonds, moving the vacancy from one atom to the next. This vacancy, which behaves like a positive charged particle, is called "hole".

Most common semiconductor elements are Silicon (Si) and Germanium (Ge). Also Carbon (C) has semiconductor properties if used in its allotropic diamond form. All three semiconductors have a cubic central structure, with a band gap of 0.66 eV in Ge, 1.14 eV in Si [28] and 5.5 eV in C [29].

From now on the attention on this chapter will be focused exclusively on Silicon devices.

### 2.1.1 Physical properties of silicon

Silicon has an electron structure of  $[\text{Ne}]3s^23p^2$ , with  $3s^23p^2$  being the valence electrons. In a silicon crystal, every single valence electron forms a covalent bond with an electron from another close silicon atom, generating a face-centred diamond cubic lattice[29]. As mentioned previously, Silicon is a semiconductor, which means that it acts like a insulator at 0 K and like a weak conductor at higher temperatures. The higher the temperature, the higher the probability that more electrons can move from the valence to the conduction band. The probability of electrons to move to the conduction band is described by the Fermi-Dirac distribution [30] [31] (Fig. 2.1):

$$f(E, T) = \frac{1}{1 + e^{\frac{E-E_f}{k_B T}}} \quad (2.1)$$

Where  $E$  is the energy of the particle,  $E_f$  the maximum energy of the electron which occupies the highest energetic state at 0 K, called Fermi energy,  $k_B$  the Boltzmann constant and  $T$  the temperature.

### 2.1.2 Charge motion in silicon

Once electrons switch from the valence to the conduction band, they become mobile carriers. In silicon their motion is mainly dominated by two phenomena: diffusion and drift. Diffusion happens constantly in silicon and depends from the temperature. Drift instead only happens only if an external electric field is applied in the silicon bulk.

**Diffusion** Diffusion is a temperature dependent phenomenon and has a random nature. In specific conditions, diffusion depends also from the carrier concentration gradient in the silicon lattice. For example, electrons and holes will diffuse from regions with higher carrier concentration to region with lower carrier concentration. Considering electrons and holes in silicon, each of them with an energy of  $\frac{N}{2}k_B T$ , with  $N$  the number of degree of freedom, their motion is simply a random scattering

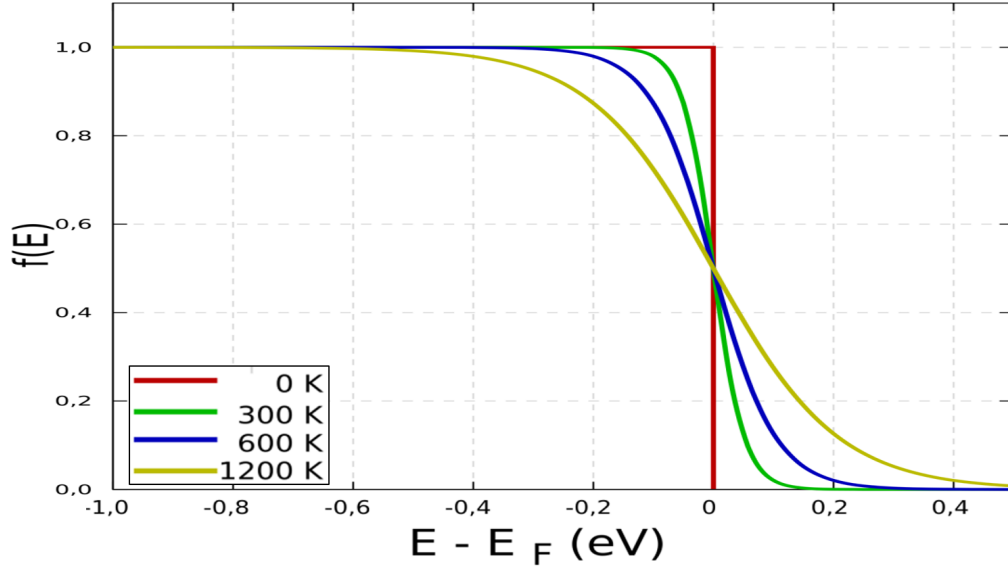


Figure 2.1: Fermi-Dirac probability in function of the electron energy. Every single plot is related to a different system temperature. Higher the temperature and higher the probability that a certain number of electrons switch to higher energy states.

process against other atoms and electrons of the silicon lattice. Considering the mean free path  $l$  between two collisions and the time of free flight  $\tau_l$ , the average diffusion velocity can be expressed as the ratio of those quantities

$$v_{diff} = \frac{l}{\tau_l}. \quad (2.2)$$

At thermal equilibrium and with an uniform concentration of carriers, diffusion is a completely random motion (Fig. 2.2.A): The distribution of the free flight distances due to diffusion have a Gaussian distribution with variance of:

$$\sigma = \sqrt{2D_{e,h}\tau_l} \quad (2.3)$$

Where  $D_{e,h}$  is the diffusion coefficient and can be obtained from the kinetic energy of the carrier

$$\frac{1}{2}k_B T = \frac{m^*_{e,h}v^2_T}{2}, \quad (2.4)$$

Where  $m^*$  is the so called effective mass of the carrier, which is the mass that physically the carrier seems to have when a force is applied on it [29].

The diffusion coefficient has the following definition:

$$D_{e,h} = lv_T = \frac{m^*_{e,h}v^2_T}{q_{e,h}} \times \frac{q_{e,h}\tau_l}{m^*_{e,h}} = \mu_{e,h} \frac{k_B T}{q_{e,h}} \quad (2.5)$$

Where  $\mu_{e,h}$  is the charge mobility which is an index of how fast a charge can move in the silicon lattice [29].

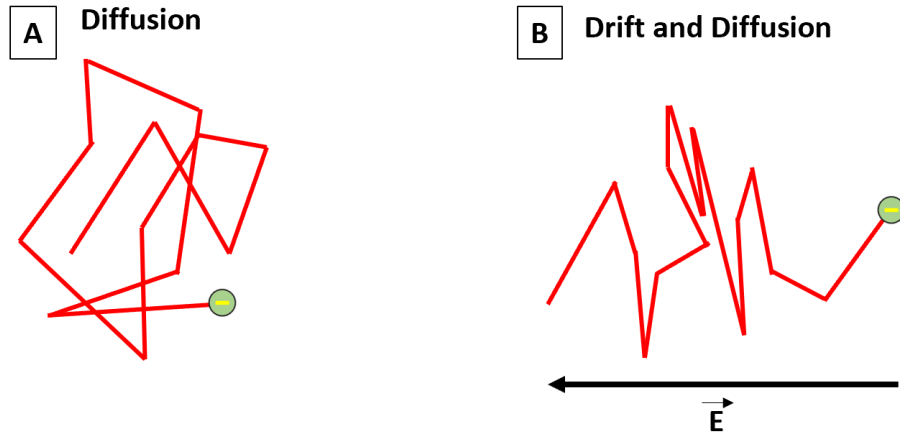


Figure 2.2: General pattern of charge motion in silicon. (A) only diffusion if there is no external electric field. (B) Drift under the effect of an electric field.

The charge mobility plays an important role through this entire work, starting from the simulation of the sensor operation in saturation velocity until its use in transient simulations.

**Drift** Drift is the motion of the charges in reaction to an electric field in the solid. In order to find the relation between the drift velocity  $v_d$  and the electric field, a simplified electrical circuit with an silicon element, long  $l$ , is considered. Considering a single carrier with charge  $Q$  passing the entire element in a time of  $t_r$ , the resulting current is equal to

$$I = \frac{Q}{t_r} = \frac{Qv_d}{l}. \quad (2.6)$$

The dependency on the drift velocity  $\vec{v}_d$  and the electric field  $\vec{E}$  is simply obtained using classical physics. The total force applied on a moving charge in the silicon by an electric field is:

$$\vec{F} = q\vec{E} - \frac{m\vec{v}_d}{\tau_l}, \quad (2.7)$$

Where the first term is the force applied by the electric field and the second term describes the dynamic effect of charge scattering through the silicon lattice [29].  $\tau_l$  is still, as previously shown for the diffusion (Eq. 2.2), the average collision time. Assuming that the charge is already accelerated at maximum drift velocity and the effects of scattering equal the electric force, the drift velocity depends on the electric field as

$$\vec{v}_d = \left( \frac{q\tau_l}{m} \right) \vec{E} = \mu \vec{E}, \quad (2.8)$$

as previously shown in equation 2.5,  $\mu$  is the charge mobility [29].

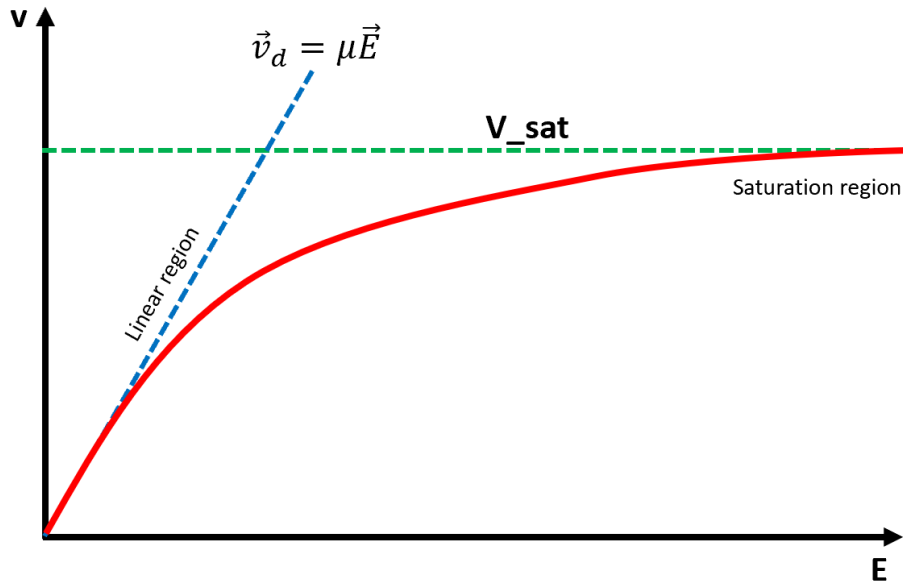


Figure 2.3: Velocity saturation in silicon.

**Velocity saturation** For relatively small electric fields, the charge mobility is constant and drift velocity increases linear with the electric field. For stronger electric fields (1 kV/cm is normally used as reference [32]), scattering becomes more dominant and drift velocity starts to saturate (Fig. 2.3). This phenomena is called velocity saturation [32]. Velocity saturation can be included by modelling charge mobility according to the behaviour of the semiconductor band structure [33]. One of the simplest models is represented by equation 2.9 and is calculated experimentally for intrinsic silicon

$$\mu(\vec{E}) = \frac{\mu_0}{1 + \frac{\mu_0 |\vec{E}|}{v_{sat}}}, \quad (2.9)$$

Where  $v_{sat}$  is  $1.07 \times 10^7 \text{ cm/s}$  for electrons and  $8.3 \times 10^6 \text{ cm/s}$  for holes, according to [33].

### 2.1.3 Doping

Pure, or intrinsic, silicon does not have the correct electrical properties to be used for any electrical application. In order to change its electrical characteristics, the silicon is mixed with low concentrations of other elements. This procedure, called doping, allows to add, in small percentages, other elements which add an additional number of free carriers in the silicon lattice. Based on the element used, the doped silicon is called *n*-type or *p*-type. *n*-type doping consists in mixing pentavalent atoms which makes part of the 15<sup>th</sup> group of the periodic table, like arsenic, antimony or

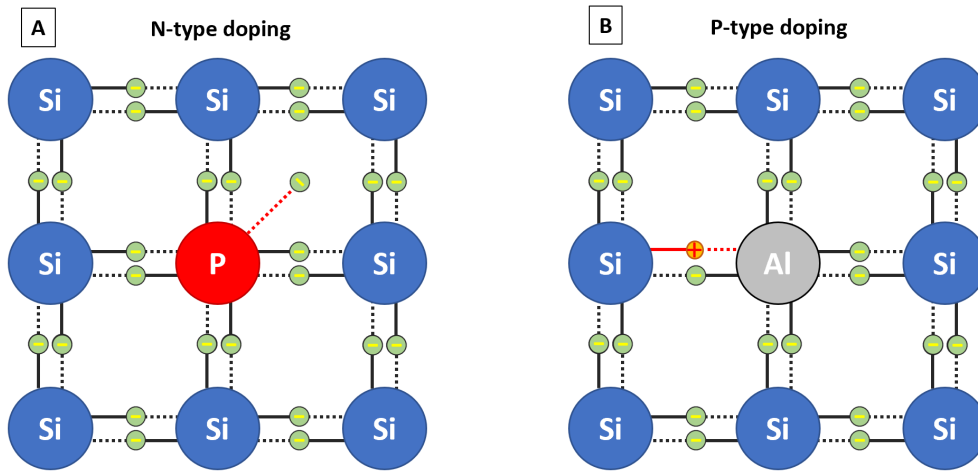


Figure 2.4: *n*-type (A) and *p*-type (B) doping compared. The additional electron and hole are highlighted by the red circle.

phosphorus. The effect of those atoms in the silicon is that 4 of its 5 valence electron forms covalent bonds with the closest silicon atoms. The fifth valence electron stays free to move in the lattice. Due to this effect, doping elements that increase the number of free moving electrons in the material are called donors and the doping is called *n*-type, to highlight the fact that the negative electrons are the majority mobile carriers. *p*-type doping instead includes elements from the 13<sup>th</sup> group of the periodic table like aluminium, boron or gallium. Those elements have only 3 valence electron, which means that they can form only 3 out of 4 possible covalent bonds with the silicon lattice. The last non formed bond leaves a vacancy that can be occupied by other electrons diffusing from other bonds close to the vacancy. The moving vacancy with the behaviour of a positive charged particle, is called hole. Due to the fact that the generated vacancies attract external electrons, the *p*-dopants are called acceptors and the doping type is called *p*-type, considering that the positive charged holes are the majority carriers in the silicon (Fig. 2.4) [32]. In both cases, the increment of free carriers leads to an increment of the conductivity of the silicon, which is also facilitate from the formation of additional energy levels close to the energy bands which reduces bandgap, facilitating transition from valence to conduction band. Another aspect of doping is the reduction of the minority carriers in a specific doped silicon. For example, in *n*-type doped silicon, some of the electrons occupy some of the holes presents in the silicon, reducing the number of free moving holes, according to the law of mass action [32].

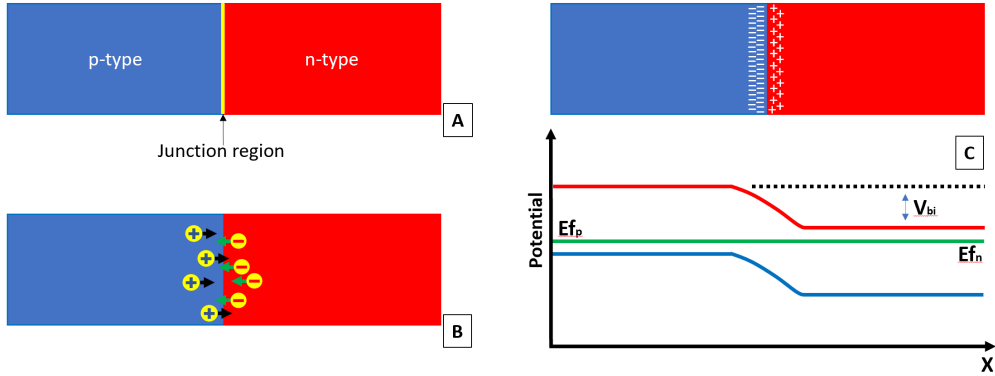


Figure 2.5: General description of a pn-junction. (A) doping profile of a pn-junction. (B) diffusion of the majority carriers. (C) pn-junction in thermal equilibrium and potential distribution over the junction.

## 2.2 The pn-junction

If a silicon crystal is doped in different areas with a  $p$ -type and  $n$ -type doping and these areas touch, the surface in between forms a "pn-junction" (Fig. 2.5.A). At the beginning the junction is globally neutral with two volumes containing mostly holes or electrons as majority carriers. Due to the different gradient of carrier concentration around the junction, electrons and holes diffuse, as described previously in section 2.1.2, from regions with higher concentration to regions with lower carrier concentration. This means that electrons will diffuse from the  $n$ -doped region to the  $p$ -doped region and holes the other way around (Fig. 2.5.B). Reaching the  $p$ -type region, electrons will recombine with the local holes, leaving a globally negative charged volume without mobile carriers. Holes on the other hand, when reaching the  $n$ -type region, will recombine with the electrons leaving a negative charged area also free from mobile carriers. This phenomenon will continue until the charge around the junction is sufficiently large to generate a potential barrier strong enough to stop the charge diffusion. The potential difference along the diode forms the so called built-in potential  $V_{bi}$  [32] (Fig. 2.5.C). In this status the pn-junction is in thermal equilibrium. The built-in voltage depends mainly from the temperature of the silicon, its intrinsic carrier concentration  $n_i$  ( $1.45 \times 10^{10} \text{cm}^{-3}$  at 300 K) and the concentration of donors and acceptors per  $\text{cm}^3$  ( $N_d$  and  $N_a$  respectively) [32]

$$V_{bi} = \frac{k_B T}{e} \log\left(\frac{N_a N_b^2}{n_i}\right), \quad (2.10)$$

Applying an external potential on the junction reduces or enhances the effect of the built-in voltage, obtaining different electrical behaviour of the junction.

If a higher potential is applied on the  $p$ -doped area than the  $n$ -doped, the potential barrier is lowered and a current flows through the silicon. This configuration is called

forward bias and the pn-junction conducts a current. Instead, if a greater potential is applied on the  $n$ -doped area than the  $p$ -doped, the potential barrier is increased and this lowers even more the charge flux and increases the depleted area. This configuration is called reverse bias.

The most common application for a pn-junction is the diode, a device capable of passing current only if forward biased and blocking the passage in reverse bias. The electrical response of a solid state diode is described by the Shockley equation [34].

$$I(V) = I_0(e^{\frac{eV}{k_B T}} - 1), \quad (2.11)$$

Where  $I_0$  is the reverse saturation current. The Shockley equation describes most of the operational range of a diode but for large inverse bias voltages it does not work properly. In fact, at higher reverse voltages the electric field inside the diode is so large that it not only depletes the entire diode but increases so much the kinetic energy of the carriers that they start to ionise other silicon atoms, producing secondary free moving and ionising electrons. This avalanche effect, if not properly handled, causes damage to the diode by thermal effects due to the large current. This phenomena is called *breakdown* and the voltage at which this phenomena starts is called the "breakdown voltage" 2.6.

## 2.3 Silicon diode as particle sensor

The most common application of a pn-junction in high energy physics is as reverse biased diode. In this configuration, the reverse bias voltage allows to keep the diode volume empty of mobile carriers. This depleted volume, called also *sensitive* or *active* volume, works like an ionisation chamber. If an ionising particle crosses the active volume, it ionises the silicon along its path, generating electron hole pairs, which drift to their respective collector electrodes, inducing a current which can be detected by dedicated electronic.

### 2.3.1 General characteristics

**Depletion and capacitance** If in thermal equilibrium, the pn-junction has already a small depleted volume around the junction with a width of

$$w = \sqrt{\frac{2\epsilon(V_{bi})}{Ne}} \quad (2.12)$$

Where  $N$  is the dopant concentration,  $\epsilon$  is the dielectric constant and  $V_{bi}$  is the built in potential. If a reverse bias potential  $V$  is applied on the diode, the width of the depleted volume increase since  $V_{bi}$  becomes  $V_{bi} + V$ . If the depleted volume does not reach directly the electrodes, leaving a not completely depleted volume, the sensor is partially depleted. This partially depleted volume, free from mobile

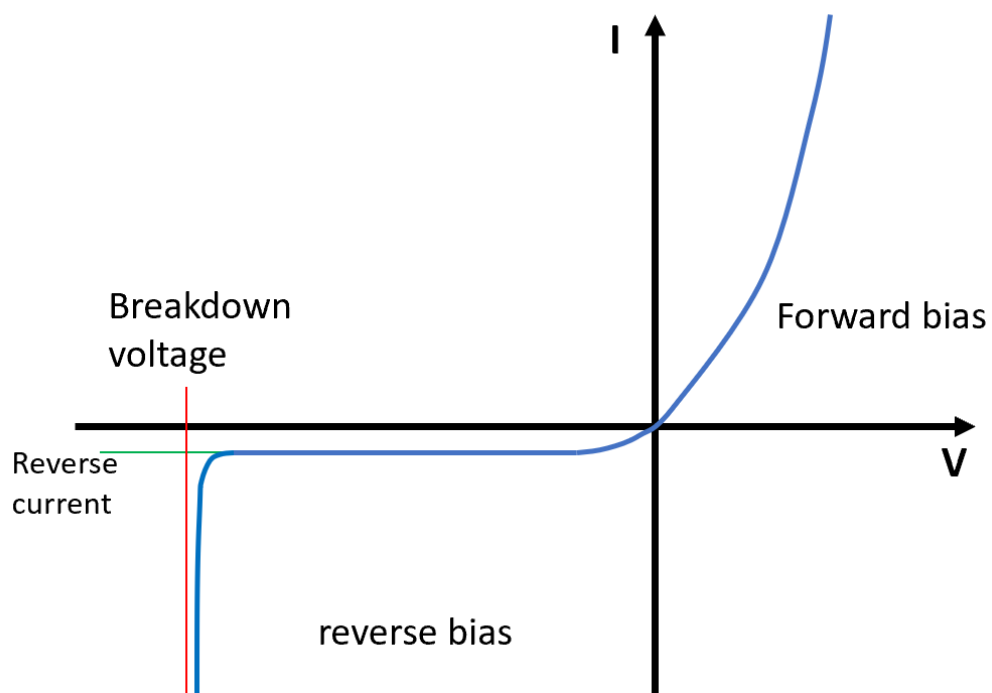


Figure 2.6: IV curve of a diode. In forward bias voltage, a large positive current flows through the pn-junction. In reverse only a small current, the dark current, flows through the diode. For larger reverse bias voltages, avalanche effects can happen. The diode is in breakdown.

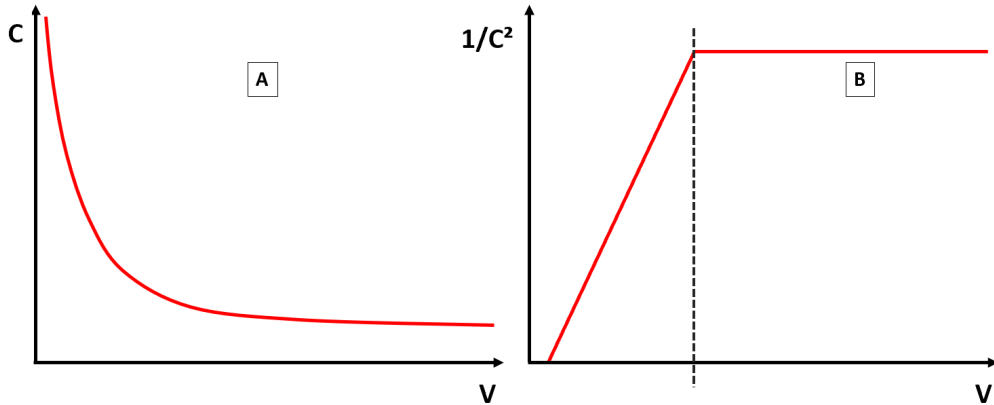


Figure 2.7: (A) Sensor capacitance vs bias voltage and  $C^{-2}$  vs voltage (B). Plot (B) is a perfect estimation to determine the minimum voltage needed to fully deplete the silicon junction.

carriers and having a charge distribution at its extremities, behaves like a capacitor. For a traditional planar junction, the capacitance depends from the surface of its electrodes  $A$  and their distance  $w$ .

$$C = \epsilon \frac{A}{w} = A \sqrt{\frac{eN\epsilon}{2(V_{bi} + V)}}, \quad (2.13)$$

As it will be shown in the next chapters, the capacitance of the sensor is a major source of noise and jitter and must be reduced in order to increase the time resolution of the system. In a planar sensor, as shown in equation 2.13, the capacitance can be reduced by using smaller electrodes or increasing the sensor thickness  $w$ . The first approach benefits especially sensors used in tracking because its better space resolution, considering that, for square electrodes with pitch  $p$  and binary readout, the spatial resolution is equal to  $p/\sqrt{12}$ . On the other hand, the second approach has some issues, like a large bias voltage or the long charge collection times needed to fully absorb all electron-hole pairs generated by an ionising particle. For this case, an optimisation of the sensor size related to its specific application must be performed. Measuring the capacitance of the sensor as a function of the voltage can determine the voltage at which the entire volume is depleted. Using equation 2.13 plot of the quantity  $C^{-2}$  as a function of the bias voltage is displayed in figure 2.7. It can be seen that once full depletion is reached, no more volume can be depleted and the maximum capacitance is achieved.

**Dark current** Even after reaching full depletion, a silicon diode still presents a small reverse current (Eq. 2.11). This current has only thermal origin and does not

depend from external radiation and it is usually called *dark* current. In the Shockley equation it is represented as  $I_0$  and it depends mainly from the band-gap energy and the temperature of the lattice

$$I_0 \propto T^2 \exp\left(\frac{E_g}{2k_B T}\right). \quad (2.14)$$

**Electric field** For the most common silicon sensor architecture, plane electrodes face each other at a distance  $d$ , which is also the wafer thickness. For low bias voltages, the silicon junction is partially depleted and the electric field is applied only on the depleted volume of the sensor. Assuming that the electric field is applied along the x-direction, its amplitude is:

$$|E(x)| = \frac{eN}{\epsilon}(w - x) = \sqrt{\frac{2NeV}{\epsilon}} \times \left(1 - \frac{x}{w}\right) = E_{max} \left(1 - \frac{x}{w}\right), \quad (2.15)$$

Where  $E_{max}$  is the highest value of the electric field, obtained close to the electrode with the lower bias voltage. Full depletion happens if  $w = d$ . The corresponding potential is  $V_d = \frac{Ned^2}{2\epsilon}$ . For voltages higher than full depletion, the electric field amplitude is a sum of 2 terms, one constant term, depending only on the inter-electrode distance and the applied voltage, and the small ramp due to the potential difference between the electrodes

$$|E(x)| = \frac{2V_d}{d} \left(1 - \frac{x}{d}\right) + \frac{V - V_d}{d}, \quad (2.16)$$

For very high bias voltages equation 2.16 can be approximated to  $\frac{V}{d}$ .

### 2.3.2 Particle-matter interaction

Signal formation in a silicon sensor depends strongly on the kind of interaction between the incoming radiation (particles or photons) and the atoms of the active medium. Most interactions are electro-magnetic in nature and since they happen between the incoming radiation and the valence electrons. Depending on the distance between the incoming particle and the electron, the energy transfer can be sufficient to raise the electrons to a higher energy state or rip them completely off, generating a free moving electron and a positive ion. The first process, called excitation, can be detected by observing the emitting photon generated when the electron falls back into its initial orbital. The second process, called ionisation, depends from the nature of the ionising particle and can be divided into direct and indirect ionisation. Direct ionisation is caused mostly by charged particles, indirect ionisation instead is caused by secondary particles which were generated after a direct interaction of the primary (or projectile) particle with the atoms, transferring them enough energy to rip of one or few electrons or even entire charged nucleus fragments, in

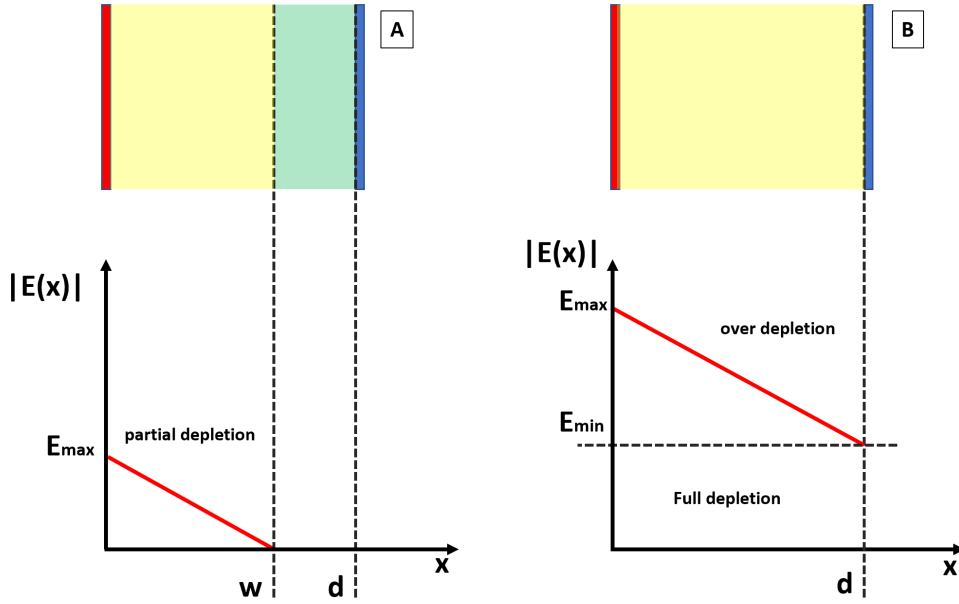


Figure 2.8: Electric field in a planar sensor. (A) partial depletion. (B) Full depletion and over depletion.

case of collisions between their nuclei. In some cases electrons are not only ripped off from their atoms but receive also enough energy to ionise other atoms of their own. These electrons, with energy far below the 1 MeV threshold, are responsible for large Landau fluctuation in the energy released by the primary particle and are called *delta-rays*.

### 2.3.3 Energy transfer of charged particles

Considering a charged particle crossing the active medium of a sensor, the stopping power  $S$  is defined as:

$$S = -\frac{dE}{dx} \quad (2.17)$$

**Energy loss due to charged particles** The stopping power for a particle with charge  $z$  crossing at a velocity  $v$  a material with average atomic number  $Z$ , mass number  $A$  and density  $\rho$  is described by the Bethe-Bloch formula [35]:

$$-\frac{dE}{dx} = \frac{4\pi e^4 z^2}{m_0 v^2} N Z \left[ \ln \left( \frac{2m_0 v^2}{I} \right) - \ln \left( 1 - \frac{v^2}{c^2} \right) - \frac{v^2}{c^2} \right], \quad (2.18)$$

Where  $Z$  and  $N$  are the average atomic number and numerical density of the traversed material,  $ze$  and  $m_0$  are the total charge and mass of the projectile particle. According to [37], the Bethe-Bloch equation can be extended by adding further

terms which includes the effects of polarisation of the medium. Analysing equation 2.18 for all velocity ranges it is clear that for non-relativistic velocities, energy transfer varies with  $1/v^2$  and energy transfer increases with lower velocity. On the other hand, at higher velocities and especially when the particle approaches the speed of light, energy deposition becomes smaller until it saturates at a minimum value, which is similar for most of the charged particles at ultra-relativistic speeds. Particle with this small energy transfer are called minimum ionising particles or MIPs. Electrons normally reach those values at lower energies, ca. thousand times less than protons due to the lower mass. This decreasing energy transfer at high velocities can be qualitatively described by comparing the time an ionising particle interacts with the electrons of the atom. For slower particles, the interaction time is longer and also the energy transfer is larger. For faster particles the interaction time is smaller and so the energy transferred with it [35].

### 2.3.4 Signal formation in silicon sensors

Signal formation in silicon sensors follows the same principles of most of the solid state sensors. An ionising particle crosses the active volume of the sensor, releasing along its path an total energy  $E$ . The transferred energy generates an average charge  $Q$  which is related to the energy

$$Q = \frac{E}{E_i} e, \quad (2.19)$$

Where  $E_i$  is the mean energy needed to generate a single electron-hole pair, which in silicon is equal to 3.6 eV [36], and  $e$  the electron charge.

If the sensor is fully depleted, the electric field forces the electron-hole pairs to move to their respective collecting electrodes. During the motion, every charge induces a current on both electrodes which, if high enough, is read by a dedicated front-end. The evolution in time of this current is well described by the Shockley-Ramo theorem [39] [40], which is presented in the following paragraph.

**Shockley-Ramo theorem:** The way a moving charge induces current on a specific electrode is described by the *Shockley – Ramo theorem* (SRT). Considering a particle sensor built up by  $N$  grounded electrodes ( $V = 0$ ) in which a single mobile charge  $q$  is injected inside the active medium. Surrounding the charge with a small equipotential sphere, the electric field between the conductors must satisfy

$$\nabla^2 V = 0. \quad (2.20)$$

On the other hand, applying the Gauss law, the small charge generates an electrostatic field by its own equal to:

$$\int_{surf} \frac{\partial V}{\partial n} ds = 4\pi q \quad (2.21)$$

At this point, the charge is removed and on one specific electrode an unitary potential ( $V_1 = 1$  V) is applied (the readout electrode), so that  $\nabla^2 V_1 = 0$ . The electric field formed with those boundary conditions has a potential  $V_{q1}$  at the same position where previously the charge was in place. In this conditions, according to the Green theorem [38]

$$\int_{vol} [V_1 \nabla^2 V - V \nabla^2 V_1] dv = \int_{surf} [V_1 \frac{\partial V}{\partial n} - V \frac{\partial V_1}{\partial n}] ds \quad (2.22)$$

Due to the boundary conditions (on  $\nabla^2 V$  and  $\nabla^2 V_1$ ), the left side of equation 2.22 is zero and the right part reduces to the first term ( $V_1 = 1$  and  $V = 0$ ). Meanwhile, on the surface around the charge the difference of both conditions gives that

$$-V_{1q} \int \frac{\partial V}{\partial n} ds + V_q \int \frac{\partial V_1}{\partial n} ds = 0. \quad (2.23)$$

The second part of this integral is zero because in that condition, the moving charge was removed, therefore there is no electric field along the surface. Combining at this point what is left from the right part of equation 2.22 and 2.23, the total sum of those contributions is

$$-V_{1q} \int \frac{\partial V}{\partial n} ds + V_q \int \frac{\partial V_1}{\partial n} ds = 4\pi Q_A + 4\pi q V_{1q} = 0. \quad (2.24)$$

Focusing the attention on the right part of equation 2.24, the equation reduces to

$$Q_A = -q V_{1q}. \quad (2.25)$$

At this point it is very simple to obtain the induced current on the electrode A, by applying the derivative in time:

$$I_A = \frac{dQ_A}{dt} = -q \frac{dV_{1q}}{dt} = -q \frac{dV_{1q}}{dx} \frac{dx}{dt} = -q E_{wf,x} v_x \quad (2.26)$$

Equation 2.26 can be extended to all 3 dimensions, to assume the following form

$$I_A = -q \vec{v} \cdot \vec{E}_{wf}, \quad (2.27)$$

where  $\vec{E}_{wf}$  is the weighting field of the electrode system and  $\vec{v}$  is the velocity of the moving charge. Equation 2.27 represents the basic concept of the Shockley-Ramo theorem: the current induced by a moving charged on a specific electrode depends only on its velocity and the behaviour of the weighting field generated by the electrode.

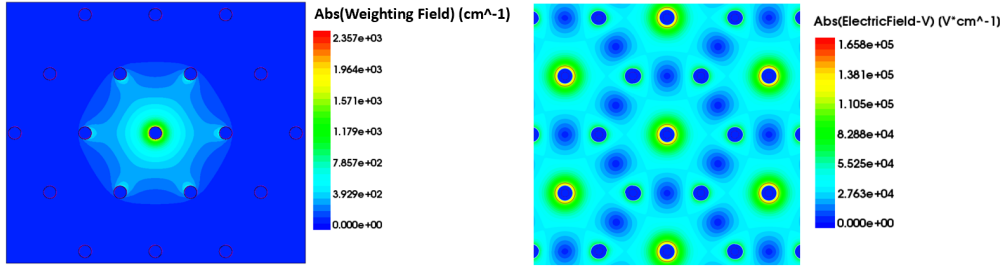


Figure 2.9: Weighting field (left) vs electric field (right) of the same electrode system. Simulation performed using Sentaurus Synopsys TCAD.

**The weighting field:** One fundamental concept of the SRT is the weighting field. The weighting field is basically a vector field which describes how strong a moving charge is coupled to a specific electrode inside an sensor system. The basic conditions needed to calculate the weighting field for a specific sensor built by  $N$  electrodes are

- that all electrodes, except the readout electrode, must at 0 bias;
- the readout electrode must be set to unitary potential;
- no free moving charge must exist along the sensor system.

Based on those boundary conditions, the weighting field can be computed like an electric field by simply integrating over the entire volume the Poisson equation taking into account the necessary boundary conditions. Sometimes the weighting field is wrongly interpreted as a normalised electric field. Indeed, the only similarity between the two is that both depend on the electrode geometry. The electric field of the sensor is obtained by applying the operational bias voltage over all voltages, the weighting field instead is generated following the boundary conditions previously presented. Only in 2-electrode systems a weighting field has the same direction as an electric field, for multiple electrode systems instead the shape changes strongly as shown in figure 2.9. For specific electrode configurations the SRT allows also an analytical solution, that is the parallel electrode configuration and the double spherical sensor. Considering the scope of this work, only information of the parallel plate configuration is presented. For the other solutions it is recommended to have a look at [39]

**Analytical solution for a parallel plate geometry:** The parallel plate configuration is the most common electrode configuration for silicon particle sensors. The configuration consists of two parallel electrodes facing each other at a distance  $d$ . The electric field for bias voltages much larger than the full depletion voltage is equal to:

$$\vec{E} = \frac{V_b}{d} \hat{n} \quad (2.28)$$

Where  $\hat{n}$  is the direction of the electric field. The weighting field is applied using the same criteria as shown previously.

$$\vec{E}_{wf} = \frac{1}{d}\hat{n}_{wf} \quad (2.29)$$

Where  $\hat{n}_{wf}$  is the direction of the weighting field. In this case, electric and weighting field have the same shape over the entire active volume due to the two-electrode structure. The electric field in equation 2.28 determines the drift velocity of both carriers

$$\vec{v}_d = \mu\vec{E} = \mu\frac{V_b}{d}\hat{n}, \quad (2.30)$$

Replacing equation 2.28 and 2.29 in 2.27 the current induced on a electrode of a sensor with parallel plate configuration is equal to

$$i = q\vec{v}_d \cdot \vec{E}_{wf} = q\mu\frac{V_b}{d^2}\hat{n} \cdot \hat{n}_{wf}. \quad (2.31)$$

Since weighting field and electric field for a 2-electrode system share the same direction and shape,  $\hat{n} \cdot \hat{n}_{wf} = 1$ , which brings to the conclusion that the induced current is equal to

$$i = q\mu\frac{V_b}{d^2} \quad (2.32)$$

At this point the only part left is to analyse the signal evolution in time for this configuration. There are 2 solutions:

**Electron-hole pair generated close to one electrode:** In this case the total drift time corresponds simply to the time the only mobile carrier left needs to cross the entire active sensor volume to reach its collector electrode:

$$t_c = \frac{d}{v_d} = \frac{d}{\mu\frac{V_b}{d}} = \frac{d^2}{\mu V_b} \quad (2.33)$$

In this case the charges which have the longest collection time are the holes, due to their lower mobility. A second important factor is the inter-electrode distance, which strongly influences charge collection time. Halving inter-electrode distance means to reduce charge collection time by a factor 4, which can be very important if the sensor is needed for time measurements.

The total collected charge  $Q$  is (ignoring charge trapping):

$$Q = it_c = q\mu\frac{V_b}{d^2}\frac{d^2}{\mu V_b} = q \quad (2.34)$$

So, all the ionised charge is collected at the end of the drift process. In figure 2.10 the respective current signals for electrons and holes are displayed.

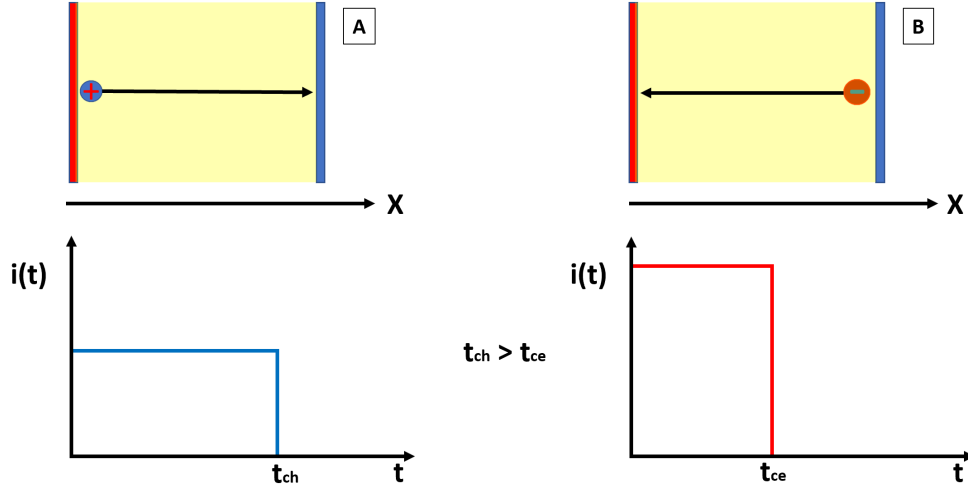


Figure 2.10: Signal formation for electron-hole pairs generated close to the electrodes. Current signal amplitude and collection time is higher and shorter respectively for electrons than for holes.

**Electron-hole pair at a distance  $x$  from the electrode:** If the electron-hole pair is generated at a distance  $x$  from the diode electrode, collection time will be different for each carrier.

$$\begin{cases} t_{ce} = \frac{x}{v_{de}} = \frac{x}{\mu \frac{V_b}{d}} = \frac{dx}{\mu_e V_b} \\ t_{ch} = \frac{d-x}{v_{dh}} = \frac{d-x}{\mu \frac{V_b}{d}} = \frac{(d-x)d}{\mu_h V_b} \end{cases} \quad (2.35)$$

The charge induced by electrons and holes on the electrode is

$$\begin{cases} Q_e = it_{ce} = e \frac{x}{d} \\ Q_h = it_{ch} = e \left( 1 - \frac{x}{d} \right) \end{cases} \quad (2.36)$$

Summing both equations in 2.36, the total charge is still  $e$ . The characteristic shape of a current signal generated by an electron-hole pair created at a distance  $x$  from one electrode assumes a stair-like shape as shown in figure 2.11. Starting with a signal which amplitude is equal to the sum of the electron and hole contribution, it slowly decreases to one contribution after one of the carriers is absorbed. Without repeating all formulas, using directly the more detailed formula for the electric field shown in equation 2.16, which describes most of the electric fields in planar silicon sensors, equation 2.35 changes slightly and the induced current is no more constant but depends also from the position of the charge inside the active region. This modifies a bit the signal shape, adding an additional tilt in the current signal, which

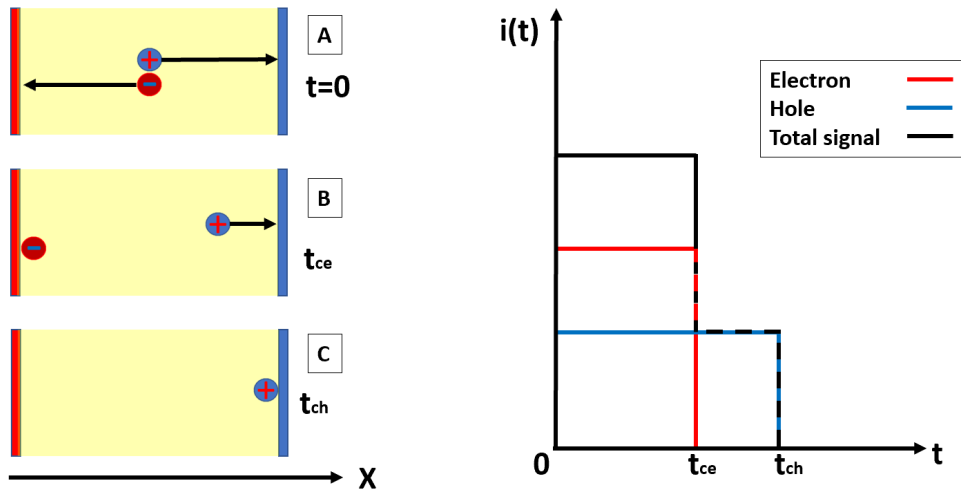


Figure 2.11: Signal formation for electron-hole pairs generated at a distance  $x$  from one electrode. (A) instants after their generation. (B) first carrier is absorbed, leaving the second one. (C) second carrier is absorbed.

becomes negligible for very high bias voltages (Fig. 2.12). Depending on how strong the electric field is, effects on velocity saturation changes more the slope along the current signal, according to equation 2.9. Both signal shapes shown in figure 2.11 and 2.12 are important for further studies in the next chapters and will be referred to in different occasions.

## 2.4 Radiation damage

Solid state sensors are not immune to ionising radiation. Every particle with enough energy is capable of damaging the material, altering its physical and electrical properties. In LHC experiments, where the radiation levels close to the interaction points are extremely high, solid state sensors and readout electronics must be specifically designed to withstand for long time those radiation dose, without changing their performances.

There are two types of radiation damages with different effects:

**Bulk damage** One damage mechanism consists in displacing one or more atoms from their fixed positions in the silicon lattice. This kind of damage is more related to the entire silicon bulk and in most silicon sensors is the main damaging effect. The average energy to move a single silicon atom from its position is 25 eV [41]. Once the atom is moved from its position to different location out of the lattice structure, a Frenkel pair is formed [42] which acts like a trapping or recombination center. For relatively low energies, displacement damage will generate defects in

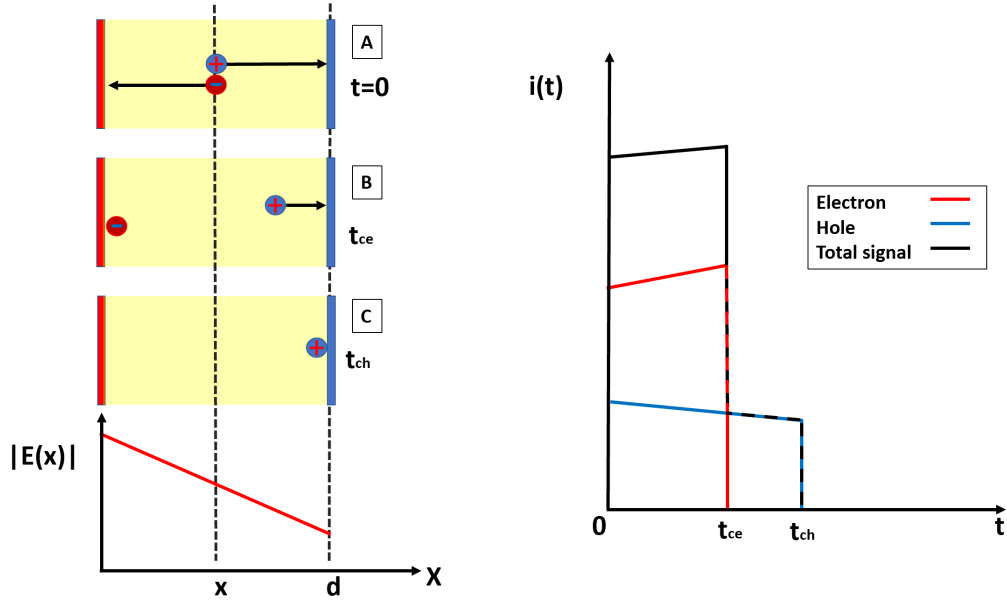


Figure 2.12: Signal formation for electron-hole pairs generated at a distance  $x$  from one electrode including electric field variation through the medium. (A) instants after their generation. (B) first carrier is absorbed, leaving the second one. (C) second carrier is absorbed.

the silicon lattice involving one of few atoms. For energies above the 35 keV for neutrons and 8 MeV for electrons, displacement damage will cause more extended and clustered defects [41], involving thousands of atoms [43].

Displacement clusters or points have important effects on the performance of the sensor. One of them is the formation of mid-gap states which alter the energy bands of the silicon, acting as recombination and generation centres, that increase the leakage current and the noise. A second effect is the gradual type inversion of  $n$ -type doped silicon, which gradually changes in behaviour like  $p$ -type doping.

Bulk damage depends strongly on the particle type and charge. For example, the energy needed to generate a Frenkel pair is about 260 keV for electrons and 175 keV for neutrons [44]. In order to have a better understanding of the effects of different particles, the non-ionizing energy loss (or NIEL) scaling is used. NIEL consists in scaling the effects on bulk damage caused by a specific particle to the damage release by a 1 MeV energetic neutron. The conversion is done using the following expression

$$\phi_{neq} = k\phi, \quad (2.37)$$

Where  $\phi$  is the fluency of the particle beam and  $k$  is the hardness factor which depends on the material and sensor technology.

**Surface damage:** Surface damage depends on ionisation effects on insulator materials, like silicon oxide ( $\text{SiO}_2$ ). Ionisation energy in silicon oxide is 18 eV and, like silicon, electron-hole pairs are formed. Electrons have a good mobility in  $\text{SiO}_2$  ( $\mu_e = 20 \text{ cm}^2\text{V}^{-1}\text{s}^{-1}$ ) and drift to the closest collector electrode. Holes instead, have a bad mobility ( $\mu_h = 2 * 10^{-5} \text{ cm}^2\text{V}^{-1}\text{s}^{-1}$ ) and the probability of getting trapped in the insulator layer is high. The same mechanism occurs for the few holes left which reach the oxide-silicon interface, which are most probably trapped by interface traps generated by lattice mismatch along the interfaces. This high concentration of charged spots through the interface causes two main effects, a larger conductivity along the insulator-silicon interface and a parasitic electric field [32]. Also an increase of the capacitive coupling between neighbour pixel is a direct consequence of surface damage.

### 2.4.1 Radiation damage effects on sensor performance

**Reverse bias current** Reverse bias current increases with radiation exposure due to the generation of mid-gap states which reduces the band-gap and allows thermal carriers to switch easier from the valence to the conduction band

$$I = I_0 + \alpha\Phi Ad, \quad (2.38)$$

where  $\alpha$  is the damage coefficient related to a specific particle,  $\Phi$  is the fluency and  $Ad$  the volume between the electrodes. The leakage current is a critical factor for timing, considering that it will increase the noise (and with it the jitter) of the sensor.

**Doping inversion** Displacement damage causes the formation of acceptor like states in the silicon lattice which modify the effective doping concentration  $N_{eff}$ . For  $n$ -doped volumes this modification has important effects. The gradual increase of acceptor like states reduces the effective doping concentration in the bulk, until the silicon reaches an equivalent zero dopant concentration. For even higher fluencies, it is possible that the concentration increases even further changing the behavior of the bulk from donor to acceptor. This process is called type inversion and a first systematic study of the type inversion was done by Wunstorf [45] (Fig. 2.13). Due to the change in effective doping concentration, the depletion voltage of a particle sensor increases and becomes larger with increasing concentration.

$$V = \frac{e}{e\epsilon} |E_{eff}| d^2 \quad (2.39)$$

It is important to notice in equation 2.39 that  $V$  depends on the square of the sensor thickness/inter-electrode distance. Thinner sensors or sensors with closer inter-electrode distance can be a good solution to reduce this effect.

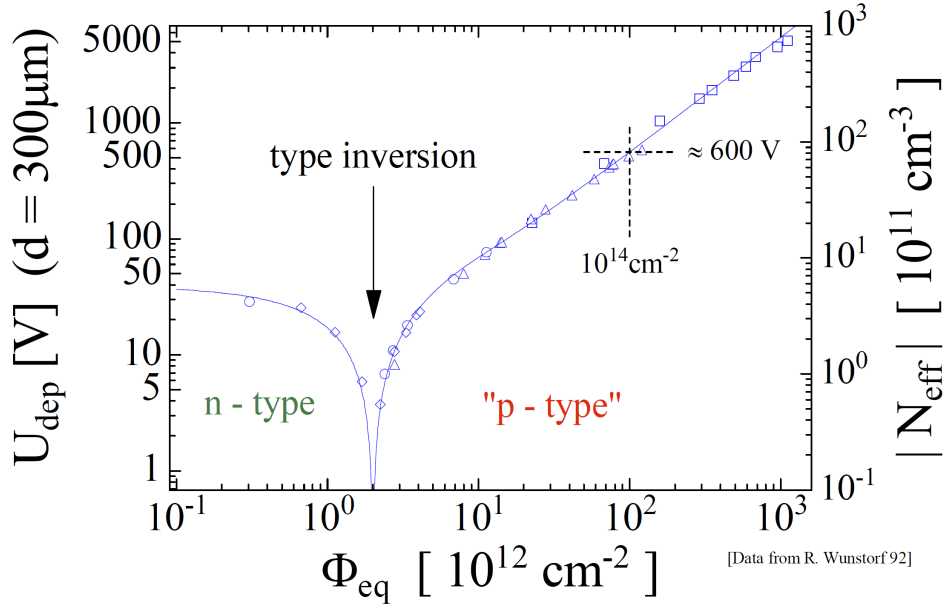


Figure 2.13: Type inversion in p-doped silicon in function of the fluence [45].

### 2.4.2 Radiation damage effects on signal formation

As shown previously, radiation damages the silicon and alters the electrical properties of the sensor. Excluding the increment of leakage current, the main effect of radiation damage is the formation of charge traps. Charge traps are already present in the silicon lattice even before being irradiated, this is due to fluctuations during the crystal growth phase and, later, during the sensor fabrication.

A charge trap is nothing else than a point in the silicon lattice which presents a local potential which allows to trap a mobile carrier. Depending on the nature of the trap, the average temperature of the carrier and the applied electric field a trapped charge can be released again. Considering a charge  $Q_0$ , generated instants after the passage of an ionising particle, trapping will slowly cause a reduction of this quantity with exponential decay.

$$Q(t) = Q_0 \exp\left(-\frac{t}{\tau}\right) \quad (2.40)$$

[32], where  $\tau$  is the average lifetime of every single carrier, which depends on the number of traps and mobile carriers left in the silicon.

### 2.4.3 Radiation damage mitigation techniques

It is possible to reduce the effects of radiation damage by properly modelling the geometrical features and material properties. The easiest approach is by reducing charge collection time which would lower the probability of trapping. This approach in planar sensors presents some limitations due to the reduction of deposited charge

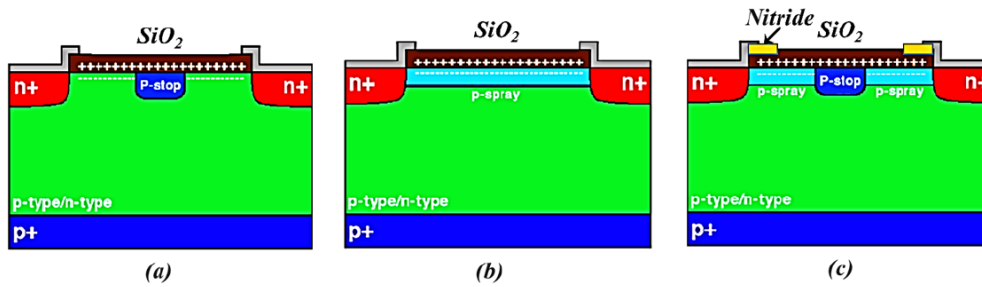


Figure 2.14: Different surface damage mitigation techniques. (a) *p*-stop, (b) *p*-spray and (c) moderated *p*-spray [48].

in the silicon in thinner sensor layers which is difficult to measure.

About surface and bulk damage there are different approaches that can reduce drastically radiation damage.

The first approach is the use of *p*-type high resistive sensor wafers instead of *n*-type doped layer, avoiding type inversion. A second approach is to add secondary impurities in the silicon like oxygen or carbon in the silicon. The oxygen atoms help reducing the variation of effective doping concentration caused by radiation [46].

The positive charge trapped in the oxide-silicon interface along the sensor surface can be reduced by using thin *p*-doped layers or structures like *p*-spray, *p*-stop or moderated *p*-spray [47] (Fig. 2.14).

## 2.5 Overview of particle sensors

This section shows a general overview of current state of the art sensors used in high energy physics:

### 2.5.1 Planar sensors

Most of the existing silicon sensors are based on planar technology, which means that the electrodes are built on the surface of the high resistive, 200-300  $\mu\text{m}$  thick, silicon wafer. The electrode structure is generally formed by one large bias electrode at the bottom of the silicon wafer and a high granularity implant matrix on the other surface. Depending on the doping type of the wafer and the readout electrode, four main sensor configurations can be realised:

- *p*+ readout electrode on a *p*- or *n*- doped bulk. Those configurations are called *p*-in-*p* and *p*-in-*n* respectively.
- *n*+ readout electrode on a *p*- or *n*- doped bulk. Those configurations are called *n*-in-*p* and *n*-in-*n* respectively.

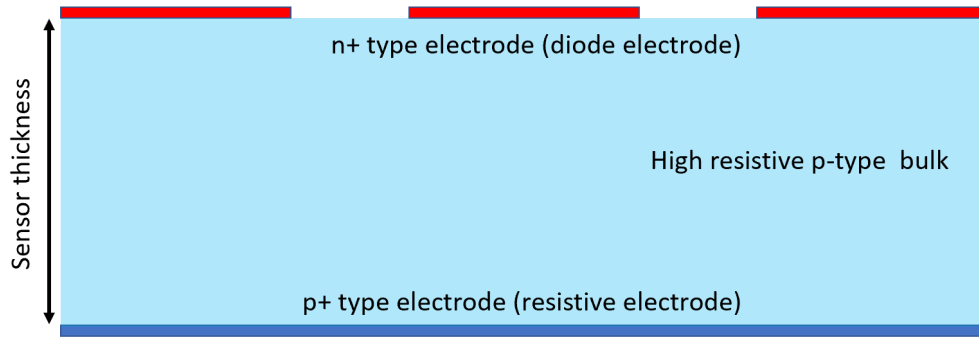


Figure 2.15: Typical structure of a planar  $n$ -in- $p$  sensor.

Depending on the position of the pn-junction, the electrode is called diode-electrode when the  $n$ -type ( $p$ -type) electrode is implanted by a  $p$ -type ( $n$ -type) bulk or ohmic-electrode when the  $n$ -type ( $p$ -type) electrode is implanted in a same doping type bulk with different doping concentration (Fig. 2.15). As shown previously, due to type inversion during high radiation damage,  $p$ -type bulk doping is preferred especially for harsh radiation environments.

An example of a classical planar sensor with high granularity pixel matrix developed for tracking purposes is the LHCb-Vertex Locator (VELO) for the phase I upgrade [19]. Each planar sensor is a rectangular pixel matrix built of by 256 times 768 pixel with a square pixel shape  $55 \times 55 \mu m^2$  large.

### 2.5.2 Avalanche sensors

As described in section 1.2, increasing the reverse bias voltage over a certain threshold gives the electrons enough energy to ionise other atoms of the silicon medium, causing an avalanche of carriers which, if not properly handled, causes sensor break-down. Avalanche sensors use this process to increase signal to noise ratio for different applications, like photon counting or for spectroscopy. Some examples are avalanche photo diodes (APDs) [49] or Silicon Photo Multipliers (SiPM) [50].

**LGAD** A special focus in this section is dedicated on Low Gain Avalanche Detectors (LGAD). The LGAD uses the same working principle as APDs, based on the impact ionisation at high electric fields but with a modified doping profile [71] and first prototypes were fabricated in CNM-IMB [52] in 2014. In principle, a LGAD is a planar,  $n$ -in- $p$ , silicon sensor with the addition of a  $p^+$  doping layer between the  $n^+$ -doped cathode and the silicon bulk (Fig. 2.16). By applying an reverse bias voltage, the electric field which forms between the electrodes, reaches its maximum in the area between the  $p^+$  doped layer and the cathodes, allowing charge

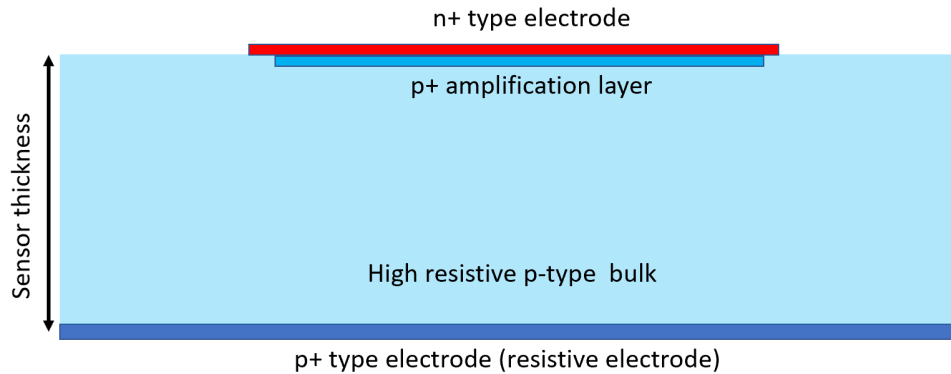


Figure 2.16: General structure of a LGAD sensor.

multiplication. The electrons generated by the avalanche process are immediately collected by the cathode, the holes instead drift to the lower resistive electrode. The result is a strong signal current which depends mostly by the drifting holes. This feature makes LGADs ideal sensors for high resolution time measurement far below 100 ps, as proposed in [53] and demonstrated in different works like [54]. Especially LGADs with small sensor thickness have a large time resolution. Despite this good performances, the LGAD technology suffers some critical issues. One is strongly related to radiation damage at high fluencies on the  $n$ -doped cathode. In fact, at high radiation fluencies, the radiation damage causes a slow degradation of the gain layer due to boron removal. A second problem is related to the sensor thickness. Reducing sensor thickness increases sensor capacitance and, as demonstrated in the next chapters, will reduce signal to noise ration and time resolution.

### 2.5.3 3D sensors

A possibility to obtain strong current signals, without using impact ionisation and still holding charge collection time below 1 ns achieving good time resolution is with the 3D-sensor technology. 3D silicon sensors are the main subject of this work and the next chapter is fully dedicated on all aspects of this sensor technology.

# Chapter 3

## 3D sensors for fast timing applications

The incoming environmental changes at the HL-LHC opens new challenges on sensor technology. The increased high event pile-up associated with the increased fluency will inevitably require a sensor capable of resisting the harsh radioactive environment and at the same time provide fast timing at tens of ps. Classical planar sensors, as currently used in most tracking detectors, like the LHCb VELO [18], its 2019 upgrade [16] or most of the inner tracking systems like the ATLAS IBL [56] and CMS, are insufficient to operate in high luminosity conditions as shown in chapter 1. Two factors play an important role to define the next tracking detector generation to use in future HL-LHC:

- High radiation tolerance up to  $10^{16}$   $1 \text{ MeV n}_{\text{eq}}\text{cm}^{-2}$  in regions close to the interaction point.
- Fast charge collection, possible lower than 1 ns.

Classic planar sensor cannot achieve fast charge collection due to their large thickness. Even if operating in velocity saturation, an electron would take  $\sim 1 \text{ ns}$  for travelling  $100 \mu\text{m}$  of silicon, holes even longer. A solution to reduce charge collection time is to fabricate thinner planar sensors but, reducing sensor thickness, reduces the collectable energy, with negative effects on the signal to noise ratio. A possible solution is to use charge amplification like in LGAD sensors which allows to generate signals with high signal to noise ratio with small energy deposits. Current state of the art LGAD sensors have a sensor thickness below  $50 \mu\text{m}$  and achieve tens of ps of time resolution [54]. Despite this promising fast charge performance, LGADs suffer high radiation degradation especially on their gain layer due to acceptor removal, which reduces inevitably the gain and time resolution.

A possible candidate which is potentially capable of satisfying the high radiation hardness with the high time performance is the 3D silicon sensor technology.

This chapter will describe the general aspects of the 3D sensor technology and

presents some applications. Half of the chapter is dedicated to timing applications of 3D silicon sensors, main scope of this work, and introduces to timing theory in silicon sensor based detector systems.

## 3.1 3D sensors

The 3D silicon sensor is a relatively new solid state sensor technology and was first proposed by S.I. Parker, C.J. Kenney and J. Segal in 1997 [21]. Main technological characteristic of 3Ds is the decoupled inter-electrode distance from the wafer thickness, achieved by fabricating the electrodes in vertical structures deep inside the silicon bulk using micro-machining techniques. This characteristic has positive repercussions on the sensor performances, especially on:

- **Fast charge collection:** Decoupled electrode spacing allows to use thick sensor wafers and still achieving fast charge collection by reducing the electrode spacing at few tens of micrometers. Charge drift is horizontal instead of vertical and large charge deposits up to  $\sim 8000$  e/h pairs every  $100 \mu\text{m}$  of sensor thickness can be collected, depending on the electrode spacing, in less than 1 ns ( $\sim 100$  ps every  $10 \mu\text{m}$  drift path for electrons in velocity saturation) (Fig. 3.1).
- **High radiation hardness:** Fast charge collection reduces the probability of charge trapping and increases charge collection efficiency even at high fluency rates. This property was already demonstrated theoretically and experimentally in [57], [58], [59], [60] and [62].
- **Smaller bias voltage:** Sensors with smaller inter-electrode distances need a lower bias voltage to deplete the entire sensor volume (even less than 10 V are possible, depending on the electrode spacing). This characteristic has positive repercussions on the power consumption of the detector system.

### 3.1.1 Structure and fabrication

A 3D sensor can be distinguished by the technological fabrication process and its electrode structure.

The fabrication of the electrodes is based on micro-machining techniques like the anisotropic *Deep Reactive Ion Etching* (DRIE). DRIE allows to build complex structures, like holes, deep in the silicon with large depth-to-width ratios even higher than 40:1 in the latest production runs [63] and excavate in silicon with velocities higher than  $3 \mu\text{m}/\text{min}$  by holding the non-uniformities at levels below 5 %. Standard procedure for DRIE is the Bosch-Process [64] [65], which consists of an alternation of two fabrication processes based on an etching process with a successive passivation of the realised structures in order to not damage them in the successive etching step

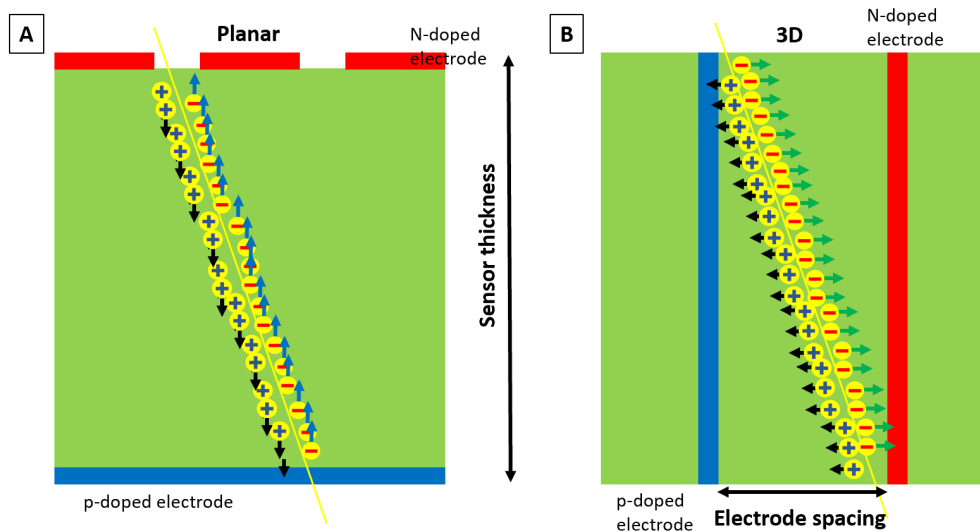


Figure 3.1: (A) Planar vs. (B) 3D sensor with same sensor thickness. Reducing inter-electrode spacing allows to reduce charge collection time

[66] (Fig. 3.2). Electrode structures built in 3D sensors have commonly a columnar shape. Recent advances in fabrication processes allows also to built high density trenched structures with wall width lower than  $5\ \mu\text{m}$  [63].

Columns were the first electrode structure proposed [21], fabricated and applied in an experiment [56]. Compared to trenches their structure is easier to build because the etching along the sides of the columns is isotropic due to their circular shape. Trenches on the other hand have different etching rates around the rectangular section due to the different exposed surface but presents more advantages in terms of uniform sensor response, as it will be shown in chapter 4.

**Fabrication processes** 3D sensor fabrication processes changed during the last 20 years and different approaches were proposed and tested. A 3D fabrication process can be divided up into 3 main categories.

- **Semi-3D:** Semi-3D technology consists in building only one kind of electrode in 3D structures, while the second one is realised in classic planar technology. FBK used this approach (FBK-STC) with two main variations concerning the p+ doped electrodes: one passing through the entire wafer thickness and the second one with partially passing electrodes [67].
- **Full-3D single-side:** Single-side approach was firstly introduced by Stanford University using Silicon On Oxide wafers[68]. A successive improvement of the technology was introduced by FBK for the LHC phase-II upgrade[69]. In this approach, the sensor wafer is wafer-bonded on a second low resistive

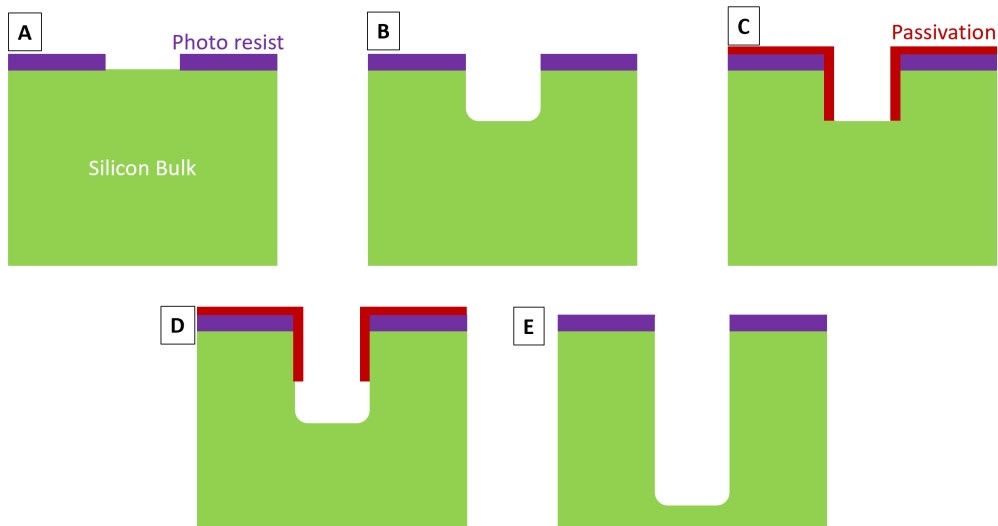


Figure 3.2: General description of deep reactive ion etching based on the Bosch process. (A) Photo resist applied on the silicon. (B) First etching step. (C) Passivation of the obtained structure. (D) Successive etching step. Procedures (C) and (D) are repeated N-times until the structure is completely build (E).

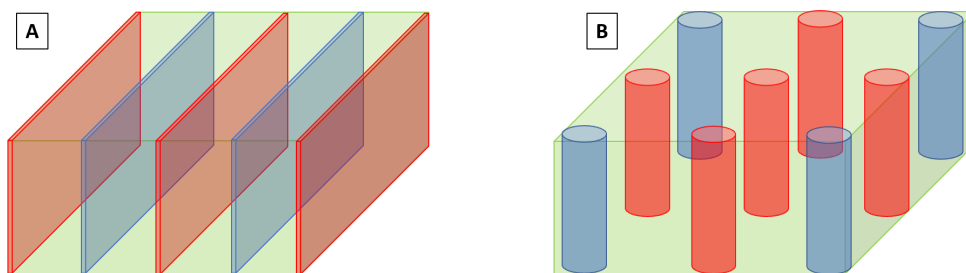


Figure 3.3: General 3D sensor electrode configuration. (A): Trench electrode configuration. (B) Column electrode configuration.

support wafer which is used during fabrication to enhance mechanical stability. p+ doped (resistive) electrodes are etched in a first phase through the entire sensor wafer, reaching the support wafer. This allows to establish electrical contact to the support wafer which will be used to provide from the back side the bias voltage. n+ doped diode electrodes instead are etched only partially through the sensor wafer and stops at short distance from the support wafer (around 20  $\mu\text{m}$ ) in order to prevent sensor breakdown (Fig. 3.4.B). At the end of the fabrication process most of the support wafer is removed, leaving a small layer of it, which is metallised and used to provide the bias voltage. FBK also demonstrated the validity of this approach using a *Silicon On Insulator* (SOI) support wafers, achieving to etch through the silicon oxide layer [70]. Using a SOI wafer instead of a common low resistive support wafer allows to limit electrical contact only on the areas where the columns passes through the silicon oxide, reducing leakage. On the other hand this technology is more difficult to handle during the etching process of the silicon oxide, which is less reactive than the silicon.

Single side fabrication allows also the realisation of active edges [68], which are trench structures able to limit the dead volumes around the edges of the sensor array and handle the leakage current along the borders of the sensors matrix, acting like the guard ring in a planar sensor.

- **Full-3D double side:** Double-side approach was developed independently by CNM [71] and FBK [73]. This approach cannot rely on the use of support wafers and needs thicker sensor wafers. In double side 3D fabrication each electrode is etched from a different surface of the wafer (Fig. 3.4.A). This technology does not allow the realisation of active edges due to the double side fabrication of the sensor wafer. An alternative to active edges in double side 3D sensors are *slim edges* [73] which are basically areas with resistive electrodes which surround the frame of the sensor matrix. They act similar to guard rings or active trenches but need a larger area in average.

### 3.1.2 Applications

3D sensors can be used in different applications, from dosimetry to particle tracking or for medical applications. Same sensor arrays can be organised electrically, depending on the application, by properly arranging the electrical connections of the electrodes into strip, pad or pixel detectors.

**HEP applications** High radiation hardness and fast charge collection makes 3D silicon sensors ideal candidates for particle tracking in regions with high radiation fluencies. The first large scale application of 3D sensors in a tracking detector was made by the ATLAS collaboration, including them in the Insertable B-Layer (IBL)

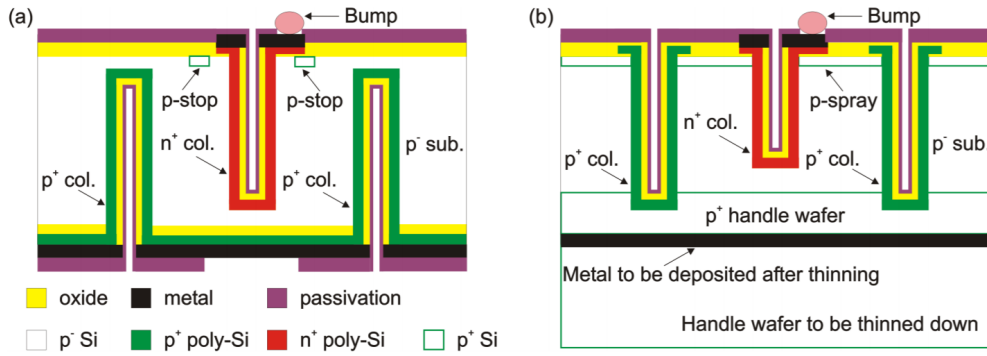


Figure 3.4: FBK full-3D fabrication processes: (A) Double side approach. (B) Single side approach. [69].

[56], which design started with the ATLAS 3D collaboration in 2009. The designed sensors, based on a double side approach, were produced by two different foundries, CNM [71] and FBK [73], and their layout was arranged for the FE-I4 front-end chip design [56] which is directly bump bonded on the sensor. 3D sensors in the IBL makes 25 % of the used sensors. Their position in the single tracking modules (Fig. 3.5) is at the extremities, where two staves are positioned. The middle part of the staff is covered by 12 modules built with planar sensors.

With the official EoI of the High Luminosity upgrade, a second reason motivates the need for 3D silicon sensor in high energy particle experiments: timing. As shown previously in chapter 1, the high event pile-up requires high granularity pixel sensors which are also able to be fast enough to measure the time of the single events during a bunch crossing. The TIMESPOT initiative is a direct answer to this critical issue and is currently developing a timing-optimised 3D silicon sensor with dedicated electronics in order to understand the feasibility of this technology.

**Neutron detection** Neutron detection has important applications in medical imaging or in the detection of radioactive materials. Silicon sensors are not directly able to detect neutrons due to their neutral charge and need to be coupled with a converter material to be sensitive for them. The idea of using 3D sensor technology instead of planar technology was already tested previously by Uher et. al [76]. The study has shown the advantages of 3D sensor in neutron detection, presenting a tracking efficiency of 33 percent of 3D-neutron sensors compared to 4.9 percent of a simple planar design and 6.3 percent of an enhanced planar design with small 3D structures using pyramidal dips. A more recent and interesting application of 3D sensors for neutron detection is the *HYbrid DETectors for neutrons* (HYDE) project, carried out by the University of Trento in collaboration with the FKB and INFN-LNL [77]. The developed neutron detector is based on a 3D silicon sensor coupled with a polysiloxane rubber converter which provides the neutron conversion into other detectable products. The 3D sensor used for this application

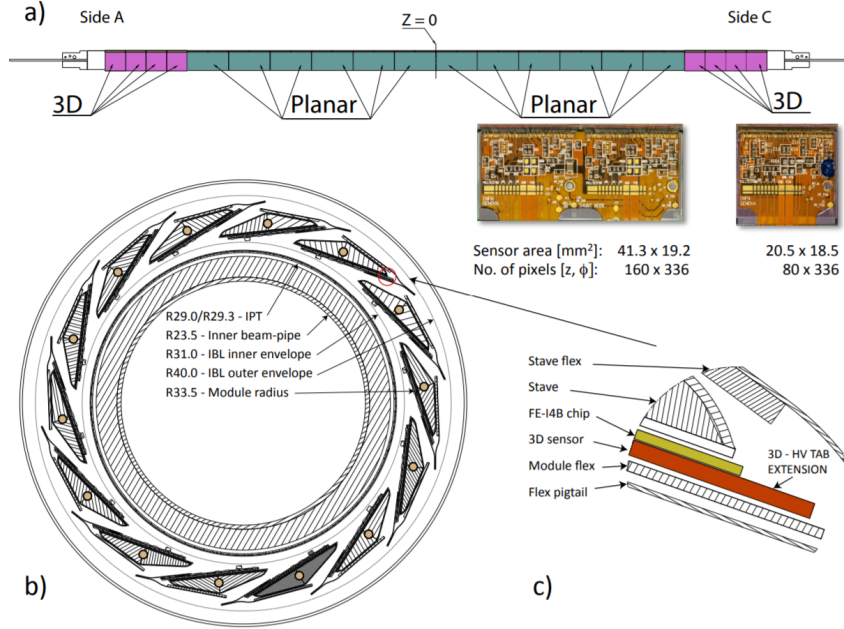


Figure 3.5: ATLAS Insertable B-Layer layout and tracking modules [74]. (A) Stave layout. (B) Layout of the IBL. (C) Single stave layout.

is based on a semi-3D design developed and fabricated by FBK with  $200\ \mu\text{m}$  large and n+ doped cavities, which are filled with the converter material, and normal p+ doped planar electrodes on the other side. The sensor has been produced and tested with neutron fluxes of more than  $10^6\ \text{n}/(\text{cm}^2\text{s})$  and also without converter material, showing promising results. For future application a full 3D sensor is under development in order to apply *time of flight* necessary to discriminate gamma from neutron radiation [77].

## 3.2 3D and timing

This section describes general aspects of time resolution tracking detectors, with a special focus on 3D sensors.

### 3.2.1 Total time resolution of a particle detector system

According to [78], the total time resolution of a detector system is the contribution of 3 factors:

$$\sigma_{tot}^2 = \sigma_{tw}^2 + \sigma_j^2 + \sigma_{TDC}^2. \quad (3.1)$$

Where  $\sigma_{tw}^2$  is the error contribution due to time-walk,  $\sigma_j^2$  is the error contribution due to noise/jitter and  $\sigma_{TDC}^2$  is the resolution of the TDC.

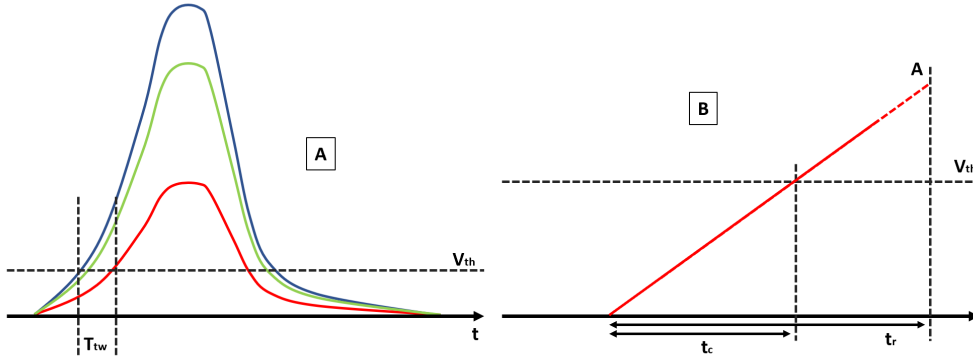


Figure 3.6: (A): Example of a time walk distribution: All 3 signals share same shape but signals with high amplitude cross the threshold in less time than signals with small amplitude. (B): Linear approximation of the rising edge of one single signal, showing the crossing time  $t_c$ , signal amplitude  $A$ , the rise time  $t_r$  and the threshold  $V_{th}$

**Time-walk** The concept of time-walk is strongly related to the amount of energy a particle releases in the sensor and the trigger mechanism of the discriminator in the readout electronics. In order to reduce false trigger due to noise, a threshold  $V_{th}$  is applied high enough to safely trigger on the rising edge of the signal. Assuming for simplicity an analog front-end which produces output signals with invariant shape, a linear rising edge with rise time  $t_r$  and amplitude  $A$ . Also assuming that those signals are sent to a discriminator with static threshold  $V_{th}$ . Then, as shown in figure 3.6, the time  $t_c$  necessary for every signal to cross the threshold is equal to:

$$t_c = \frac{t_r V_{th}}{A} \quad (3.2)$$

Signal amplitude is proportional to the deposited energy in the silicon sensor and, therefore, larger deposits will generate signals with higher amplitude and higher amplitude means faster rising edge. Depending on fluctuations in the energy deposits and noise, signal amplitude changes from signal to signal and with it the  $t_c$ . Especially in the case of energy deposits generated by MIPs, the generated amplitude distribution follows a Landau distribution as shown in [79]. Following this study, it was measured experimentally that the width of the Landau distribution increases with decreasing sensor thickness. This factor is certainly due to the energy deposit generated by secondary particle emission, like delta rays, which results more dominant if compared to the primary MIP. The distribution in energy deposits observed by the sensor directly contributes to the distribution in crossing time, whose root mean square defines the time walk distribution

$$\sigma_{tw}^2 = RMS[t_c] = RMS\left[\frac{t_r V_{th}}{A}\right]. \quad (3.3)$$

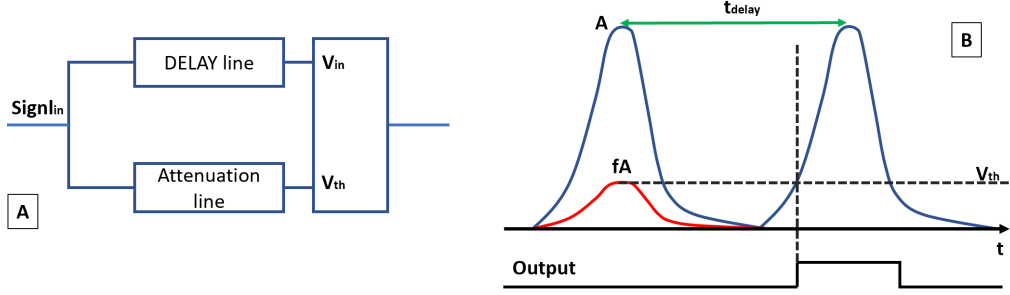


Figure 3.7: (A): General architecture of a constant fraction discriminator. (B): Working principle of a CFD.

If  $V_{th}$  is set as constant, time walk can only be reduced by reducing  $V_{th}$ , but this approach has limits related to the noise level of the detector system, which need to be taken into account.

It is possible to reduce time walk by changing the trigger technique which will be described in the next section.

**Time-walk mitigation techniques: CFD** Single threshold or leading edge discriminators are not the best solution for fast time measurement because, as shown previously, they cannot reduce the time walk due to fluctuations in the released energy deposits. It is possible to use other, more interactive techniques which are able to minimise the time walk contribution, increasing time resolution. One solution is using a Constant Fraction Discriminator (CFD). A CFD circuit works as follows: The signal with amplitude  $A$  entering the CFD is doubled and sent to two different lines. The first line delays the signal by a time  $t_d$ . The second line applies an attenuation of the signal by a factor of  $f$  and measures the signal amplitude, which is now  $fA$ . Both signals reach a comparator, which uses the value of the attenuated amplitude  $fA$  as threshold as trigger for the delayed one.

$$V_{th} = fA \quad (3.4)$$

Considering the delay time  $t_d$  needed for the signal to reach the comparator and the time  $t_c$  to cross the threshold, using equation 3.4 in equation 3.2, the time at which the comparator fires is:

$$t_{cCFD} = t_c + t_d = \frac{t_r V_{th}}{A} + t_d = \frac{t_r A f}{A} + t_d = f t_r + t_d. \quad (3.5)$$

Considering that  $t_d$  is still a constant parameter but  $t_r$  depends from the signal amplitude, using equation 3.4 in equation 3.2, the uncertainty introduced by a CFD depends only from the signal rise time and the attenuation factor.

$$\sigma_{tw}^2 = RMS[t_c] = RMS[f t_r + t_d] = RMS[f t_r] \quad (3.6)$$

**Jitter** Signal noise introduces fluctuations in time that can strongly influence the trigger time of the discriminator. The uncertainty in time introduced by noise is called jitter and depends from the noise level  $\sigma_n$  and how the signal changes in time (Fig. 3.8)

$$\sigma_j = \frac{\sigma_n}{\frac{dV}{dt}}. \quad (3.7)$$

Assuming that the leading edge of a signal can be approximated in a constant slope, which means that  $\frac{dV}{dt} = \frac{A}{t_r}$ , equation 3.7 becomes:

$$\sigma_j \approx \frac{\sigma_n t_r}{A}, \quad (3.8)$$

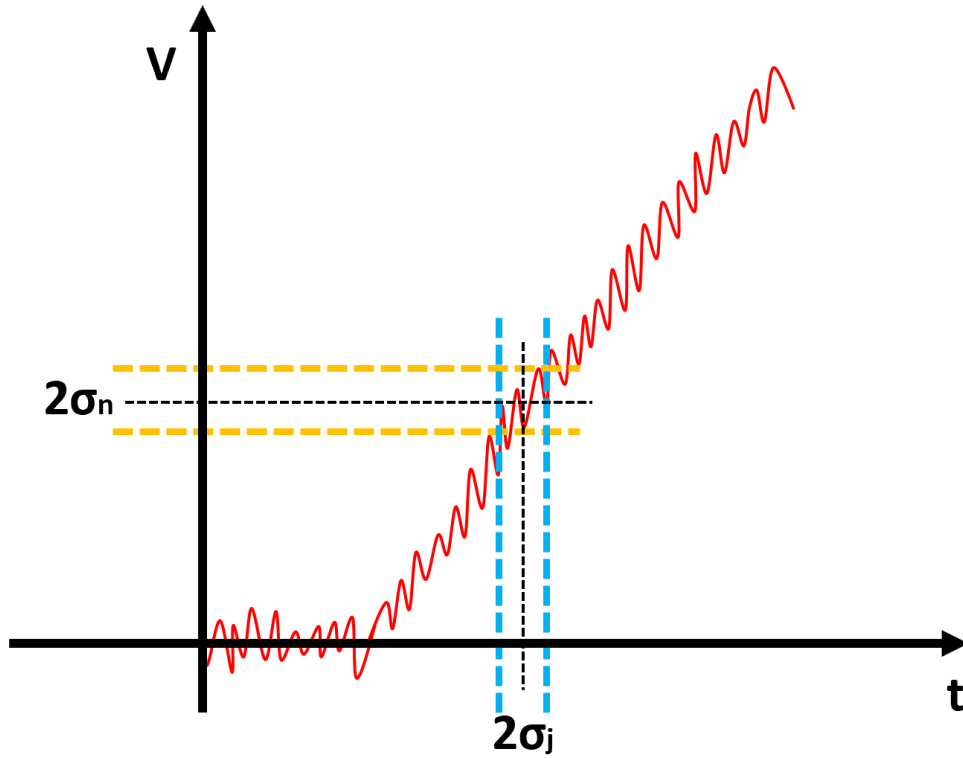


Figure 3.8: Signal jitter related to signal noise.

where  $t_r$  is and  $A$  is signal rise time and amplitude respectively. In order to reduce  $\sigma_j$ , an optimisation of the rise time of the amplifier chain must be done. Considering an amplifier chain with  $n$  stages, the total rise time  $t_{ra}$  of the signal is the sum in quadrature of the the individual rise times [32]:

$$t_{ra} = \sqrt{t_1^2 + t_2^2 + \dots + t_n^2}. \quad (3.9)$$

Choosing a this point a sensor with a total charge collection time  $t_{ct}$  and connecting it with the amplifier chain, then, if the rise time of the amplifier chain is far greater than the collection time, the electronic noise will be dominated by the amplifier rise time rather than the collection time [32]:

$$N \propto \sqrt{\frac{1}{t_{ra}}} \quad (3.10)$$

At the same time the slope of the total signal is dominated by the amplifier rise time:

$$\frac{dV}{dt} \propto \frac{1}{t_{ra}}, \quad (3.11)$$

And the jitter becomes:

$$\sigma_t \approx \frac{\sigma_t t_r}{A} = \frac{1}{V_0} \sigma_t t_r \propto \frac{\sqrt{t_{rc}}}{V_0} \sqrt{\frac{t_{rc}}{t_{ra}} + \frac{t_{ra}}{t_{rc}}}, \quad (3.12)$$

$V_0$  depends mainly from the collected charge  $Q_0$  and the capacitance of the sensor  $C_s$ , showing that equation 3.12 becomes:

$$\sigma_t \propto \frac{\sqrt{t_{rc}} C_s}{Q_0} \sqrt{\frac{t_{rc}}{t_{ra}} + \frac{t_{ra}}{t_{rc}}}. \quad (3.13)$$

Relation 3.13 describes how a reduction of the system jitter is achieved by properly set the rise time of the amplifier chain equal to the charge collection time. A second factor which influences strongly jitter is the sensor capacitance. The higher the sensor capacitance and the higher the jitter contribution. This means that jitter can be reduced acting on two different parameters, front-end rise time and sensor capacitance.

**Time to digital converters** Contribution in the total time resolution introduced by the TDC is given by the least significant bit (LSB)

$$\sigma_{TDC} = \frac{LSB}{\sqrt{12}}. \quad (3.14)$$

**Total time resolution** Using equation 3.14, 3.6 and 3.7 in equation 3.1, the total time resolution of a usual detector system is equal to:

$$\sigma_{tot}^2 = \frac{LSB}{\sqrt{12}} + \frac{\sigma_n}{\frac{dV}{dt}} + RMS\left[\frac{t_r V_{th}}{A}\right]. \quad (3.15)$$

Focusing the attention only on the contribution of the sensor, its main contribution is related to the system time walk and jitter. Especially time walk can be minimised by using dedicated discrimination techniques like CFD but Jitter will still be present.

### 3.2.2 Timing error sources in 3D silicon sensors

3D silicon sensors, as shown previously, present some special characteristics which make them theoretically the ideal candidate for fast timing measurement in harsh radiation environment. The potentialities and critical issues of timing applications with 3Ds are described for the first time in detail in [22]. The work explores most of the factors which can influence negatively time resolution on detector based on 3D silicon sensors.

**Electrode geometry** In a planar sensor with applied over bias voltage, the electric field inside the active volume is mostly uniform and corresponds to  $\frac{V}{d}$  as shown in chapter 2. The electric field uniformity is not an intrinsic characteristic of 3D sensor because, as it will be demonstrated in chapter 4, not every electrode configuration allows to generate a strong and uniform electric field inside the active volume of the sensor.

Electric field dis-uniformity is a critical aspect for timing because it affects signal rise time, shape and charge collection time depending on where and how the ionising particle crosses the active volume. Special cases are regions between electrodes at same potential where the electric field drops to zero, slowing down drift velocity, affecting negatively charge collection time and current signal amplitude. Longer charge collection time means a higher probability that charges can be trapped during drift, especially if the sensor is already exposed to radiation, reducing charge collection efficiency.

A way to reduce this critical issue is achieved by reducing electrode spacing, which allows stronger electric fields with lower bias voltage and a more efficient charge collection. Also, using an dedicated electrode geometry reduces the presence of low electric field regions. The best solution to achieve an uniform sensor response is to apply directly a *parallel wall electrode* (or trench) geometry, as proposed for the first time by [22]. This geometry would allow fast and uniform charge collection with minimum current signal variations over all the active volume.

**Landau fluctuations and delta-rays** Landau fluctuations are variations of the deposited energy with respect to the most probable value. Main cause of Landau fluctuations in silicon sensors are delta-rays, which are electrons generate by ionisation with enough energy to produce further ionisation in the medium. According to [22], the number  $n$  of delta rays generated per  $1\ \mu\text{m}$  path of the primary ionising particle depends inversely to their kinetic energy as:

$$n = \frac{3.15\text{keV}}{T_1} \quad (3.16)$$

with  $T_1$  the average kinetic energy of the delta ray. Delta rays with small energy are more probable but at the same time their ionising path is very small and their ionisation ends at distances lower then  $500\ \text{nm}$  from their generation position. On

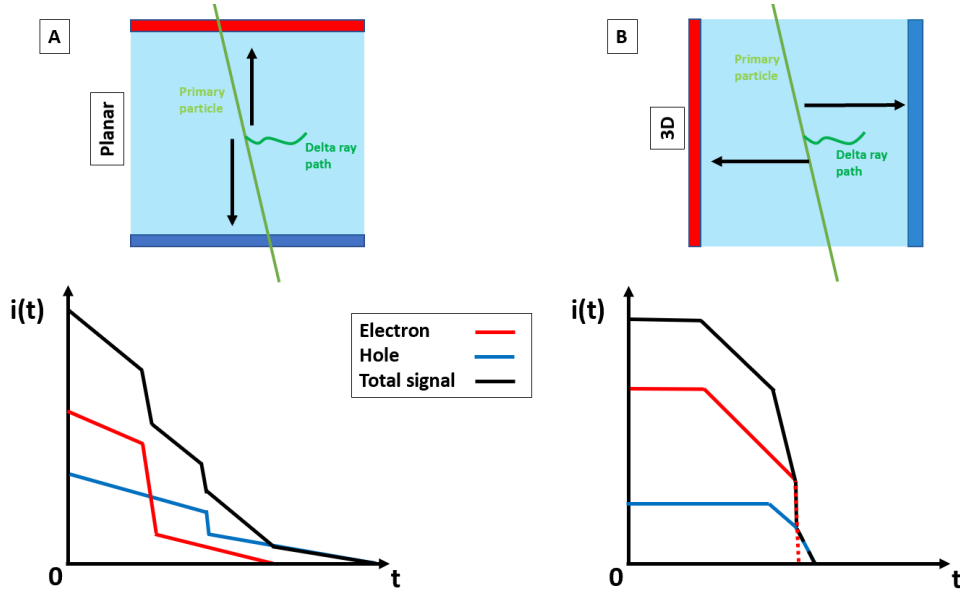


Figure 3.9: Representation of current signal evolution in a planar (A) vs a 3D sensor (B) in presence of a delta ray with higher energy. Random absorption of the electrons and holes in planar sensors makes it difficult to have an uniform sensor response and, therefore, good timing performances. In 3Ds absorption is almost done simultaneously on both deposits, achieving a smoother signal response.

the other hand, delta rays with larger energy are less probable but can generate ionisation paths of few micrometers in length. In planar sensors, energy deposits generated by delta rays have negative effects on timing because their random position in space causes random absorption in time, affecting signal shape. Compared to planar sensors, 3Ds are more immune against delta rays due to their geometry. In fact, if the electrodes are directed parallel to the incoming ionising particles, charge collection of primary and secondary particle deposits happens mostly simultaneously, obtaining a smoother signal response [22] (Fig. 3.9). Delta rays play an important role during this entire work and their influence on signal formation is included in most transient simulations used to explore sensor response. For this reason a special, GEANT4 based Monte Carlo, was designed to include the energy deposits generate with GEANT4.

**Diffusion** Charge motion is dominated by drift and diffusion as shown in chapter 2. Considering the dispersion of the electron-hole pairs along the ionising path at the beginning of their formation as negligible, the energy deposit can be approximated as a straight line distribution. During drift, the charge cloud expands due to diffusion and increases in diameter with a Gaussian distribution of the charge density [22]. Considering the time needed for the electrons and holes to be absorbed,  $t_{drift} = \frac{s}{\mu_{e,h}E}$ ,

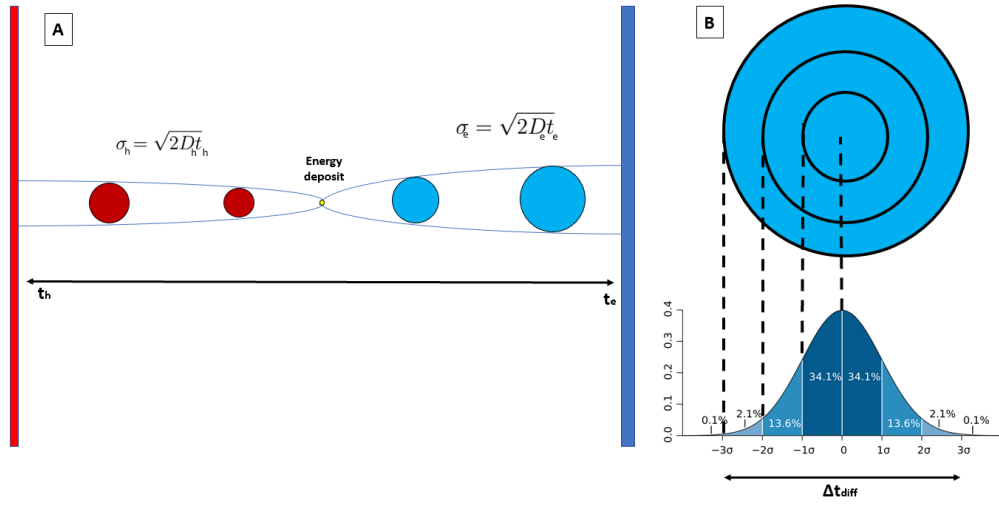


Figure 3.10: (A) Charge cloud expansion in time due to diffusion. (B) Simplified representation of the charge distribution after a specific drift time and how total charge collection is distributed in time.

their distribution in space is increased by a factor of :

$$\sigma = \sqrt{2Dt} = \sqrt{2D \frac{s}{\mu_{e,h}E}} \quad (3.17)$$

Where  $s$  is the drift distance and  $\mu_{e,h}E$  is the drift speed. The spread in arrival time is therefore dominated by charge diffusion and is equal to:

$$\sigma = \sqrt{2Dt} = \sqrt{2D \frac{s}{(\mu_{e,h}E)^3}} \quad (3.18)$$

Which also means that the time needed to collect 99.5 % of all charges is approximated  $6\sigma$ . This is an important factor and becomes dominant in silicon sensors with large drift distances. In 3D sensors with small electrode spacing, the effect of diffusion should be negligible compared to other effects, except if low field regions are present over their drift path.

### 3.2.3 First experimental results

A first study based on simulation and experiment performed in the framework of the CERN-RD50 collaboration and published by Kramberger in 2019 [80] used a simple 3D sensor design with pillar electrodes and a sensor pitch of  $50 \mu\text{m}$ . Time resolution of the device was measured using a set-up built with a LGAD, a dedicated front-end and cooling system. The particle source used was a strontium-90 source which emits electrons per beta decay with a maximum energy of 2.3 MeV. The results obtained on this device for vertical tracks has shown a resolution of 45 ps. Considering that

the geometry of the device is not timing optimised, it is supposed that the resolution can improve even better on devices with a dedicated geometry.

### 3.3 Approach to develop a timing optimised 3D sensor

Based on the data and suggestions made in [22], the development of a timing optimised 3D silicon sensor for TIMESPOT is being focused on different aspects of the future device:

**Sensor geometry** Sensor geometry plays a more important role in 3Ds than in planar sensors. An accurate study of the electrode configuration must be done in order to achieve a final design with a mostly uniform and fast sensor response, reducing or completely removing low electric field regions. A second aspect concerns the volume occupied by the electrodes themselves. The entire volume, at same potential, does not have an internal electric field and is basically insensitive to ionising radiation. Its reduction is therefore an important aspect and can be carried out with a geometrical study but, most important, with a downscaling of the structures, which is a more technological aspect and depends from the fabrication process. The design study also includes a minimisation of the sensor capacitance, which is crucial to reduce jitter and so time resolution.

**Sensor operation** Sensor operation simulation is considered the final virtual evaluation of the designed model and allows to make first estimations of the expected performances and helps also the better develop the front-end electronics. In order to obtain a most accurate and realistic sensor response possible, most of the expected effects must be added in the tools used to simulate its operation. Starting from the energy deposits and the front-end transfer function.

**Sensor test** First prototypes will be tested and the obtained results compared with simulation. Possible discrepancies can be used in order to correct some physical aspects of the sensor behaviour which can then be used for successive studies and sensor developments.



# Chapter 4

## Sensor development and production

This chapter presents the design of a timing optimised 3D silicon sensor. The design study involved different pixel shapes and electrode geometries, some of them were selected for first prototype production. The chapter will first introduce the problems related to a timing optimised 3D silicon sensor, describe some of the explored solutions and presenting the Ramo map approach, developed to explore quantitatively signal amplitude and qualitatively the potential time performance of the sensors. The chapter ends with a brief description of the first technological tests and prototype production made by FBK in Trento, Italy [11].

### 4.1 Description of the problem

Considering the specifications presented in chapter 1 for a particle tracking detector which must operate close to the interaction point in the future high luminosity LHC, a valid sensor technology with high radiation hardness and fast charge collection times must be chosen. The best alternative seems to be the 3D-silicon sensor technology presented in the previous chapter and already used in the ATLAS IBL tracker [56].

Despite its optimum radiation hardness due to the short drift distances which allow to reduce charge collection time in few hundreds of ps, its timing performance presents some critical issues and only few studies were performed in the last years [22] showing encouraging performances for specific sensor geometries.

A fundamental aspect of a 3D sensor is the electric field generated by its geometry. In comparison, a planar sensor, as shown in chapter 2, generates a almost uniform electric field in over bias. The problem with standard planar sensors is that their sensor thickness and, therefore, the distance between their electrodes, must be hold thick enough in order to collect enough energy from crossing particles. State

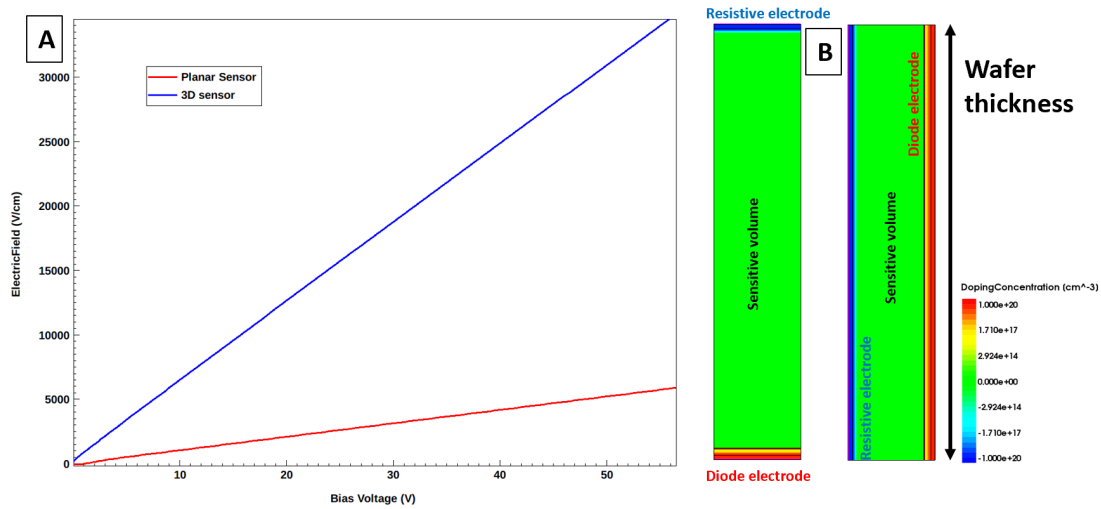


Figure 4.1: Left plot: Comparison of the Electric Field generated inside the sensitive volume of a 3D-like sensor and a planar one with same wafer thickness (Right models).

of the art planar sensors have normally more than 200  $\mu\text{m}$  thickness, which limits charge collection in few nanoseconds if the sensor is operated in velocity saturation. Also velocity saturation is difficult to achieve in planar sensors because higher bias voltages need to be applied in order to reach electric field amplitudes of 10  $\text{kV}/\text{cm}$  necessary to achieve saturation. 3D sensors do not have this problem on the other hand because they can be built on relative thick sensor wafers but with junction and resistive electrode positioned relatively close. An example is shown in figure 4.1.B, which represents the preliminary simulation made with Synopsys Sentaurus TCAD of a 150  $\mu\text{m}$  thick sensor wafer. One model was modelled as a planar sensor and the second one as a 3D sensor with an inter-electrode distance of 25  $\mu\text{m}$ . The simulation consisted in measuring the electric field amplitude with increasing reverse bias voltage. The result shown in plot 4.1.A and demonstrates how the electric field rises faster in 3D with shorter inter-electrode distance, reaching velocity saturation in less than 20 V.

Despite this great advantage, the electric field generated by a column-electrode-based geometry presents strong dis-uniformities. An example is shown in figure 4.2 which represents an electric field map of a section of a hexagonal pixel with columnar electrodes. Despite the short inter-electrode distance of only 55  $\mu\text{m}$ , the electric field is almost zero between electrodes at same potential, and reaches its highest amplitude close to the central junction electrode. This large variation in electric field amplitude has strong repercussions in charge collection time and, therefore, in signal shape and charge collection efficiency affecting negatively time resolution. A second critical region is the volume occupied by the electrodes themselves, which are built inside the sensitive volume of the sensor. Those volumes, full of mobile

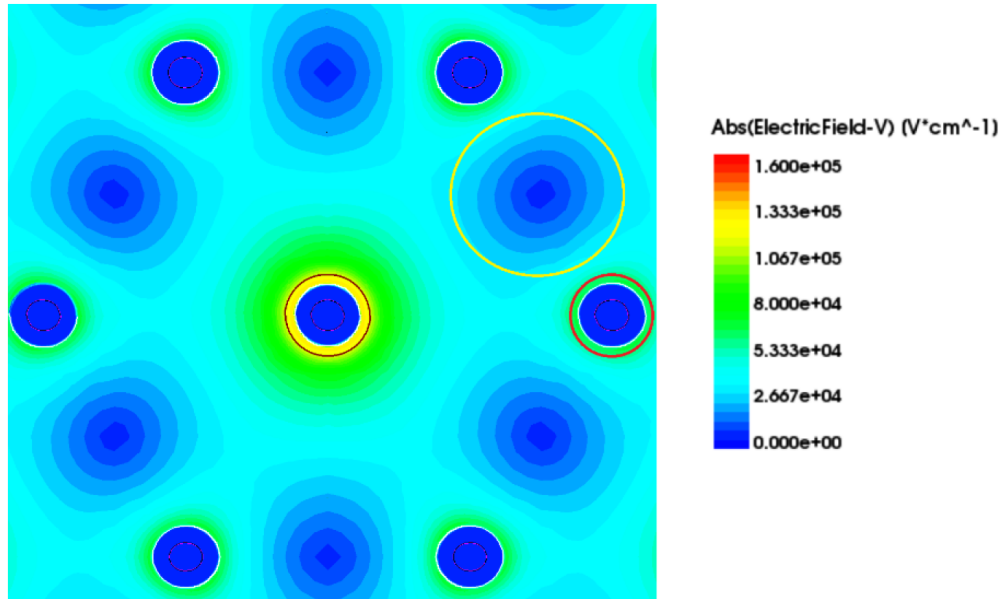


Figure 4.2: 2D model showing a section of a hexagonal 3D sensor. The red circle shows a non-sensitive area introduced by the electrode. The yellow circle shows a low electric field area. For high resolution time measurements, a reduction of those areas is from primary importance.

carriers and with no electric field inside, are not sensitive to ionising radiation and must be kept as small as possible.

The weighting field shape is also depending on the electrode geometry. This makes necessary to develop a timing optimised sensor by studying the electric and weighting field in function of the electrode geometry.

## 4.2 Specifications and design approach

**Specifications** For the TIMESPOT tracking detector a timing optimised 3D silicon sensor is required which has a TIMEPIX-3 ASIC compatible pixel matrix, like the VELOPIX [17], with a pixel pitch of  $55\ \mu\text{m}$  for square shaped sensors or  $55\ \mu\text{m}$  diameter for hexagonal shaped pixel. The pixel matrix will be fabricated by FBK using its single side technology. The fabrication uses a high resistive, p-doped and  $150\ \mu\text{m}$  thick sensor wafer which is wafer-bonded on a high conductive and p++ doped support wafer [24]. The FKB single side approach allows to excavate the holes for the resistive trenches through the entire sensor wafer, reaching the support wafer. The junction electrodes instead cannot pass through the entire layer, because it would cause sensor breakdown at relatively low bias voltage due to the short distance, and stops at  $130\ \mu\text{m}$  depth,  $20\ \mu\text{m}$  from the bottom. A closer distance of the junction electrode to the support wafer would increase breakdown voltage,

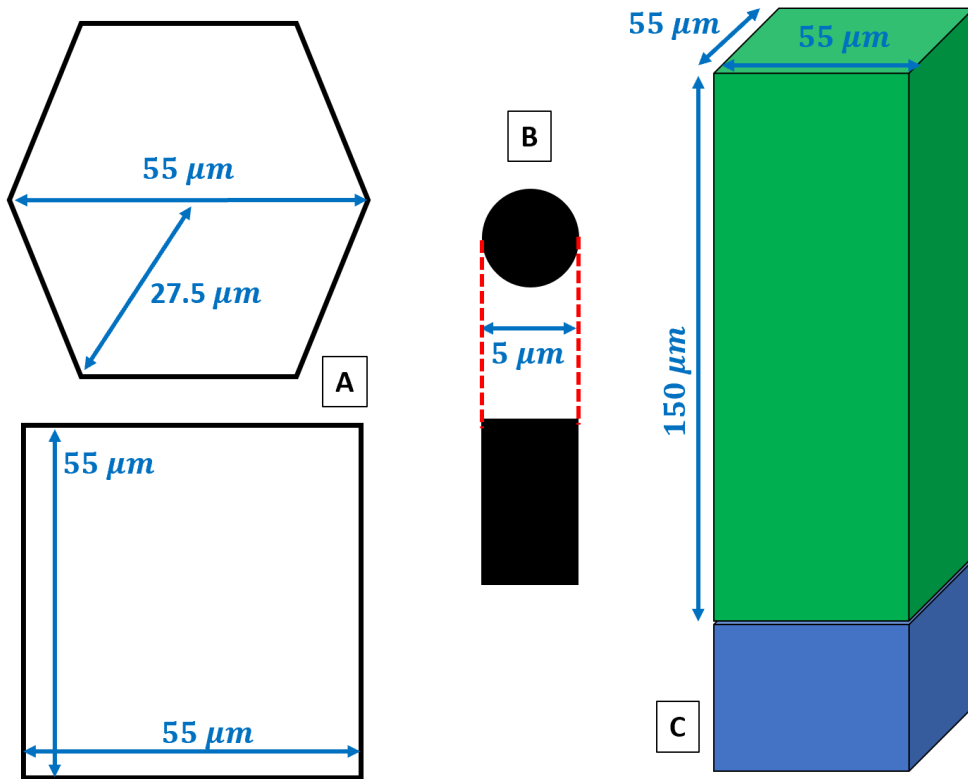


Figure 4.3: Sensor dimensions following specifications. (A): Main pixel shapes simulated. (B) Trench width and column width. (C) 3D animation of the square pixel showing the thickness of the sensor wafer. Blue volume is related to the attached support wafer.

on the other hand, a shorter junction trench would affect charge collection time for deposits released in the bottom of the sensor. The best solution is to keep the deepest point of the junction trench at a distance from the bottom wafer equal as the inter-electrode spacing.

Electrodes can be produced as columns or trenches. Considering that FBK is able to fabricate them with a diameter of few micrometers this study considered a more conservative width of  $5 \mu\text{m}$  (Fig. 4.3).

**Design Approach** To design and analyse different sensor geometries, the Sentaurus Technology Computer Aided Design tool (TCAD) was chosen [33]. TCAD allows to define solid state devices starting from their fabrication process and analysing their electrical characteristics in stationary and transient conditions. The tool itself is divided in different sub-tools, each of them with a specific function. For this geometry study a direct design approach was adopted, using the Sentaurus Structure

Editor (SDE) for sensor modelling and the Sentaurus Device (SDevice) for stationary simulation. TCAD is a very powerful tool and allows to simulate sensor behaviour with an theoretically unlimited level of detail, which depends on the applied mesh grid. The smaller the used mesh size and the higher the detail and precision of the simulation. On the other hand, a very dense mesh grid has an elevated cost in simulation time, due to the large number of points that need to be computed during the simulation. For example, 3D models built up by more than one million points, simulation time can easily exceed more than 3 days in quasi stationary simulations or even 2 weeks for 500 ps long transient simulations. Designing all possible electrode geometries using only a 3D modelling-based design approach would cost too many time and result too inefficient on a simple working time point of view. In order to speed up this study, a multiple step approach based on a progressive enhancement of the level of detail was used.

The design approach is divided into into two main design and simulation steps. During the first design and simulation step, a 2D model design approach was used. The 2D models used represent the section of a single pixel geometry. This approach loses all information of the electric/weighting field along the Z-axis but preserves the most important information of the sensor, its electrode geometry. Due to the symmetry of 3D sensors, charge motion is dominated mostly over the XY plane and not along Z, where the electric field component is negligible compared to the X and Y components. The sensor sections are simulated using a quasi stationary voltage ramp, which applies a reverse bias starting from 0 V and stopping at -100 V, which is used as reference voltage to compare the sensors among them. The final evaluation of the designed electrode geometries is done by observing the electric field of the pixel inside the pixel matrix and calculating the potential current induced on the junction electrode by an instantaneous generated electron-hole pair. This approach, based on the Ramo theorem, is called Ramo map and it will be shown in the next sections.

The pixel geometries considered as most suitable for fast timing applications are then remodelled in a 3D model and re-simulated again before fabrication, in order to have first estimations of their electrical characteristics.

## 4.3 Explored Geometries

A total of 20 different pixel geometries were designed and simulated, using different combinations of square and hexagonal pixel shapes with trench or column electrodes. Some of the geometries were simulated using different electrode spacing or trench lengths in order to understand how the electric field changes with them [81].

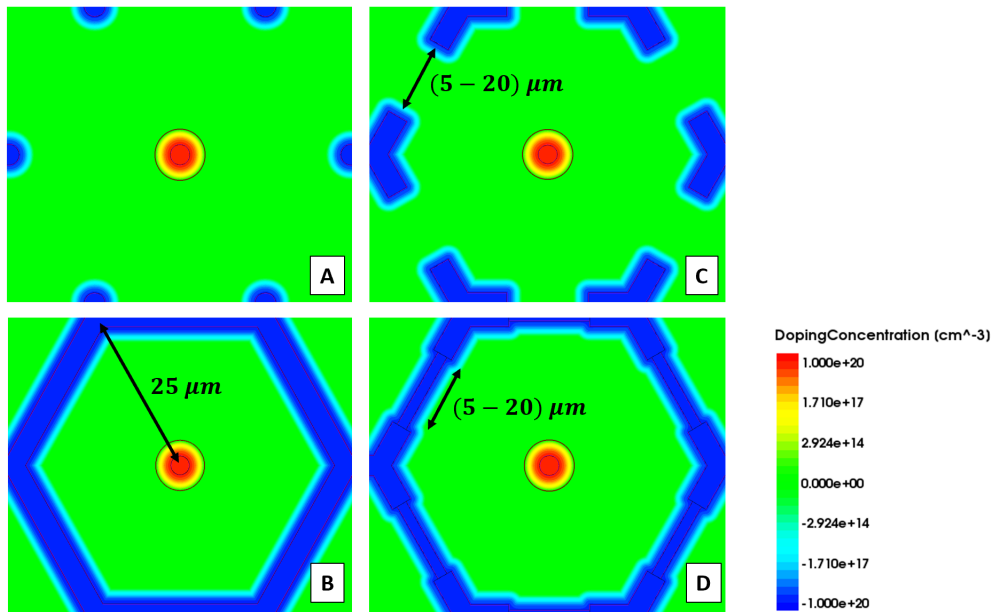


Figure 4.4: Doping map showing the main hexagonal geometries studied. (A) Solution with columnar electrodes. (B) Open trench configuration. (C) Closed trench configuration. (D) Hybrid solution with different trench width.

### 4.3.1 Hexagonal pixel geometries

**Column electrodes design:** This sensor was already produced by FBK but only used for radiation damage tests [82] and uses only columnar shaped electrodes (Fig. 4.4.A). The volume occupied by the columns is the lowest among all explored hexagonal pixel (less than 5 % of the total pixel volume), increasing sensitive volume of the entire pixel. For timing applications this design looks less optimised considering the large electric field variations, with values close to 0 V/cm between resistive electrodes and 15 kV/cm close to the junction electrode (Fig. 4.5.A).

**Closed Hexagon geometry:** Similar to the previous geometry, this sensor was already designed and fabricated but this time by BNL in 2014 [83]. This design presents a columnar junction electrode and a single hexagonal trench around the pixel perimeter is used as resistive electrode (Fig. 4.4.B). This approach allows to insulate the electric field and weighting field of the pixel from neighbour pixel. Electric field presents a higher amplitude and low electric field regions are far inferior compared to the complete column-based pixel. This greater performance is achieved by losing more active volume which is occupied by the resistive trench (around 10 % of the entire volume) (Fig. 4.5.B).

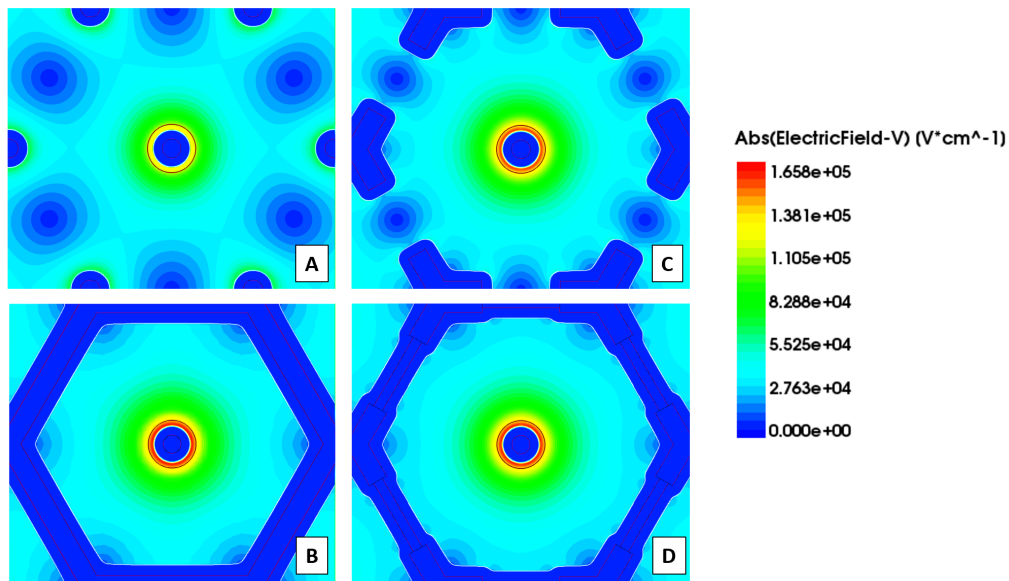


Figure 4.5: Simulated electric field of the main hexagonal geometries studied. (A) Solution with columnar electrodes. (B) Open trench configuration. (C) Closed trench configuration. (D) Hybrid solution with different trench width.

**Semi-Closed Hexagon geometry:** This geometry aims to find a compromise between the column electrode geometry and the closed hexagonal geometry by simply building a discontinuous ohmic electrode build up by 6 trench elements (Fig. 4.4.C). This solution confines the low electric field regions between the ohmic trenches (Fig. 4.5.C), but does not seem to be a valid option for fast timing. Different trench lengths were designed and simulated for this study, spacing from  $5\ \mu\text{m}$  to  $20\ \mu\text{m}$  of distance.

A similar approach which used 6 discontinuous trenches drilled along the perimeter of the hexagon, excluding the angles of the pixel, is presented in section 4.3.3.

**Closed Hexagon geometry with variable trench width:** This design is a superposition of the two previous presented electrode configurations (Fig. 4.4.B and C) and more intended as a Gedankenexperiment (Fig. 4.4.D). The larger trench structures at the corner of the hexagon are built with the intention to reduce the low electric field present at the corners of the closed hexagon, thanks to the angled structures which adds additional high electric field areas close to the low electric field areas (Fig. 4.5.D). This approach costs more sensitive volume due to the larger corner trenches and the effects on the electric field coverage were less than expected. On a technological point of view it is not sure if this device can be really fabricated.

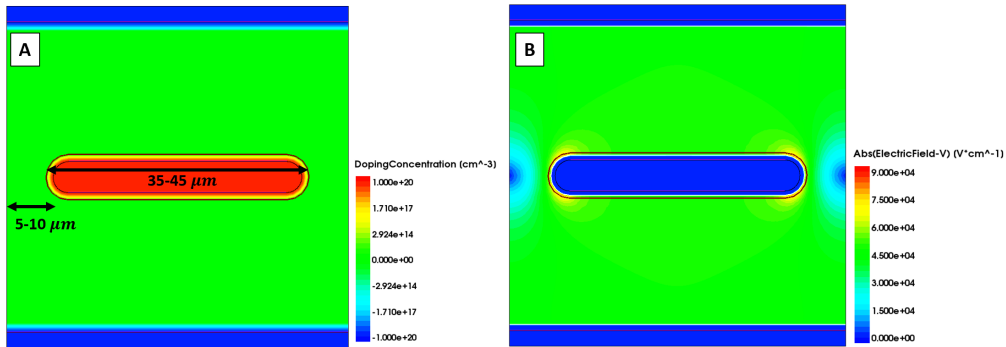


Figure 4.6: Parallel trench geometry. (A) Doping map showing the explored trench lengths. (B) Electric Field Map.

### 4.3.2 Square shaped geometries

This section will mostly show the explored solutions included in the first prototype production run and is focused on a more detailed description of the parallel trench geometry which was already considered and proposed as most suitable geometry for fast timing application and already fabricated by Stanford University.

**Parallel trench geometry:** The parallel trench geometry is one of the simplest explored electrode geometries. Already proposed as design by Sherwood Parker [22] and produced by Stanford [84], this geometry presents some smaller differences related to its application in a TIMEPIX compatible matrix. The geometry has a 3 electrode structure divided into 2 resistive electrodes and one junction electrode in the middle of the sensor (Fig. 4.6.A). Both resistive trenches are built continuously over all the pixel matrix and provide bias for multiple pixel. In order to achieve space sensitivity, the junction electrode is built in segments. 16 different models with different junction electrode length, spacing from 5 μm to 15 μm, were designed and simulated. The best compromise was considered all the solutions with junction electrode length spacing from 50 μm to 40 μm. In fact the generated electric field resulted mostly uniform over all the sensitive area of the pixel, with some smaller low electric field areas between junction electrodes and some stronger electric field peak along the interface of the extremities of the tips (Fig. 4.7.B).

Analysis of the weighting field showed that it decreases strongly outside the pixel area. Only particles crossing close to the pixel at few micrometers have potential the possibility to generate strong enough signals due to the high weighting field (fig. 4.7). The weighting field between junction electrodes presents an even more interesting behaviour, by inverting its amplitude from positive (close to the junction electrode of the pixel) to negative (close to the junction electrode of the neighbour pixel), which basically means that it induces only on the other pixel. Besides this interesting property, it is not considered that it can have really any applications in

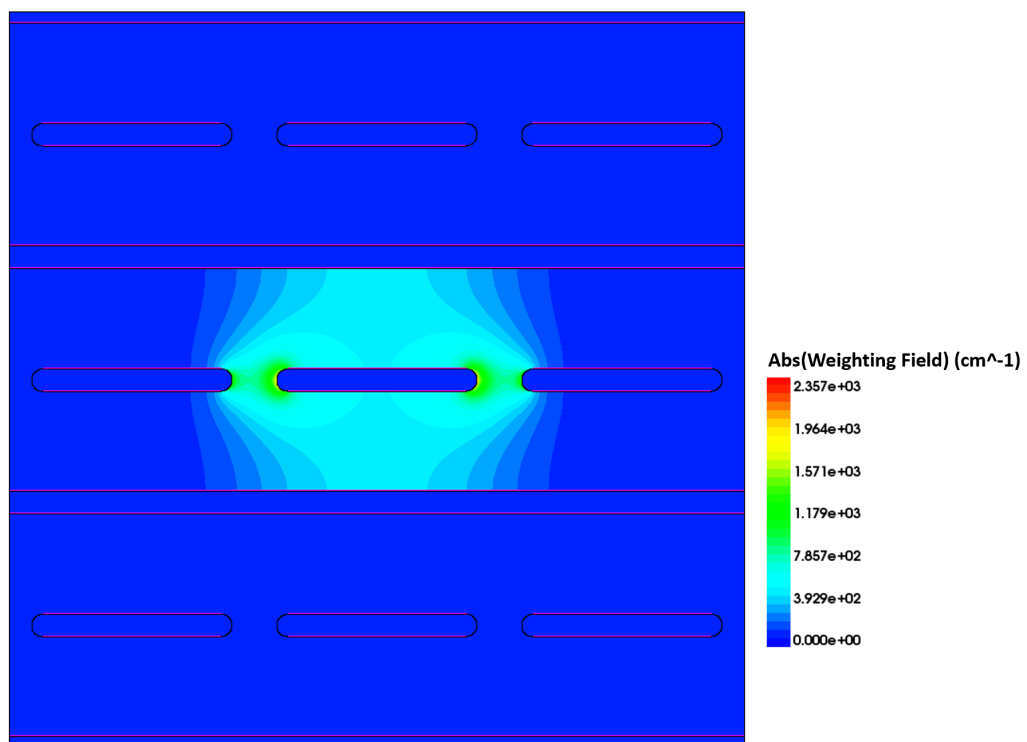


Figure 4.7: Weighting Field of the central pixel inside a 3x3 pixel matrix. Most of the weighting field is confined inside of the pixel area and decreases fast in the areas of the neighbour pixels.

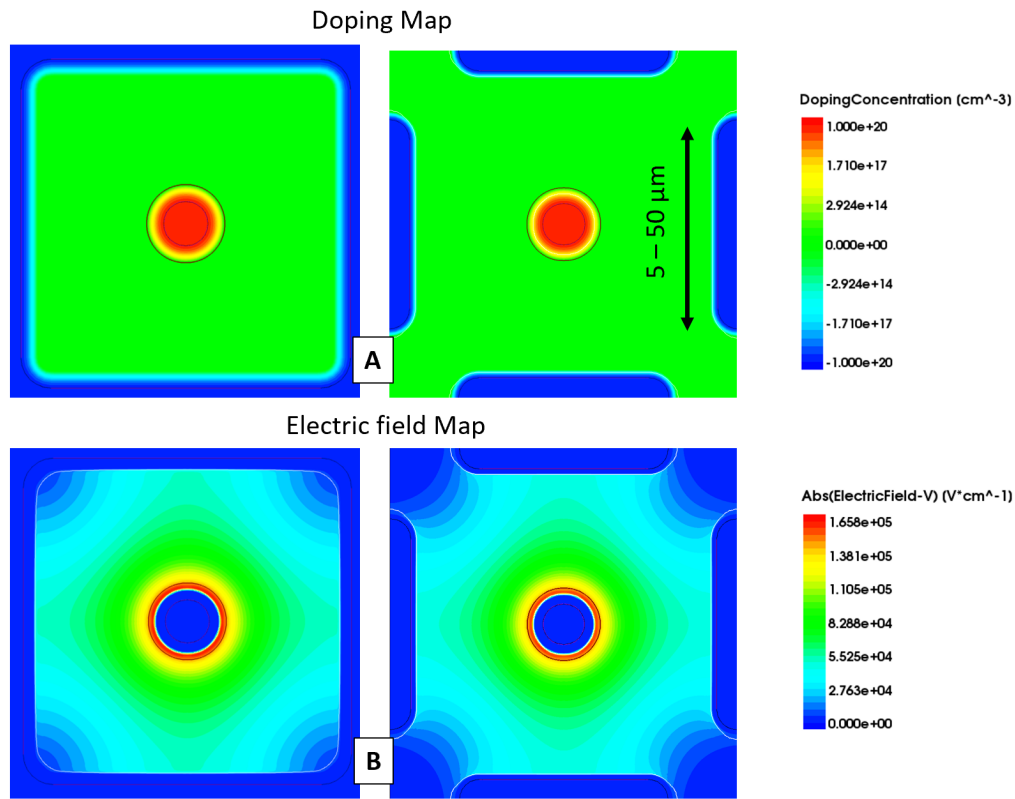


Figure 4.8: Square pixel geometries with trench electrodes designed and simulated. (A) Doping concentration maps. (B) Electric field maps.

high energy physics due to the variation of the particle track. A better explanation of this behaviour is later shown in section 4.4, using the Ramo Map approach.

**Closed and semi-closed square geometry:** This configuration is built up by a central diode column electrode, surrounded by a frame made by a combination of 4 trench electrodes (Fig. 4.8.A). This geometry has a similar electrode to sensitive volume ratio of 10 % as the closed hexagon. The electric field generated by the geometry drops to zero along the corners of the bias frame, increasing the sensitive area of the pixel but results relatively strong for the rest of the active area (Fig. 4.8.B).

**Column electrode-based geometries:** Two different square pixel geometries built up by using only columnar electrodes are tested: One with the same 9 column configuration as proposed by Parker in its first paper [21], and the second a more simplified version using 5 columns, following an similar geometry as already used in the ATLAS IBL [56] (Fig. 4.9.A) with the only difference that the cell is squared instead of rectangular.

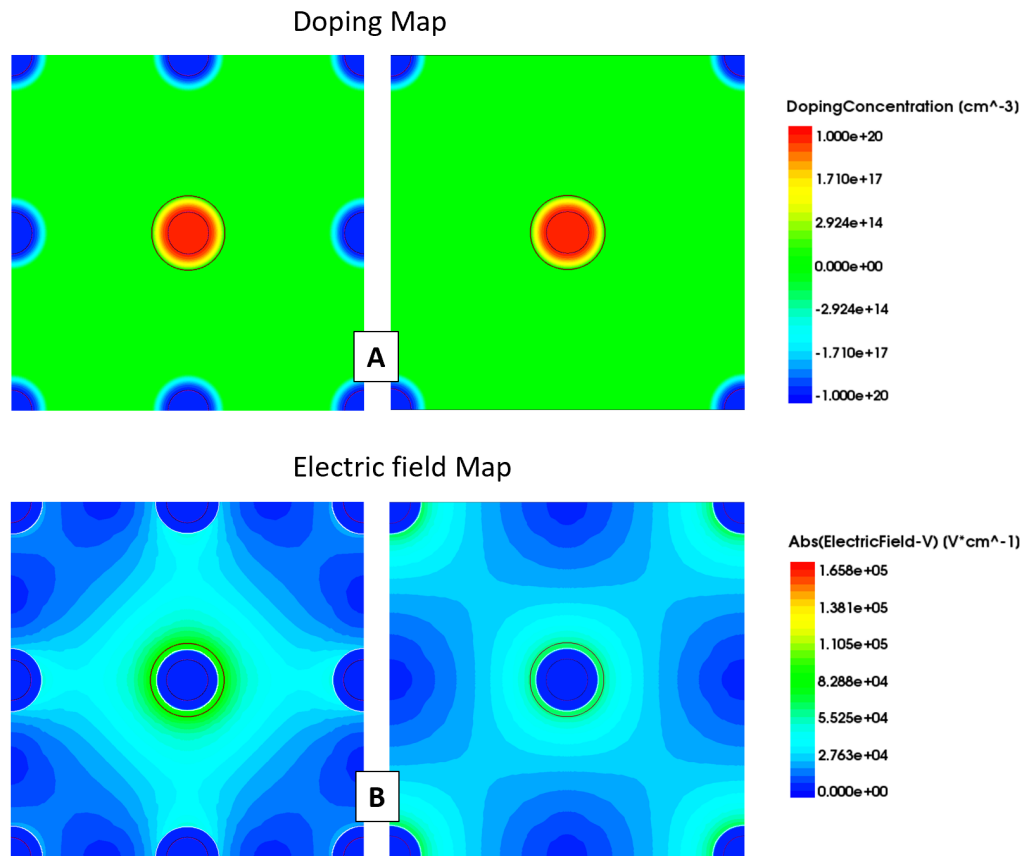


Figure 4.9: Square pixel geometries built with only columnar electrodes. (A) Doping concentration maps. (B) Electric field maps.

In both geometries the generated electric field presents large low field areas and the electric field varies strongly from the center to the external regions (Fig. 4.9.B). The 9 column version presents a stronger field but lacks around the corners, the 5 column version instead covers a bit better the active area.

### 4.3.3 Evaluation of closed and semi-closed pixel geometries

As previously shown, there are two geometries which used a resistive trench which surrounds the entire frame of the sensor. Those geometries have the advantage to generate a strong electric field with small low field areas along the corners. At the same time this geometric approach allows to generate a weighting field with the same shape of the electric field and electrically decoupled from electrodes from other pixels.

On a technological point of view, the extended trench structures introduces mechanical instability which can be partially restored by filling the trenches with poly-silicon.

This instability is probably higher if the pixel geometry is applied for a large pixel matrix. So the idea is if, instead of using a continuous frame around the pixel, a segmented frame would allow to gain mechanical stability without losing performance in the generated electric and weighting field.

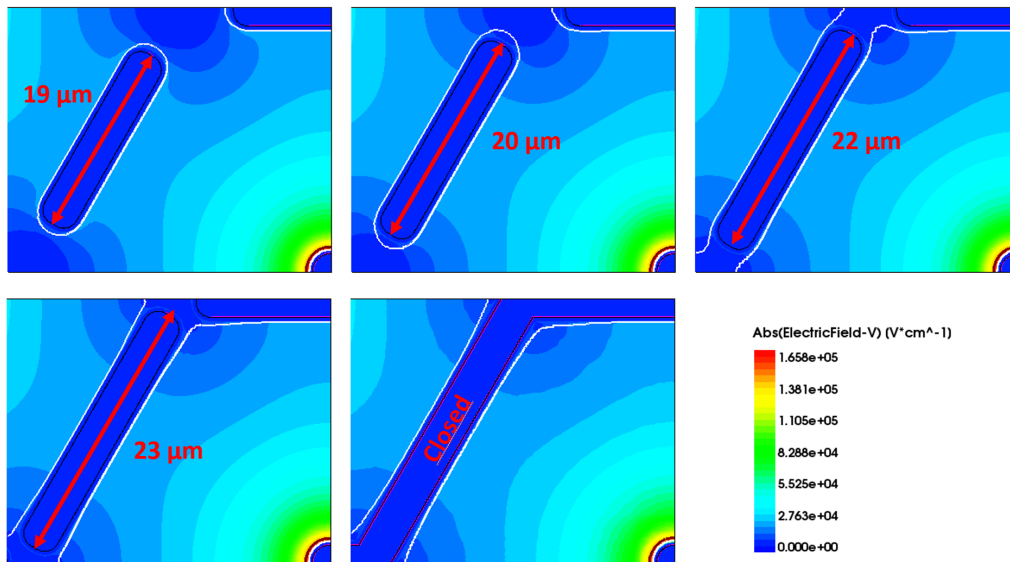


Figure 4.10: Electric field behavior at the corner of semi-closed and closed hexagon pixel geometries. For Trench lengths of over  $18 \mu\text{m}$  the electric field shape and amplitude does not change significantly. Over  $20 \mu\text{m}$  trench length the corner stays undepleted, as shown by the white delimitation line.

The approach used the closed square and hexagonal pixel and explored 10 different trench lengths. In figure 4.10 and 4.11 it is shown how the electric field does not change significantly at the corner of the hexagonal and squared pixel structure for trenches longer than  $18 \mu\text{m}$  for hexagons and  $40 \mu\text{m}$  for square pixel. The effects produced by those trenches is that the corner regions has basically a 0 electric field and results un-depleted at 100 V bias, properties which already have the pixels with closed frame. The only difference is that the corner regions are still made by silicon of the sensor wafer with an intact lattice structure. A discontinuous frame approach is most probably more suited for fabrication than the complete closed frame.

## 4.4 Ramo Maps

The Ramo map approach was developed in order to have a first general overview of the timing performances of the sensor in terms of its intrinsic time-walk distribution, which influences the time resolution of all detector system as shown in chapter 3. For the time-walk distribution of a sensor is influenced mainly by Landau fluctuations of the energy deposit released by the crossing MIPs and potential varying electric

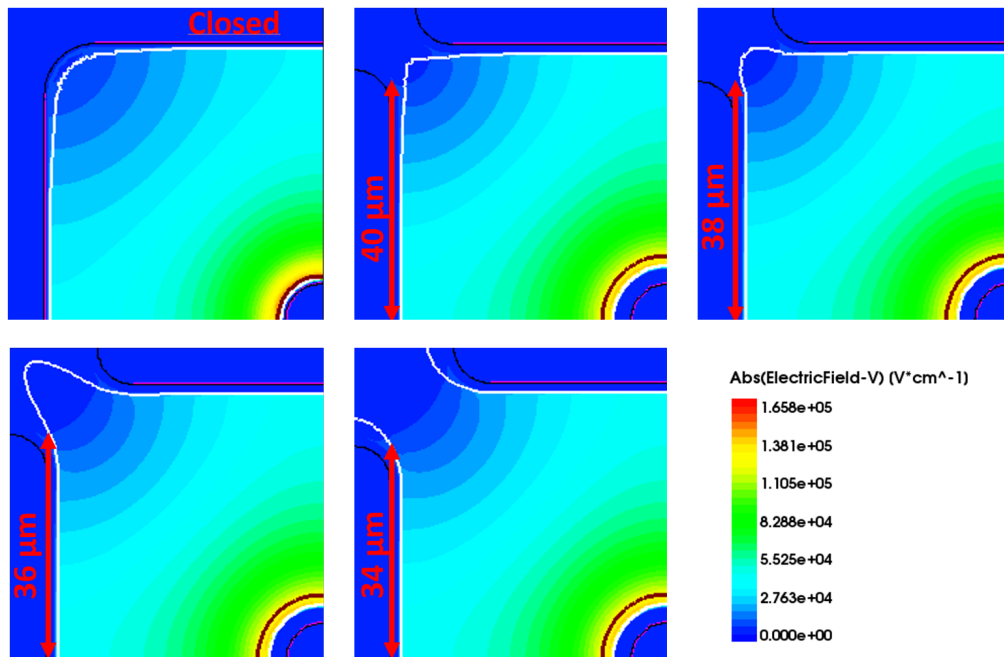


Figure 4.11: Same analysis of the electric field applied on a square pixel. The corner region stays undepleted for trench lengths over 40  $\mu\text{m}$ .

or weighting field. Landau fluctuations basically cannot be eliminated so the only source of large time-walk is the sensor geometry which defines the electric field shape and, therefore the shape of the induced current signal. For this reason the so called Ramo-map approach was developed.

Ramo-map approach is based on the following design and simulation procedure:

The chosen pixel geometry is reproduced on a 2D model of a simplified pixel matrix. The pixel which will be analysed (or pixel of interest, PoI) is positioned in the middle and surrounded by other pixel which are used to reproduce the boundary condition inside a pixel matrix (Fig. 4.12). Two different TCAD simulations are then executed. One considers the operating bias voltages of the pixel matrix, in this case -100 V for the resistive electrodes and 0 V for the junction electrodes. The second simulation is executed with an bias voltage of 1 V on the junction electrode of the PoI and 0 V on every other else, exactly the boundary conditions required for the Ramo theorem, shown in chapter 2. The bias voltage of -100 V is a more personal motivated choice and motivated by the fact to be sure that most of the pixel is operating in velocity saturation, which in 3D sensors is commonly obtained at bias voltages below 100 V.

A post-simulation analysis then takes from the first simulation the maps of electric field and charge mobility (for both carrier type) and from the second simulation the weighting field map. The information contained in the 4 maps is then implemented

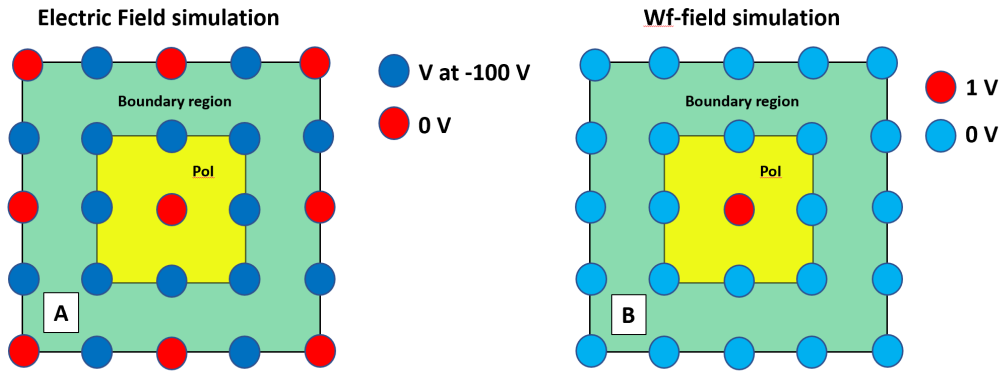


Figure 4.12: Design approach and boundary conditions to generate a Ramo-Map. The schematic uses a columnar electrode based sensor to better understand the approach. (A): Model and simulation boundary for the Electric Field simulation. (B): Model and simulation boundary for the Weighting field simulation.

using the Ramo theorem (Fig. 4.13).

$$I(x, y) = q_{e^-} * (v_{d_e}^{\vec{}} * \vec{E}_w) + q_{h^+} * (v_{d_h}^{\vec{}} * \vec{E}_w) \quad (4.1)$$

The generated induced current distribution over the XY plan is called Ramo Map, in honour of Simon Ramo, and represents the amount of current induced instantaneously on a specific electrode by an electrode-hole pair generated in a specific position and moving instantaneously at drift velocity.

This approach does not consider the acceleration that electrons and holes suffer during the first ps after their generation. The reason is that, for an ideal uniform electric- and weighting field it would simply add a uniform offset without changing the shape of the Ramo-map.

With the Ramo-Map approach it is also possible to estimate the current signal shape. For this purpose, it is necessary to separate the Ramo-Map in its hole and electron contribution. Starting from any possible point on the map and following the electric field lines, adding for every point of the line the hole and electron contribution. The charge collection time can be estimated by calculating the time needed by the charged to drift to their electrodes at saturated velocity (Fig. 4.14).

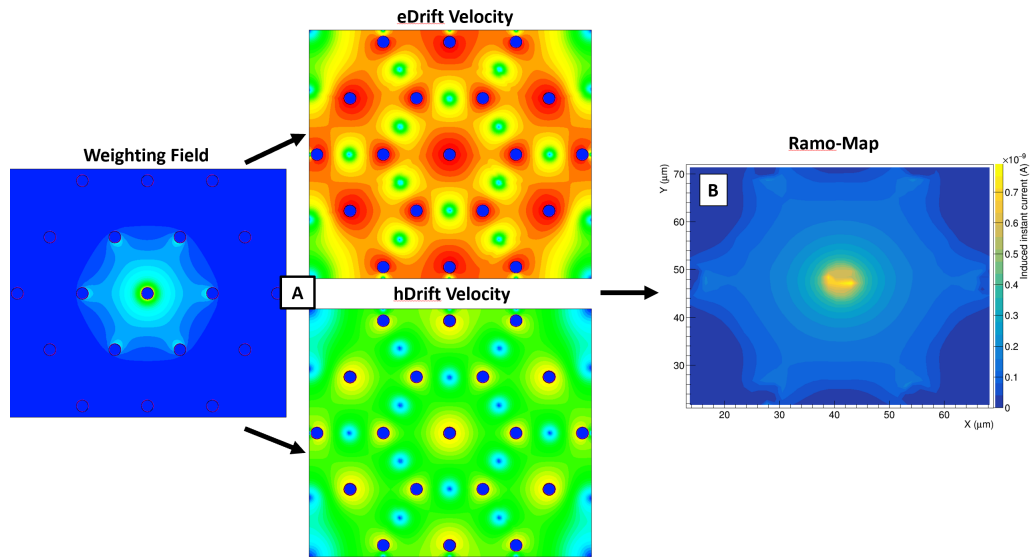


Figure 4.13: Generation of a Ramo-Map. The dot product of the Weighting field and charge drift velocities (A) generates the final Ramo-Map (B)

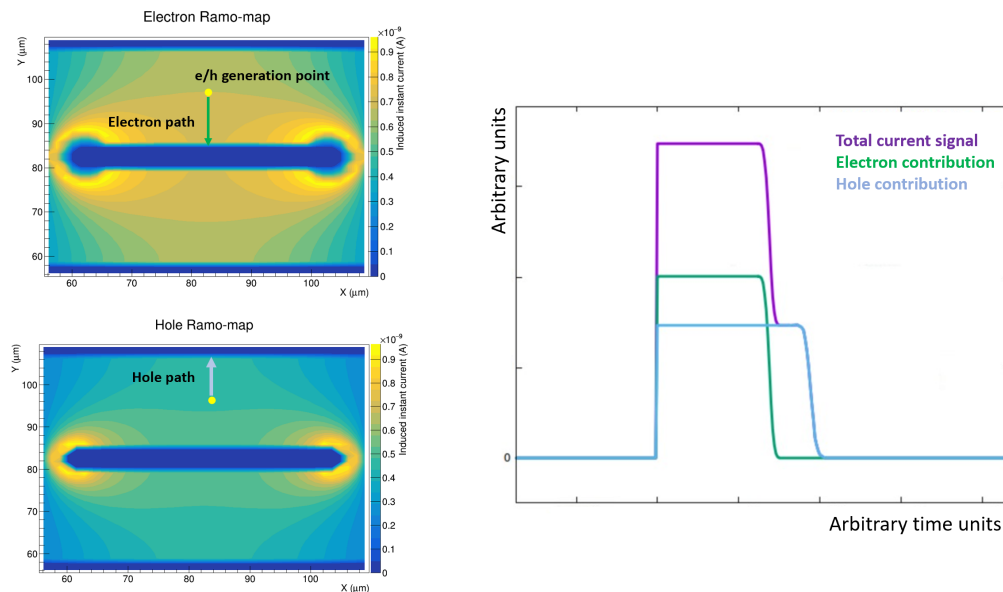


Figure 4.14: Reproduction of the shape of a current signal generated by the drift of a single electron-hole pair by simply reading their motion on a Ramo map.

The Ramo-Map approach was applied on 6 different electrode geometries: The parallel trench, the closed hexagon, the closed square pixel and all fully columnar electrode-based geometries. The Ramo map approach allowed to see important differences between pixel with trenches and columns. For pixel built with trenches,

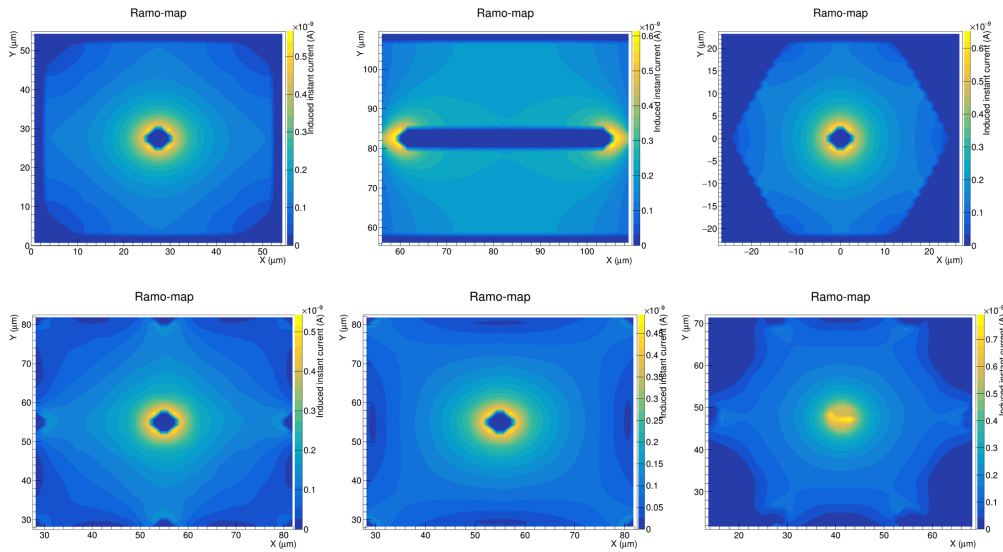


Figure 4.15: All generated Ramo-Maps for the final sensor geometry selection. Trenched electrode-based geometries present a less variable and higher current induction over all the sensitive area.

charge induction is on average higher and more uniform than for pixels with column electrode. The parallel trench geometry demonstrated the most uniform and highest current induction among all explored solutions, becoming the primary choice for prototype production (Fig. 4.15). Focusing the attention on the parallel trench pixel configuration, the Ramo map allows to identify 3 interesting properties of the sensor. At first, the sensor response is characterized by the highest current induction among all explored geometries. A second factor is the behaviour of the current induction in the region between two diode electrodes. Considering only the electric field, this region would be classified as timing inefficient due to its low electric field. But, considering also the effect of the Weighting field, the Ramo-map reaches its highest value suggesting that current induction is at its maximum and could benefit time performance. In the same critical area, current induction (as mentioned previously) suffers an inversion across the region between two pixels. This effect has the advantage that, in the region between two different diode trenches, it is possible to distinguish perfectly in which pixel the ionising particle crosses the region. A second Ramo map, with a 3D representation in space of the induced current and extended on the other two lateral pixel, shows how current induction for the PoI drops almost to zero in less than  $5\ \mu\text{m}$  (Fig. 4.16). The final geometry exploration ended with the selection of 5 geometries. One of them as the main pixel geometry and the other 4 as test pixels:

- The parallel trench geometry with different diode electrode spacing from  $39\ \mu\text{m}$  to  $49\ \mu\text{m}$ .

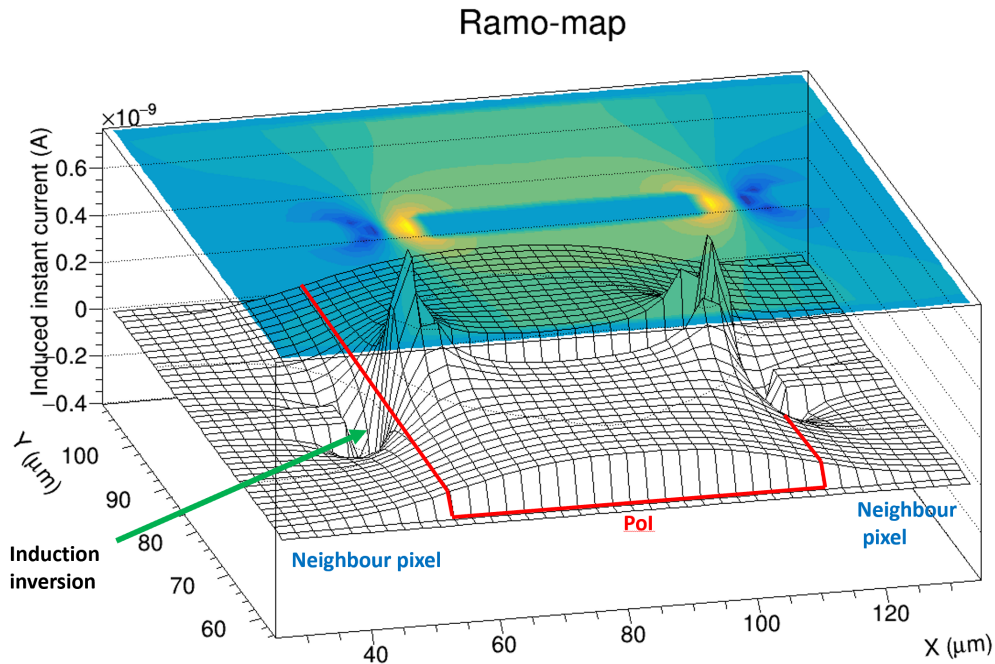


Figure 4.16: Extended Ramo-Map of the parallel Trench Geometry. The 3D representation helps to better describe the induced current over all the active area. The red frame highlights the pixel of interest.

- Both square pixel with 9 and 5 column structure and one hexagonal shaped pixel with 7 electrode structure.
- One hexagonal and one square pixel with semi-closed electrode structure.

Layouts of the selected geometries are shown in section 4.6.

## 4.5 3D sensor modeling

After the selection of the main geometry, further simulation studies are needed to understand the performances of the sensor and estimate its electrical properties. Those studies need a 3D modelling approach. The designed models respect the technological specifications of the FBK single side fabrication [23] with a  $150\ \mu\text{m}$  thick high resistive and p-doped sensor wafer, wafer-bonded on a high conductive p-doped support wafer which is represented by a thin p++ doped layer. Resistive electrodes passes through the entire thickness of the sensor wafer and junction electrodes stops at  $20\ \mu\text{m}$  from the support wafer [23]. Depending on the study, different 3D models were designed (Fig. 4.17):

- A  $55 \times 55 \times 151\ \mu\text{m}^3$  model containing 2 half pixels for sensor response simulation (Fig. 4.17.A).

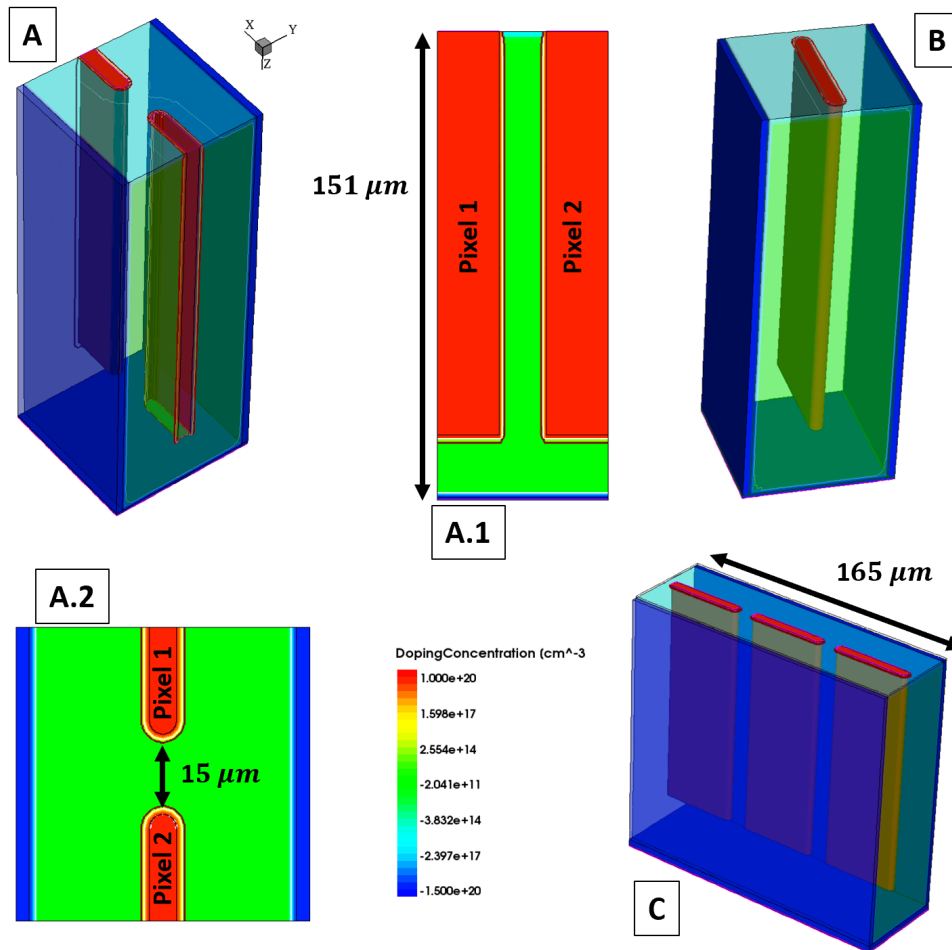


Figure 4.17: Different 3D models of the parallel trench geometry 3D sensor. (A) Double half pixel model. (A.1) Section along X direction and (A.2) section along Z direction. (B) Complete pixel model. (C) 3x1 Pixel array.

- $55 \times 55 \times 151 \mu m^3$  model of a complete single parallel trench pixel for sensor response simulation (Fig. 4.17.B).
- A  $55 \times 55 \times 151 \mu m^3$  model of a complete single parallel trench pixel with all electrical contacts for capacitance measurement.
- A  $27.5 \times 27.5 \times 151 \mu m^3$  model representing one quarter of the sensor for faster 3D transient simulations on TCAD.
- A  $165 \times 55 \times 151 \mu m^3$  model containing 3 pixels for eventually other studies (Fig. 4.17.C).

### 4.5.1 Capacitance simulation

The use of a complete 3D model allows to make a better estimation of the sensor capacitance. The capacitance is estimated using Sentaurus TCAD small AC analysis [33]. This procedure consists on solving the frequency dependent admittance matrix  $Y$  between two specific circuit nodes of an explored electronic circuit. Given a specific excitation frequency  $\nu$ , the equivalent small signal model can be solve, using equation 4.2.

$$\delta\vec{I} = Y * \delta\vec{V} \quad (4.2)$$

Where  $\delta\vec{I}$  is and  $\delta\vec{V}$  are complex current and voltage excitation vectors at the selected nodes.  $A$  is the system conductance and  $C$  capacitance matrix [88]:

$$Y = A + i2\pi C \quad (4.3)$$

Small signal analysis in TCAD is coupled with quasi stationary simulations. The simulation applies a voltage ramp, starting from 0 V. For every voltage step, an AC analysis simulates the electrical properties of the simulated system by applying a small periodic signal at a specific frequency (1 MHz for default). The system then solves the equivalent small signal model equation and capacitance matrix.

**Results:** For the parallel trench pixel with an inter-pixel spacing of 15  $\mu\text{m}$  showed for bias voltages over 20 V the capacitance goes below the 120 fF threshold (Fig. 4.18.A).

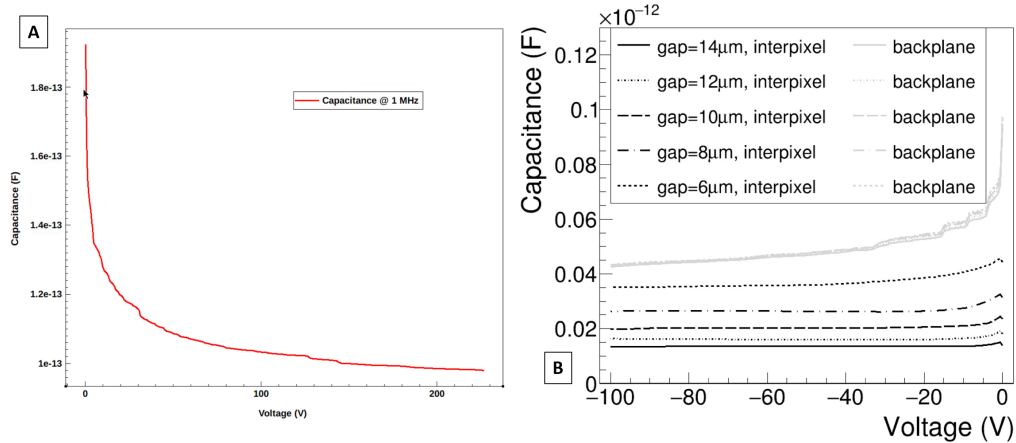


Figure 4.18: (A) Total capacitance of a single parallel trench pixel with 15  $\mu\text{m}$  distance between junction electrodes. Full depletion is achieved at  $\sim 10$  V and saturation velocity at  $\sim 30$  V. The total capacitance reaches 50 fF for 100 V reverse bias voltage. (B) Interpixel and backplane capacitance at different distances between junction electrodes [77].

A second capacitance simulation series performed by Mendicino et al. on a 3D model which includes two half pixel was used to simulate the backplane and inter-pixel contribution to the total capacitance at different distances [77]. Backplane and inter-pixel capacitance at different distances between junction electrodes is shown in figure 4.18.B. Backplane capacitance is basically unaffected by the different spacing of the junction electrodes and decreases linear with increasing reverse voltage, going below 50 fF for reverse bias voltages higher than 40 V. Inter-pixel capacitance instead increases with decreasing spacing, showing that from 12  $\mu\text{m}$  to 6  $\mu\text{m}$  the capacitance doubles in value.

The total pixel capacitance for the parallel trench pixel is estimated to be between 100 fF and 160 fF at 100 V reverse bias voltage depending on the inter-electrode distance between junction electrodes.

## 4.6 Prototype sensor production

The main sensor geometry, together with the secondary geometries, is fabricated using FBK 3D single-side technology (3DSS) [70] [85]. 3DSS was previously used for column electrodes and the only experience made by FBK using trenched electrodes are the fabrication of active edges [86].

Preliminary technological tests on the 3DSS were carried out in order to optimise its fabrication steps to the trench electrodes. A special focus was on the deep ion reactive etching (DRIE) and photoresist bake, trying different variations and permutations of them using for example atmospheric and vacuum baking and trying different types of photoresist layers with different thickness. The best combination which allowed a good etching process with regular trenches consists in a 6  $\mu\text{m}$  thick photoresist layer together with a vacuum bake (Fig. 4.19). Poly-crystal silicon deposition (Fig. 4.20) and contact pads for bump bonding were also tested and evaluate.

**First prototype production run** After the fine tuning of the fabrication steps, a first prototype production batch was started at FBK. 11 super structures per wafer were fabricated, each of them containing the main pixel sensor, compatible with the TIMEPIX/VELOPIX ASIC, and a smaller area filled with different test structures. Most of them are based on the main design but differs in inter electrode distances, distances between junction electrodes and how those electrodes are bounded electrically together (strips, single pixel or junctions). Also 4 different geometries were also implemented, including the hexagonal and squared pixel with surrounded frame and all column electrode based designs.

Sensor production ended in July 2019 and first test structures were immediately tested by FBK for IV and CV response. Timing tests on the test structure are described in chapter 7.

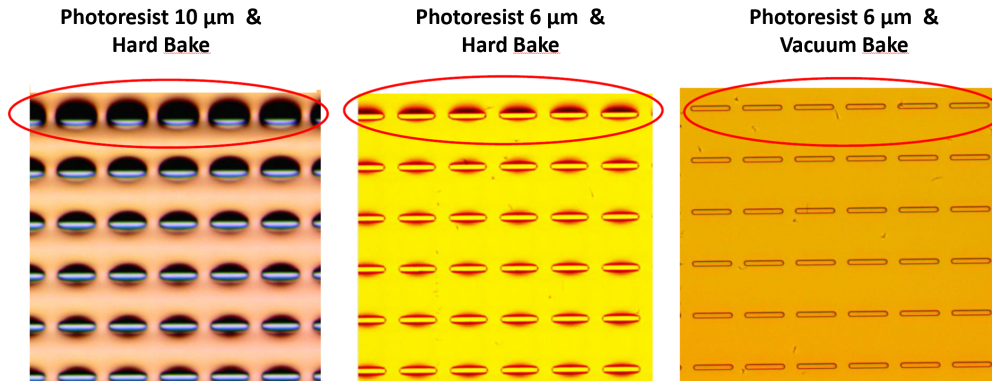


Figure 4.19: Comparison between 3 different test structures built using different combinations of photoresist and bake. Higher deformation of the external trenches was observed for thicker photoresist layers associate to hard bake. Source: FBK

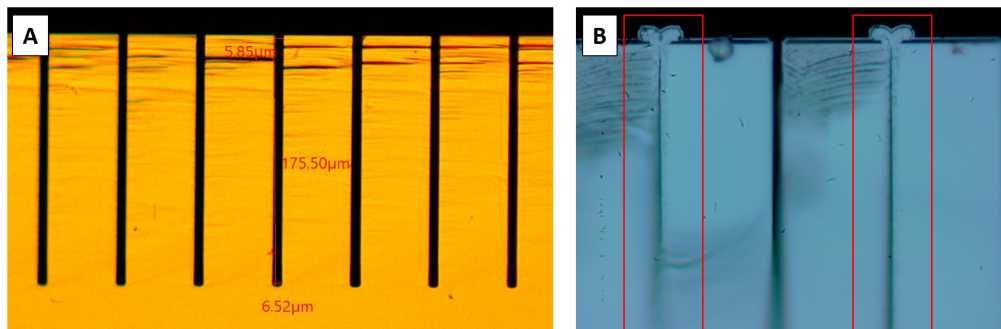


Figure 4.20: Lateral view of the trenches obtained by cutting the test structure. (A): Test structures built during the fine tuning of the technology. (B) Test fills with N<sup>++</sup>-doped polysilicon on junction trenches. The red squares highlights the polysilicon deposit [77].

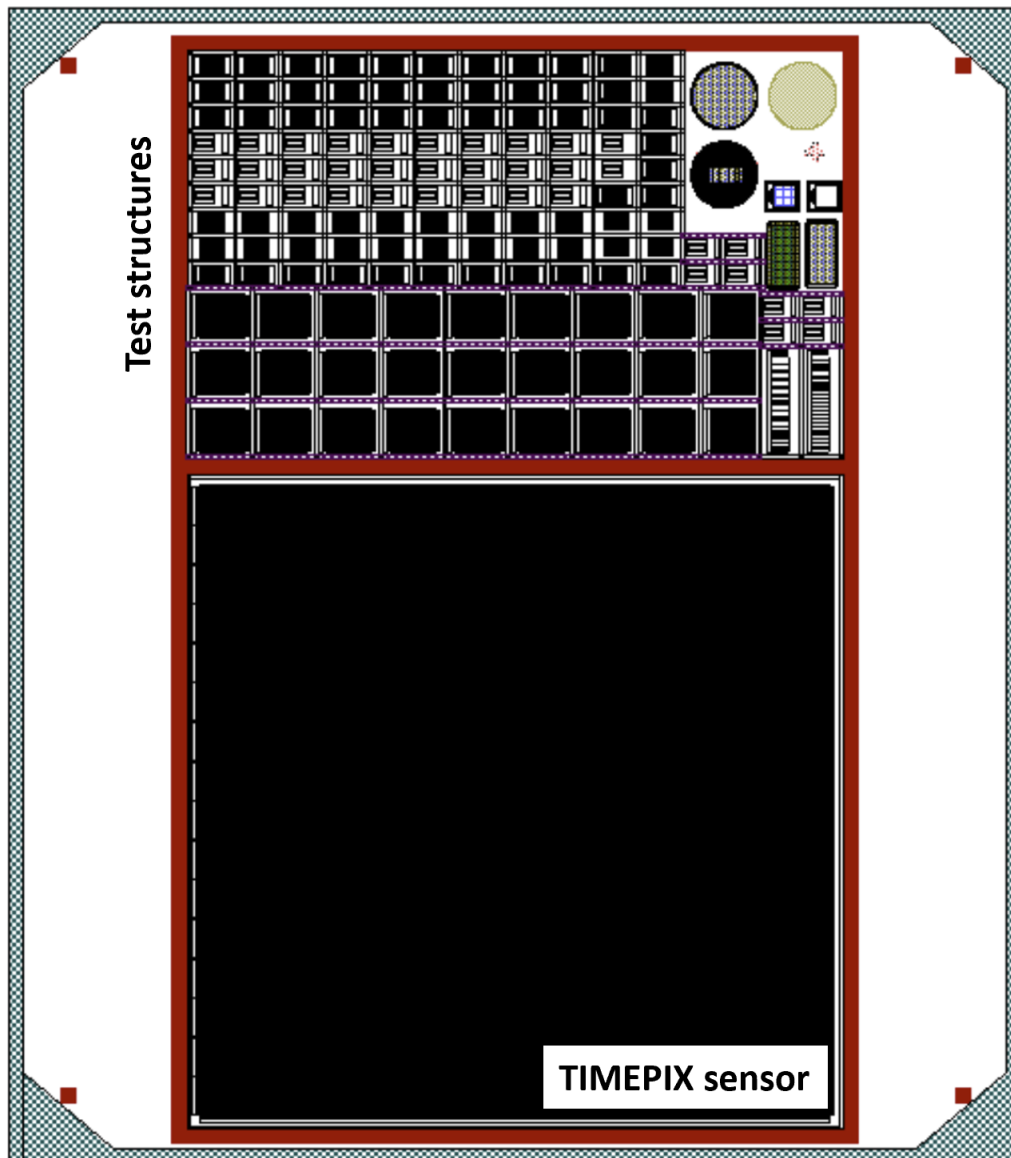


Figure 4.21: Superstructure containing the TIMESPIX sensor matrix and 3D test structures [77].

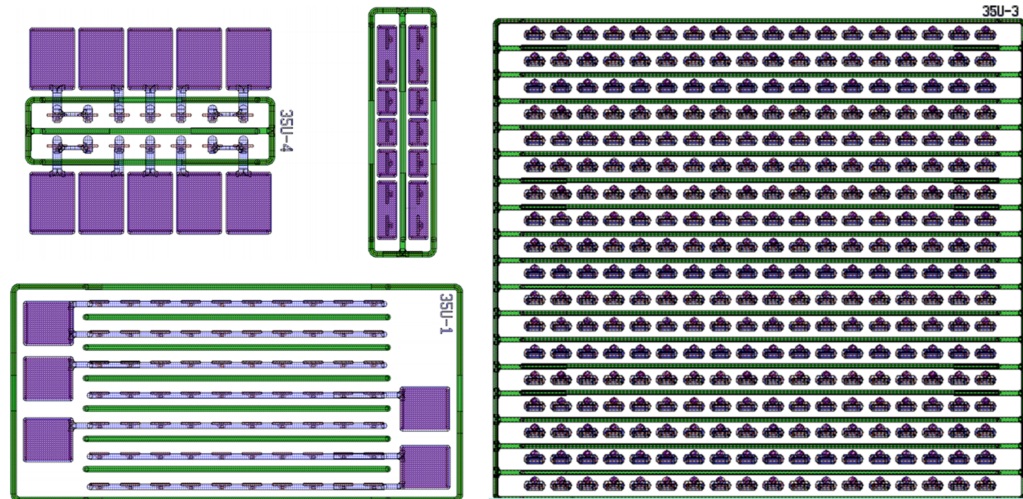


Figure 4.22: Test structures containing different configurations of the parallel trench pixel. Some structures include single pixel, strip pixel configuration and smaller pixel matrix [77].

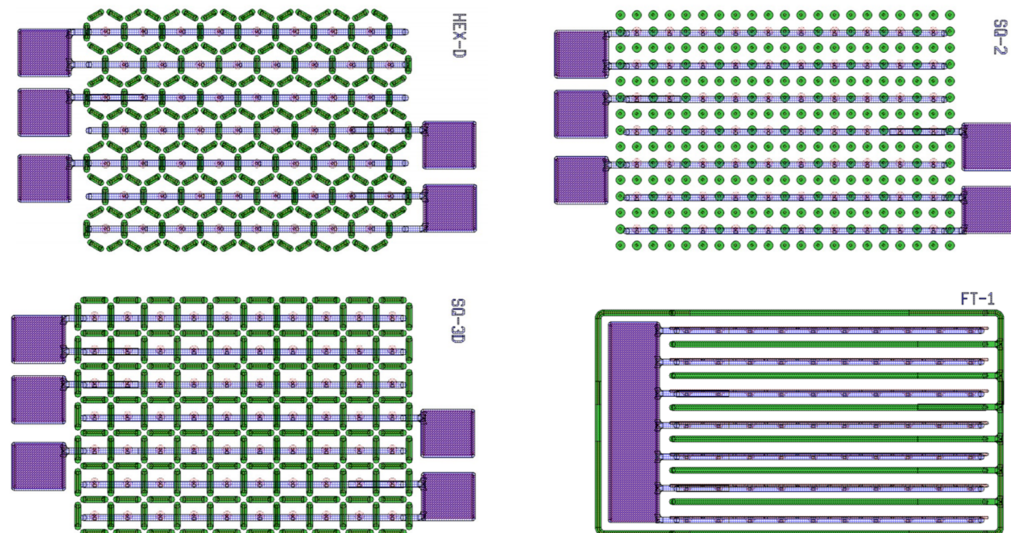


Figure 4.23: Test structures including different pixel geometries in strip configuration [77].



# Chapter 5

## Sensor operation simulation

### 5.1 Motivation

The design of a silicon sensor cannot rely only on the analysis of its stationary physical quantities like the electric and weighting field or the charge mobility. An important part of the simulation activity is carried out by transient simulations which are needed to predict and observe the response of the sensor when crossed by an ionizing particle. Focusing the attention on the TIMESPOT timing optimized 3D silicon sensor, transient simulations are important to study the time resolution contribution of the sensor in the complete detector system.

As mentioned in chapter 2, the two main contributions in time resolution of a silicon sensor are the jitter, which depends proportionally to the sensor capacitance as explained in [78], and the time walk. Jitter contribution can be estimated easily and the best way to reduce this contribution is to increase the signal/noise ratio which corresponds to reduce the sensor capacitance. Time walk instead is more difficult to estimate and needs a completely different approach. The best way to predict the time walk of a sensor is to use a large number of simulated current signals and analyse the time walk distribution. Having different energy deposits with different track locations, orientations, energy deposit fluctuations and, eventually, secondary particle emission ensures a large variety of output signals and a detailed description of the time walk distribution of the sensor.

To simulate the time walk distribution of the sensor is needed:

- 1) A complete model of the pixel or a portion of the pixel matrix. The latter approach would allow to understand how particles crossing outside the pixel of interest can affect its signal response.
- 2) The number of simulated signals must be as high as possible. The Larger the number of simulated signals, the higher the precision to estimate the time walk distribution. To achieve this result, a special focus on the simulation time must be considered to achieve a large statistic in reasonable computing time.

- 3) High randomisation and detailed description of the energy deposits. Holding a large variation of the generated events allows to include every possible current signal. Also, the energy deposit must take into account possible fluctuations like delta ray production.
- 4) A transfer function must be defined to transform the current signal into a voltage signal. It is only after the conversion from current to voltage signal that time walk distribution can be calculated.

This chapter presents all the steps done to study the sensor response and gives a first estimation of the intrinsic time resolution of the TIMESPOT sensor, starting from ordinary TCAD transient simulations, improved with GEANT4 support and finishing with the use of the TCoDe simulation tool, specifically developed for this purpose. The chapter also shows all difficulties encountered to perform this study and the applied solutions, showing how the only use of the TCAD for transient simulations in HEP applications does not provide an efficient solution, forcing the search for alternative tools.

## 5.2 Sentaurus TCAD transient simulations

Signal simulation on TCAD requires specific models to emulate the effects of energy deposition and ionization caused by ionizing particles in silicon medium. For a good signal simulation, it is necessary to know the energy of the particle, the way the particle penetrates the silicon medium and its energy transfer to the silicon and the number of electron-hole pairs generated by the released energy.

The minimum specification needed for a sentaurus TCAD transient simulation are the sensor construction in a 2D or 3D model using the sentaurus structure editor (SDE) [87] and the sentaurus device tool which performs the transient simulations on the previously designed object [88]. A common sdevice simulation is managed by programming its command file (\*CMD). Every command file is divided into 5 main sections:

- The input/output sections which defines the input and output files.
- The electrode section which defines the electrodes of the device and their bias voltage at the beginning of the simulation.
- The physics section which defines all physical models needed to run the simulation.
- The math section which defines the mathematical computing technique.
- The solve section which defines the type of simulation (transient/quasi stationary/AC/etc.)

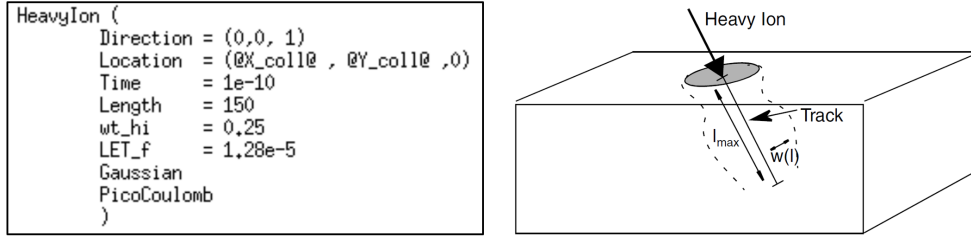


Figure 5.1: 1 Sentaurus Heavy Ion model. Left: Code used for signal simulation, displaying all variables. Right: Schematic view of the Heavy ion model. Source: [88]

### 5.2.1 Sentaurus Device Heavy Ion Model

Sentaurus TCAD is capable of simulating the effects produced by ionising radiation in the silicon medium with 3 different models, the AlphaParticle model, the HeavyIon (HI) model and the gamma exposure. Their implementation in a sdevice simulation must be performed by activating their program code in the sdevice comand file physics section. The AlphaParticle model is designed specifically to describe energy deposition by alpha particles and is less recommended to simulate the effects of high energy particles. The Gamma Radiation model is used only to study the damage caused by long gamma exposure of semiconductor devices, by specifying the total dose received over a specific exposure time [88]. The only radiation-matter interaction model capable of emulating the effects of high energy particles is the heavy ion model.

Basically, the heavy ion model emulates the effects of ionization in silicon by heavy ions by simply injecting along a specified path a specific charge density. The model itself does not require any information about the heavy ion itself. Only start time of the ionization, start position, length and orientation of the track, linear energy transfer (LET) and width of the deposit with respect of the path are required (fig. 5.1). This makes possible to modify the parameters of the heavy ion model to set the effects of ionization caused by high energy particles in silicon. In the case of ultra-relativistic charged particles, the ionization of the silicon medium is at its minimum and equal to  $388 \text{ eV}/\mu\text{m}$  [89]. The generation of the heavy ion injected charge density along a path with length  $l$ , at the time  $t$  and with a deposit width of  $w$ , is computed using formula 5.1:

$$G(l, w, t) = G_{LET}(l)R(w, l)T(t) \quad (5.1)$$

$G_{LET}(l)$  is the energy transfer function in 3D objects, which is defined by equation 5.2 [88]:

$$G_{LET}(l) = a_1 + a_2l + a_3e^{a_4l} + k/2\pi w^2 * (c_1(c_2 + c_3l)^{c_4} + LET(l)) \quad (5.2)$$

By default, all parameters, except  $k$ , which is equal to 1, are set to 0 (fig. 5.2). The linear energy transfer parameter  $LET(l)$  must be set on the sdevice heavy ion code, as shown in figure 5.1, and it describes the amount of charge (in pC) deposited per  $\mu\text{m}$  of path.

	$s_{hi}$	$a_1$	$a_2$	$a_3$	$a_4$	$k$	$c_1$	$c_2$	$c_3$	$c_4$
<b>Keyword</b>	s_hi	a_1	a_2	a_3	a_4	k_hi	c_1	c_2	c_3	c_4
<b>Default value</b>	2e-12	0	0	0	0	1	0	1	0	1
<b>Default unit</b>	s	pairs/cm <sup>3</sup>	pairs/cm <sup>3</sup> /cm	pairs/cm <sup>3</sup>	cm <sup>-1</sup>	1	pairs/cm <sup>3</sup>	1	cm <sup>-1</sup>	1
<b>Unit if PicoCoulomb is chosen</b>	s	pairs/cm <sup>3</sup>	pairs/cm <sup>3</sup> /μm	pairs/cm <sup>3</sup>	μm <sup>-1</sup>	1	pC/μm	1	μm <sup>-1</sup>	1

Figure 5.2: Sentaurus device default parameters for the Heavy Ion model. It is possible to change them by changing the parameter file which defines the default TCAD physics [88]

The function  $R(w, l)$  describes the spatial distribution of the charge deposit around the heavy ion path. The charge density is modeled at a distance  $w$  around the track with a Gaussian shape (equation 5.3):

$$R(w, l) = \exp\left(-\left(\frac{w}{wt_{hi}(l)}\right)^2\right) \quad (5.3)$$

With  $wt_{hi}(l)$  the characteristic distance settable on the sdevice heavy ion code. The last function,  $T(t)$ , describes the time dependence of the charge generation. The function is dominated by a Gaussian distribution, weighted by an error function (equation 5.4):

$$T(t) = \frac{2 * \exp\left(-\left(\frac{t - t_0}{\sqrt{2} * s_{hi}}\right)^2\right)}{\sqrt{2\pi} * s_{hi} * \left(1 + \operatorname{erf}\left(\frac{t_0}{\sqrt{2\pi} * s_{hi}}\right)\right)} \quad (5.4)$$

With  $s_{hi}$  the characteristic time constant of the generation rate. For a more detailed view of the heavy ion model, it is recommended to read the sdevice manual [88]. Modelling the time dependent contribution with a Gaussian function influences highly the organisation of the transient simulation. The generation function, centred at  $t_0$ , starts to inject charge even before  $t_0$  due to its Gaussian behaviour. To avoid charge loss during the simulation, it is recommended not to set the heavy ion directly at the beginning of the transient simulation but some time later. An example is shown in figure 5.3 for a heavy ion simulation with  $s_{hi}$  equal to 2 ps and start time at 100 ps. A first transient simulation with relatively large time steps goes from 0 ps to 90 ps. A second transient simulation starts immediately after the 90 ps mark with a 10 fs initial step. Maximum and minimum time step must be

hold lower than 1 ps to describe with enough precision the charge injection in the device. Using time steps with an almost identical length of  $s_h i$  will cause charge loss due to the low time resolution used to describe the process.

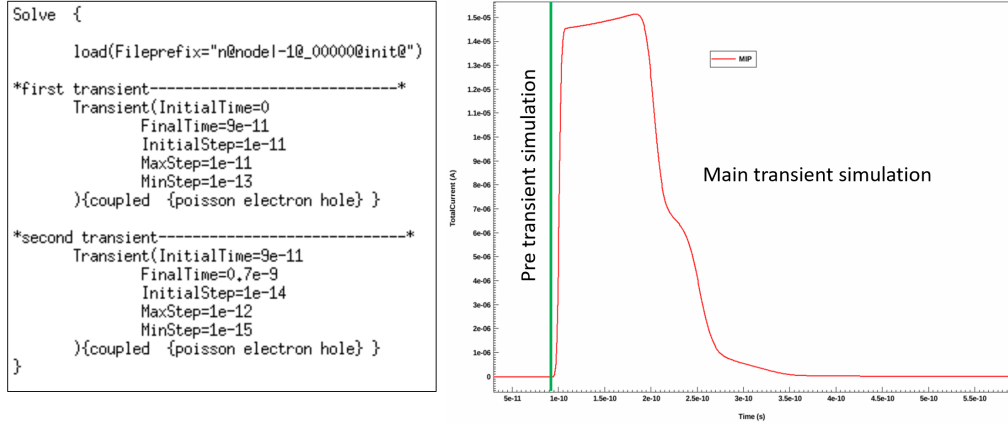


Figure 5.3: Senstaurus TCAD transient simulation. Left: Code organisation. Right: Simulated signal. The green line is used to highlight both transient simulations implemented in the code.

### 5.3 Critical aspects of pure TCAD sensor operation simulation

Using sentaurus TCAD to simulate sensor operation is the first logical step if the tool was used previously to design the sensor. Using TCAD Transient simulations organized to study the time performance of sensors developed to operate with a time resolution of few ps shows some limits related to the software itself.

**Critical issues of the Heavy Ion model for HEP applications** The heavy ion model, especially if used with default parameters, is not the best solution to simulate device operation of fast timing sensors. The problem depends on the time function of the generation rate (equation 5.4). As previously described, using a Gaussian function which is centred at a specific ionisation time means that half of the generated charge is obtained even before the particle crosses physically the silicon medium, which is wrong on a physical point of view. On a computing point of view this approach is correct, considering that TCAD computes continuous physical quantities and needs to model charge injection in a continuous way too. Also, TCAD was developed for completely other purposes which do not consider physical phenomena in 10 fs - 10 ps range. A second aspect on the time dependent generation function is related to its characteristic constant  $S_h i$ , which by default is set to 2 ps. This parameter in its default value, which is also used for the alpha particle model,

is an estimation of the time behaviour due to the thermalization of the charges after some instants from their generation and is only valid for alpha particles and heavy ions with energies of 1-10 MeVs with velocities lower than  $0.14 c$  [90]. For fast timing sensors operating in velocity saturation and crossed by ultra-relativistic charged particles with velocities over  $0.99 c$ , the Heavy Ion model does not have an experimental validation and has to be applied with carefulness.

A possible reinterpretation of the  $s_{hi}$  parameter for HEP applications could be the description of charge acceleration during the first instants after ionization, but a short calculus demonstrates how even this phenomenon has negligible impact on silicon sensors. Considering that for a free moving electron in silicon the kinetic energy is equal to  $1/2kT$  for every degree of freedom, a fast calculus shows that its average thermal velocity is already of the order of  $10^7$  cm/s at 300 K, which has the same order of magnitude as their drift velocities in velocity saturation conditions. This means that free electrons and holes, generated by ionization, do not suffer an acceleration intended as speed increment but their motion is only oriented in the direction to the electric field force lines. The only observable rise time in a current signal is related to the time the energy deposit is formed during the passage of the ionizing particle.

An example is given by the passage of an ultra-relativistic charged particle through  $150 \mu\text{m}$  thick silicon. Considering energy transfer from the particle to the medium as almost instantaneous, the time needed to ionize silicon along the path is equivalent to the time needed to pass the entire layer: 500 fs.

The space distribution of the sentaurus Heavyion charge deposit presents also some critical aspects. In detail, single heavy ion model with default parameters just generates a cylindrical energy deposit with uniform charge density overall the length  $l$  and a width  $w$ . For a first rough estimation of the signal response this approach is enough because it describes the deposit generated by the main ionizing particles, but it does not consider random fluctuations of the deposits or even secondary particle generation along the path. It is possible to generate more complicated energy deposits by using more than one heavy ion model during the same transient simulation, with a maximum of 64 heavy ions at a time, but the fluctuations need to be computed randomly. A special focus on energy fluctuations and delta rays can be easily done by assisting energy deposition in silicon using Monte Carlo tools like GEANT4. This approach is explained in section 6.

**Mesh strategy for transient simulations** An accurate TCAD simulation depends strongly from the applied mesh grid. A wrong applied mesh grid, especially if the mesh size is too large, introduces numerical error [91]. TCAD simulations are basically computational fluid dynamics (CFD) simulations, and one of most crucial parts is the definition of an appropriate mesh grid needed to compute with enough precision the evolution in time of the charge drift and diffusion. One main error source introduced by a wrong applied mesh strategy is false diffusion, which causes

an artificial dispersion of the charge cloud in time.

A series of test simulations were performed to develop an optimized mesh strategy for 3D silicon sensor and the obtained efforts and results are shown in section 5.5.

**Simulation time** Simulation time plays a very important role. The lower the time needed to simulate a single sensor response, the higher the statistics that can be collected in a specific time interval. TCAD is capable of simulating with high accuracy sensor operation at the cost of using a large amount of computing resources and time. It is possible to speed up sensor simulation by using customized tools, conserving most of the physics computed by TCAD, replacing only the physical processes which are time consuming. For this reason, the TIMESPOT Code for Detector simulation (TCoDe) was specifically developed and its results displayed at the end of this chapter. A more detailed description of TCoDe and its validation are presented in chapter 5.

## 5.4 TCAD simulations with GEANT4 deposit

As mentioned in the previous section, TCAD uses a simplified description of the energy deposits generated by the ionization of high energy particles. Energy deposit fluctuations and deposits generated by secondary particles like delta-rays are not considered. A solution to include more realistic deposits consists to add particle-silicon interaction information using the Geometry and Tracking 4 (GEANT4) tool [92].

The idea behind this approach consists in rebuilding in GEANT4 a pixel model of the same shape and size of the pixel and to add a particle source which shoots ultra-relativistic particles against the silicon model. The released energy and particle track inside the silicon model are then saved and converted into an equivalent sentaurus heavy ion model which is added in the sdevice command file. This approach guarantees a more detailed description of the energy deposition in silicon compared to the exclusive TCAD approach.

**GEANT4 Sensor model** The GEANT4 sensor model used for this approach is a replica the TCAD model and shares the same position and orientation in space. The model presents a simplification compared to the original TCAD model which is related to the doping concentration along the interface regions which is completely absent. Only the sensitive area and the electrodes are considered. The single pixel model can be replicated on multiple pixel matrices and even detector stations for other applications (fig. 5.4).

**GEANT4 physics and particle source** The GEANT4 physics list is based mostly on the Electromagnetic standard option 2 (G4EMstandardopt2) [93]. This EM option is specifically designed for LHCb environments and therefore ideal to

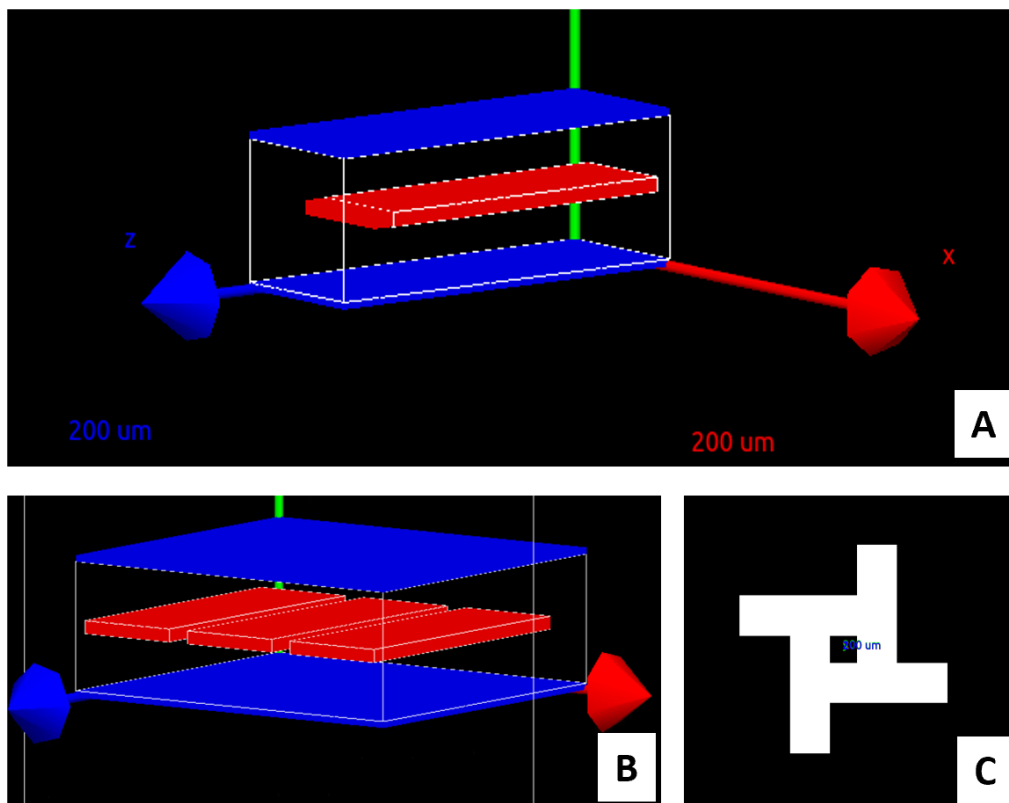


Figure 5.4: 3 Possible pixel configurations in the GEANT4 simulation: (A) GEANT4 replica of the silicon pixel. (B) Configuration in a 3-pixel matrix. (C) Sensor array configuration built with over 780000 independent pixels.

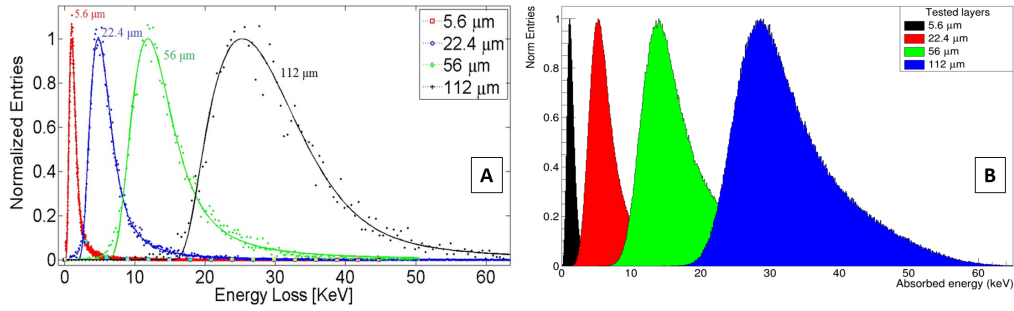


Figure 5.5: 4 Energy absorption in thin silicon layers. Comparison between experimental data form [79] (A) and GEANT4 simulation (B).

emulate the environment present inside the LHCb detector. A slightly modification of this model was applied concerning the formation of delta rays in silicon by adding the GEANT4-MicroElec extension. The MicroElec extension, developed by CEA [94], models the effects of energy deposition produced by low energy electrons, protons or heavy ions in silicon with the purpose to study those effects on integrated circuits. In this case the MicroElec model helps to describe more in detail the energy deposition in silicon.

As particle source, the GEANT4 general particle source (GPS) was selected. This allows to select a larger particle variety and to set more parameters related to their interactions. Following the study of energy deposits from minimum ionizing particles in thin silicon sensors from Passeri et. al [79], a positive charged pion ( $\pi^+$ ) with average energy of 12 GeV was selected. This choice also allows to make a full validation of the GEANT4 physics using the data acquired by the experiment (see Fig. 5.5). The most difficult part of the particle source is related to its orientation in space. Two different options were considered and tested. The first option is a complete randomization of the position of the source which is positioned around the sensor with the possibility to shoot particles from every position. This approach has the advantage to follow the main requirement needed to estimate the time walk contribution of the sensor. The second approach follows a more realistic approach and consists to organize the GPS like in a real collision point at LHC, with a variation of 5  $\mu\text{m}$  in X and Y direction and a maximum angle of 300 mrad.

**Conversion from GEANT4 to sentaurus TCAD** Conversion of the energy deposit from GEANT4 to the sentaurus heavy ion model is completely automatic and was implemented in GEANT4 with a customized class. The data transfer class developed for this special purpose is activated every time a particle releases energy inside the sensitive volume. All the information about the energy deposit (orientation, position, time and energy deposited) is recalled by the stepping action class. The stepping action class outputs all information related to one single track. All possible data is then saved and converted into an equivalent Heavy Ion code. At the

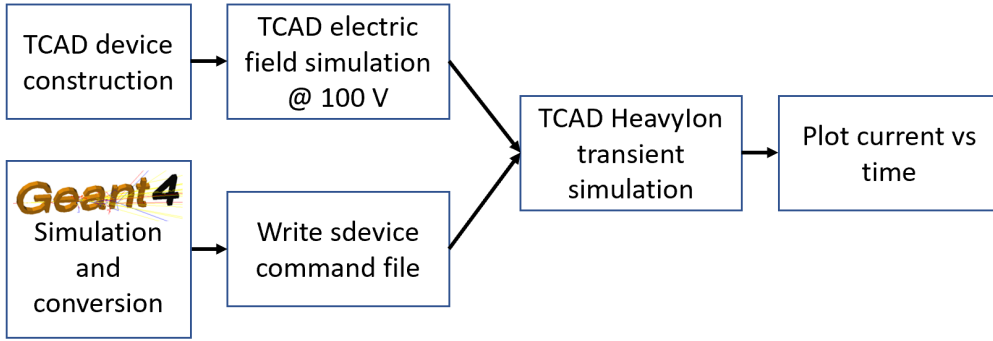


Figure 5.6: TCAD transient simulation assisted with GEANT4 energy deposit simulation.

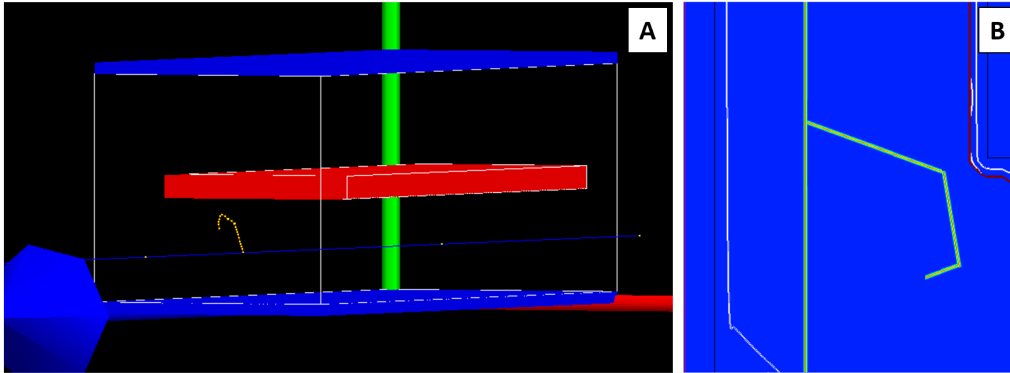


Figure 5.7: (A) Single GEANT4 simulation showing the passage of a pion (blue track) and the generation of a 131 keV delta ray (red track). (B) Its reproduction in TCAD displayed along a cut of the sensor.

end of the simulation, GEANT4 outputs a complete sdevice command file (\*.cmd) which is then added in the Sentaurus TCAD project (fig. 5.6). The only important conversion performed in the data transfer class is the conversion of the energy deposit of the track from the GEANT4 to the TCAD nomenclature. GEANT4 displays the total energy deposit per track in keV, TCAD in  $\text{pC}/\mu\text{m}$ . In order to perform this conversion, it is necessary to take into account the average energy needed in silicon to generate an electron hole pair, which is 3.6 eV, and the track length  $l$ . The final conversion algorithm implemented in the GEANT4 data transfer class is (5.5):

$$E_{depTCAD} = \frac{E_{depG4}}{3.6 * 10^{-3} \text{keV} * l} \quad (5.5)$$

With  $E_{depG4}$  the GEANT4 energy deposit and  $l$  the track length. Figure 5.7 shows a single GEANT4 simulation with single delta ray production which presents a longer ionization path and its TCAD conversion. Simulation results are displayed in the final paragraph of this chapter.

## 5.5 Mesh strategy for 3D model transient simulation

False diffusion is a kind of error which can appear in Computational Fluid Dynamics (CFD) simulations. False diffusion occurs when the applied mesh grid structure is not aligned with moving flow or the mesh size is not fine enough to compute with enough precision the moving physical quantities (depending on the application it can be a mass density wave or a charge cloud moving in space like in this case).

From De Vahl Davis et al [91] it is known that the influence of false diffusion in a 2D device simulation depends directly from the mesh size ( $\Delta x$  and  $\Delta y$ ) and the angle  $\Phi$  between the velocity vector  $V$  and the x-direction (equation 5.6):

$$\Gamma_{false} = \frac{\rho V \Delta x \Delta y \sin(2\Phi)}{4(\Delta y * \cos^3(\Phi) + \Delta x * \cos^3(\Phi))} \quad (5.6)$$

From equation 5.6 it results that a mesh refinement with smaller mesh size reduces the effects of false diffusion. Therefore, the key for an accurate TCAD simulation is a fine mesh structure. The simplest approach could be to define a finer global mesh over the entire model, but, using a finer mesh grid is very inefficient on a computing point of view and increases the necessary computing time needed to run the simulation. For example, for a  $1 \mu m^3$  large cube with a 100 nm mesh grid, the number of total points is 1000. If the mesh size is reduced to 50 nm, the number of mesh points increases by a factor of 8 and also computing time will increase with similar proportion depending on the available hardware. In order to find a compromise between simulation accuracy and simulation time, a series of test simulations were performed with the main purpose to define an optimized mesh strategy for 3D silicon sensor simulation.

The main idea behind of those tests is that a fine mesh grid needs to be applied only in regions where something dynamically happens during a transient, like the passage of a charge density cloud. All other regions which presents stationary physical properties over the entire transient can be described by the larger mesh grid. This should allow to increase precision where it is needed without stretching considerably simulation time. Considering that, as shown in chapter 2, the Ramo theorem has an analytic solution for a planar electrode configuration, the model used for these tests is a simplified 2D model of a PN-junction with a planar electrode structure (fig. 5.8). Energy deposit is applied exactly in the middle of the model with direction parallel to the electrodes. 3 different tests were performed:

**First test series** During the first test trial, an energy deposit of 800 electron-hole pairs was injected exactly in the middle of the model. Charge drift was observed for a 400 ps long transient. Figure 4 shows how with increasing space resolution TCAD was able to better define the output current signal (fig. 5.9). For a mesh structure equal or higher than  $3 \mu m$  length, the heavy ion model failed to inject the charge

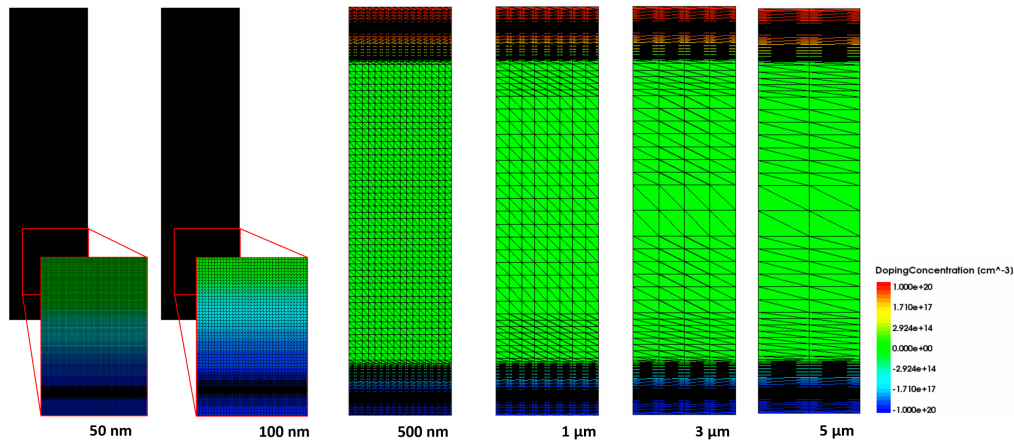


Figure 5.8: All mesh grids used on the sensor test structures, spacing from sub-micron to micrometer scale mesh grid.

in the sensor and no output signal was observed. For models with maximum mesh size lower than 100 nm the current signal changed completely form and assumed a stairs-like form, as predicted using the analytic solution of the Ramo theorem (comparison in fig. 5.10) shown in chapter 2, equation 3.36.

**Second test series** The second test series was focused on defining a fine mesh grid around the applied energy deposit and changing only the global mesh grid around the first one (fig. 5.11). This test helps to understand distortion effects on the signal caused by moving charges crossing mesh grids with different size. Figure 5.12 shows all simulated signals. It is possible to see how for global mesh sizes of 100 nm the current signal presents a peak 10 ps after the leading edge. When the global grid size is lower or equal to 100 nm, this peak is not present. The reason of those peaks is related to the acceleration the charges suffers when passing from a fine mesh area to a coarse mesh area. The gradient in mesh size causes a large false diffusion which also increases charge velocity. The effect has repercussion on signal formation which is visible with this characteristic peak. Other characteristic is that charge absorption happens almost 30 ps before the charge clouds reach the electrodes, which is also a demonstration of false diffusion.

**Third test series** The third test performed had a more qualitative aspect and is needed to show qualitatively the effects of false diffusion in different meshed systems. For this purpose, the model received a fine mesh of 100 nm on its left side and a larger 1 μm mesh grid on the right side. The results displayed on figure 5.13 shows how the right half of the energy deposits suffers false diffusion due to the larger mesh size, compared to the left half, which spreads slower in time.

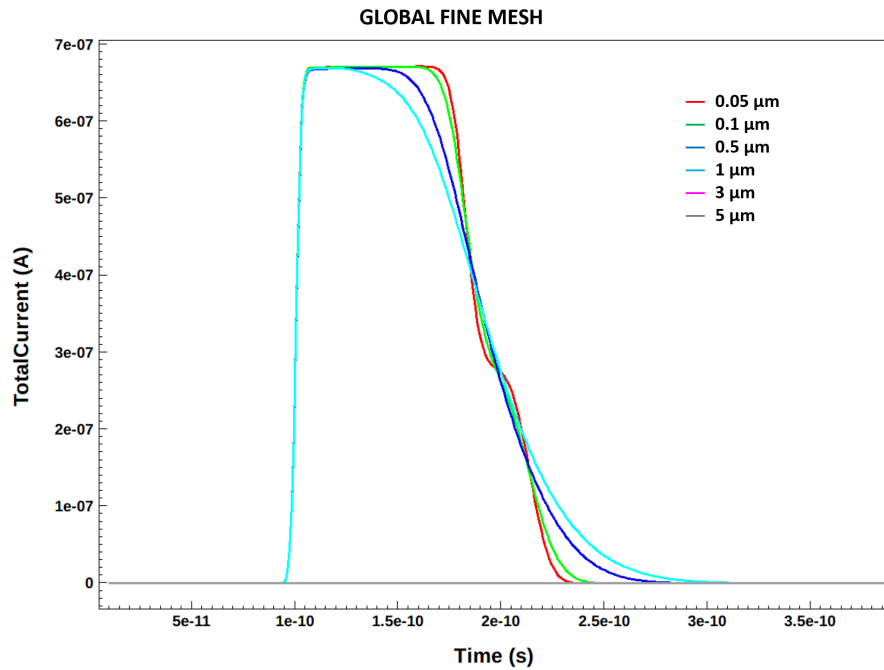


Figure 5.9: Current signals simulated using models with different mesh dimensions. The lower the mesh dimension and the higher the signal accuracy.

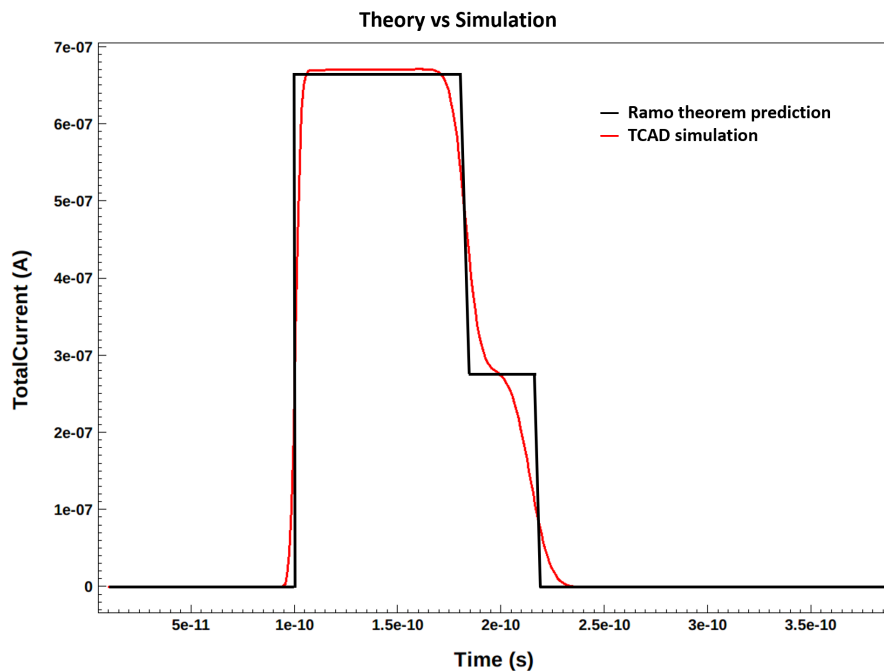


Figure 5.10: Signal comparison between Ramo theorem prediction and TCAD simulation with high resolution meshing. The Ramo prediction does not take into account charge diffusion.

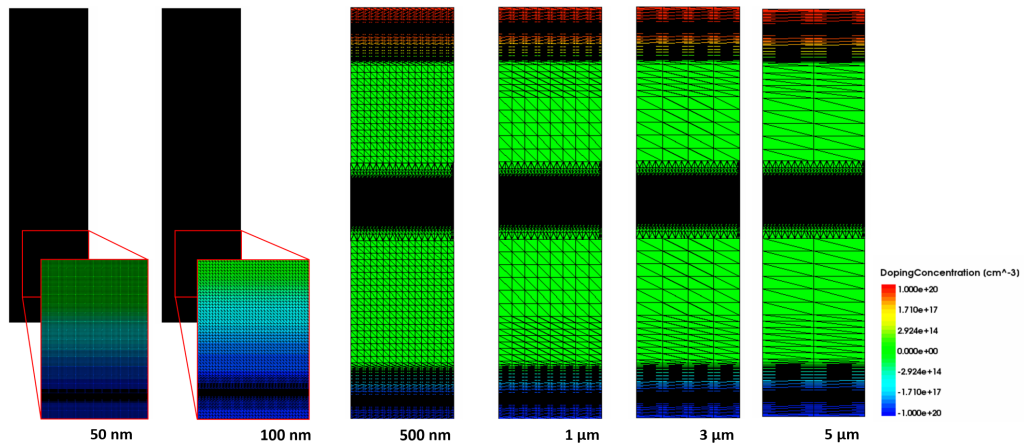


Figure 5.11: Second test model used. The area where the charge is applied presents a finer mesh grid.

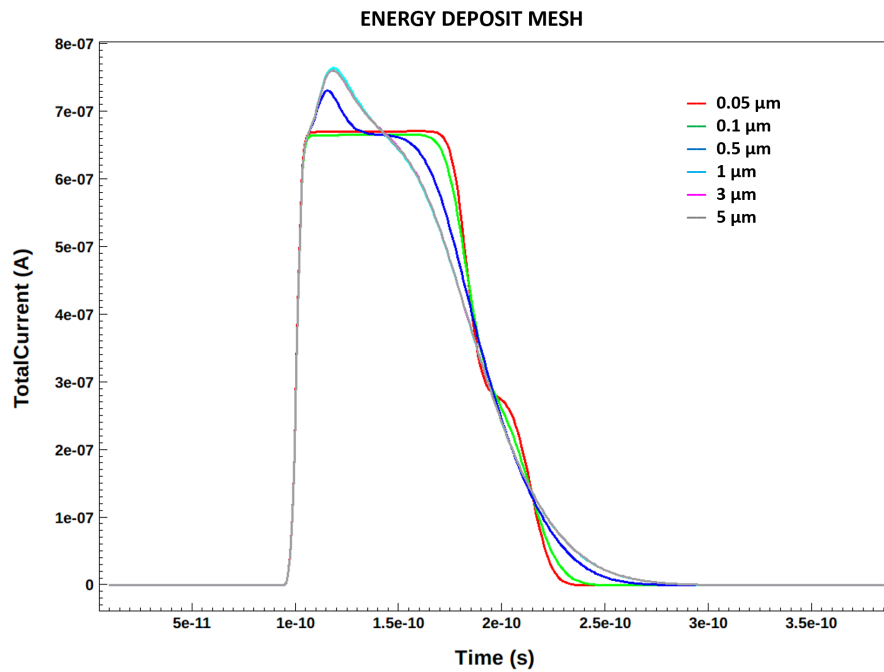


Figure 5.12: Plots showing the effects on signal formation due to the passage of different mesh grids.

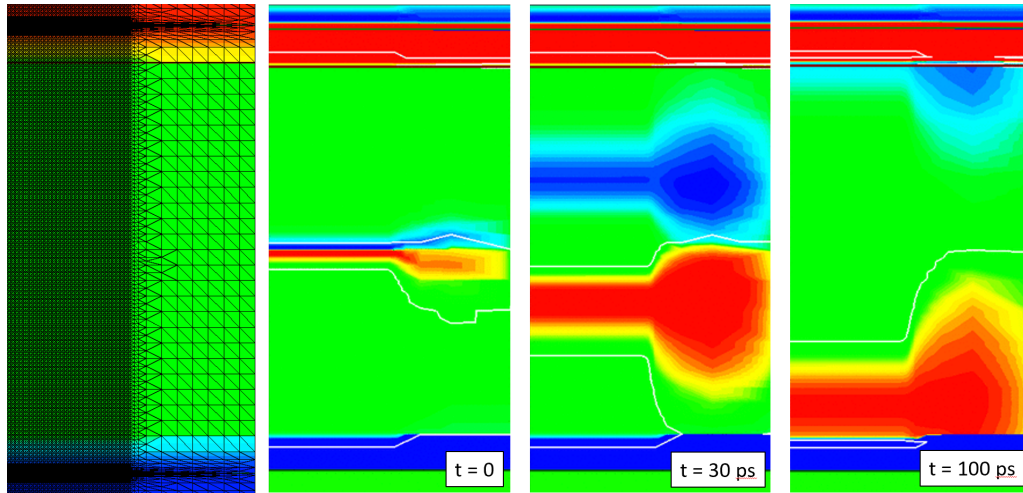


Figure 5.13: Evolution of a charge cloud in a different meshed model (red: holes, blue: electrons). First model shows the applied mesh grid. The other 3 models show the evolution of the cloud during the 100 ps long transient simulation

**Mesh strategy applied on TIMESPOT sensor** All 3 tests have clearly demonstrated that a fine mesh grid along the drift path need to be applied to perform very accurate TCAD transient simulation. The maximum mesh size applicable that does not show relevant signal deformation due to false diffusion is 100 nm. Moreover, the fine mesh grid must be applied uniformly over the entire drift path and contain the entire charge cloud. If the charge cloud is able to leave the fine meshed area, a signal distortion will be the effect.

To obtain a confirmation of the developed mesh strategy, a 2D model representing a XY section of the TIMESPOT sensor was chosen as test model. The parallel trench geometry of the sensor can be approximated by a planar sensor like the previous test device, which means that a point like charge deposit applied between diode and resistive electrode will induce a signal with a similar shape as predicted by the analytic solution of the Ramo theorem.

For the simulation, an energy deposit of the equivalent of 100 electron hole pairs was injected between the electrodes at the coordinate of  $(13.75 \mu\text{m}, 13.75 \mu\text{m})$ . The applied mesh grid which is needed to describe charge drift and diffusion goes from the resistive to the diode electrode and has a width of  $2 \mu\text{m}$ . The width was chosen, considering the expansion of the charge cloud due to charge diffusion according to equation 2 of [22]. The final fine meshed area is shown in figure 5.14 and works practically as a high definition path for the electron and hole clouds. The new mesh strategy was compared with the old approach based on the local description of the energy deposit and tested during the second test series. Both simulations were compared not only in signal formation but also observing the evolution of the charge cloud in time. As shown in figure 5.15, the new mesh strategy allows a detailed description of the charge cloud during the entire transient. Instead, the old mesh

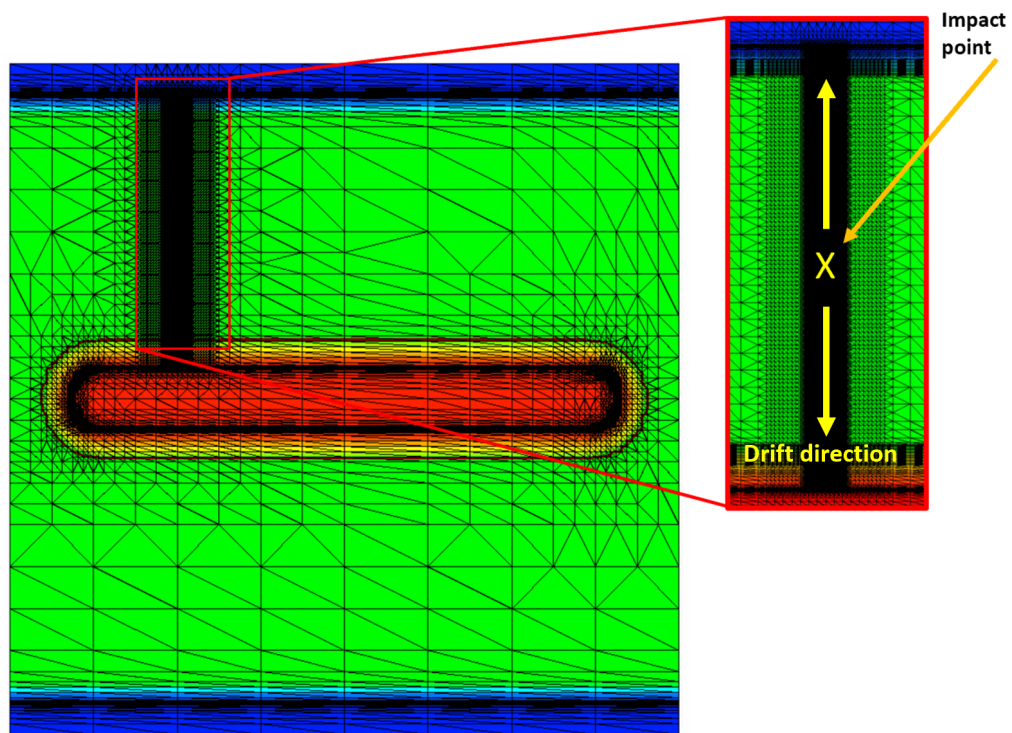


Figure 5.14: Mesh strategy applied on a 2D model of the XY section of the TIMESPOT sensor. Only the drift path of the e/h pairs presents a fine mesh structure in order to compute with high accuracy charge drift and diffusion.

strategy causes immediately false diffusion effects in the moment the charge leaves the fine mesh area. This effect has also repercussions on the signal formation.

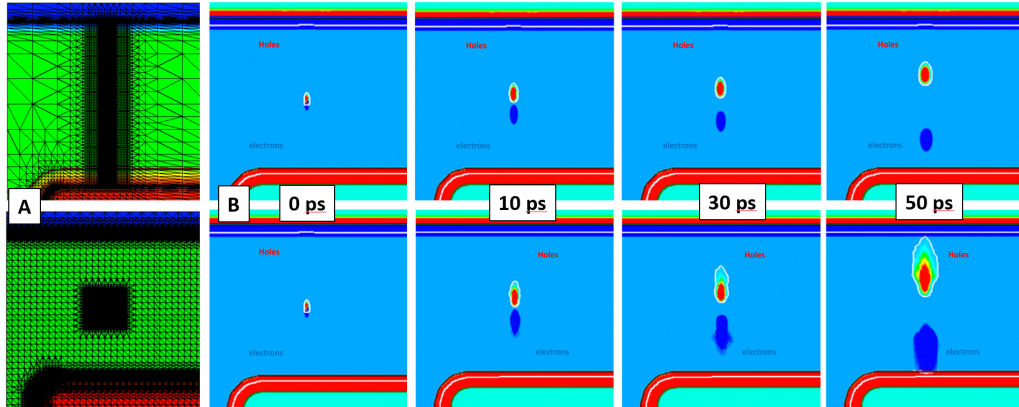


Figure 5.15: (A): Applied Mesh strategies. (B): Evolution of the charge cloud during the first 50 ps. It is possible to observe how false diffusion is dominant after the cloud leaves the fine meshed area.

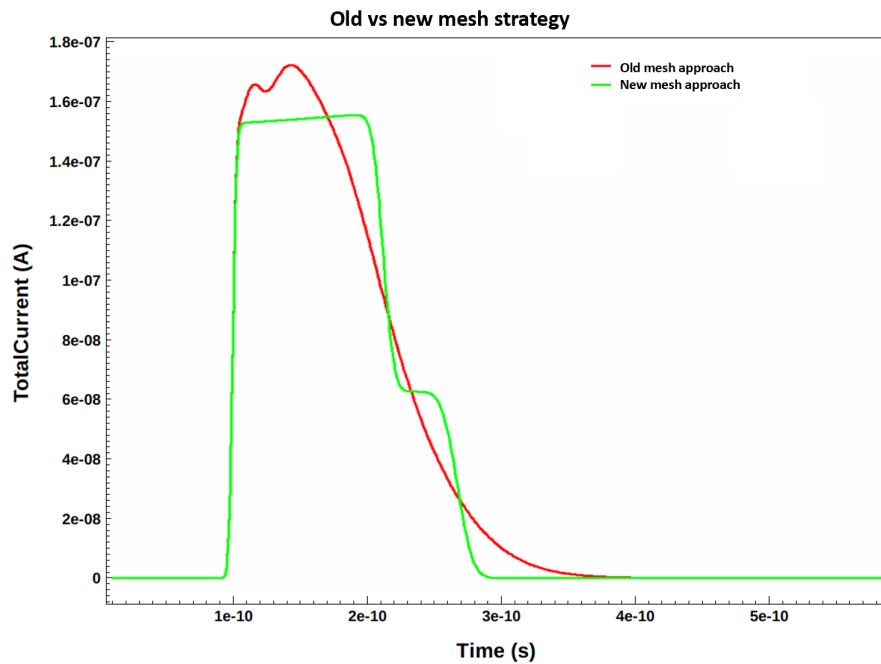


Figure 5.16: Comparison of new and old mesh strategy. False diffusion changes completely the signal shape due to the accelerated expansion of the charge cloud.

As displayed on figure 5.16, for the signal obtained with the new mesh strategy, a Ramo solution like shape has been obtained. For the old strategy instead, the signal

presents two peaks. The first peak, immediately after charge injection, is caused by the electron cloud which at first leaves the finer meshed area. The second peak is caused by the holes, which leave ps after the electrons the finer meshed area, increase their speed like the electrons before, inducing a larger amount of current on the electrode.

## 5.6 Results

This subsection shows all obtained results using all different simulation approaches.

### 5.6.1 TCAD 2D model simulation

2D model simulation was organized using 2 different models. One model representing a XY section of the pixel and a second model representing half YZ section of the pixel. The first model was prevalently used to understand the effects of current induction caused by energy deposits between the electrodes and to estimate charge collection time. Also, a comparison with the Ramo map was done for further validating the Ramo map approach. The second model was used as an approximation of sensor simulation using 3D models.

**XY section** Transient simulations performed over these 2D models consisted in injecting the equivalent charge amount of 80 electron-hole pairs in a single point. The positions of those charge deposits were organized in an array of 11x7 points, distributed over one quarter of the entire sensor model, considering that, for sensor symmetry, it is useless to cover the entire model with energy deposits (fig. 5.17). Particular attention was dedicated on observing how the signal shape changes with respect to the x position, to understand how the region between diode electrodes affects signal formation. The following 6 plots shows how the signal changes by varying the X coordinate, holding Y constant (fig. 5.18,5.19,5.20,5.21,5.22 and 5.23). All plots present the same signal evolution. For events close to the end of the diode electrode, a characteristic peak is observable which is at its maximum for deposits generate at  $X = 1 \mu\text{m}$  and starts to be less significant when the deposit is injected in the area where diode and resistive electrodes face each other. This peak can be described by analysing the weighting field and Ramo map of the sensor and depends mostly on the drift of the electrons. Electrons generated for  $X < 7 \mu\text{m}$  crosses at the beginning an area with a lower weighting field and then, when close to the diode electrode, the weighting field suddenly increases, inducing this characteristic current peak (fig. 5.24). In regions where the electrodes face directly each other, this high increment of the weighting field is less pronounced, and the current signal assumes a more stairs-like shape. The same analysis can be done by tracing the drift path of the electrons over the Ramo map. Concerning the contribution of current induction of the holes, no significant signal changes by changing the X coordinate are observed.

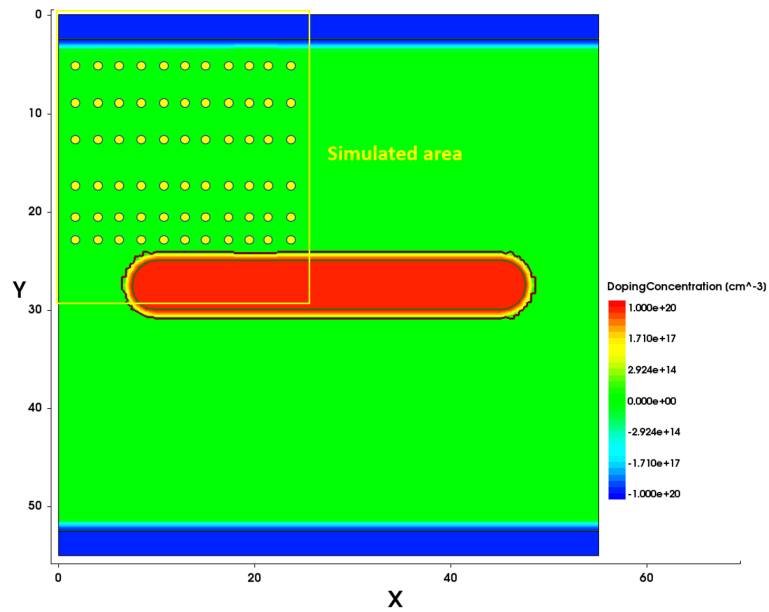


Figure 5.17: Applied simulation strategy. Every yellow dot represents one charge deposit injected in the model.

This is due to the weighting field which stays more constant close to the resistive electrode.

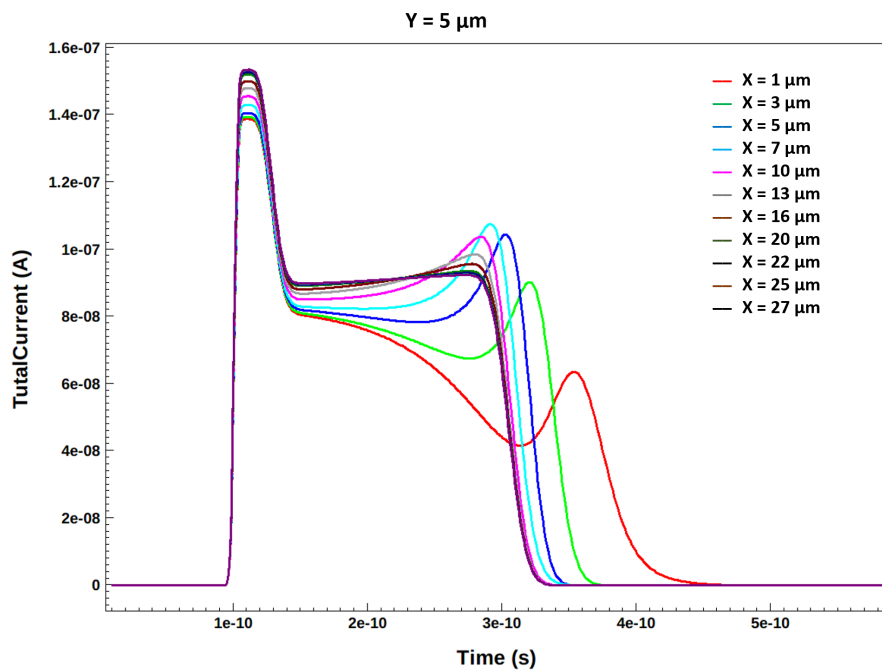
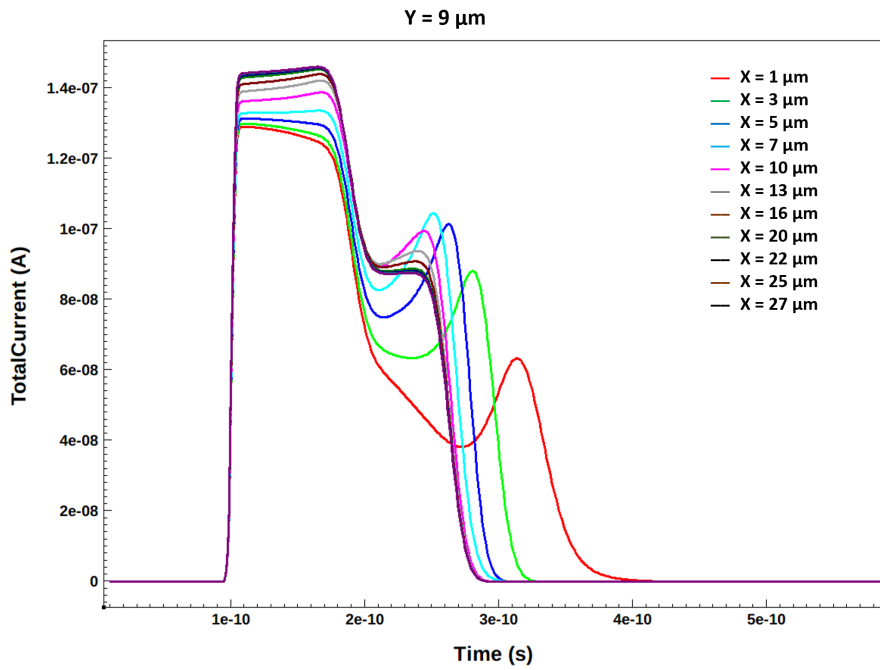
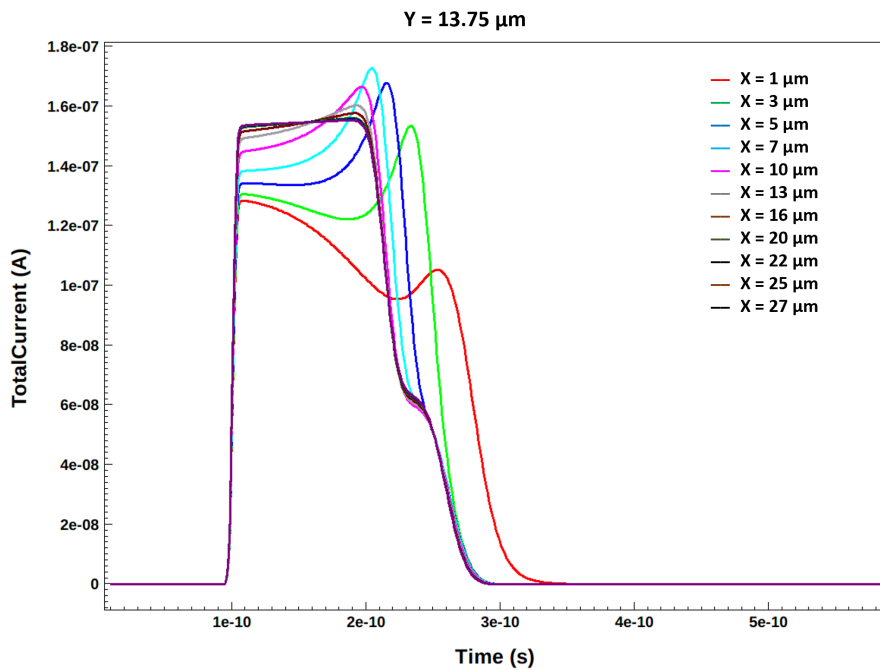
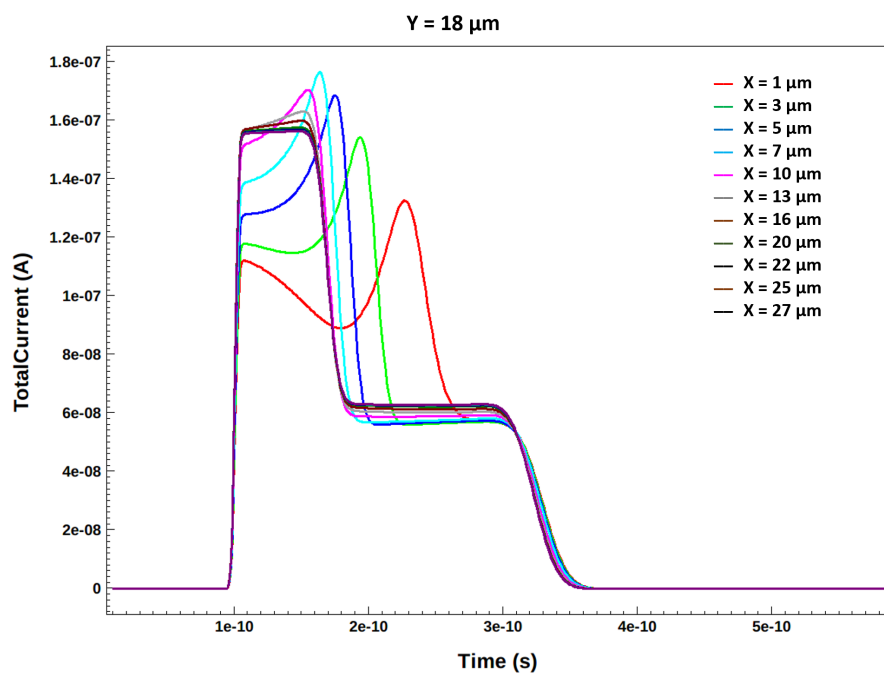
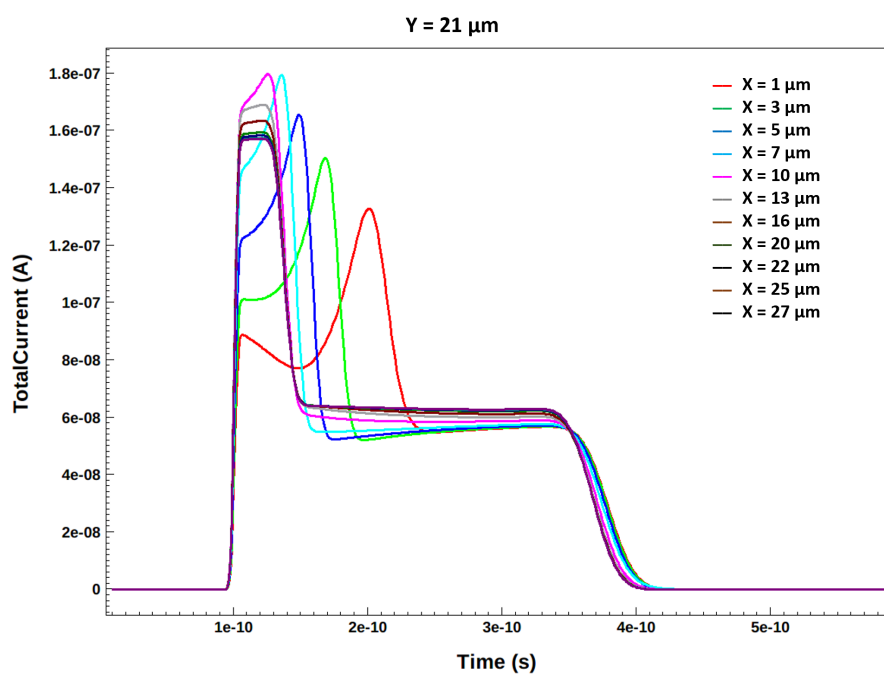


Figure 5.18: Signals generated with charge deposits around  $Y = 5 \mu\text{m}$ .

Figure 5.19: Signals generated with charge deposits around  $Y = 9$ .Figure 5.20: Signals generated with charge deposits around  $Y = 13$ .

Figure 5.21: Signals generated with charge deposits around  $Y = 18$ .Figure 5.22: Signals generated with charge deposits around  $Y = 21$ .

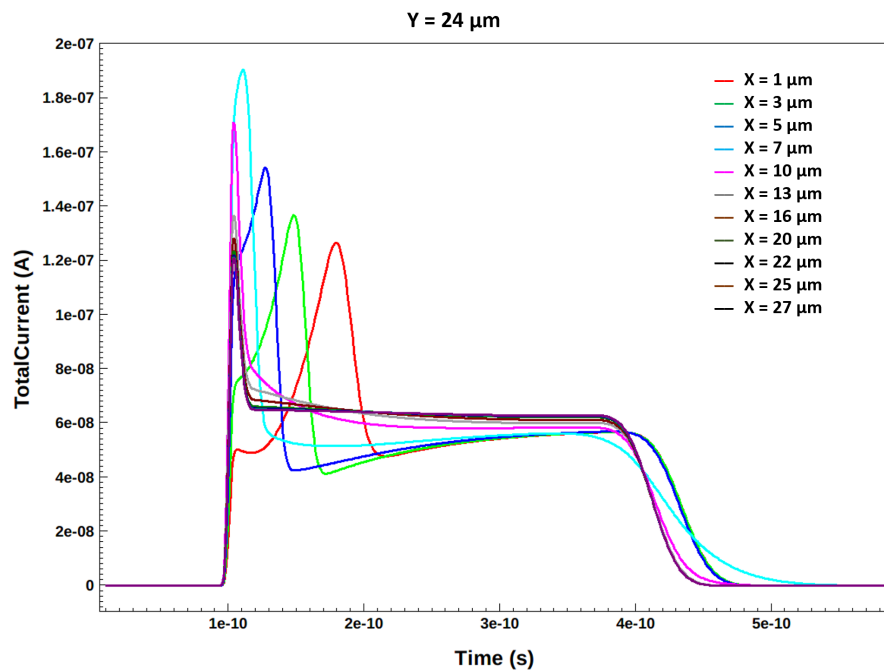


Figure 5.23: Signals generated with charge deposits around  $Y = 24$ .

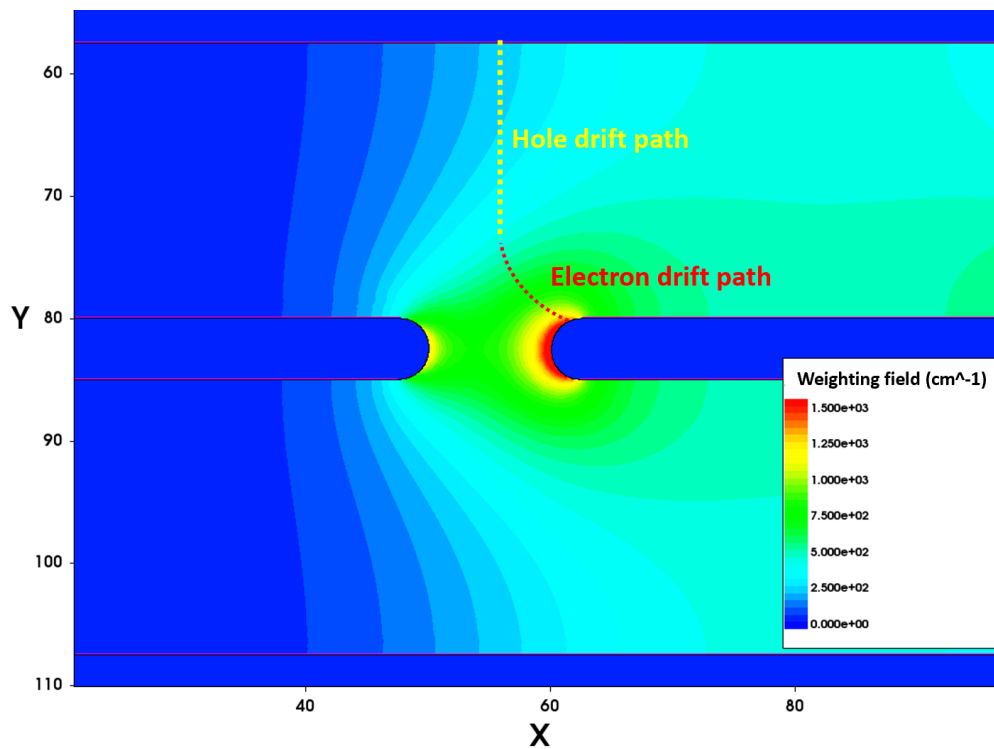


Figure 5.24: Weighting field of the TIMESPOT sensor and approximated drift path for charges generated between two diode electrodes.

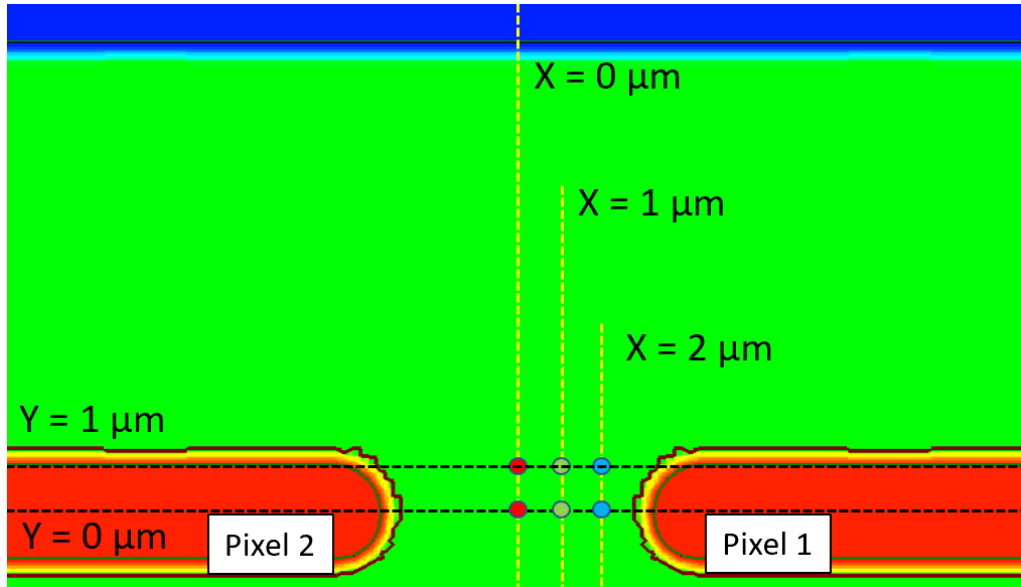


Figure 5.25: Analysis of the sensor response between two diode electrodes. The figure shows the applied charge deposits.

A second set of transient simulations were performed in the region between two diode trenches to fully validate the Ramo map approach and study signal shape in this critical area where the electric field results low and at the same time the weighting field results very high. For this reason, 6 charge deposits were applied: Four close to one electrode and two of them positioned exactly between the two electrodes (fig. 5.25). The obtained plots are resumed in figure 5.26, 5.27, 5.28 and 5.29 and show how the same charge deposit have different induction effects on both pixels. Current signals observed on the right pixel present a positive amplitude which is 3 times higher than the average amplitude observed from the previous plots, as expected from the Ramo map of the parallel trench geometry showed in chapter 4 (fig. 4.16). If the current signal is observed on the left pixel, the effect is exactly the opposite, showing a minimum with an almost symmetric shape. This evidence consolidates even more the validity of the Ramo map approach.

All those initial parts of the signal are mostly electron contributions and vanish in less than 30 ps after the rising edge. After electron absorption, only drifting holes are left which cross the entire inter-electrode distance. Their contribution to the induced signal is low and positive, independent of the used electrode, still according to the Ramo map.

A special case happens when the charge is injected exactly between both electrodes. In this situation the charge cloud splits into two equal parts. One drifts to the left electrode and the other to the right electrode. Having two identical charge clouds that cross areas with an opposite weighting field causes that the current induction do by electrons cancel each other. The only components which is observed is the

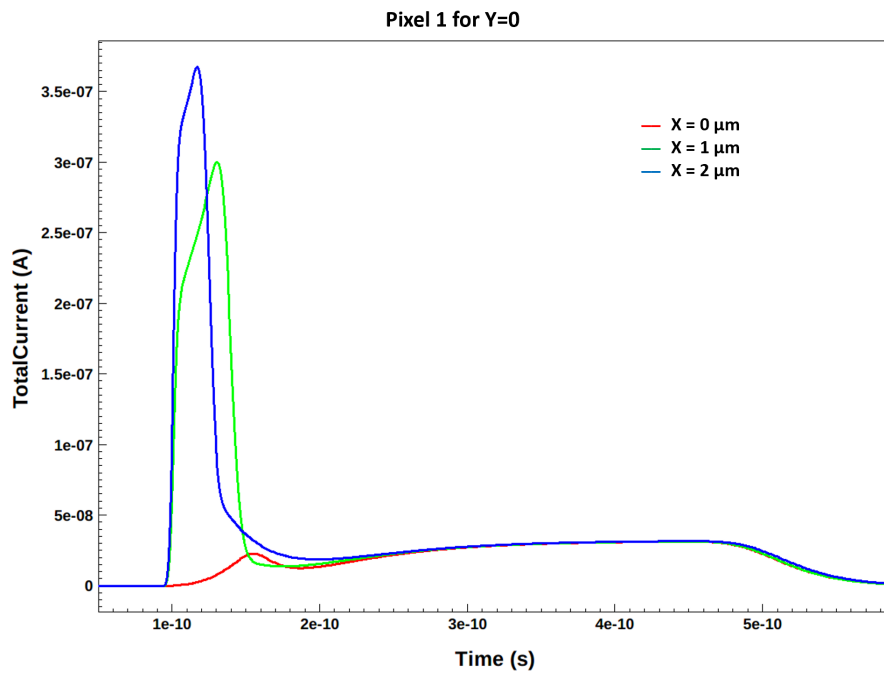


Figure 5.26: Current signals for charge deposits applied along  $Y=0$  observed from Pixel number 1.

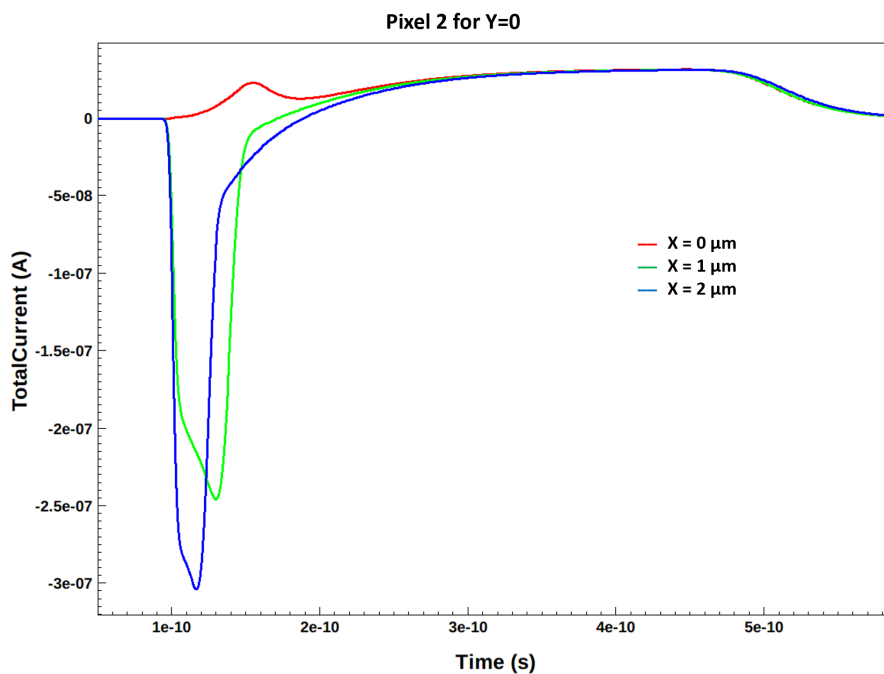


Figure 5.27: Current signals generated from charge deposits applied along  $Y=0$  but observed from Pixel number 2.

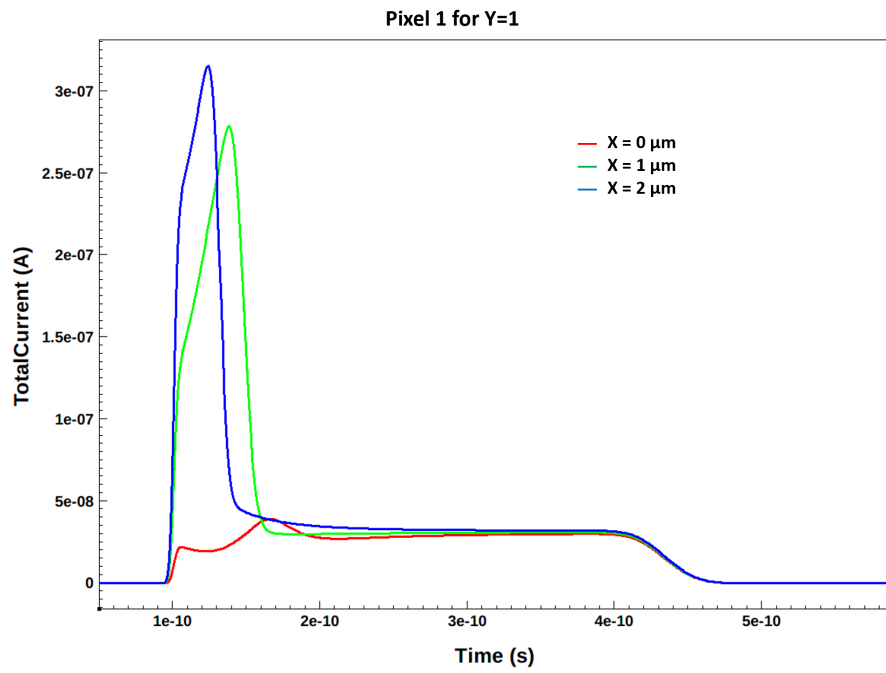


Figure 5.28: Current signals for charge deposits applied along  $Y=0$  observed from Pixel number 1.

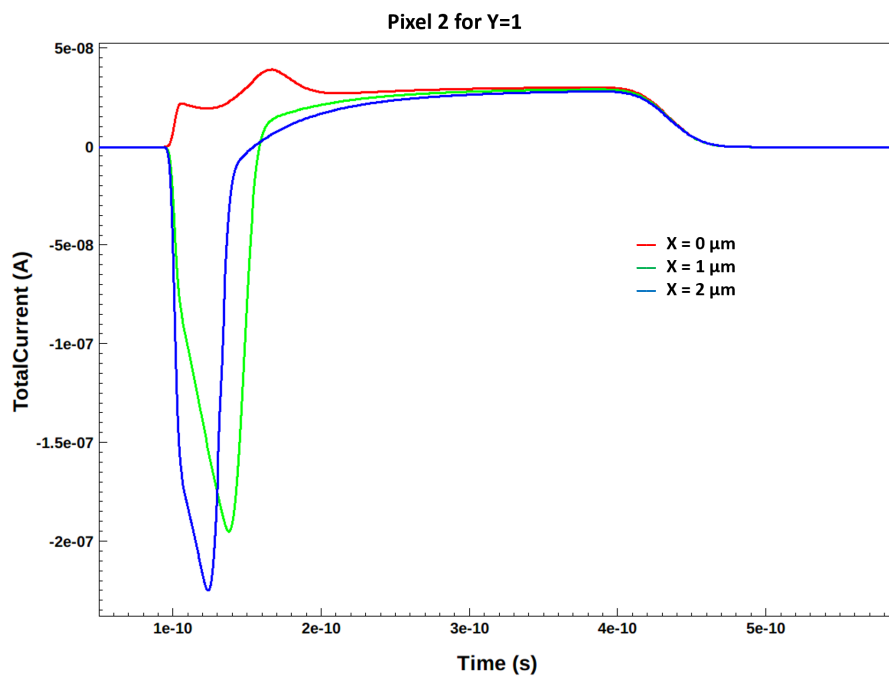


Figure 5.29: Current signals generated from charge deposits applied along  $Y=1$  but observed from Pixel number 2.

Region:	X Direction:	Y Direction:	Z Direction:
First 10 $\mu\text{m}$	17 %	65 %	18 %
From 10 $\mu\text{m}$ to 120 $\mu\text{m}$	17 %	82.5 %	0.5 %
From 120 $\mu\text{m}$ to 150 $\mu\text{m}$	5 %	41 %	54 %
Average	10 %	55 %	33 %

Table 5.1: Electron and Hole dynamic over the entire TIMESPOT sensor.

hole contribution.

**YZ section simulation** The second 2D model used to simulate sensor response is a YZ section of the TIMESPOT pixel. This approach was initially intended as an alternative to the complete 3D model device simulation, because the computing resources available to simulate charge drift and diffusion over an entire 3D model are limited. In fact, the current computing resources allow only to operate transient simulations for devices built up with a mesh grid of less than 2 million points. Every model with a number of mesh points beyond 2 million need more RAM than available. The choice to design this model is based on the analysis of the charge dynamics over the entire sensitive volume. The analysis is mainly based on the electric field, which defines the drift velocity. Applying an uniform mesh grid over the entire model, the analysis calculated the percentage of each electric field component related to the electric field amplitude. The result of this analysis showed that over the entire silicon pixel, 10 % of the motion is along the X direction, 55 % along Y and 35 % along Z. More in detail, the analysis showed that, for the region where the electrode faces each other, motion along the Z direction is negligible (< 1%) (table 5.1). Below 120  $\mu\text{m}$ , the Z component suddenly makes more than 50 % of the entire dynamics. Based on these facts, the designed YZ model is a good choice to simulate the sensor response in a symmetric position in the middle of the sensor. This model was used to simulate a total of 8 vertical, 4 inclined and 4 horizontal deposit (figure 5.30, 5.31 and 5.32). From all simulated signals it is possible to observe current signals with a charge collection time still below the 600 ps and a large current amplitude. Some of the simulated current signals were later reused to validate the TCoDe tool.

### 5.6.2 3D model simulation

A further step to improve sensor operation simulation is to use a complete 3D model of the TIMESPOT pixel instead of the 2D models used as approximations. This approach presents some difficulties related to the large amount of computing resources needed to run the simulation. The mesh strategy presented in the previous chapter must be extended in 3D models to the Z direction. This extension multiplies

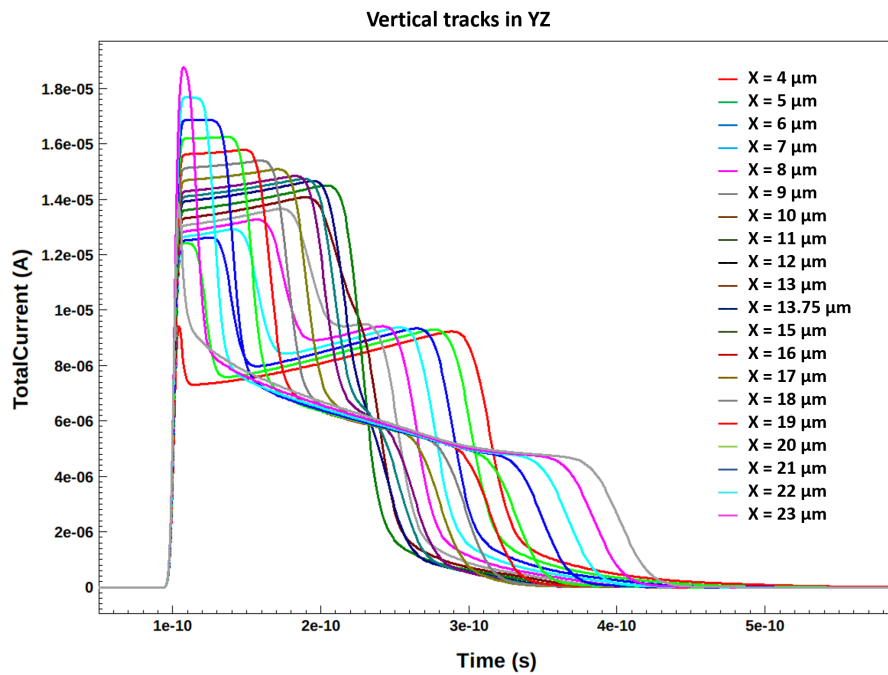


Figure 5.30: Current signals obtained by vertical energy deposits.

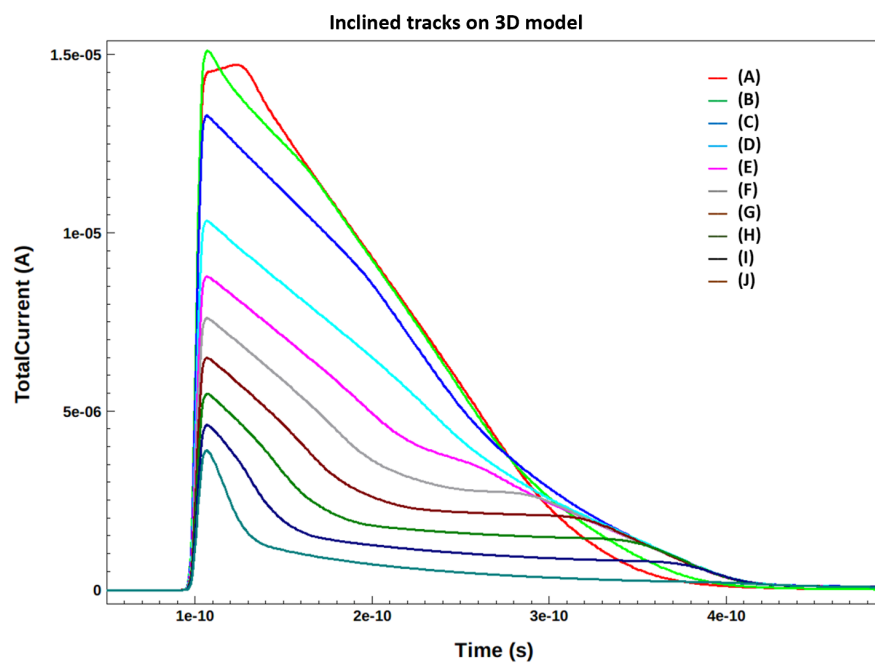


Figure 5.31: Current signals obtained by inclined energy deposits. Orientation is displayed in figure 5.33.

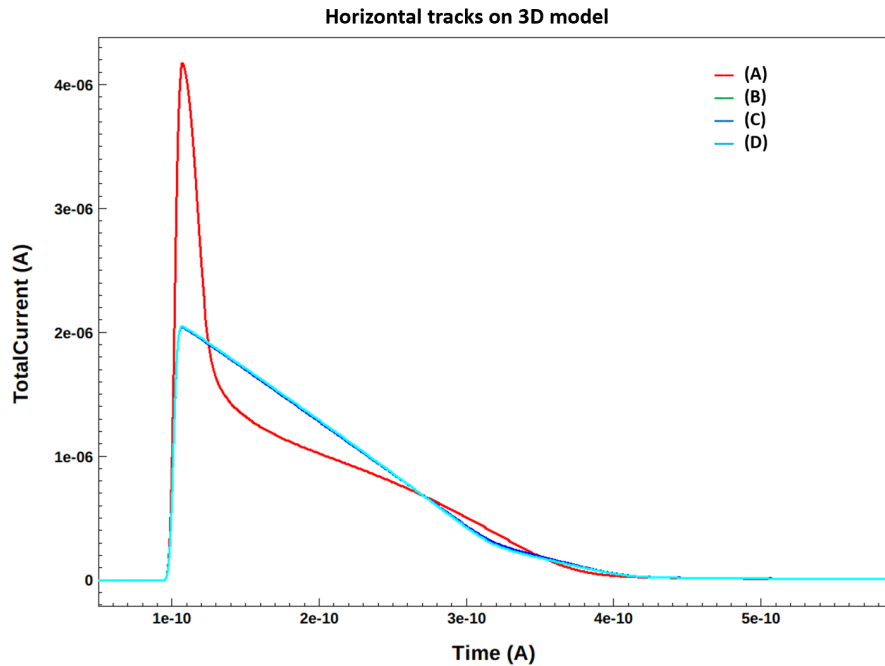


Figure 5.32: Current signals obtained by horizontal energy deposits. Orientation is displayed in figure 5.33

the number of grid points by a factor proportional to the number of fine mesh layers present in the Z direction. For example, the model displayed in figure 5.14 is described by a mesh grid with a total of 95000 points, 70 % of them only to define the drift path of the charges. Following the same approach applied on the 150  $\mu\text{m}$  thick TIMESPOT sensor, this means that, along the Z direction the mesh layers, described using a 100 nm small mesh grid, the total number of mesh points increases by a factor of 1500, reaching almost the 150 million mark. The available computing resources are not enough to simulate such a sensor, so some evaluations were done to understand if some energy deposits could be simulated.

The evaluation included vertical, horizontal and inclined energy deposits. Inclined energy deposits need an accurate mesh grid on all 3 directions, which means that they cannot be simulated. Horizontal energy deposits need only for the drift path less than 400000 points, so it should be possible to simulate them. Vertical tracks can not be simulated if the fine meshing is applied on all 3 directions, but it can be approximated if the fine meshed area includes only the X and Y direction, reducing considerably the mesh grid along Z. This approach presents some risks of false diffusion, especially along the bottom volume of the pixel where charge motion is dominated along Z but takes into account that most of the injected charge is present in the area where diode and resistive electrode face each other. For this simulation only 5 signals were simulated and displayed in figure 5.34. The overall computing limitations and needed computing time to obtain a result were too inefficient and



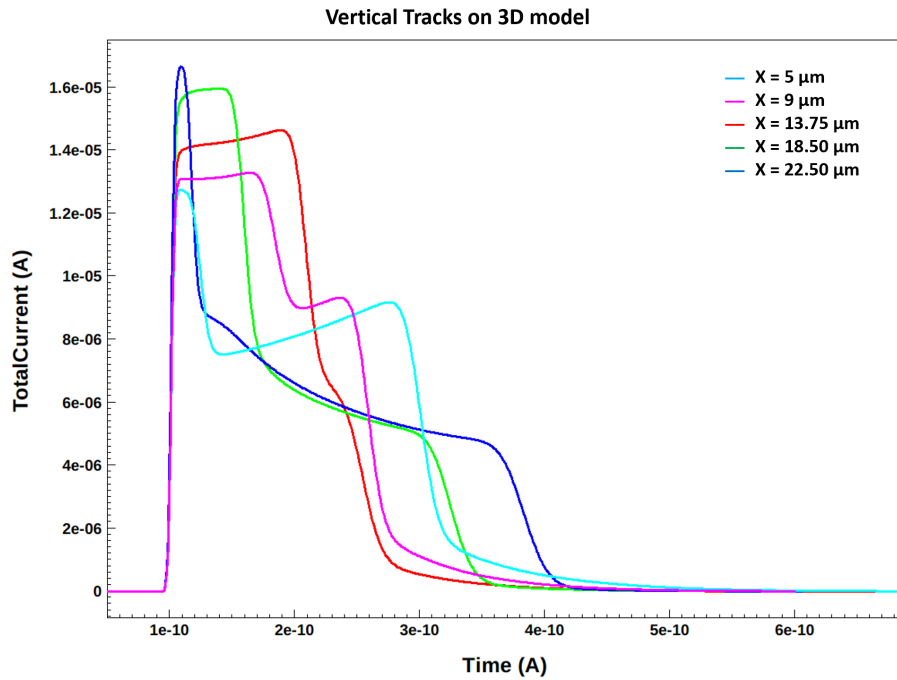


Figure 5.34: Current signals obtained by horizontal energy deposits from a complete 3D sensor model.

suggested to look for alternatives to simulate those signals in less time, holding same accuracy. TCoDe, which will be described in chapter 6, is intended to solve this computing issue without losing all the physical information get from the simulations done with TCAD.

**Effects on signal simulation using GEANT4 support** GEANT4 support on TCAD transient simulation was verified using 2D and 3D model simulation. Only one test deposits is presented, showing that the procedure to translate an energy deposit from GEANT4 to TCAD is possible. The deposit was generated (fig. 5.35) from the deposit shown previously in figure 5.7 and shows a special case with a higher energy delta ray. Its ionization along the silicon was 5 times higher than the pion and has the effect to increase twice as much the current signal amplitude.

### 5.6.3 Results obtained with TCoDe

The first application of TCoDe in TIMESPOT uses the sensor at a bias voltage of 100 V and a temperature of 300 K. In order to have a better coverage, both double half pixel and complete pixel model were used to collect sensor response.

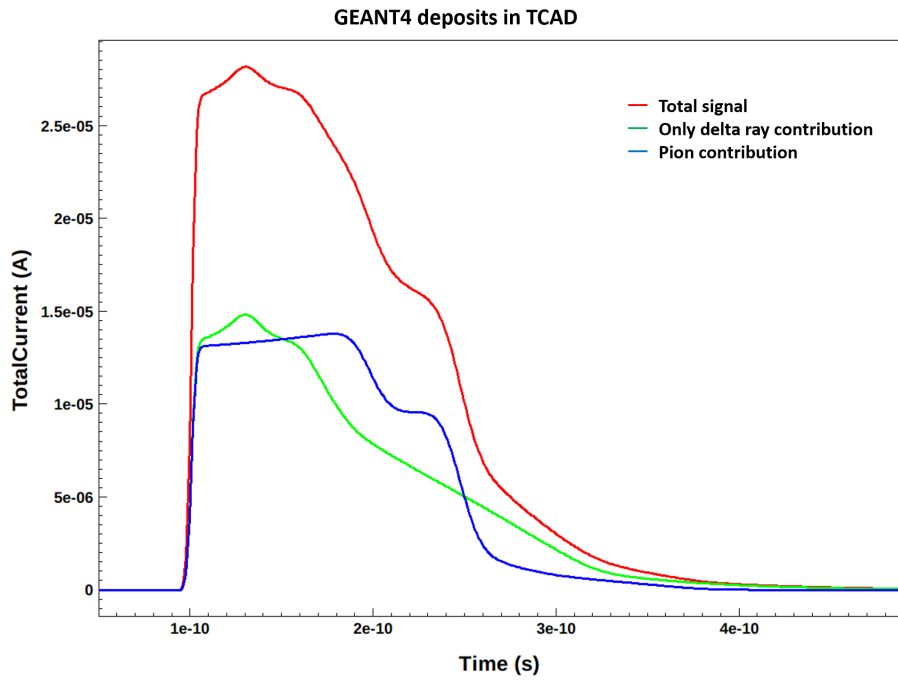


Figure 5.35: Current signal simulated using TCAD using a GEANT4 modeled energy deposit. The plots show total signal, pion and delta ray contribution.

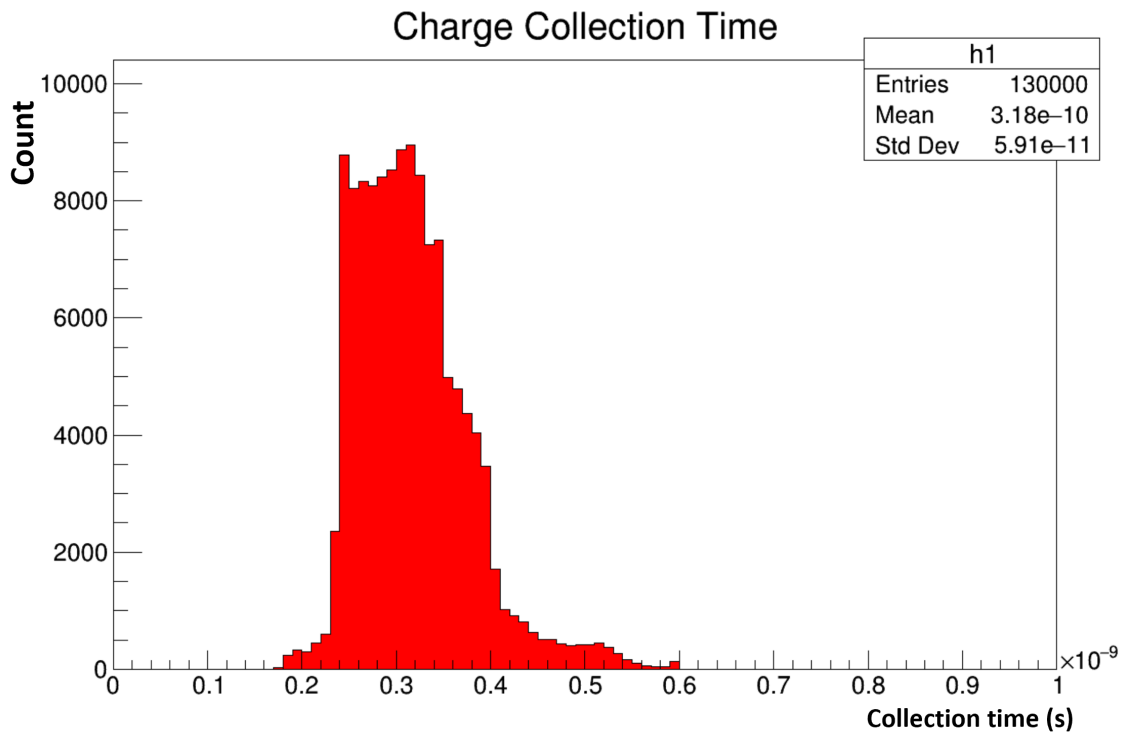


Figure 5.36: Charge collection time distribution over all the TIMESPOT sensor using TCoDe.

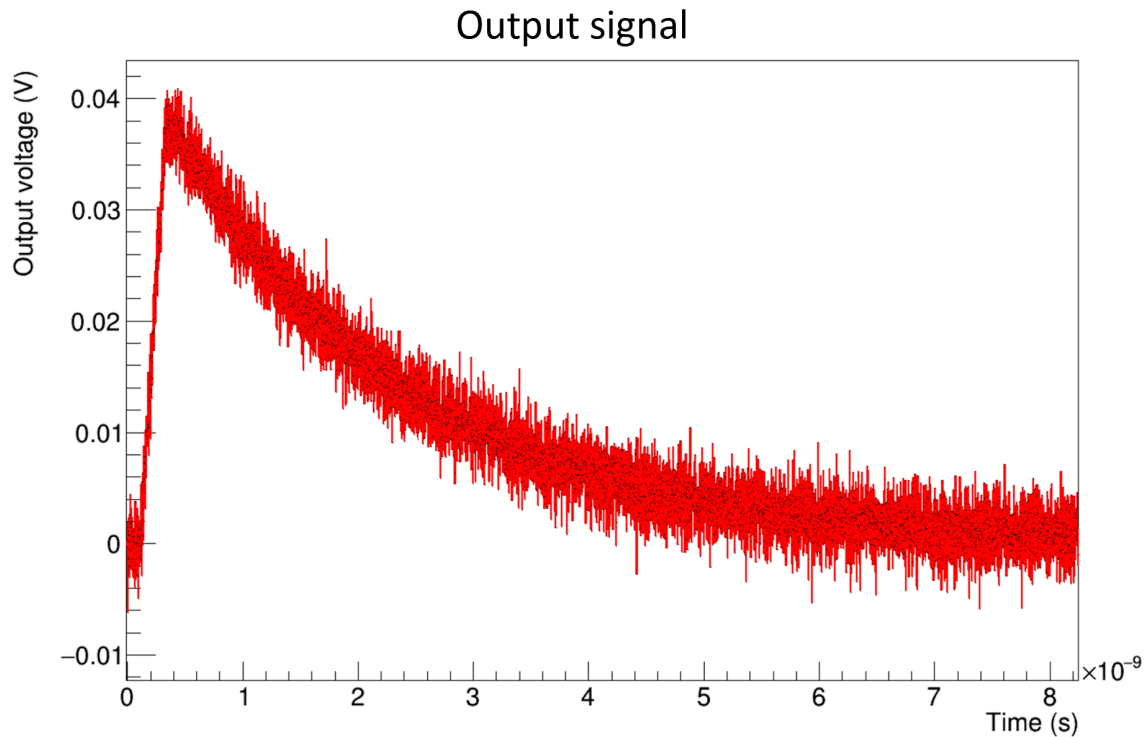


Figure 5.37: Simulated output signal from the readout board using TCoDe

Different simulations were considered. The simplest among them consisted in measuring the charge collection time distribution of small charge clusters positioned in a regular grid inside the entire volume. Charge collection time was then measured using a threshold set at 10 % from the amplitude. The result is shown in figure 5.36. The parallel wall sensor shows an average charge collection time of 318 ps. Most probable charge collection happens between 220 ps and 400 ps and is related to the volume between parallel electrode. The slower collections time beyond 400 ps is related to the bottom region of the sensor and the region between junction electrodes (which can be reduced by reducing the distance between them). The faster charge collection times below 220 ps are related to the deposits generated close to areas with high electric field, like the interface between the junction electrode and the p-spray layer.

A second and preliminary simulation series is currently ongoing in parallel to the first measurements (more details chapter 6). For this purpose, the transfer function (section 4.3 in [95]) of the main readout board used during the measurements has been implemented in TCoDe (together with its measured noise level) and approximately 126000 signals were simulated using GEANT4 energy deposits generated by shooting a 12 GeV pion against the pixel. The angle distribution of the produced pions is the same as for the observable events in LHCb.

The obtained voltage signals (Fig. 5.37) have an average amplitude of  $\sim 40$  mV and

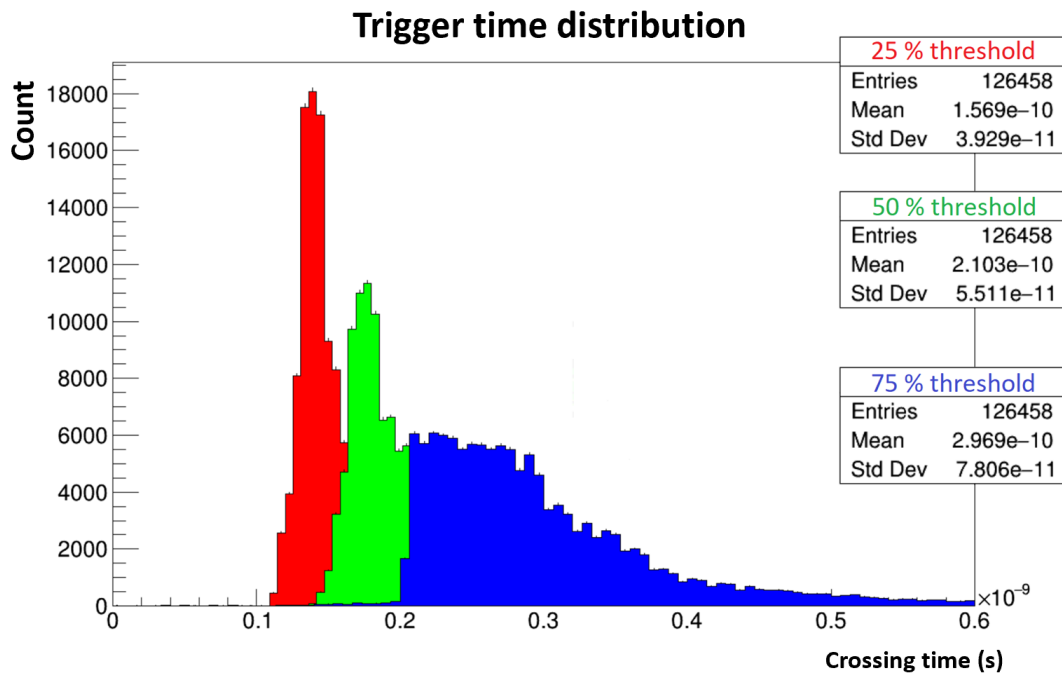


Figure 5.38: Trigger time distribution of the readout board with parallel trench sensor using TCoDe.

correspond to the signals measured from the board during the laser tests (chapter 7). A first simplified estimation of the timing performances was also done by implementing in TCoDe an equivalent Constant Fraction Discriminator. The simulation was repeated 3 times, using 3 different thresholds: 25 %, 50 % and 75 %. The obtained distribution shows the trigger time distribution for all 3 thresholds (Fig. 5.38). From a first preliminary analysis it seems that the sensor presents, in a CDF configuration, a better time resolution for lower thresholds. This behaviour has to be better understood and further analysis and simulations are currently ongoing.



# Chapter 6

## TCoDe

This chapter presents the TCoDe simulator, a new solid state sensor transient simulator developed with the purpose to extremely reduce simulation time and achieve in this way a large number of simulated signals. The chapter shows its main structure and the implemented algorithms. At the end of the chapter a first indirect validation of the program is presented, comparing its simulated current signals with reference signals obtained using Synopsys Sentaurus TCAD.

### 6.1 Motivations and general description

As outlined in chapter 5, TCAD transient simulations used to simulate sensor response present a main disadvantage due to the large computing resources and the time needed to run a single simulation. For example, running a TCAD model built up by almost one million points, a 600 ps long transient simulation takes in average 31 hours (Fig. 6.1). Since a detailed study of the timing performances of the sensor or a fine tuning of the front-end, needed before fabrication, requires a large number

	 SDE	 SDEVICE	 SDEVICE			
	Sensor construction	Electric field simulation	Transient simulation			
		voltage	init	point		
1				[n5]: 97966, sec		
2	[n1]: 2239, sec	[n2]: --	[n3]: 12521, sec	[n4]: --	[n12]: --	[n13]: 96093, sec
3						[n14]: 95504, sec
4						[n15]: 109201, sec

Figure 6.1: Simulation flow of a sentaurus TCAD project used to simulate vertical energy deposits on a 3D model built up by 985000 mesh vertexes. Average time to complete a transient simulation is approximately 31 hours (last column).

of those transient simulations to be performed using TCAD for this kind of application is un-practical. Therefore, a dedicated software, the TIMESPOT Code for Detector simulation (TCoDe), is currently under development. TCoDe is a C++ 14 based tool, which runs on top of the HYDRA Multithreaded Data Analysis Framework [96], capable of running transient simulation of solid-state sensors in very short time thanks to its simplified computing structure and multithread capabilities which allow it to run on different CPU- and GPU-based systems using OpenMP [97], TBB [98] and CUDA back-ends [99].

The idea behind the current version of TCoDe is that the tool just computes the required transient simulations using all available information obtained from other tools previously used to simulate all stationary physical quantities of the sensor over all its volume like the electric field or charge mobility. For example, TCoDe used within the TIMESPOT collaboration uses physical maps computed with sentaurus TCAD and energy deposits simulated with GEANT4. The only physics that TCoDe provides is the charge motion and current induction on the readout electrode. This allows to change from the slow computing TCAD to the fast computing TCoDe without the need to recompute and remodel everything done before with TCAD.

At the moment TCoDe is on its first alpha release [100] and mainly set to work within the requested applications of the TIMESPOT project, but future extensions and improvements are already under idealization to transform TCoDe in a complete detector simulator system.

## 6.2 Program structure

TCoDe, on its current configuration, is divided up into two main computing blocks, the system configuration and the simulation block. During the configuration, TCoDe uploads all information needed to run the simulation, builds the energy deposit in the sensor as an equivalent electron-hole pair distribution in space and sets the time step and the transient length. After the configuration phase, the transient simulation takes place and saves all generated data (Fig. 6.2).

### 6.2.1 Configuration

**Physics maps** Most of the configuration phase is focused on uploading the physics maps. TCoDe needs 4 maps for a simulation:

- Electric field map
- Weighting field map
- Electron and hole mobility maps

Electric field and mobility maps must be previously simulated at the same bias voltage and temperature and are needed to compute charge motion. The weighting

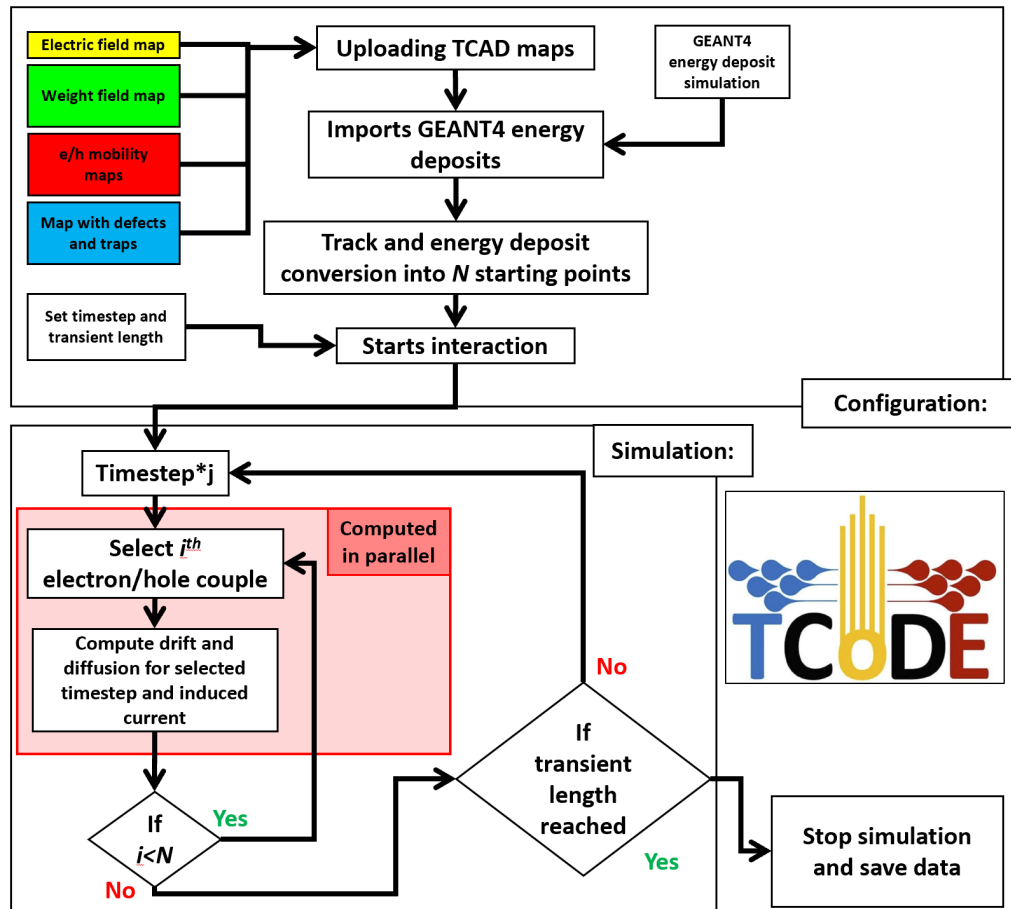


Figure 6.2: TCoDe Simulation flow and symbol.

field is needed to calculate current induction on the electrodes. TCoDe is very adaptable and allows to add other maps in TCoDe which contain other physical information, like the distribution in space of charge traps or defects, for more specific simulations like sensor response in function of the radiation damage or the inclusion of defects in the semiconductor lattice. Maps can be uploaded in \*.cvs or \*.txt format and their format is by default settings a 6 column file containing all the coordinates of the mesh vertex (first 3 columns) and the components of the physical quantity (last 3 columns). There is also a possibility to include other 2 columns which include the material and the region of the sensor where the point is positioned. In this way it is possible to highlight signal formation in potentially critical areas/material.

**Energy deposits and geometrical reconstruction** Energy deposit construction is one of TCoDe's most important features. Like Weightfield2 [101] or Allpix<sup>2</sup> [102] the energy deposit is defined as a distribution in space of electron hole pairs represented as point-like particles instead of a charge density in space like TCAD. This

approach allows to focus the computing resources only on the motion of the charges. Each charge motion is computed in a separate thread (either in CPU or GPU).

Compared to this approach, the computation of charges represented in space as continuous distribution would mean that the Poisson and continuous equation must be computed for every time step overall the entire volume. The volume, which is described by a grid, is defined by a large number of points. Solving the equation means that the calculation must be performed on every single point for every single time step. For a  $55 \times 55 \times 150 \mu m^3$  large model, the number of grid point is in the order of one million. The average number of electron-hole pairs generated by a minimum ionizing particle over a distance of  $150 \mu m$  is only 12000.

TCoDe is able to generate its own energy deposit or import it from other tools like GEANT4. Its intrinsic energy deposit generator is very simplified and allows to generate only linear deposits and including Landau fluctuations of the released energy. This deposit is generally used for more practical purposes. For realistic energy deposits an input from an external Monte Carlo, like GEANT4 is needed.

In both cases the construction of the deposit in space follows the same approach: The input parameters needed by TCoDe for an energy deposit  $E_{dep}$  released along a straight path of length  $l$  are the start and end point of the ionization path  $((X_i; Y_i; Z_i)$  and  $(X_f; Y_f; Z_f))$ , the energy deposit  $E_{dep}$ , the dispersion of the charges at the beginning  $\alpha_i$  and end  $\alpha_f$  of the path. Also a particle identification number  $P_{ID}$  can be added in order to discriminate later signal contribution from secondary particles like delta rays.

The charge distribution is defined by converting the energy deposit along the track into an equivalent number of electron-hole pairs  $N_{max}$ . This operation is done by simply dividing the energy deposit by the average energy needed to generate an electron hole pair which, in case of silicon, is equal to 3.6 eV. The number is then used to place all  $N_{max}$  points along the ionization track using parametric equations of line in 3D space:

$$\begin{cases} x(t) = X_i + (X_f - X_i)t + \sigma_x \\ y(t) = Y_i + (Y_f - Y_i)t + \sigma_y \\ z(t) = Z_i + (Z_f - Z_i)t + \sigma_z \end{cases} \quad with \quad \begin{cases} t \in [0; 1] \\ t = i/N_{max} \\ i \in [0, 1, \dots, N_{max}] \end{cases} \quad (6.1)$$

With  $(X_i; Y_i; Z_i)$  and  $(X_f; Y_f; Z_f)$  the begin and end of the ionization track and  $t$  the line parameter which is calculated with reference to  $N_{max}$ .  $\sigma_{x,y,z}$  describe the radial charge distribution orthogonal to the ionization path. The computation of  $\sigma_{x,y,z}$  follows few steps. The first defines the maximum vertical distance from the ionization path where the charges are generated and the shape of this distribution, which can be set as Gaussian, Exponential or uniform:

$$disp \in [-\alpha; \alpha] \quad disp = \alpha \exp(-|b|) \quad disp = \alpha \exp\left(-\frac{b^2}{2\alpha}\right) \quad (6.2)$$

Where  $\alpha$  is the maximum distance from the ionization track (parameter must be set during configuration phase) and  $b \geq 0$  generated with a random number generator

with uniform distribution.  $\alpha$  can change along the ionization path with a linear shape by simply applying the same formula used in equation 6.1:

$$\left\{ \alpha = \alpha_i + (\alpha_f - \alpha_i)t \quad \text{With} \quad \begin{cases} t \in [0; 1] \\ t = i/N_{max} \\ i \in [0, 1, \dots, N_{max}] \end{cases} \right. \quad (6.3)$$

The dispersion parameter is then oriented randomly in space around the origin of the coordinate system with angles  $\theta$   $\phi$ , using the following rotation:

$$\vec{r}_{disp} = \begin{cases} disp_x = disp \times \sin \theta \cos \phi \\ disp_y = disp \times \sin \theta \sin \phi \\ disp_z = disp \times \cos \theta \end{cases} \quad \text{With} \quad \begin{cases} \theta \in [0; 2\pi] \\ \phi \in [-\frac{\pi}{2}; \frac{\pi}{2}] \end{cases} \quad (6.4)$$

The obtained vector  $\vec{r}_{disp}$  needs now to be rotated with a random angle  $\gamma$  vertically around the direction of the ionization track  $(u_x; u_y; u_z)$ .

$$\begin{pmatrix} \sigma_x \\ \sigma_y \\ \sigma_z \end{pmatrix} = \begin{pmatrix} \cos \gamma + u_x^2 A & u_x u_y A - u_z \sin \gamma & u_x u_z A - u_y \sin \gamma \\ u_x u_y A + u_z \sin \gamma & \cos \gamma + u_y^2 A & u_y u_z A - u_x \sin \gamma \\ u_z u_x A + u_y \sin \gamma & u_z u_y A + u_x \sin \gamma & \cos \gamma + u_z^2 A \end{pmatrix} \times \begin{pmatrix} disp_x \\ disp_y \\ disp_z \end{pmatrix} \quad (6.5)$$

With  $A = (1 - \cos \gamma)$  and  $\gamma$  generated randomly between  $[0; 2\pi]$ . This method allows to obtain different energy deposits in space in any possible shape and dimension (Fig. 6.3). This feature is important especially if the effects of large ionized areas needs to be simulated. This algorithm allows to produce all kinds of energy deposits, from the simplest deposit generated by a minimum ionizing particle to larger deposits generated by infrared laser.

If the deposit is more elaborate and includes ionization paths with different directions and forms, the approach remains the same and TCoDe provides a construction of the deposit ionization path after ionization path. For more elaborated deposits defined by curved paths, TCoDe is able to approximate them into a composition of small linear segments, which are processed one after the other.

For energy deposits imported from other tools the approach remains the same. It can be that the way the energy deposit is represented on the other tool needs to be converted in a different way but this is up to the user. An example of how energy deposits simulated from external tools is converted in TCoDe is shown in figure 6.4. It can be seen that, the deposits generated by the pion and the delta ray are well reproduced in shape. The distribution along the path is kept constant in order to better highlight the ionization path.

**TCoDe Drift and Diffusion Model** Charge drift and diffusion are the only physical processes implemented in TCoDe. Their computation follows a similar approach as presented in [103] by computing separately both quantities and adding their effects only at the end of the time step.

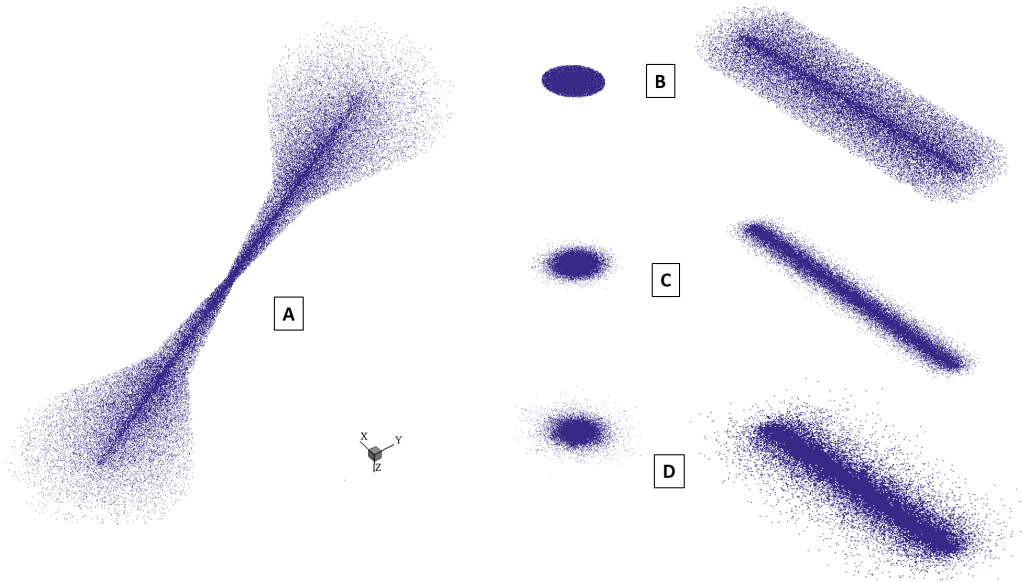


Figure 6.3: Different Examples of customized energy deposits. (A): Energy deposit with the form of a cone. (B), (C) and (D): Different dispersion shapes of the charges with respect to the track. (B) uniform, (C) Gaussian and (D) exponential.

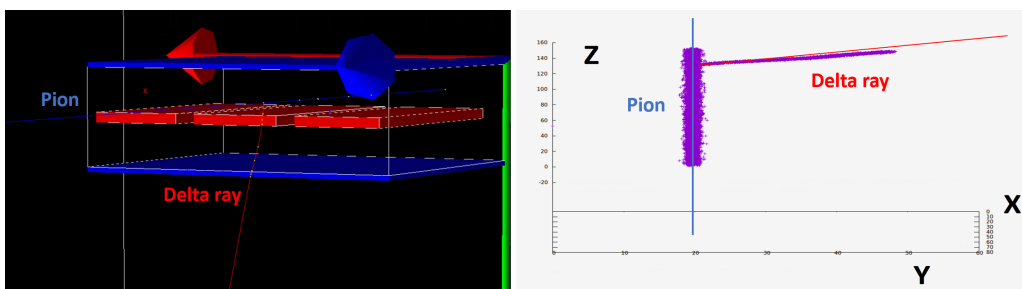


Figure 6.4: Energy deposit generated with GEANT4 (left) and its conversion in electron-holes using TCoDe (right).

**Diffusion:** Diffusion is defined by the diffusion coefficient  $D$  which depends on the temperature of the silicon.

$$D = \frac{k_B T}{e} \mu_{e,h} \quad (6.6)$$

Where  $k_B$  is the Boltzmann constant and  $\mu_{e,h}$  are the electron (hole) mobility which is directly taken from the mobility maps. For a time step  $\Delta t$  the path traveled by the charge is equal to

$$\sigma_{diff} = \sqrt{2D\Delta t} \quad (6.7)$$

Diffusion direction is a completely random process and for every time step its direction and distance varies randomly. In order to include this aspect in the simulation,  $\sigma_{diff}$  is computed as the variance of a random number generator with Gaussian distribution with mean value 0. This allows to compute for every  $\Delta t$  a random drift distance within the desired distribution. The orientation of the diffusion step is also randomly computed by rotating the vector of length  $\sigma_{diff}$  around the origin with an angle  $theta$  and  $\phi$ .

$$\delta \vec{r}_{diff} = \begin{pmatrix} X_{diff} \\ Y_{diff} \\ Z_{diff} \end{pmatrix} = \begin{pmatrix} \cos(\phi)\sin\theta & -\sin(\phi) & -\cos(\phi)\sin\theta \\ \sin(\phi)\cos\theta & \cos(\phi) & -\sin(\phi)\cos\theta \\ \sin(\theta) & 0 & \cos\theta \end{pmatrix} \times \begin{pmatrix} \sigma_{diff} \\ \sigma_{diff} \\ \sigma_{diff} \end{pmatrix} \quad (6.8)$$

With  $\theta$  and  $\phi$  randomly generated angles between  $[-\pi, \pi]$  and  $[0, 2\pi]$  respectively.

**Charge drift** Charge drift is computed by solving the following differential equation which describes charge motion in semiconductors under effects of an electric field:

$$\frac{\delta \vec{r}_d}{\delta t} = \mu \vec{E} \quad (6.9)$$

As integration method the Runge Kutta 4th order algorithm [104] [105] was implemented. The algorithm computes for the time step  $N$  the drift motion step  $\vec{r}_{dN+1}$ .

$$\vec{r}_{dN+1} = \vec{r}_{dN} + \frac{\Delta t}{6} (k_1 + 2(k_2 + k_3) + k_4) \quad (6.10)$$

With  $k_{1,2,3,4}$  the Runge Kutta parameters, which are:

$$\begin{cases} \vec{k}_1 = \mu_{e,h}(t_n, \vec{r}_{dN}) \vec{E}(t_n, \vec{r}_{dN}) \\ \vec{k}_2 = \mu_{e,h}(t_n + \frac{t_{step}}{2}, \vec{r}_{dN} + \frac{1}{2} \vec{k}_1 t_{step}) \vec{E}(t_n + \frac{t_{step}}{2}, \vec{r}_{dN} + \frac{1}{2} \vec{k}_1 t_{step}) \\ \vec{k}_3 = \mu_{e,h}(t_n + \frac{t_{step}}{2}, \vec{r}_{dN} + \frac{1}{2} \vec{k}_2 t_{step}) \vec{E}(t_n + \frac{t_{step}}{2}, \vec{r}_{dN} + \frac{1}{2} \vec{k}_2 t_{step}) \\ \vec{k}_4 = \mu_{e,h}(t_n + \frac{t_{step}}{2}, \vec{r}_{dN} + \frac{1}{2} \vec{k}_3 t_{step}) \vec{E}(t_n + \frac{t_{step}}{2}, \vec{r}_{dN} + \frac{1}{2} \vec{k}_3 t_{step}) \end{cases} \quad (6.11)$$

The electric field  $\vec{E}$  and mobility  $\mu_{e,h}$  are extracted from the imported physics maps. At the end of the computing step,  $\vec{r}_{dN+1}$  and  $r_{diffN+1}$  are added together, getting the distance travelled by the charge:

$$\vec{r}_{N+1} = \vec{r}_{dN+1} + r_{diffN+1} \quad (6.12)$$

**Current induction:** Current induction is calculated by applying the Ramo theorem, presented previously in chapter 2.

$$i_{e,h} = q_{e,h}(v_{x_{e,h}}E_{w_x} + v_{y_{e,h}}E_{w_y} + v_{z_{e,h}}E_{w_z}) \quad (6.13)$$

The contribution of every single charge is added at the end of every single time step and saved on the output file. In default settings the output includes the time step, the total induced current in time and integrated charge in time. It is also possible to save the contributions of the electrons and holes separate as well as the charge generated by primary and secondary particles. In this way it is possible to analyze the contribution of electrons and holes separately or the contribution from deposits generated by primary or secondary particles. Moreover it is possible to save the drift path of every single charge and use the data to visualise the entire process (Fig. 6.5).

## 6.3 Validation, Performance

TCoDe output must be validated before starting to use it for sensor design and optimisation. There are mainly two ways to validate it. A first indirect validation which consists in comparing with an already validated tool the current signal simulated with an identical energy deposit. The best available tool to perform this comparison is Synopsys Sentaurus TCAD. The second approach is an experimental validation, however, this will be possible only once the devices, designed by means of the use of TCoDe, will be available from production.

### 6.3.1 Performance

Performance of TCoDe simulation compared against TCAD simulation. Unfortunately due to the management of the computing resources, TCAD and TCoDe run on different computers:

1. TCAD: Workstation with 4 CPUs with 6 cores each (model Intel(R) Xeon(R) CPU E5645) and a maximum of 24 independent threads. RAM memory is 48 GB and main storage is a 2 TB mechanic hard disk drive. TCAD simulations themselves run in CPU-multithread with a maximum of 20 threads.
2. TCoDe in single thread: TCoDe runs on a PC with weaker resources with just 2 CPUs with 4 cores each (model Intel(R) Xeon(R) CPU X5450) with 8 independent threads. RAM memory is 10 GB large and main storage has the same characteristics as the TCAD PC.
3. TCoDe in multithread mode: Laptop with a 8 core CPU (model Intel(R) Core(TM) i7 7700HQ CPU), 16 GB of RAM 512 GB of SSD and a graphic card NVIDIA Geforce GTX 1050 (768 CUDA cores, 3GB GDDR5 at 1.5 GHz).

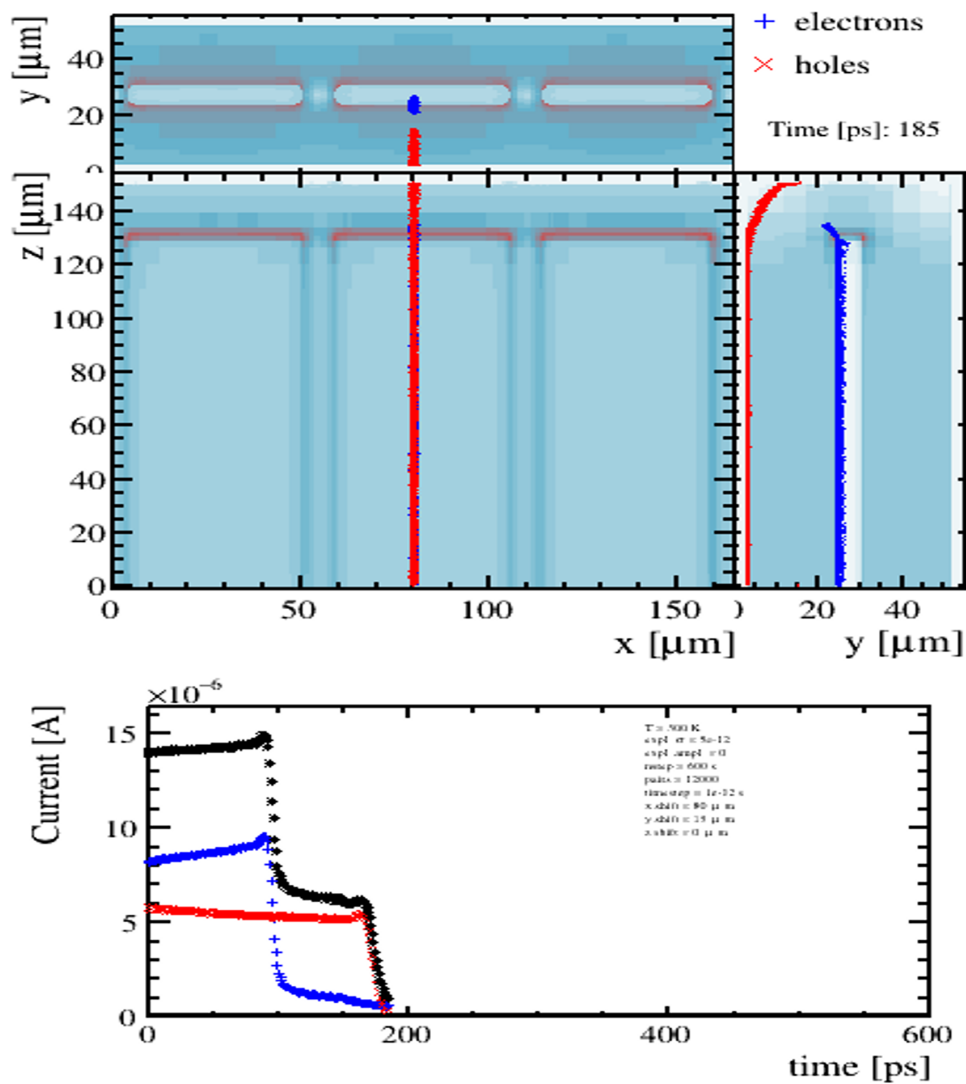


Figure 6.5: Frame of a .gif animation reproduced using TCoDe. The upper part of the animation displays charge motion (red are hole, blue are electrons) inside the electric field (in this case a 3 pixel model). The lower plot shows the evolution in time of the current signal.

TCAD	TCoDe (single thread)	TCoDe (GPU multithread)
113234 s	11 s	543 ms

Table 6.1: TCAD vs TCoDe simulation speed comparison.

On a hardware point of view the workstation used to run TCAD presents a definitely higher benchmark than the other two PCs.

**Comparison** Simulations with same energy deposit were computed using all 3 systems. The simulated scenario uses the TIMESPOT 3D silicon sensor and simulated sensor response from a vertically applied energy deposit of approximately 2 fC (12000 electron-hole pairs). A transient simulation with a duration of 600 ps was set to simulate charge collection and signal formation. Results are displayed in table 6.1. In this test TCoDe resulted to be almost 11000 times faster in single thread mode than TCAD. Computing in GPU multithread even increased this gap.

### 6.3.2 Tool validation using TCAD

The tool validation was performed on a software level comparing TCoDe output signals with TCAD output signals generated by the same energy deposit. The idea behind this approach is that a comparison with a widely used software can be considered a validation.

For the validation a 3D model of a planar sensor was designed on purpose. To enhance further the validation, the TIMESPOT 3D-silicon sensor was later used to confirm the correct operation of the TCoDe.

**Planar sensor** The designed planar sensor is a simple  $5 \times 5 \times 10 \mu\text{m}^3$  large PN-junction. The model is divided in 3 main areas, a low doped p- bulk, which works as active area, and two highly doped layers at the top and bottom surface, one p++ and one n++ doped layer which works as sensor electrode (Fig. 6.6). The small dimension of the sensor are needed to define the sensor model with an enough dense mesh grid (following the mesh criteria defined in chapter 5) and a larger model could exceed the requested computing resources. A total of 7 signals were simulated. One vertical, one horizontal and 5 inclined tracks (Fig. 6.7-6.11). All deposits are then compared in order to qualitatively evaluate the differences in the signal shapes.

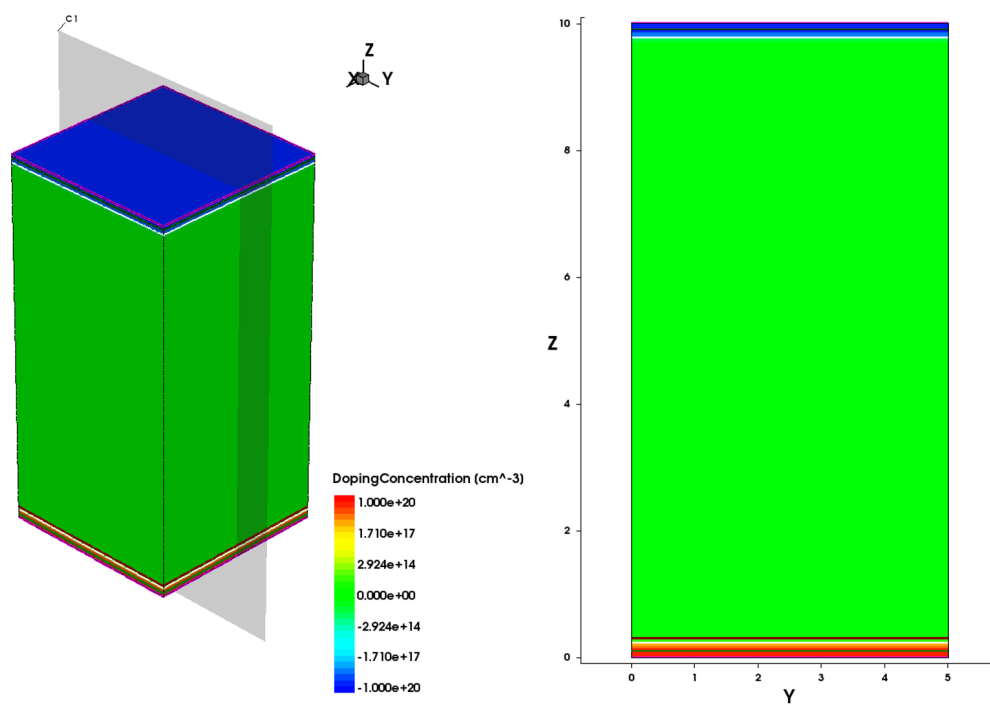


Figure 6.6: PN-junction used as reference sensor for the TCoDe validation. 3D model (left) and cut through Y direction (right).

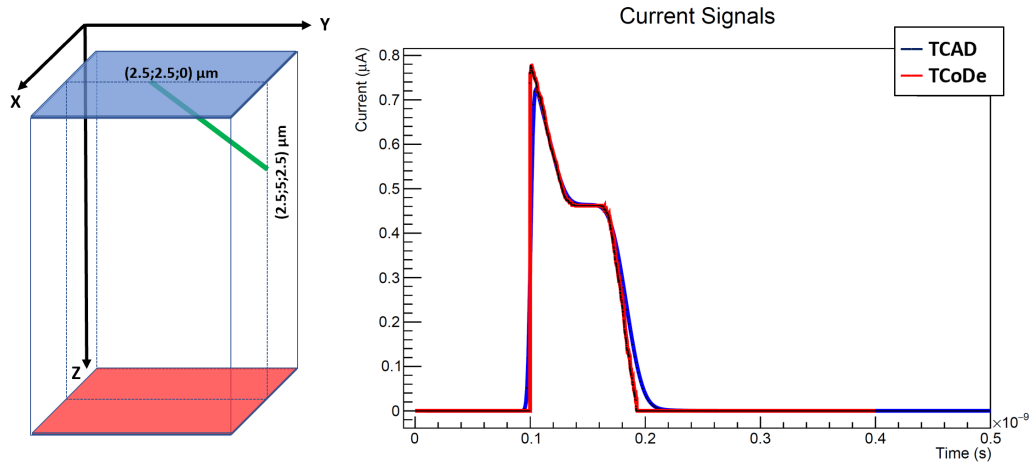


Figure 6.7: First energy deposit simulated with TCoDe and TCAD and then compared. Left: Position of the deposit inside of the sensor. Right: Comparison between the obtained current signals.

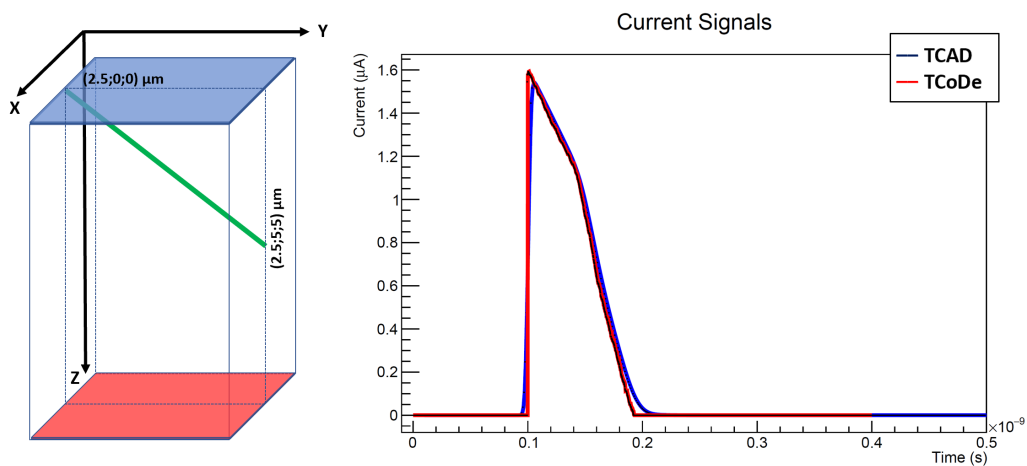


Figure 6.8: Second energy deposit simulated with TCoDe and TCAD and then compared. Left: Position of the deposit inside of the sensor. Right: Comparison between the obtained current signals.

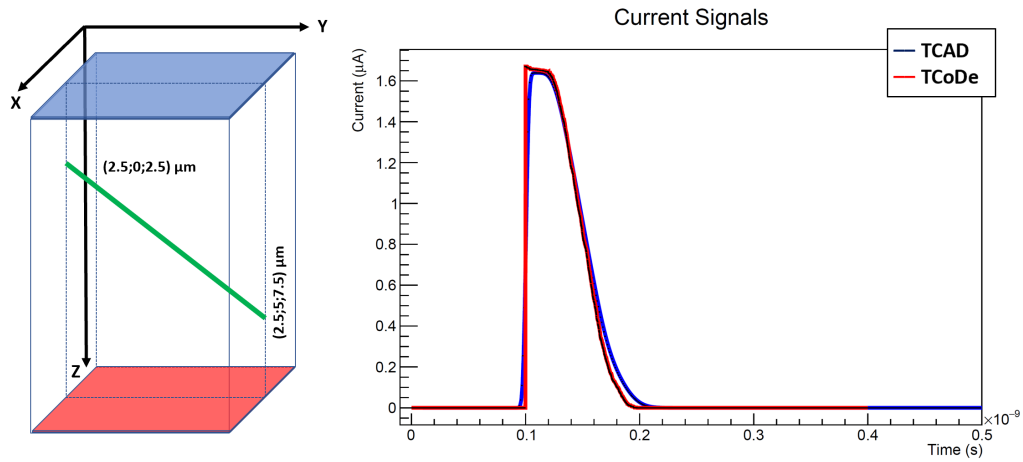


Figure 6.9: Third energy deposit simulated with TCoDe and TCAD and then compared. Left: Position of the deposit inside of the sensor. Right: Comparison between the obtained current signals.

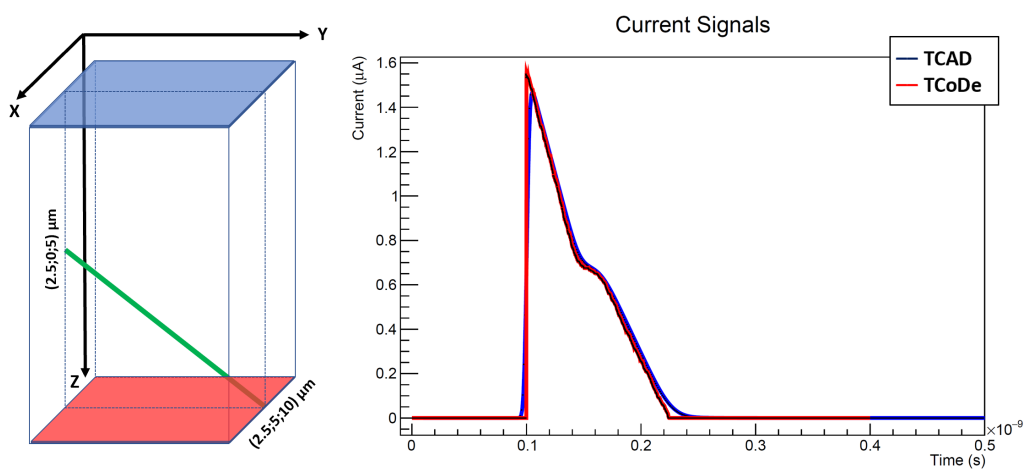


Figure 6.10: Fourth energy deposit simulated with TCoDe and TCAD and then compared. Left: Position of the deposit inside of the sensor. Right: Comparison between the obtained current signals.

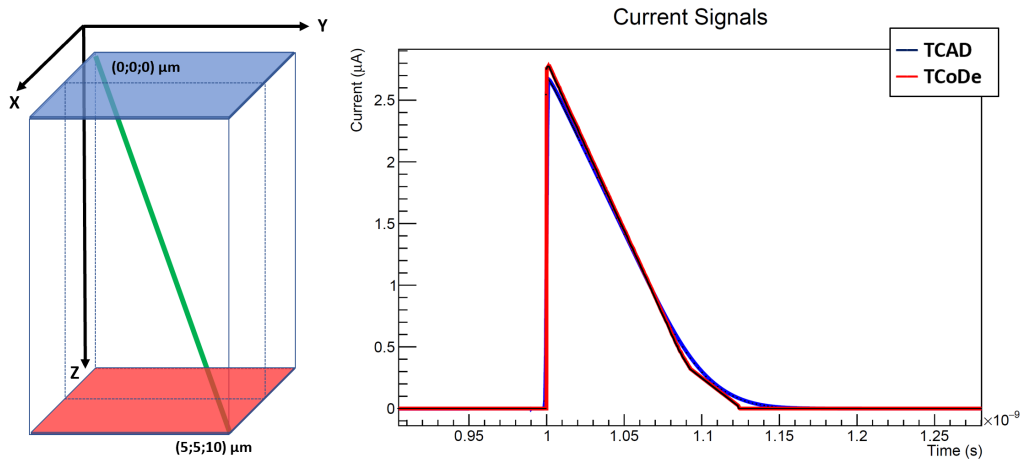


Figure 6.11: Fifth energy deposit simulated with TCoDe and TCAD and then compared. Left: Position of the deposit inside of the sensor. Right: Comparison between the obtained current signals.

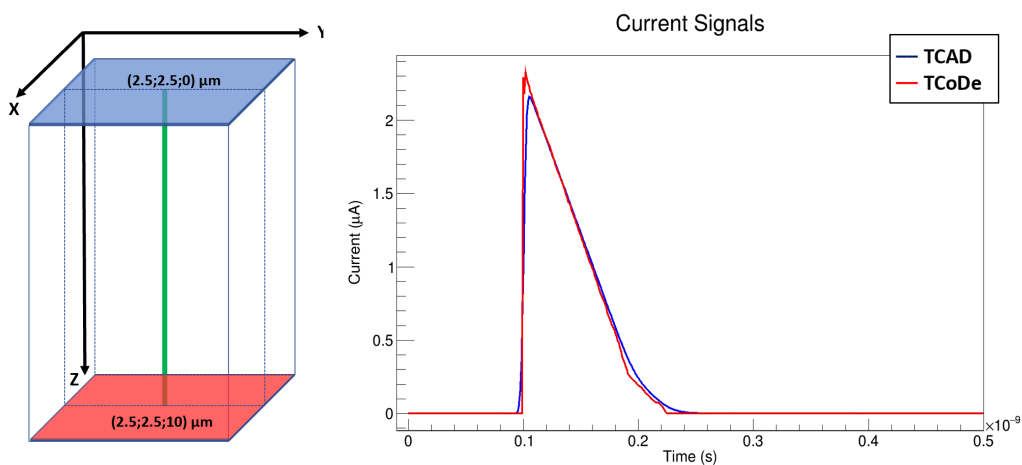


Figure 6.12: Vertical energy deposit simulated with TCoDe and TCAD and then compared. Left: Position of the deposit inside of the sensor. Right: Comparison between the obtained current signals.

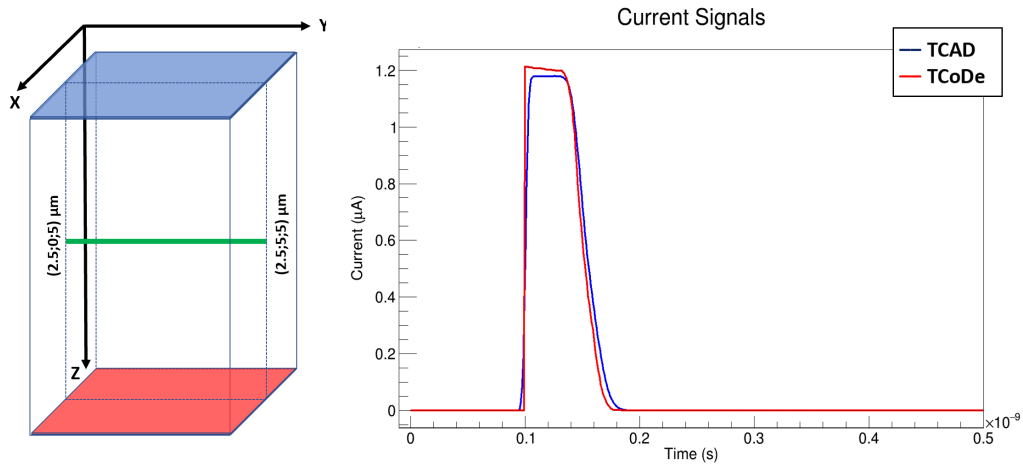


Figure 6.13: Horizontal energy deposit simulated with TCoDe and TCAD and then compared. Left: Position of the deposit inside of the sensor. Right: Comparison between the obtained current signals.

**TIMESPOT sensor** A second series of comparisons between TCoDe and TCAD simulated current signals used a 3D model of the TIMESPOT 3D-silicon sensor. In this case the simulated signals were in total 7, with 5 at different Y and 2 inclined energy deposits. The plots, presented in figure 6.14-6.18, confirm the validity of the TCoDe approach.

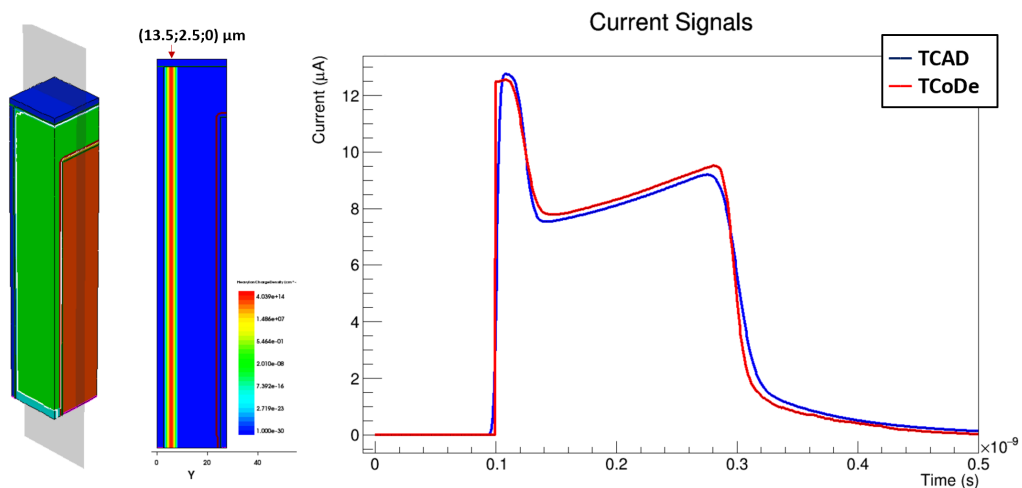


Figure 6.14: Vertical energy deposit simulated with TCoDe and TCAD on the TIMESPOT silicol sensor and then compared. Left: Position of the deposit inside of the sensor (TCAD model). Right: Comparison of the current signals.

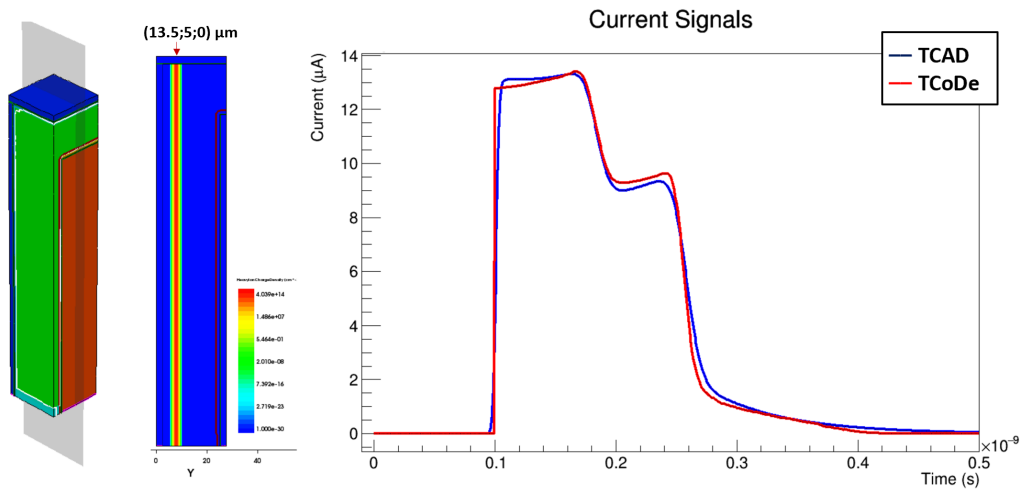


Figure 6.15: Vertical energy deposit simulated with TCoDe and TCAD on the TIMESPOT silicid sensor and then compared. Left: Position of the deposit inside of the sensor (TCAD model). Right: Comparison of the current signals.

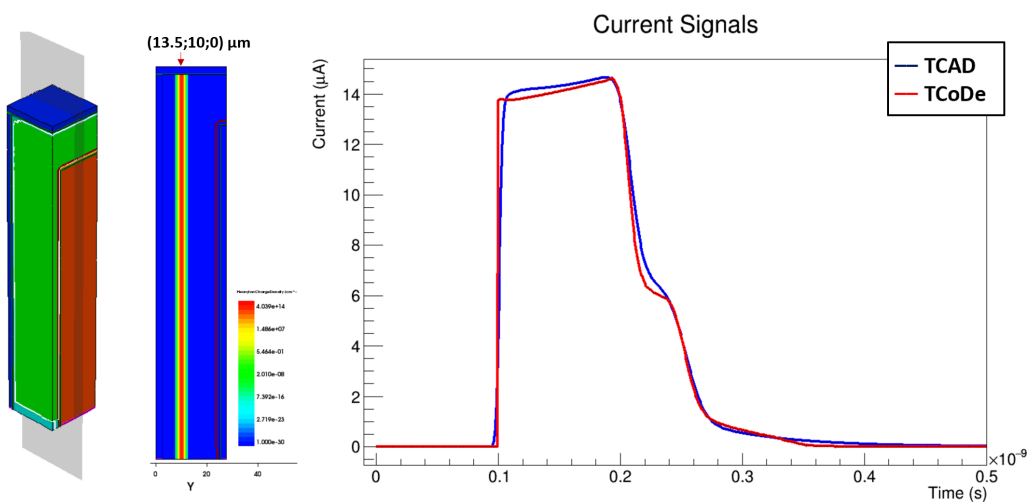


Figure 6.16: Vertical energy deposit simulated with TCoDe and TCAD on the TIMESPOT silicid sensor and then compared. Left: Position of the deposit inside of the sensor (TCAD model). Right: Comparison of the current signals.

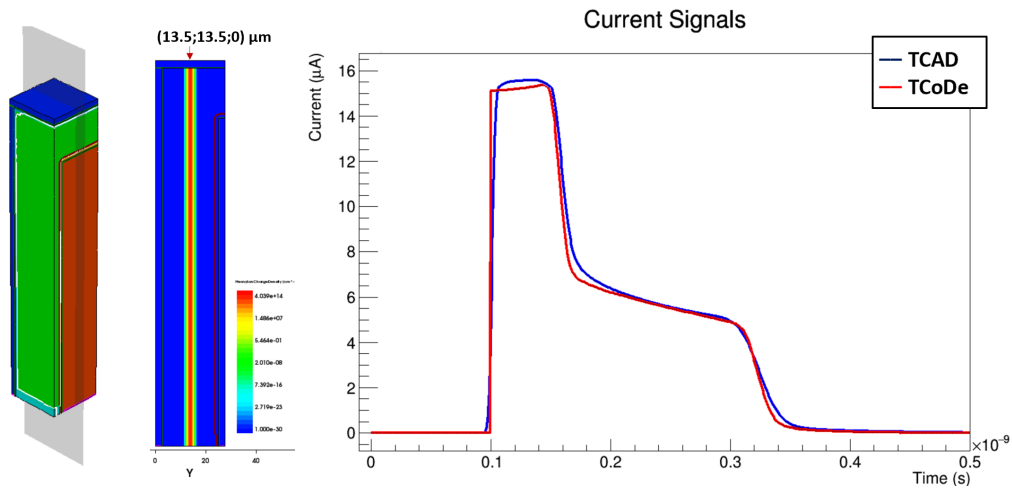


Figure 6.17: Vertical energy deposit simulated with TCoDe and TCAD on the TIMESPOT silicid sensor and then compared. Left: Position of the deposit inside of the sensor (TCAD model). Right: Comparison of the current signals.

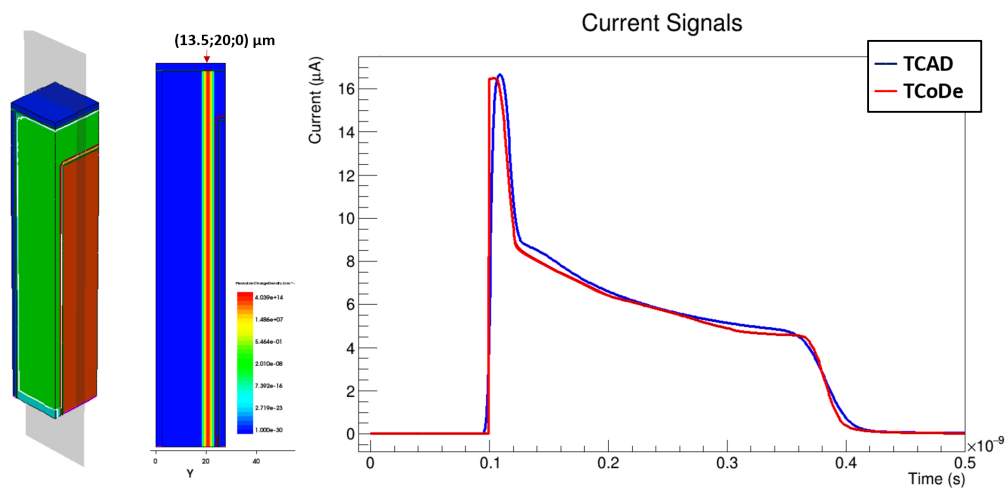


Figure 6.18: Vertical energy deposit simulated with TCoDe and TCAD on the TIMESPOT silicid sensor and then compared. Left: Position of the deposit inside of the sensor (TCAD model). Right: Comparison of the current signals.

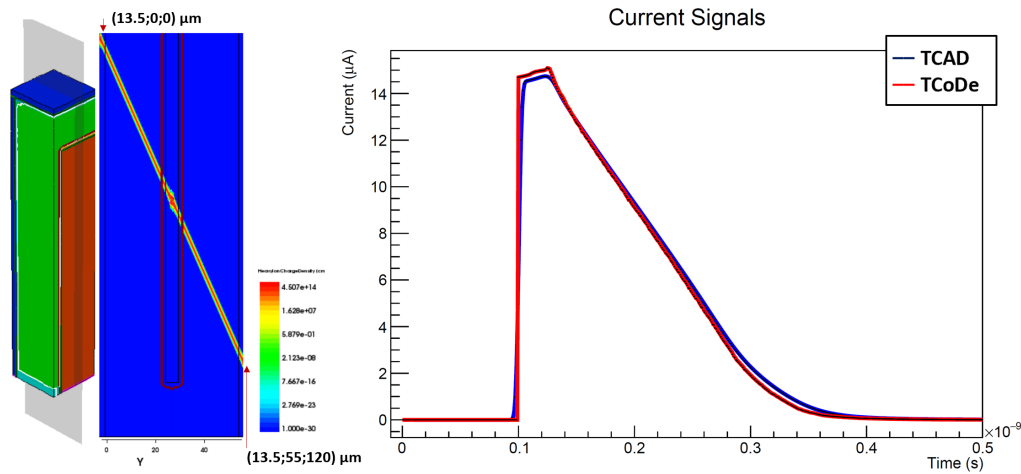


Figure 6.19: Inclined energy deposit simulated with TCoDe and TCAD on the TIMESPOT silicon sensor and then compared. Left: Position of the deposit inside of the sensor (TCAD model). Right: Comparison of the current signals.

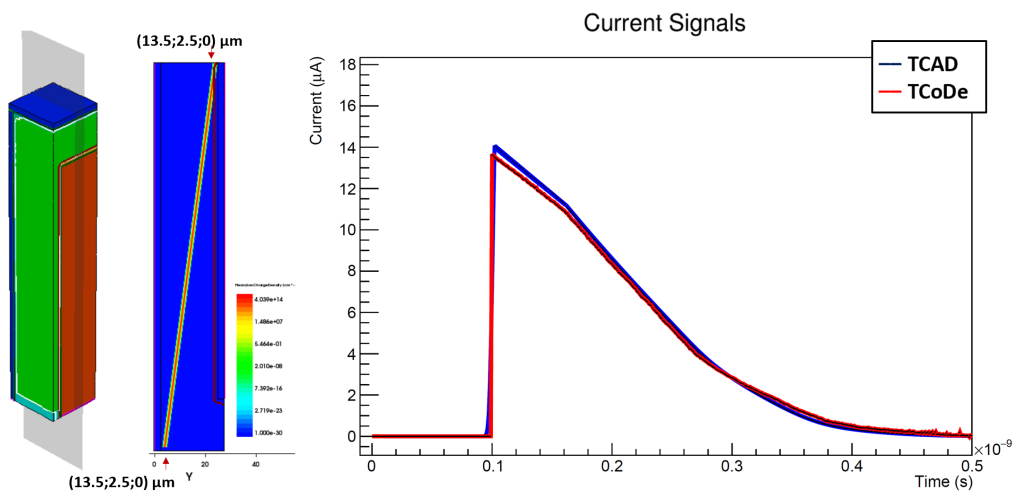


Figure 6.20: Inclined energy deposit simulated with TCoDe and TCAD on the TIMESPOT silicon sensor and then compared. Left: Position of the deposit inside of the sensor (TCAD model). Right: Comparison of the current signals.

## 6.4 Next developments

TCoDe on its current release presents all essential functions needed to simulate sensor response of non-irradiated solid state sensors. Next improvements will add the possibility to include radiation damage and its effects on signal simulation and will make compatible TCoDe with diamond sensor technology. In more distant futures TCoDe will add the possibility to simulate solid state sensors with

amplification layers, like LGAD silicon sensors. Also the possibility to include a front-end response and a graphical user interface are currently under discussion.



# Chapter 7

## TIMESPOT sensor tests

To understand the performances of the new parallel trench sensor, a series of first test were performed, including a infra-red laser stimulation and a test beam. This chapter shows first preliminary tests performed with a 200 fs fast IR laser pulse on one test structure in anticipation to the first test beam which will be performed at the Paul Scherrer Institut (PSI) in Zurich in October 2019.

### 7.1 The test structures and board

Sensor production finished in July 2019 and first test structures have been available few weeks later. A first wafer test which consisted in measuring the electrical characteristics of the single test structures was performed by FBK and Trento University. After the tests, the large test structures were cut in half, separating the large TIMEPIX-III pixel matrix from the area containing all test structures (Fig. 7.1). The last one was also cut in few elements containing 4 structures each. Among all test structures, 2 were chosen for first measurements:

- A pixel strip device, containing single (double) strip structures, with 10 (20) pixels each. For the tests a single pixel line was bonded (Fig. 7.2.A). The selected strip has a junction trench length of 39  $\mu\text{m}$ .
- A single pixel device which presents two main structures which differ from each other by the position of their pads (one has them directly integrated over the the junction trenches and the other outside the pixel matrix on large pads). For the test the double pixel structure was selected and wire bonded on the board (Fig. 7.2.B). The selected pixel has a junction trench length of 39  $\mu\text{m}$ .

Both structures were selected together with one FBK 3D single side hexagon pixel with column electrodes [82] as comparison between both technologies (Fig. 7.2.C). All selected structures were again tested individually and their IV response compared with the wafer test before being glued on the readout boards.

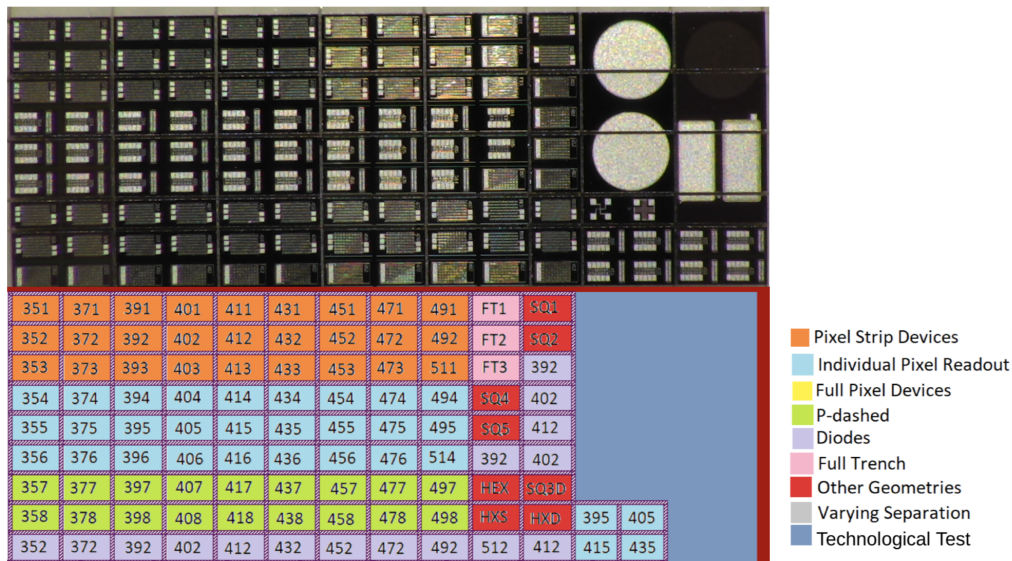


Figure 7.1: Cut element of the wafer area containing 3D sensor test structures and respective map of the test structures. (Source: FBK)

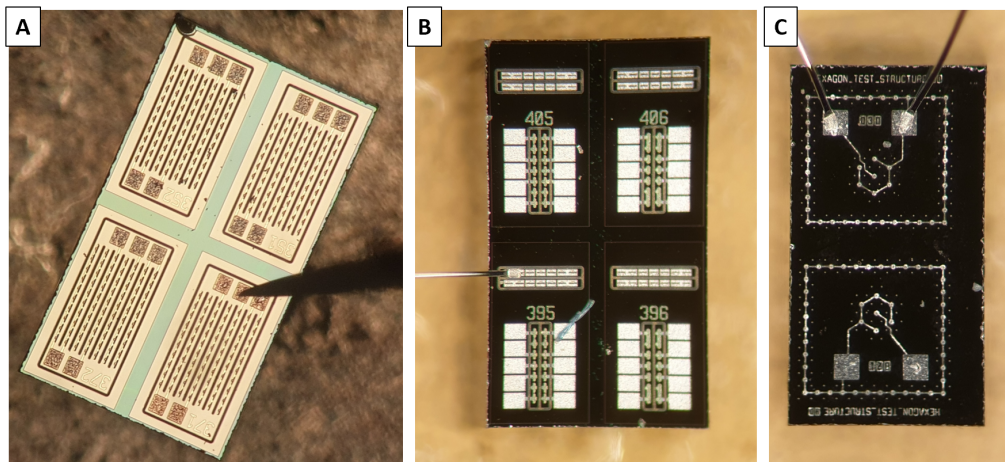


Figure 7.2: Selected structures for first tests: (A) Pixel strip devices, (B) individual pixel devices and (C) hexagonal pixel devices based on a FBK-3DDS technology.

**Readout board** The readout board chosen for the sensors is a multi-purpose board with a fast front-end design already used to measure LGAD timing performances [106]. The board is based on a low power fast amplifier designed at the Kansas University [95]. The layout of the board presents a central  $20 \times 20 \text{ mm}^2$  pad where the sensors can be glued and distributes a maximum bias voltage of 1 kV to the sensors. A series of grounded pads are located close to the sensor allow to connect to ground the guard ring or equivalent structures (active or slim edges) (Fig. 7.3.A). Three boards were purchased for the test-beam and their 8 channels were

	Channel 3:	Channel 6:	Channel 7:
Board 03:	1.77 mV	1.77 mV	1.6 mV
Board 04:	1.8 mV	1.7 mV	1.5 mV
Board 06:	1.65 mV	1.71 mV	1.6 mV

Table 7.1: Noise level measured on the selected readout channels.

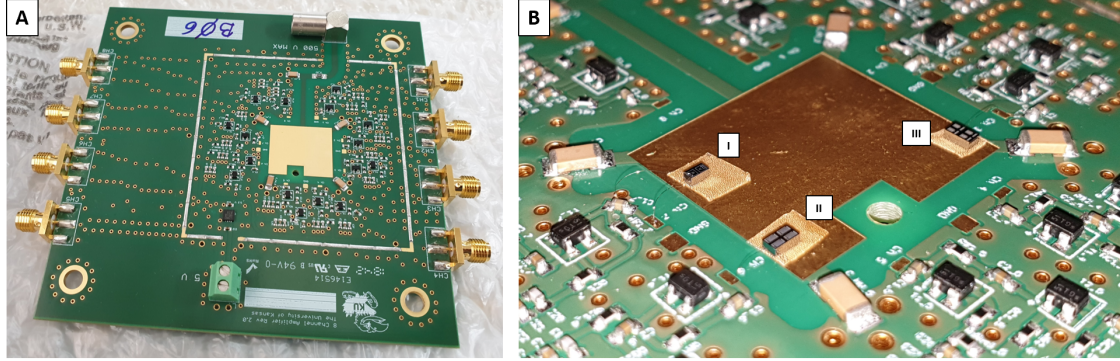


Figure 7.3: Multi-purpose readout board for fast timing applications designed by Kansas University (A). (B) Test structures glued on the pad of board 06: Hexagonal pixel (I), strip device (II) and single pixel structure (III).

tested, 3 of them (channel 3,6 and 7) were chosen for the test after a careful measurement of their noise level, selecting the channels with the lowest values (Table 7.1). The sensors were than glued, using conductive tape, on the readout pad and wire bonded on each channel. Every board was configured in the same way (Table 7.2).

	Channel 3:	Channel 6:	Channel 7:
Board 03:	Single Pixel	Strip	Hexagon
Board 04:	Single Pixel	Strip	Hexagon
Board 06:	Single Pixel	Strip	Hexagon

Table 7.2: Test structure position on each board.

## 7.2 IV characteristic measurement

First electrical measurements performed directly on the wafer by FBK and university of Trento showed an average leakage current below 100 nA for 50 V bias voltage (Fig. 7.4).

The received test-structures were again retested, measuring again their IV characteristic, using a Keithley 6517B electro-meter controlled remotely by a NI LabView based control software. The set-up simply rises the applied inverse bias voltage

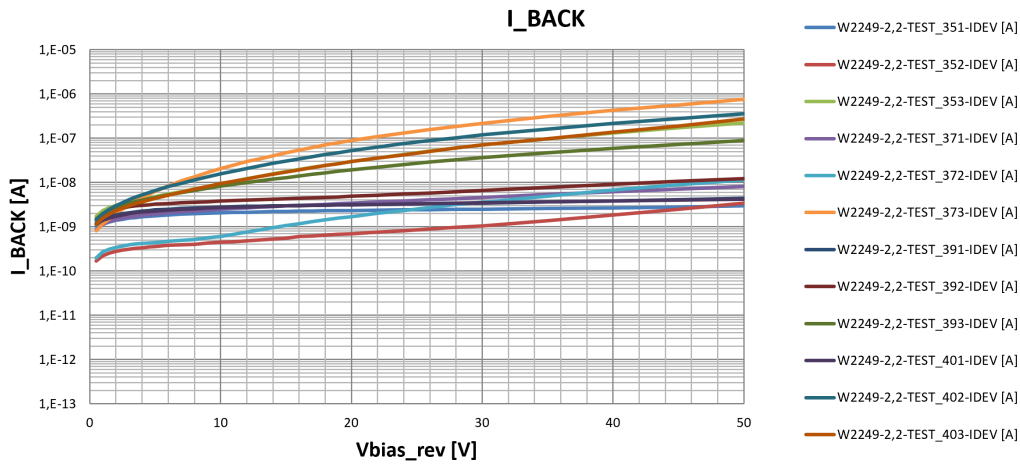


Figure 7.4: IV characteristic of the main considered test structures during wafer test performed FBK. (Source: FBK)

on the sensor and measures at the same time the dark current, with an applied threshold of  $1\ \mu\text{A}$ . If the dark current starts to increase strongly due to avalanche effects, the set-up stops and provides the breakdown voltage. The sensor itself was located in a semi-automatic probe-station, model Karl-Suss PA200. Sensor bias was provided through the chuck and the junction electrode was connected using a micro-manipulator with a  $2\ \mu\text{m}$  thick probe-needle (Fig. 7.2.A)

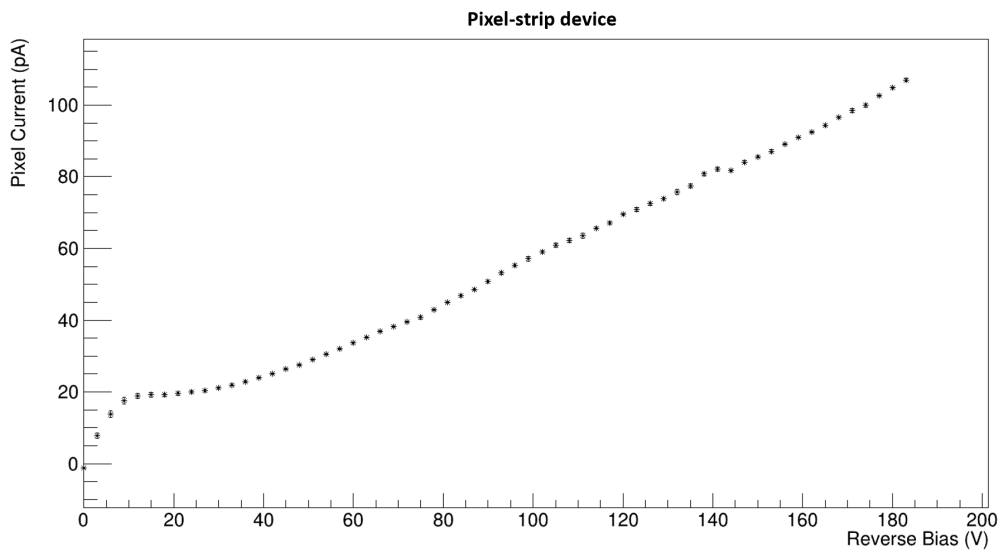


Figure 7.5: IV characteristic on the single strip device.

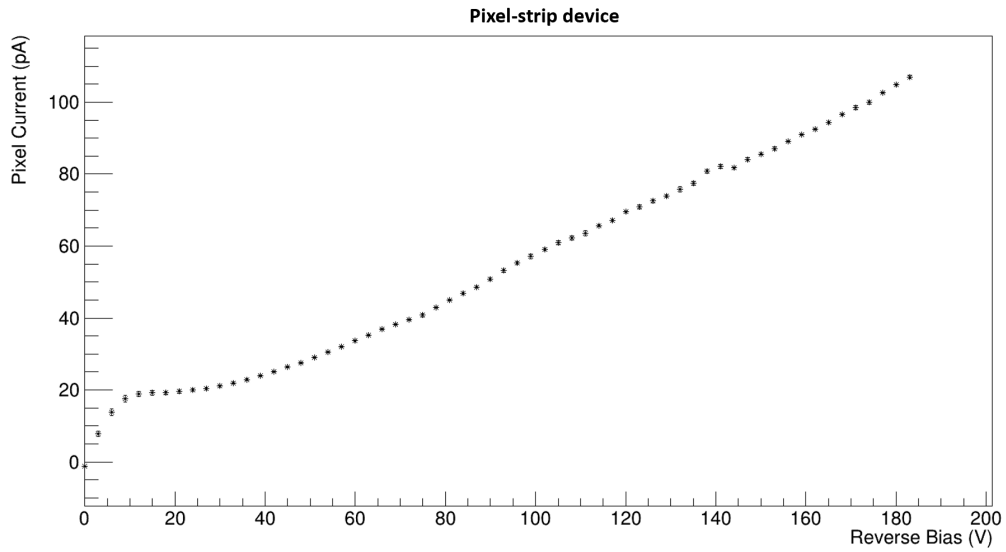


Figure 7.6: IV characteristic on the single pixel device.

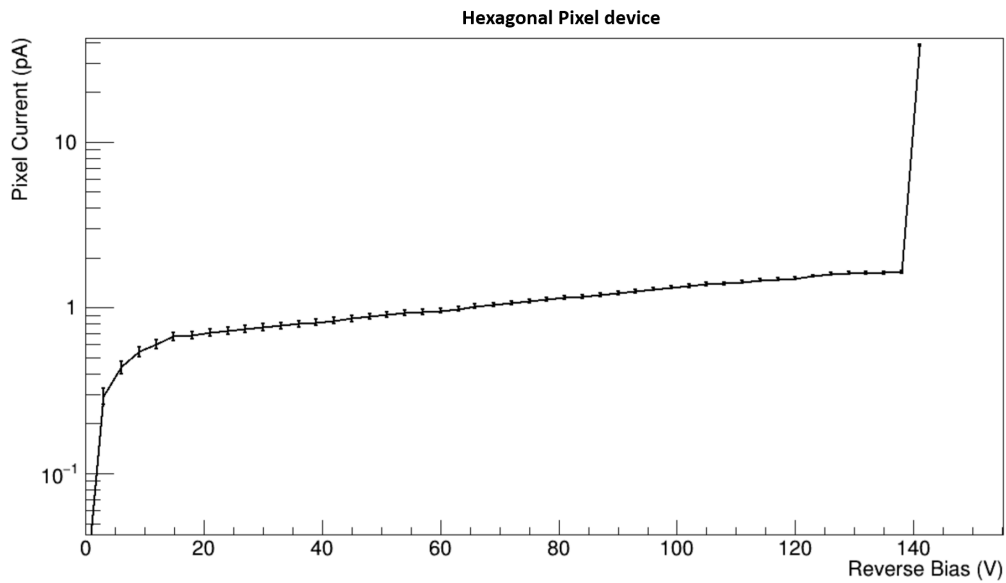


Figure 7.7: IV characteristic on the hexagonal device.

The higher leakage current measured during wafer test is due to the fact that all pixels were previously short-circuited using a single metal layer that was later removed (temporary metal). This procedure allows to measure all devices at ones without damaging the pads.

Sensor breakdown, which was not measured during wafer test, showed for the non irradiated devices an average threshold of 180 V (Fig. 7.5 7.6). The hexagonal

test structure presents instead a lower dark current and also a lower breakdown voltage of 140 V (Fig. 7.7).

## 7.3 Laser stimulation

In alternative to a particle beam, a silicon sensor can be tested using a infra-red laser beam. The principle behind is based on photon absorption through a specific medium described by the Beer-Lambert law [108] [109], which relates the intensity of the crossing radiation to the distance travelled in the material

$$I(x) = I_0 e^{-\mu_{abs} x}, \quad (7.1)$$

where  $\mu_{abs}$  is the absorption coefficient. The choice of the wavelength depends mainly on the thickness of the silicon device and secondly from the minimum energy required to generate an electron-hole pair, which is more than the band-gap of 1.14 eV. For this reason laser source with a wavelength of 1030 nm has been chosen. The photons at this wavelength have an energy of  $\sim 1.2$  eV, enough to generate an electron-hole pair and at the same time allow the radiation to travel for few millimetres.

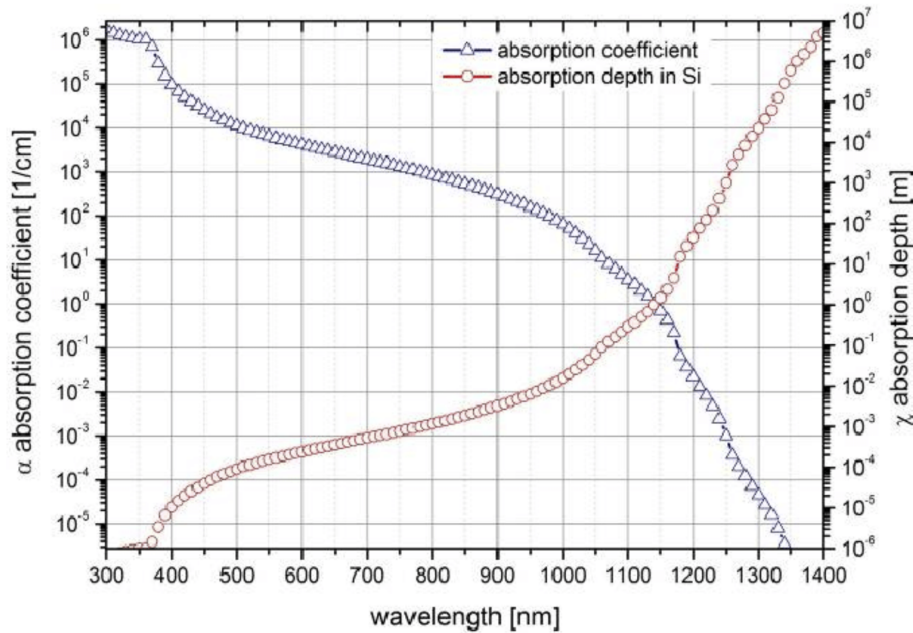


Figure 7.8: Silicon absorption coefficient and absorption length [110].

### 7.3.1 Set-up

To measure the timing performances of the sensor a new set-up was developed and built in the TIMESPOT laboratory. The set-up is capable of emulating the energy

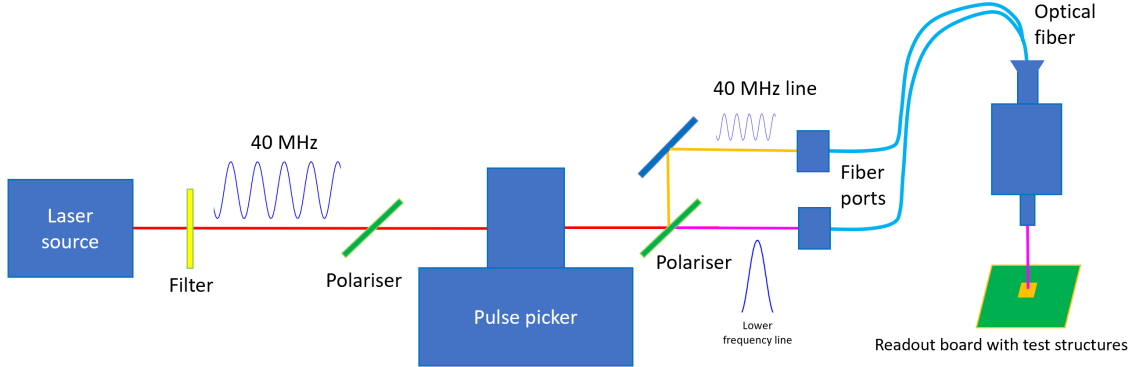


Figure 7.9: Set-up for laser tests.

deposit of a MIP using an Onefive Origami-10 IR-laser source. The laser source is capable of shooting laser pulses with 200 fs duration at a frequency of 40 MHz. Each pulse stores an average energy of 2.5 nJ (156 GeV) which can be calibrated, using filters, to deposit different energies in the silicon. In order to change pulse frequency, a pulse picker, model EKSMA Optics UP1 Ultrafast, is used to select single impulses, reducing the frequency to 1 kHz. The pulse picker works by rotating the polarisation for one or more impulses using the Pockels effect [111]. A successive polariser allows to pass only the impulses with the rotated polarisation, reflecting all the others. This allows to establish two beam lines: one for irradiation at maximum frequency of 40 MHz and the other for irradiation at lower frequencies. The beam is channelled in a Mitutoyo VMU-L4B microscope using a 1 m long optic fibre (Fig. 7.9). The entire transport of the pulse causes a final expansion in time of the pulse from 200 fs to  $\sim 400$  fs. The trigger of the entire system is a fast IR sensor with a precision of 8 ps, connected to a Lecroy Serial Data Analyser SDA 6000.

### 7.3.2 Results

First preliminary measurements consisted in irradiating all test structures using the 40 MHz beam line and measure, using the SDA, the standard deviation of the measured delay of the pulse generated by the 3D sensor with respect to the pulse of the trigger.

$$\sigma_{tot}^2 = \sigma_{sensor+FE}^2 + \sigma_{IR-diode}^2 \quad (7.2)$$

The measurement has been done for now only on the strip structure. Further measurements on the other two test structures are scheduled for October 2019.

**Pixel strip device** On the pixel strip device 4 measurements were performed, each of them in a different position: Close to the junction electrode (Fig. 7.10.A), close to the ohmic electrode (Fig. 7.10.C), at the middle of both (Fig. 7.10.C) and between junction electrodes (Fig. 7.10.D). The energy of each pulse was

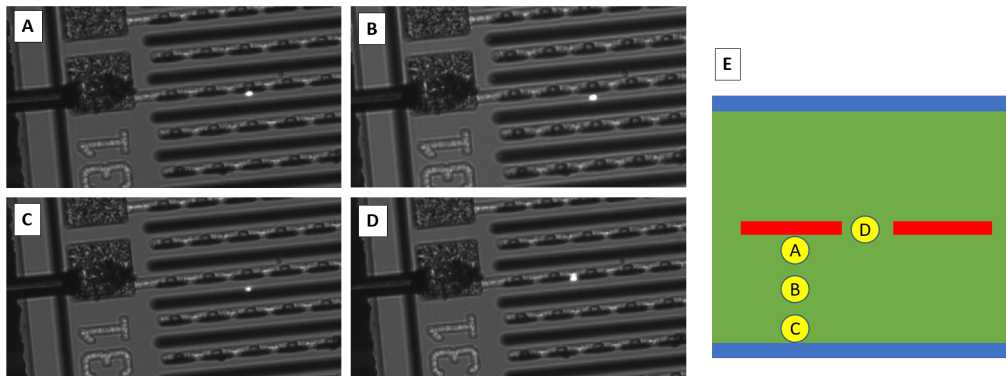


Figure 7.10: IR-laser pulse at 40 MHz irradiating the pixel strip structure. (A) Close to the junction electrode, (B) between ohmic and junction electrode, (C) close to the resistive electrode and (D) between junction electrodes. (E) schematic of the applied spots.

calibrated in order to deposit in the sensor an equivalent energy deposit of a MIP. The measurements were taken at different bias voltages, from 1 V to 60 V. The oscilloscope was programmed to save a statistic of 10000 measured pulses and the standard deviation was plotted in function to the bias voltage.

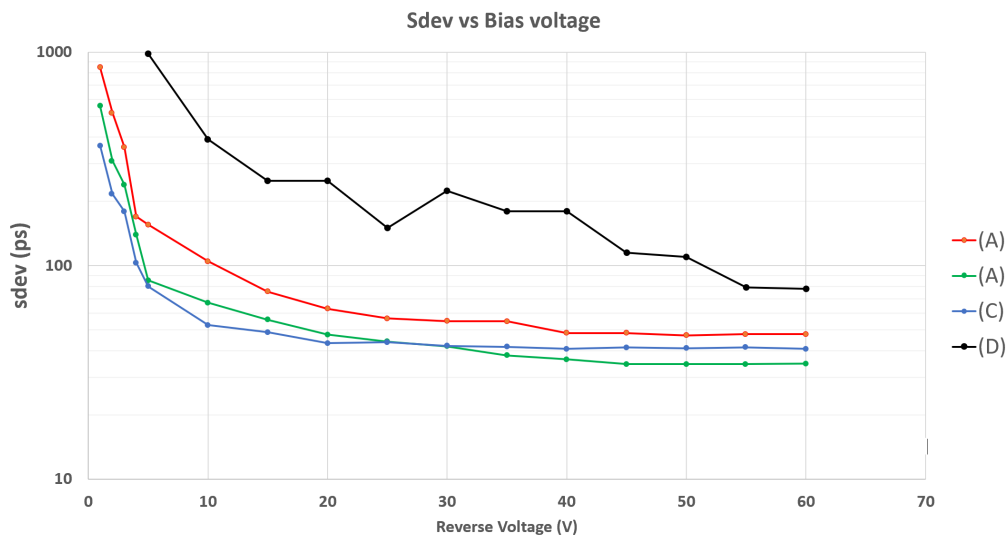


Figure 7.11: Measured standard deviation in different points of the pixel. Plots show the results taken from the spots shown in figure 7.10.

The results are shown in figure 7.11. All regions present a similar behaviour: A large standard deviation for lower bias voltages which reduces fast below 50 ps over 10 V. Over this threshold the uncertainty stays constant.

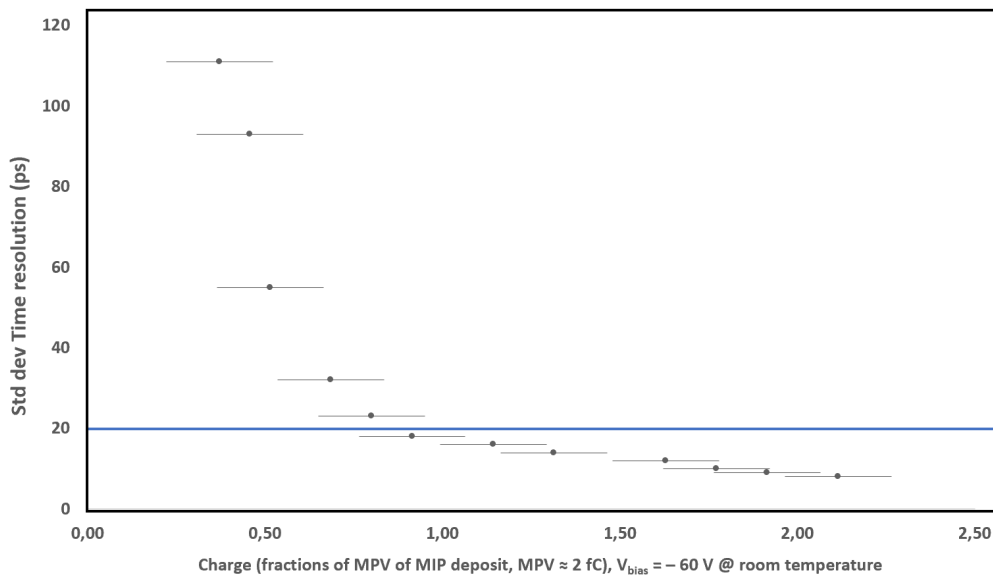


Figure 7.12: Time resolution related to the energy released in the sensor by the laser pulses [112].

A second series using the IR-laser consisted in measuring the time resolution related to signal amplitude, by increasing the power emitted by the laser using different optical filters. The plot is shown in figure 7.12 where it shows how the resolution goes below 20 ps for higher energy deposits than a single MIP. The obtained measurements are considered as very encouraging, taking into account that the sensors were not operated at higher voltages, in order to preserve the prototypes for the more important test beam. A more detailed study will be available for end October 2019.

## 7.4 Test-beam

All silicon sensors were tested in mid October 2019 using a high energy pion beam at the PSI. The test series included also the TIMESPOT 3D-diamond sensor and an alternative readout electronics. In this section the main attention is focused on the double pixel sensor and some comments of the silicon strip sensor which behaviour need more studies. This section will describe test beam set-up, procedures, analysis and results.

### 7.4.1 Set-up

The beam line used at the PSI was the high resolution  $\pi M1$  line (Table 7.3) set with a positive pion beam with a momentum of 270 MeV/c.

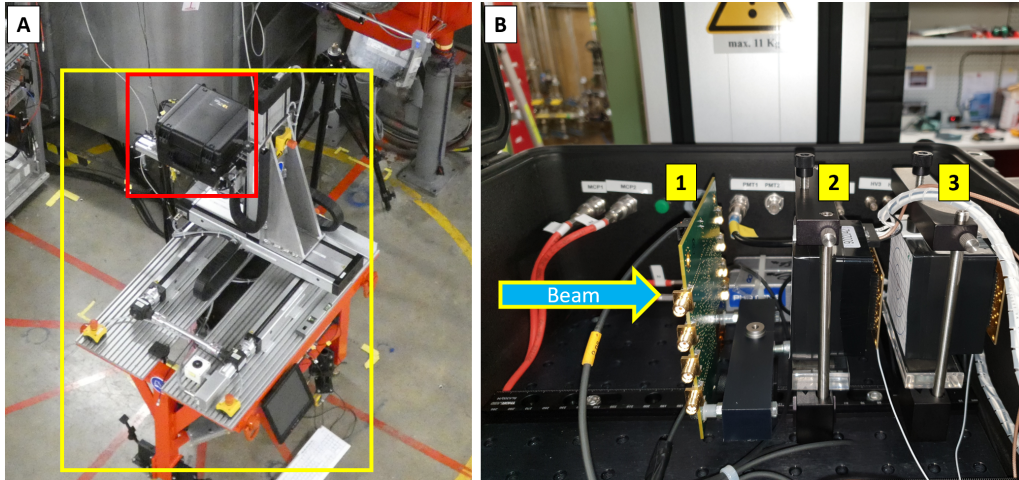


Figure 7.13: Box used to host the set-up. (A) Housing for the set-up (red square) and mechanic support (yellow rectangle) (B) Set-up inside the box: (1) TIMESPOT prototype board. (2) and (3) micro channel plates for the timing detector.

Path length	21 m
Momentum Range	100-500 MeV/C
Solide angle	6 msr
Momentum acceptance (FWHM)	2.9 %
Momentum resolution	0.1 %
Dispersion at focal plane	7 cm/%
Spot size on target (FWHM)	15 mm horizontal 10 mm vertical
Angular Divergence on target(FWHM)	35 mrad horizontal 75 mrad vertical

Table 7.3: Specifications of the  $\pi M1$  beam line [113].

Set-up was arranged in a large black box in order to insulate the system from external light sources. A small optical bench is installed inside the box in order to achieve easier alignment of all detectors. The entire box is mounted on a mechanical bench which can be controlled in remote(Fig. 7.13.A). The detectors inside the box are organised as follows:

- First detector station is the TIMESPOT test board with sensor and readout.
- Second detector station consists of two micro-channel plates (MCP), model Planacon XP85112 and Planacon XP85012 [114], positioned one behind the other. This device forms the timing reference detector and is used to determine the time resolution of the test board.

Device:	3D sensor:	Readout:	MCP-1:	MCP-2:
Voltage:	$0 \rightarrow -200 \text{ V}$	$5 \text{ V}$	$> 2000 \text{ V}$	$> 2000 \text{ V}$

Table 7.4: Bias configuration of the set-up during the last two test series.

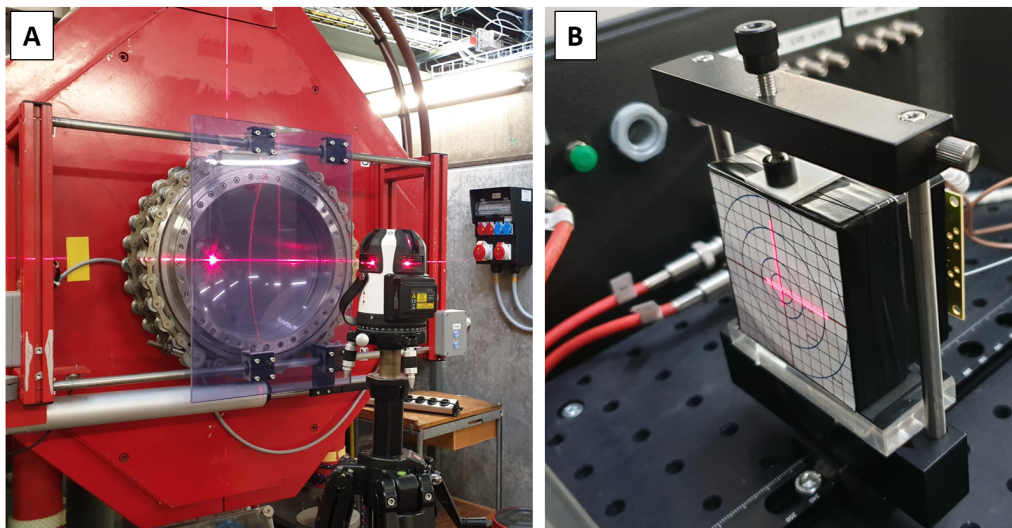


Figure 7.14: Laser alignment. (A) Laser beam. (B) Alignment of the detectors.

Three high voltage generators were used to provide sensor bias and power supply to the silicon sensor and both MCPs. A low voltage supply was used to provide power supply for the readout board (Table 7.4).

**System alignment** Alignment of the set-up was performed in two steps. A first laser alignment using two levelled laser beams as reference which cross each other along the beam line (Fig. 7.14.A). The beam line is marked in the test area with two reference points. All detectors were aligned with those beams using marks applied on the devices (Fig. 7.14.B). The second alignment procedure used directly the pion beam and was performed by measuring the flux of the particles through a small scintillation detector, previously installed behind the timing detector and aligned as well using the laser.

**Data acquisition and trigger** Data acquisition was performed using a remote controlled Oscilloscope&Schwartz Model RTP084, which acquired the signals coming from the MCPs, TIMESPOT board and synchronous reference signal of the 50 MHz radio frequency of the accelerator. For every configuration a minimum of 10000 events were acquired in order to have sufficient statistics.

The system trigger was set as a combination of few events. Main trigger is the signal generated by the TIMESPOT detector, followed by a second coincidence

trigger generated by the last micro-channel plate of the timing detector (Fig. 7.15).

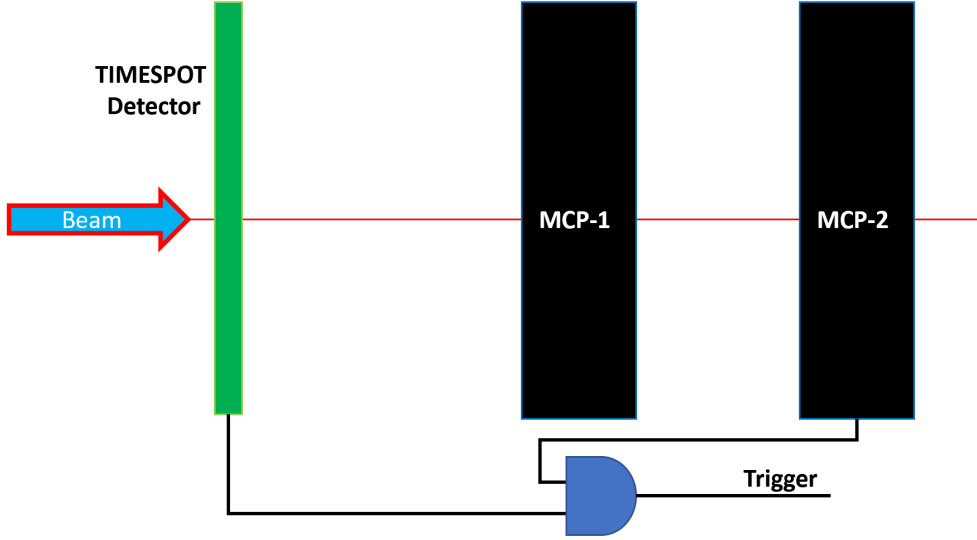


Figure 7.15: Schematic of the detector position and trigger.

### 7.4.2 Analysis

Main focus of the analysis was to determine the time resolution provided by the TIMESPOT board at a specific bias voltage of the sensor. All the information needed is contained in all 4 waveforms saved during a single trigger. The RF-signal displayed in channel 4 is needed for discrimination and background subtraction purposes.

Focusing the attention on the signals acquired with the first 3 channels, the determination of the time resolution of the TIMESPOT-board was determined by measuring the delay between the signal of the board and the signals generated by the timing detector:

$$\begin{cases} \Delta t = \left( \frac{T_{MCP_1} + T_{MCP_2}}{2} \right) - T_{TS} \\ \Delta t_1 = T_{MCP_1} - T_{TS} \\ \Delta t_2 = T_{MCP_2} - T_{TS} \end{cases}, \quad (7.3)$$

where  $T_{MCP_1}$ ,  $T_{MCP_2}$  and  $T_{TS}$  are the time over threshold for the signals of the MCP-1, MCP-2 and the TIMESPOT board (Fig. 7.16). The uncertainty associated with those measurement is respectively:

$$\begin{cases} \sigma^2 = \frac{1}{2}(\sigma^2_{MCP_1} + \sigma^2_{MCP_2}) + \sigma^2_{TS} \\ \sigma^2_1 = \sigma^2_{MCP_1} + \sigma^2_{TS} \\ \sigma^2_2 = \sigma^2_{MCP_2} + \sigma^2_{TS} \end{cases}, \quad (7.4)$$

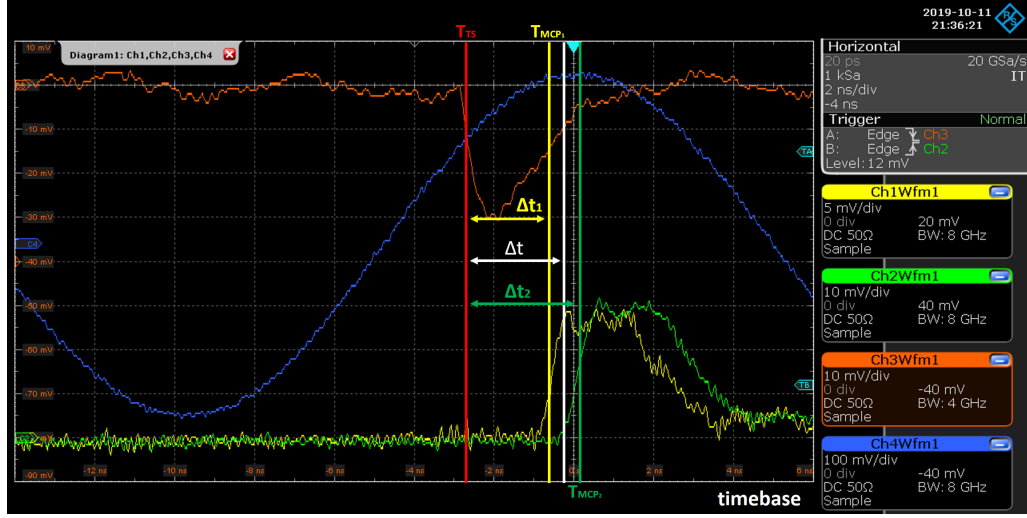


Figure 7.16: Screen shot of one trigger event and the measurements performed.

where  $\sigma^2$ ,  $\sigma^2_1$  and  $\sigma^2_2$  are obtained by fitting the distributions of the measured delays.  $\sigma^2_{MCP_1}$ ,  $\sigma^2_{TS}$  and  $\sigma^2_{TS}$  are the time resolutions of the MPCs and the TIMESPOT board respectively. The resolution of those 3 devices were determined in the following way:

- The micro-channel plates used in the experiment were different models with different time resolutions. The delay between their leading edges has a total uncertainty of:

$$\sigma^2_{TT} = \sigma^2_{MCP_1} + \sigma^2_{MCP_2} \quad (7.5)$$

- Subtracting  $\sigma^2_1$  with  $\sigma^2_2$  from 7.4 allows to obtain the following equation

$$\sigma^2_1 - \sigma^2_2 = \sigma^2_{MCP_1} - \sigma^2_{MCP_2}. \quad (7.6)$$

Subtracting and subsequently adding equation 7.6 in equation 7.5, allows to determine the resolution of both micro channel plates:

$$\begin{cases} \sigma^2_{MCP_1} = \frac{1}{2}(\sigma^2_{TT} + \sigma^2_1 - \sigma^2_2) \\ \sigma^2_{MCP_2} = \frac{1}{2}(\sigma^2_{TT} - \sigma^2_1 + \sigma^2_2) \end{cases} \quad (7.7)$$

Equation 7.7 allows to calculate the ratio between the resolutions of micro-channel plates, defined as  $\alpha$

$$\alpha = \frac{\sigma_{MCP_1}}{\sigma_{MCP_2}}. \quad (7.8)$$

Also the time resolution of the TIMESPOT prototype detector can be now calculated:

$$\sigma^2 = \sigma^2_1 - \sigma^2_{MCP_1} \quad (7.9)$$

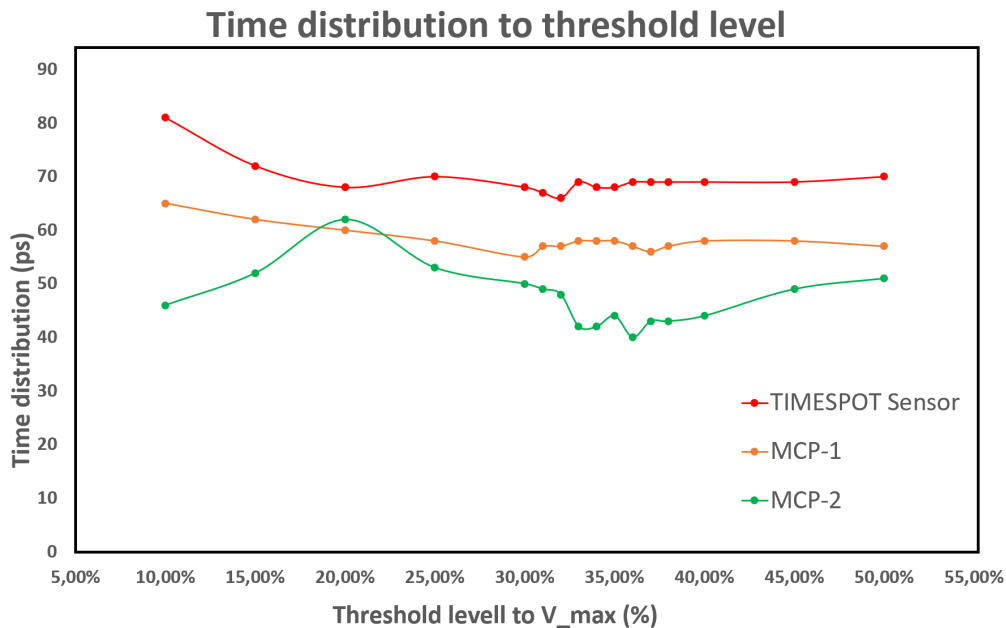


Figure 7.17: Time distribution related to the applied threshold.

**Optimisation of the measurements** The time delay between the signal of the prototype detector and the timing detector was determined by applying a dynamic time over threshold method similar to a constant fraction discriminator previously described in chapter 3. The threshold  $V_{th}$  applied on every signal depends from the amplitude of the measured signals ( $V_{th} = \beta V_{max}$ ) where  $\beta$  is the percentage from 1 % to 100 %. Before starting with the analysis, an optimisation of the  $\beta$  had to be done in order to minimise the time distribution. This operation was performed by fitting the trigger time distribution at different thresholds, from 15 % to 50 %. The distributions with the smallest standard deviation were found using a threshold between 30 % and 36 % of the signal amplitude (Fig. 7.17).

A second factor which influences negatively the measurement of the time over threshold was the interference of the 50 MHz resonance frequency of the accelerator, which interfered with the electronics, changing output signal shape. In order to remove this component, the background of the signal was subtracted. The approach consisted in a two step procedure. The first step consisted in fitting the 50 MHz sinusoid of the reference signal, saving phase and frequency and use the values to fit the plateau before signal, were only the contribution of the resonance frequency and the noise is supposed to be. Once the contribution has been determined, it is used to subtract the contribution from the entire signal, leaving only the signal of the detector with 0V offset. This approach works fine for both micro channel plates, not for the signal of the TIMESPOT board, due to the smaller signal to noise ratio which does not allow to identify clearly the signal interference for every single signal. It is still possible to remove partially this contribution by assuming that there is an

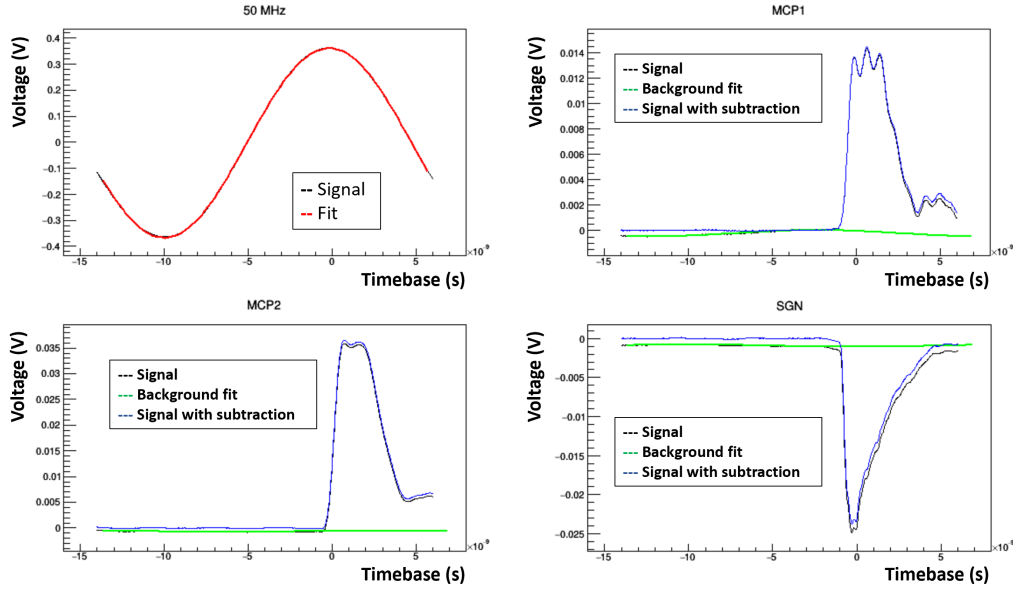


Figure 7.18: Background subtraction applied on all 3 average output signals.

average superposition of the sinusoid in the output signal. This allows to repeat the procedure using the average signal obtained as average of all acquired signals (Fig. 7.18). This approach has only a small disadvantage which is a reduced statistics of ca. 11 % due to other particles, mainly positrons and muons that arrives at different instants due to their different speed (Fig. 7.19), shifting also the induction of the resonance signals.

**Determination of the time over threshold** The time over threshold is calculated using a linear fit applied along the leading edge between 30 % and 40 % of the signal amplitude, where the time walk resulted to be the smallest among all verified thresholds:

$$f(t) = m * t + b, \quad (7.10)$$

where  $m$  and  $b$  are the parameters computed by the fit. Once the fit is completed, the system computes the time over threshold by using the inverse function of  $f(t)$  computed at  $\beta V_{max}$ .

$$t_{tof} = \frac{g(\beta V_{max}) - b}{m}, \quad (7.11)$$

This method is supposed to be more stable compared to the fit applied along the entire leading edge, which is not recommended considering that the slope of the rising edge of the board changes above 70 % of the amplitude (second plot at the bottom of figure 7.18). One sample is displayed in figure 7.20 showing the method applied on all three signals. The pink line shows the line obtained from the linear fit and the red lines are used as markers for the threshold and time over threshold.

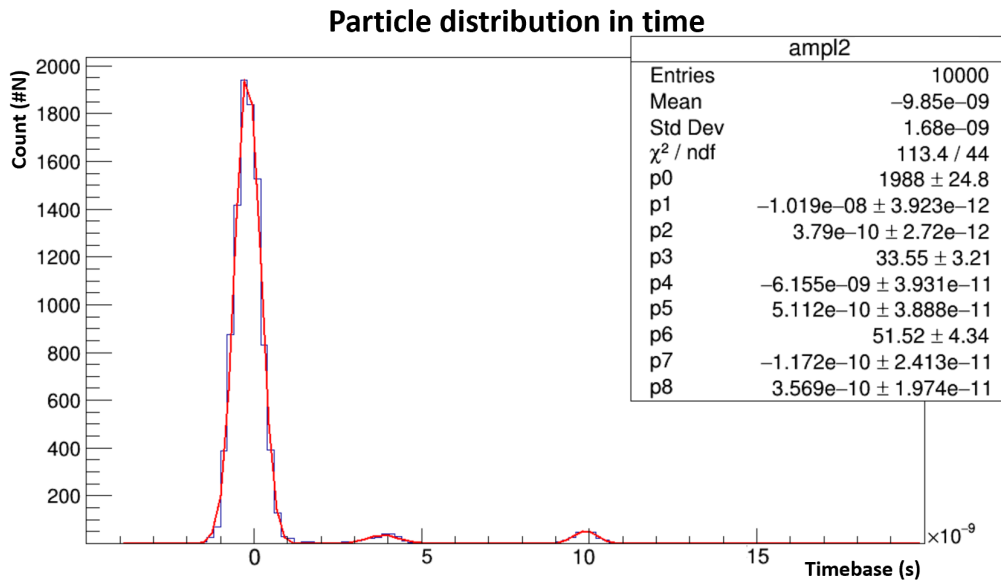


Figure 7.19: Distribution in time of all particles within a bunch using the pions as reference.

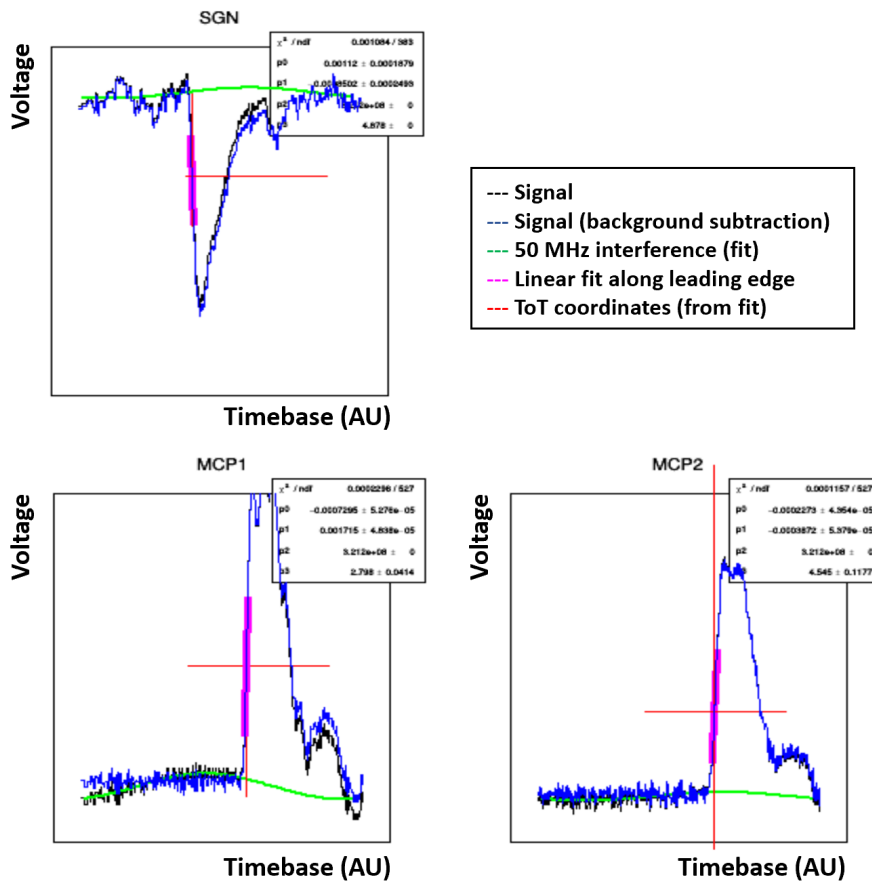


Figure 7.20: Graphical representation of the determination of the time over threshold, using a localised linear fit along the leading edge.

### 7.4.3 Results

**Double pixel device** The double pixel device was tested at different bias voltages, spacing from 5 V to 190 V, before reaching breakdown at 195 V. Applying the criteria presented in the previous section,  $\Delta t$ ,  $\Delta t_1$  and  $\Delta t_2$  were measured for every single trigger event and their values stored in histograms. Applying a Gaussian fit on the distribution, the standard deviations of those distributions (Fig. 7.21) were used to calculate the resolutions of the TIMESPOT prototype detector (Fig. 7.23) and the resolution of the timing detector and MCP (Fig. 7.22).

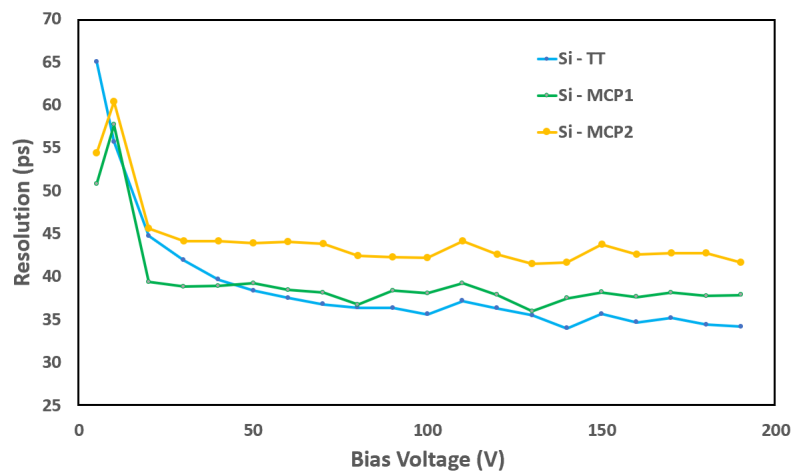


Figure 7.21: Standard deviation of the delay distributions related to sensor bias.

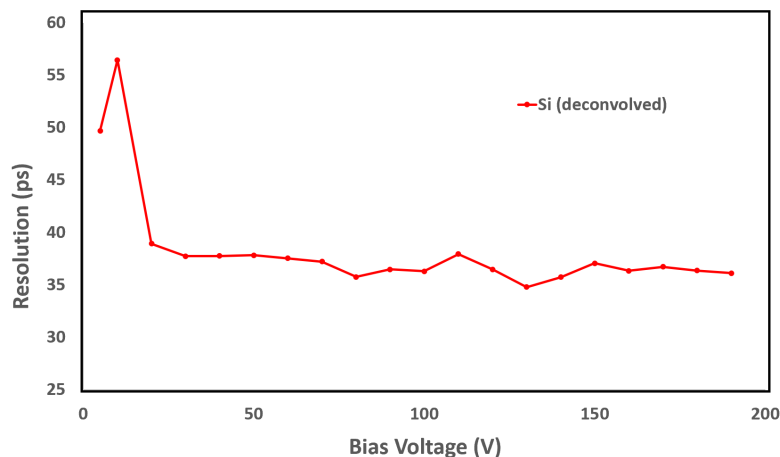


Figure 7.22: Resolution of the TIMESPOT prototype detector in function of the sensor bias.

Figure 7.21 and 7.22 allow to see how time resolution improves with increasing bias voltage. Once the bias voltage is high enough to establish saturation velocity,

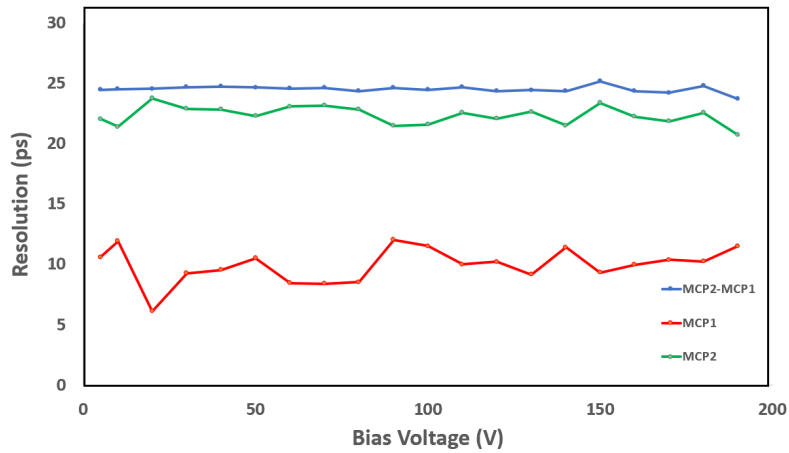


Figure 7.23: Time resolution of the timing detector and multi channel plates.

above 20 V, the time resolution stabilises around 35 ps, going below 35 ps only at 130 V bias voltage.

Measurement on a second double pixel device connected to a different front-end developed within the TIMESPOT collaboration showed a more performing delay distribution of 30.7 ps which, ones subtracted the contribution of the timing detector, becomes 28.9 ps (Fig. 7.24) demonstrating a large margin of optimisation.

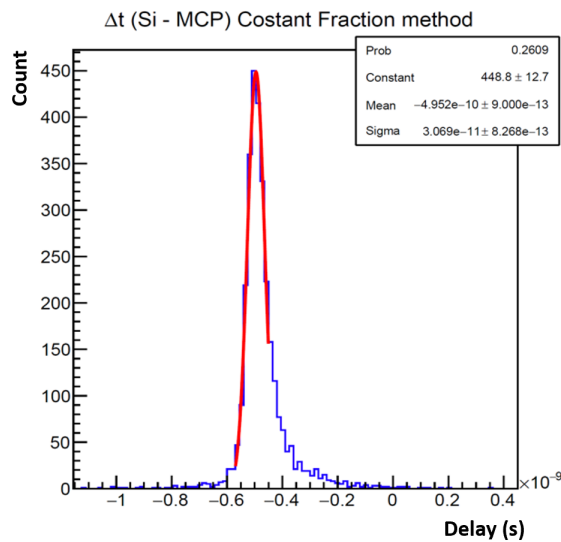


Figure 7.24: Delay distribution using a double pixel device connected to a different fast readout developed within the TIMESPOT collaboration presenting the best performance during the test-beam [112].

**Silicon strip sensor** Analysis on the data provided by the detector prototype based on a silicon strip sensor results more difficult than the double pixel device due to an unexpected profile of the delay distribution which presents not only the characteristic Gaussian peak but also a long tail which makes in the worst situation almost 40 % of the measured events. Also the distribution of delays between both MPCs resulted 5 ps larger than measured during the test with the double pixel based detector (sample at 100 V shown as example in figure 7.25).

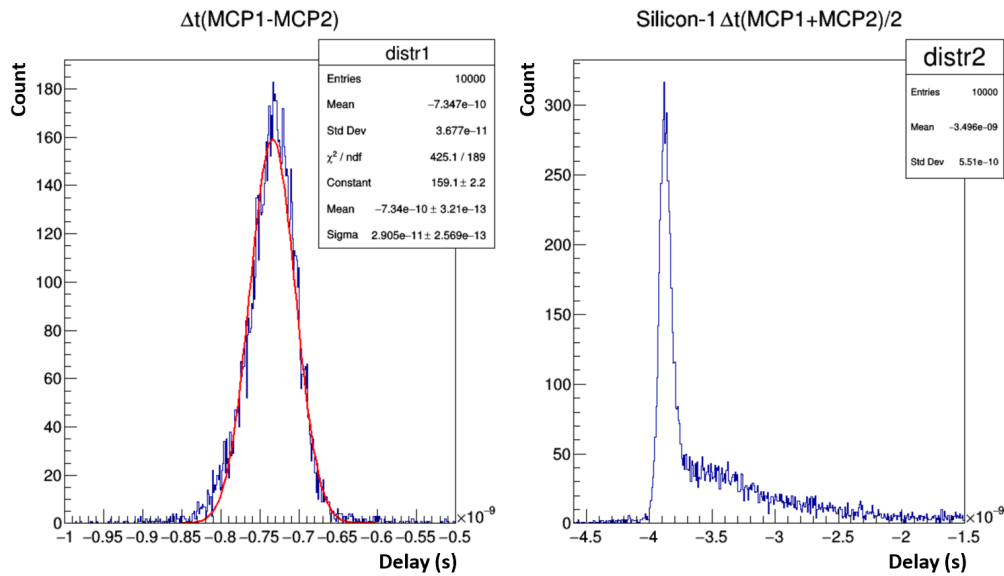


Figure 7.25: Delay distribution measured between both MPCs (left plot) and between the TIMESPOT detector and the timing detector.

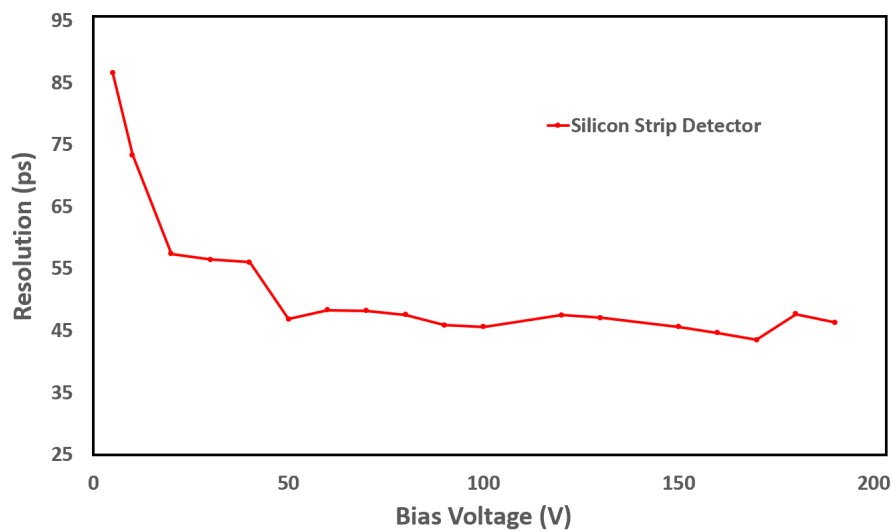


Figure 7.26: Time resolution of the silicon strip sensor based prototype detector.

Analysing signal shape of both the TIMESPOT devices and MPCs, no considerable difference was found compared to the double pixel device and, therefore, further studies must be done. Based on this situation, the resolution of the silicon strip sensor based detector was performed by cutting the tail from the distribution and fitting with a single Gaussian distribution the peak. The obtained resolution in function of the bias voltage is presented in figure 7.26 and shows a similar behaviour as the double pixel device, improving its time resolution with increasing bias voltage and stabilising it after reaching velocity saturation.

# Conclusions and perspectives

This work presented the development of a next generation 3D-silicon particle sensor optimised for high resolution time measurements. The new device is intended to be used in future 4D-tracking detectors operating in high luminosity environment, like the High Luminosity LHC, where radiation hardness is an important factor as well. The 3D silicon sensor technology was chosen as most suitable sensor technology for this application. 3Ds feature a decoupled inter-electrode distance from the wafer thickness which allows to reduce the distance between the electrodes, achieving faster charge collection and higher radiation hardness. The possibility to modify sensor geometry makes 3Ds highly customisable. This work described the design activity carried out to define a timing optimised electrode geometry. A TCAD based design study was carried out in order to study amplitude, coverage and uniformity of the electric field which one important indicator for a potential high time resolution. The design approach featured also a dedicated method, called Ramo-map, to explore the current induction of an electron-hole pair inside the active area. The method allowed to demonstrate the superiority of trench-based electrode geometries with respect to pillar electrode based geometries, showing higher and more uniform current induction. Among all designed geometries, the parallel trench electrode was selected as the main solution and produced by FBK in a first prototype together with other secondary geometries and test structures.

Concurrently with the production, transient simulations were carried out to understand the potential time resolution of the sensor by simulating sensor response using initially Synopsys Sentaurus TCAD. TCAD simulations showed strong signal bursts above  $10\ \mu\text{A}$  for vertical signals and a charge collection time below 400 ps. The slow computing speed of TCAD due to its high-detail-computation, did not allow to reproduce a large number of current signals, necessary to analyse the intrinsic time resolution of the device. This issue stimulated the development of a fast transient simulator for sensor operation, called TCoDe. TCoDe was validated by simulating and comparing with TCAD the output signals simulated using identical energy deposits. TCoDe was applied a first time to estimate average charge collection time of the TIMESPOT sensor, measuring an average charge collection time of 318 ps using a large number of  $\sim 126000$  signals simulated in few hours. A second simulation, consisted in emulating the front-end response of the fast read-out board used during the test-beam and laser test. The simulation has shown a promising time resolution

below 40 ps. Sensor production ended in July 2019 and first test structures were immediately available for first tests. Two of them were selected to be connected on the fast readout boards in preparation on the test beam scheduled for mid October 2019. Before test beam, the sensors has been tested using a IR-laser source. First measurements show a promising resolution below 36 ps at 60 V bias voltage using laser pulses releasing the same amount of energy as a minimum ionising particle. Using laser pulses with higher energy showed even better performances of the device, going below 20 ps.

A successive test-beam performed at the PSI used a double pixel and strip pixel sensor. Analysis results from the measurements obtained from the test beam showed a time resolution of 35 ps for the double pixel device and a higher resolution above 40 ps for the silicon strip device bonded on general fast readout board. A different prototype detector based on a double pixel device connected to a discrete component electronics developed within the TIMESPOT collaboration showed time resolution below 30 ps, suggesting that the current time resolution reached is mostly dominated by the electronics.

In perspective to the high luminosity upgrade, further optimisations especially on the electronics will be performed in order to achieve an even better time resolution, which appears to be at reach.

# Bibliography

- [1] The ATLAS collaboration, Observation of a new particle in the search for the Standard Model Higgs boson with the ATLAS detector at the LHC, *Physics Letters B*, Volume 716, Issue 1, 17 September 2012, Pages 1-29
- [2] The LHCb collaboration, *Phys.Rev.Lett.* 115 (2015) 072001
- [3] The LHCb collaboration, Observation of CP Violation in Charm Decays, *Phys.Rev.Lett.* 122 (2019) no.21, 211803
- [4] W. Herr, B. Muratori, Concept of luminosity, CERN, 03-09-15.3, p.361-377, 2006
- [5] The LHCb collaboration, LHCb Upgrade II Expression of interest, CERN/LHCC 2017-003
- [6] B. Schmidt, The High luminosity upgrade of the LHC, Physics and technology challenges for the accelerator and the experiments, *Journal of Physics: Conference series* 706 022002, 2015
- [7] M. Benedikt, D. Schulte, F. Zimmermann, Optimizing integrated luminosity of future hadron colliders, *Physical Review Special Topics - Accelerators and Beams*, vol 18, 2013, 10.1103/PhysRevSTAB.18.101002
- [8] D. Fournier, Performance of the LHC, ATLAS and CMS in 2011, *EPJ Web Conf.* 28 (2012) 01003
- [9] N. Styles, on the behalf of the ATLAS and CMS collaborations, Collecting and analysing data at high pile-up with ATLAS and CMS, *ATL-UPGRADE-PROC-2015-001*
- [10] G. A. Rinella, The NA62 GigaTrack: a low mass high intensity beam 4D tracker with 65 ps time resolution on tracks, *Journal of Instrumentation*, Volume 14, July 2019
- [11] <https://www.fbk.eu/it/>
- [12] Cristin H. Pea and CMS Collaboration 2019 *J. Phys.: Conf. Ser.* 1162 012035

- [13] A. Corentin, ATLAS collaboration, A High-Granularity Timing Detector in ATLAS: Performance at the HL-LHC, Nucl. Instrum. Methods A, Vol. 924, 21 April 2019, Pages 355-359
- [14] The LHCb Collaboration, The LHCb Detector at the LHC, Journal of Instrumentation, 2008 JINST 3 S08005
- [15] The LHCb collaboration, Physics Case for an LHCb Upgrade-II, Opportunities in flavour physics, and beyond, in the HL-LHC era, CERN/LHCC 2018-027
- [16] The LHCb Collaboration, LHCb VELO Upgrade Technical Design Report, CERN-LHCC-2013-021 ; LHCb-TDR-013
- [17] T. Poikela, et al., VeloPix: the pixel ASIC for the LHCb upgrade, Journal of Instrumentation, Vol. 10, C01057, 2015
- [18] The LHCb Collaboration, LHCb VELO TDR, CERN/LHCC 2001-0011
- [19] K. Hennessy, LHCb VELO upgrade, Nucl. Instrum. Methods A, vol. 845, pages 97-100, 2017
- [20] B. van der Heijden, et al., SPIDR, a general-purpose readout system for pixel ASICs, Journal of Instrumentation, vol. 12, C02040, 2017
- [21] Parker S.I., Kenney C.J., Segal J., 3D - A proposed new architecture for solid-state radiation detectors, Nucl. Instrum. Methods A, 395 (1997), pp. 328-343
- [22] Parker S.I., Kok A., Kenney C., Jarron P., Hasi J., Despeisse M., Da Via C., Anelli G., Increased speed: 3D silicon sensors; Fast current amplifiers, IEEE Trans. Nucl. Sci., 58 (2) (2011), pp. 404-417
- [23] Dalla Betta G.-F., et al., Development of a new generation of 3D pixel sensors for HL-LHC, Nuclear Instrum. Methods A, 824 (2016), 386-387
- [24] Dalla Betta G. F., et al., Development of a new generation of 3D pixel sensors for HL-LHC, Nuclear Instrum. Methods A, 824 (2016), 386-387
- [25] S. Lagomarsino, et al., Three-dimensional diamond detectors: Charge collection efficiency of graphitic electrodes, Applied Physics Letters, 103(23):233507, 2013.
- [26] A. Annovi et al., A low-power and high-density Associative Memory in 28 nm CMOS technology, 2017 6th International Conference on Modern Circuits and Systems Technologies (MOCASST), Thessaloniki, 2017, pp. 1-4. doi: 10.1109/MOCASST.2017.7937632
- [27] F. Resta et al., IC-PIX28: A 28nm read-out channel for pixel detector, Proceedings of 2015 IEEE International Conference on Electronics, Circuits, and Systems (ICECS)

- [28] B. G. Streetman; S. Banerjee, Solid State electronic Devices (5th ed.), New Jersey: Prentice Hall. p. 524. (2000).
- [29] C. Kittel, Introduction to Solid State Physics, 7th Edition, Wiley.
- [30] E. Fermi, Zur Quantelung des einatomigen idealen Gases, Zeitschrift fr Physik, Vol. 36, S. 902-912, 1926.
- [31] P.A.M. Dirac, On the Theory of Quantum Mechanics, Proceedings of the Royal Society of London, Series A Vol 112, S. 661-677, 1926.
- [32] H. Spieler, Semiconductor Detector Systems, Oxford Science Publication, 2005
- [33] Synopsys, Sentaurus Device User Guide, K-2015.06, page 396
- [34] W. Shockley, The Theory of p-n Junctions in Semiconductors and p-n Junction Transistors. The Bell System Technical Journal. 28 (3): 435489
- [35] G. F. Knoll, Radiation Detection and Measurement, third edition, Wiley, 2000
- [36] P. Lechner, L. Strder, Ionization statistics in silicon X-ray detectors - new experimental results, Nucl. Instr. and Meth. A 354 (1995) 464.
- [37] M. Tanabashi et al (ParticleDataGroup), Review of Particle Physics, Phys.Rev.D 98,030001(2018)
- [38] K. F. Riley, M. P. Hobson, S. J. Bence, Mathematical Methods for Physics and Engineering, Cambridge University Press, (2010).
- [39] W. Shockley, Currents to Conductors Induced by a Moving Point Charge, Journal of Applied Physics, Vol. 9, p. 635-636, 1939
- [40] S. Ramo, Currents induced by electron motion, Proceeding of the I.R.E, page. 584-585, 1939
- [41] G. Lindstrm, Epitaxial silicon detectors for particle trackingRadiation tolerance at extreme hadron fluences, Nucl.Instrum.Meth. A568 (2006) 66-71
- [42] Y. Frenkel, ber die Wrmebewegung in festen und fssigen Krpern (About the thermal motion in solids and liquids), Zeitschrift fr Physik. Springer. 35 (8): 652669, (1926).
- [43] M. Huhtinen, Simulation of non-ionizing energy loss and defect formation in silicon, Nucl. Instr. And Meth. A
- [44] E. Fretwurst, Radiation damage in silicon detectors, Nuclear Instruments and Methods in Physics Research A, 2003, 512(30-43).

- [45] R. Wunstorf, Ph.D. Thesis, University of Hamburg 1992, DESY FH1K-92-01, 1992
- [46] G. Lindström, et al., Radiation hard silicon detectors - developments by the RD48 (ROSE) collaboration, Nuclear Instruments and Methods In Physics Research A, 2001, 466(308-326).
- [47] C. Piemonte, Device simulations of isolation techniques for silicon microstrip detectors made on p-type substrates, IEEE Transactions on Nuclear Science, 2006, 53 (3), 1694-1705
- [48] G. Lutz, et al., Stripping detector, Patent Application Laws OS 19620081 A1 21.11.97, Germany, 1997.
- [49] S. Kagawa, T. Kaneda, T. Mikawa, Y. Banba, Y. Toyama, and O. Mikami, Fully ion-implanted p + -n germanium avalanche photodiodes, Applied Physics Letters vol. 38, n. 6, pp. 429431 (1981)
- [50] P. Eckert et al., Characterisation studies of silicon photomultipliers, Nucl. Instrum. Methods Phys. Res. A 620, 217226 (2010).
- [51] G. Pellegrini et al., Technology developments and first measurements of Low Gain Avalanche Detectors (LGAD) for high energy physics applications, Nucl. Instrum. Methods Volume 765, 21 November 2014, Pages 12-16
- [52] <http://www.imb-cnm.csic.es/index.php/en/>
- [53] N. Cartiglia et al., Timing capabilities of ultra-fast silicon sensors, Acta Physica Polonica B Proceedings Supplement No 4, Vol. 7 (2014), 659-664
- [54] J. Lange, Gain and time resolution of 45 m thin Low Gain Avalanche Detectors before and after irradiation up to a fluence of  $10^{15}$  neq/cm<sup>2</sup>, Journal of Instrumentation, Volume 12 n. 5, P05003, May 2017, AIDA-2020-PUB-2018-007
- [55] The LHCb collaboration, The LHCb VELO TDR, CERN/LHCC 2001-0011, LHCb TDR 5, 2001
- [56] The ATLAS Collaboration, ATLAS Insertable B-Layer Technical Design Report, CERN-LHCC-2010-013 ; ATLAS-TDR-19
- [57] G.F. Dalla Betta et al., 3D silicon sensors: irradiation results, in Proceedings of 21<sup>st</sup> international workshop on Vertex Detectors PoS(Vertex2012) 014
- [58] S. Parker, C. J. Kenney, Performance of 3-D Architecture Silicon Sensors After Intense Proton Irradiation, IEEE Transaction on Nucl. Science, Vol. 48, NO. 5, 2001, 1629 - 1638

- [59] C. Da Vi et. al, 3D silicon sensors with variable electrode depth for radiation hard high resolution particle tracking, 2015 Journal of Instrumentation 10 C04020
- [60] C. Da Vi et al., 3D active edge silicon sensors with different electrode configurations: Radiation hardness and noise performance, Nucl. Instr. and Methods, A 604, pages 505-511 (2009)
- [61] R. Mendicino, et al., 3D trenched-electrode sensors for charged particle tracking and timing, Nucl. Instrum. Methods A, Vol. 927, pages 24-30, 2019
- [62] C. Da Vi, S.J. Watts, The geometrical dependence of radiation hardness in planar and 3D silicon detectors, Nucl. Instr. and Methods, A 603, pages 319-324 (2009)
- [63] R. Mendicino et al., 3D trenched-electrode sensors for charged particles tracking and timing, Nucl. Instr. and Methods, A 927, pages 24-30 (2019)
- [64] F. Laermer, A. Schilp, Method of anisotropically etching silicon, United States Patent 5501893, 03/26/1996
- [65] F. Laermer, A. Schilp, Method of anisotropically etching silicon, United States Patent 6531068, 03/11/2003
- [66] B. Wu et al., High aspect ratio silicon etch: A review, J. Applied Physics, Vol. 108 (2010), 051101
- [67] C. Piemonte, et al., Development of 3D detectors featuring columnar electrodes of the same doping type, Nucl. Instrum. and Method, A 541, pages 441-448, (2005).
- [68] C. J. Kenney et al., Silicon detectors with 3-D electrode arrays: fabrication and initial test results, IEEE trans. Nucl. Sci., NS-46(4), pp. 1224, (1999)
- [69] G. F. Dalla Betta, Small pitch 3D devices, PoS (Vertex 2016) 028, Volume 287
- [70] G.-F. Dalla Betta, et al., The INFN–FBK Phase-2 RD program, Nucl. Instrum. Methods A 824 (2016) 388.
- [71] G. Pellegrini et al., First double sided 3-D detectors fabricated at CNM-IMB, Nucl. Instrum. Methods A 592 (2008) 38
- [72] A. Zoboli, et al., Double-sided, double-type-column 3D detectors at FBK: Design, fabrication and technology evaluation, IEEE trans. nucl. sci. NS-55(5) (2008) 2775
- [73] M. Povoli, et al., Slim edges in double-sided silicon 3D detectors, 2012 Journal of Instrumentation 7 C01015

- [74] G. Darbo, on behalf of the ATLAS Collaboration, Experience on 3D Silicon Sensors for ATLAS IBL, *Journal of Instrumentation*, Volume 10, May 2015
- [75] G. Giacomini et al., Development of double-sided full-passing-column 3D sensors at FBK, *IEEE Trans. Nucl. Sci.* 60-3 (2013) 2357–2366.
- [76] J. Uher, J. Jakubek, Detection of fast neutrons with particle tracking detector Timepix combined with plastic scintillator, *Radiation Measurements*, Vol. 46, Issue 12, December 2011, Pages 1624-1627
- [77] R. Mendicino, et al., Novel 3D silicon sensors for neutron detection, *Journal of Instrumentation*, Volume 9, C05001, 2014
- [78] N. Cartiglia et al., Performance of Ultra-Fast Silicon Detectors, *Journal of Instrumentation*, Volume 9, February 2014
- [79] S. Meroli, et al., Energy loss measurement for charged particles in very thin silicon layers, *Journal of Instrumentation*, Volume 6 (2011) P06013
- [80] G. Kramberger et al., Timing performance of small cell 3D silicon detectors, *Nucl. Instrum. Methods, Section A*, Vol. 934, 1 August 2019, Pages 26-32
- [81] A. Loi, 3D detectors with high space and time resolution, *IOP Conf. Series: Journal of Physics: Conf. Series* 956 (2018) 012012
- [82] D. M. S. Sultan, Development of SmallPitch, Thin 3D Sensors for Pixel Detector Upgrades at HLLHC, PhD Thesis, University of Trento, 2017
- [83] Montalbano A. et al., A systematic study of BNL's 3D-Trench Electrode detectors *Nucl. Instrum. Methods A*, 765 (2014), pp. 23-28
- [84] C. J. Kenney, S. I. Parker, and E. Walckiers, Results from 3D sensors with wall electrodes: Near-cell-edge sensitivity measurements as a preview of active-edge sensors, *IEEE Trans. Nucl. Sci.*, vol. 48, no. 6, pt. III, pp. 2405-2410, Dec. 2001
- [85] Sultan D.M.S., et al., First production of new thin 3D sensors for HL-LHC at FBK, *J. Instrum.*, 12 (2017), p. C01022
- [86] Povoli M., et al., Development of planar detectors with active edge, *Nucl. Instrum. Methods Phys. Res. A*, 658 (2011), p. 103
- [87] Synopsys Inc. 2018 Synopsys Sentaurus TCAD Version 2018.06, Sentaurus structure editor user manual, K-2015.06, <https://www.synopsys.com/silicon/tcad.html>.
- [88] Synopsys Inc. 2018 Synopsys Sentaurus TCAD Version 2018.06, Sentaurus device user manual, K-2015.06, <https://www.synopsys.com/silicon/tcad.html>.

- [89] W.-M. Yao et al. Review of Particle Physics. *Journal of Physics G*, 33: 258270, 2006. 53, 55
- [90] S. Kirkpatrick, Modeling diffusion and collection of charge from ionizing radiation in silicon devices, *IEEE TED*, Vol. ED-26, No. 11, 1979, 1742-1753
- [91] G.de Vahl Davis, G.D.Mallinson, An evaluation of upwind and central difference approximations by a study of recirculating flow, *Computers and Fluids* Volume 4, Issue 1, March 1976, Pages 29-43
- [92] S. Agostinelli, et al., Geant4 - a simulation toolkit, *Nucl. Instrum. Methods A* 506(2003) 250-303.
- [93] V.Ivanchenko, G4EmStandardPhysicsoption2, 09.11.2005, <https://geant4.web.cern.ch/>
- [94] A. Valentin, M. Raine, J.-E. Sauvestre, M. Gaillardin and P. Paillet, Geant4 physics processes for microdosimetry simulation: very low energy electromagnetic models for electrons in silicon, *Nuclear Instruments and Methods in Physics Research B*, vol. 288, pp. 66 - 73, 2012.
- [95] N. Minafra, Development of a timing detector for the TOTEM experiment at the LHC, PhD thesis, Bari, University of Bari Aldo Moro, Feb. 2016
- [96] Alves Junior, A A, MultithreadCorner/Hydra, March, 2018, 10.5281/zenodo.1206261, <https://doi.org/10.5281/zenodo.1206261>
- [97] L. Dagum, R. Menon, OpenMP: an industry standard API for shared-memory programming, *Computational Science & Engineering*, IEEE, Vol. 5, pages 44-55, 1998
- [98] C. Pheatt, Intel threading building blocks, *Journal of Computing Sciences in Colleges* archive Volume 23 Issue 4, April 2008, Pages 298-298
- [99] J. Nickolls et al., Scalable Parallel Programming with CUDA *ACM Queue*, vol. 6 no. 2, March/April 2008, pp. 40-53
- [100] <https://github.com/MultithreadCorner/TCode>
- [101] F. Cenna et al., "Weightfield2: A fast simulator for silicon and diamond solid state detector", *Nucl. Instrum. Methods*, vol. 796, pages 149-153, 2015
- [102] S. Spannagel et al., "Allpix2: A modular simulation framework for silicon detectors", *Nucl. Instrum. Methods*, vol. 901, pages 164-172, 2018
- [103] M. Brigida et al., "A new Monte Carlo code for full simulation of silicon strip detectors", *Nucl. Instrum. Methods*, vol.533, pages 322-343, 2004

- [104] W. Kutta: Beitrag zur nherungsweise Integration totaler Differentialgleichungen, Z. Math. Phys., vol. 46, 1901, pages 435-453
- [105] C. Runge: ber die numerische Auflsung von Differentialgleichungen, Math. Annalen, vol 46, 1895, pages 167-178,
- [106] N. Minafra et al., Test of Ultra Fast Silicon Detectors for Picosecond Time Measurements with a New Multipurpose Read-Out Board,
- [107] C. Elliot et al., National Instruments LabVIEW: A Programming Environment for Laboratory Automation and Measurement Show all authors, Journal of the Association for Laboratory Automation, Volume: 12 issue: 1, page(s): 17-24 Issue published: February 1, 2007
- [108] A. Beer, Bestimmung der Absorption des rothen Lichts in farbigen Flssigkeiten, in Annalen der Physik und Chemie, vol. 86, 1852, pp. 78-88.
- [109] J. H. Lambert, Photometria sive de mensura et gradibus luminis, colorum et umbrae, Augusta, Detleffsen, 1760.
- [110] N. Palina, et al., Laser assisted boron doping of silicon wafer solar cells using nanosecond and picosecond laser pulses, Conference Record of the IEEE Photovoltaic Specialists Conference, June 2011
- [111] F. Consoli, R. De Angelis, L. Duvillaret, P. L. Andreoli, M. Cipriani, G. Cristofari, G. Di Giorgio, F. Ingenito e C. Verona, Time-resolved absolute measurements by electro-optic effect of giant electromagnetic pulses due to laser-plasma interaction in nanosecond regime, in Scientific Reports, vol. 6, n 1, 15 giugno 2016
- [112] A. Lai, Results of the TIMESPOT project on sensors and electronics developments for future vertex detectors, Oral Presentation, 12th International "Hiroshima" Symposium on the Development and Application of Semiconductor Tracking Detectors (HSTD12) at Hiroshima, Japan, 14-18 December 2019
- [113] <https://www.psi.ch/en/sbl/pim1-beamline>
- [114] <https://www.photonis.com/products/planacon>